**Citation**: Ioakim, Panagiotis (2017). A high precision accelerometer-based sensor unit for the acquisition of ultra low distortion seismic signals. (Unpublished Doctoral thesis, City, Universtiy of London)

# A High Precision Accelerometer-Based Sensor Unit For the Acquisition of Ultra Low Distortion Seismic Signals

By

**Panagiotis Ioakim**

A thesis submitted for the degree of

Doctor of Philosophy

July 2017

CITY

UNIVERSITY OF LONDON

School of Mathematics Computer Science and Engineering

*Is there a more noble cause for science other than the advancement of our profound understanding of self and our surroundings? To this end, is there a more effective way to unravel the obstacles to such understanding, other than to seek out the very root of their existence?*

*To the pillars of the past, the visionaries of the present,*

*and the influencers of the future.*

# Abstract

Over 800,000 people worldwide lost their lives to earthquakes in the last decade and on average 171 people die every day due to earthquake related damage to structures and buildings. Precisely understanding the effects ground motion has on manmade structures is crucial to making them earthquake resistant. This can only be achieved by the precise measurement, recording, and analysis of ground displacement trends during a seismic event.

Although there is a vast amount of recorded seismological data available, current technology and processing methods fail to represent accurate ground displacement over time as the considerable technological challenges have yet to be overcome.

Raw seismic data has so far been primarily acquired with instruments utilising geophone or accelerometer based sensors. These instruments produce prominent time domain displacement errors due to the various system and sensor inaccuracies, and due to non-linear response. Since accelerometers provide acceleration over time data: whilst geophones are velocimeters, and therefore provide velocity over time data; in order to derive true ground displacement over time, a double, or single numerical integration is required respectively. During this essential numerical integration processes of data from such sensors, even small in magnitude errors accumulate to yield rather large displacement trend offsets over a typical event recording period of 60 to 120 seconds. In addition, the numerical integration process itself poses considerable challenges due to the theoretically infinite number of samples and the accurate determination of initial conditions required for an exact mathematical result to be obtained. The latter, is currently performed by averaging an up to 60 second pre-event data trend stored on the instrument.

Most post-integration data from current instruments appears to contain low frequency drifts amongst other noise artefacts, and generally requires baseline correction algorithms in an attempt to correct for these effects. Such corrections, although helpful, only aid to minimise the perceived effects of an assumed and collective source of error, and hence are largely unable to tackle the individual error contribution of each element within the system. Since individual element contribution is of a dynamic nature, the validity of these algorithms is limited by the

accuracy of the initial assumptions made about a specific set of data. Faced with such a multivariable and uncertain dynamic behaviour, where even mathematical system modelling is of inadequate long term accuracy, a solution that aims to directly minimise these errors at source, rather than attempt to correct them post-acquisition, is of immense importance when it comes to the recording, analysis, and understanding of earthquakes.

This thesis describes the design, implementation, and evaluation of a High Precision Active Gyro Stabilised (HPAGS) sensor unit of exceptional performance for the provision of highly accurate ground displacement data. Experimental results demonstrated that the device described herein, was able to diminish the inherent non-linear and environment-dependant effects of current sensors, and thus was able to provide highly improved time domain displacement data.

# Acknowledgements

I would like to thank all those who have directly and indirectly helped make this work possible. In particular, I would like to thank my parents for their unconditional and continual support, and their tireless encouragement throughout the years.

A special thanks to my wonderful partner Jenny for her unwavering faith, support, and trust in me and my work, during the good, and during the difficult times. Thank you for being such a fantastic and positive influence in life.

My children Sophia and Helena, who have shown great understanding of my frequent absence of mind; Lottie and Sally, who have grown to sympathise with the amount of work such an undertaking requires, and everyone's kind moral support.

My good friend and fellow engineer Mr Enyi Ogbuehi, for acting as my sounding board for even the most off-the-wall ideas.

I would like to thank Dr Andrew Chanerley for introducing me to the exciting field of seismic instrumentation, and the numerous members of staff at the University of East London for their support.

The staff at City University of London: Professor Nicholas Karcanias for his most welcoming attitude towards my research project, Professor Panos Liatsis for all his advice and research support which lead to my research fellowship at the university, Dr Stathis Milonidis for his support in the role as my second supervisor, and of course, I would like express my greatest gratitude to my exceptional supervisor and now friend Dr Iasonas Triantis, for his excellent moral support, his outstanding academic mentoring, and his extraordinary efforts beyond expectation to guide me to the successful completion of this work. I thank you.

Thank you all.

# Table of contents

*I hereby certify as the author, that to the best of my knowledge, the content of this thesis is exclusively my own work, and that any inclusions and references to other work have been appropriately acknowledged.*

*P. Ioakim*

# List of figures and tables

## *Chapter 1*

## *Chapter 2*

## *Chapter 3*

## *Chapter 4*

***Chapter 5***

# Glossary of terms

| | |
|---|---|
| **1/f noise** | Noise with a power spectral density inversely proportional to its frequency |
| **Accelerometer** | A device that measures acceleration ( rate of change of velocity) |
| **Belt (seismic)** | A narrow geographic zone on the surface of the Earth along which earthquake activity occurs. |
| **Brownian motion** | Random motion of particles resulting from their collision with fast-moving atoms or molecules in the medium |
| **Brownian noise** | Signal noise produced by Brownian motion, also known as thermomechanical |
| **Convolution** | A mathematical operation on two functions resulting in another function |
| **Critical damping** | Damping which enables the system to attain steady state at the shortest time without oscillations |
| **Cross-axis sensitivity** | The amount of output that is observed on the sensing axis stemming from accelerations on a perpendicular axis |
| **Damping** | The reduction in amplitude of an oscillation by frictional or other resistive forces |
| **Damping coefficient** | The ratio of damping to critical damping. |
| **Decimation** | The process of reducing the sampling rate of a signal |
| **De-convolution** | The inverse of convolution. See *convolution* |
| **Elastic propagation** | The propagation of waves through solid (elastic) matter |
| **Epicentre** | The point on the Earth's surface that is directly above the point of origin of an earthquake |
| **Fault** | A fracture along which the blocks of Earth's crust on either side have moved relative to one another |
| **Gain Bandwidth product** | The product of an amplifier's bandwidth and gain at which the bandwidth is measured |
| **Geophone** | A device that converts ground movement (velocity) into voltage utilising a moving magnet within a coil |
| **Ground tilt** | The deviation of the ground from what is accepted to be horizontal during an earthquake |
| **Homogeneous fluid** | A fluid that has the same proportions of its components throughout a given sample, thus uniform in composition |
| **HPAGS Sensor** | High Precision Active Gyro-Stabilised Sensor |
| **Hypocentre** | The point within the Earth where an earthquake rupture starts |
| **Least squares regression** | A statistical method used to determine a line of best fit by minimizing the sum of squares created by a mathematical function |
| **Long period instrument** | An instrument in which the resonant frequency is very low, usually designed for seismic signals in the range 1 Hz to 10 Hz |
| **Mantle** | The part of the Earth between the core and the crust |
| **MEMS Sensors** | Miniature sensors incorporating mechanical structures and electronic circuits |
| **Micromachining** | The technique for fabrication of structures on the micrometer scale |
| **Near-field Earthquake** | An earthquake which occurs close to the fault. See *fault* |
| **Piezoelectric effect** | The ability of certain materials to generate a voltage when subjected to mechanical stress or vibration |
| **Piezoresistive effect** | A change in the electrical resistivity of a material when mechanical stress is applied |
| **Polysilicon** | A high purity, polycrystalline form of silicon |
| **RS232** | A standard for serial communication transmission of data |
| **Short period instrument** | An instrument in which the resonant frequency is high, usually designed for seismic signals in the range 0.01 Hz to 0.1 Hz |
| **Slew Rate** | The maximum rate at which a system can respond to an abrupt change of input |
| **Spline** | A mathematical function defined piecewise by polynomials |
| **Subduction zone** | A point at which one tectonic plate is forced underneath another |
| **Tectonic plates** | Sub-layers of the Earth's crust that move independently over the mantle |
| **Zero length spring** | A specially designed coil spring that would exert zero force if it had zero length |

# Chapter 1

## Introduction

***Earthquake****: A sudden violent shaking of the ground, typically causing great destruction, as a result of movements within the earth's crust or volcanic action.*

*(Oxford dictionary)*

### 1.1 Preface

Nearly fifty thousand noticeable earthquakes occur every year on Earth, out of which one hundred are capable of - often devastating - damage to buildings. Over the recorded history of mankind, earthquakes have been responsible for the deaths of millions of people and the destruction of entire cities.

**Figure 1** Pescara del Tronto earthquake, central Italy, 2016. (Source: REUTERS/Adamo Di Loreto)

Most earthquakes occur in regions termed *belts*, which are coincident with the Earth’s tectonic plate margins. One of the most prominent and active belts, responsible for nearly 80% of seismic energy, is the Circum-Pacific belt, affecting New Zealand, Japan, Alaska, and the coasts of North and South America.

Tectonic earthquakes are the result of sudden relative movement of the Earth's surface plates. As these plates are in continuous motion, anomalies on their boundaries tend to cause localised frictional resistance, resulting in a large build up of energy. Stresses exceeding the natural strength of the retaining material, inevitably cause a sudden release of energy which manifests itself as a fracture or slip that can extend to several kilometres. The relative ground movement caused by these fractures is usually small, however on occasion tectonic movements will generate major earthquakes such as the 1906 San Andreas Fault event, where the ground was displaced horizontally by nearly 6 meters.

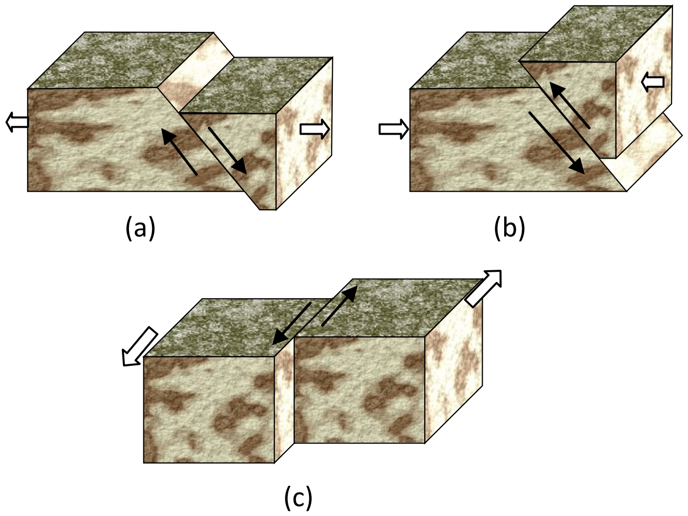

**Figure 1.1** Tectonic plate faults. (a) Normal fault. (b) Reverse fault. (c) Strike-slip fault

Tectonic plate movement can manifest itself in different ways, all capable of causing large magnitude earthquakes: It can be vertical in nature, where one plate sinks with respect to the other, or rises due lateral compressive forces, or it can be horizontal, where the two plates slip past each other in a coplanar fashion.

Due to the considerable variation in seismic motion over an area, the effects of a seismic event can be difficult to directly quantify, hence *qualitative* scales of *intensity* have been used since the late 19th century. It wasn't until the development of seismographs that *magnitude* became a *quantitative* measure of the amplitude of seismic waves generated by an earthquake. In 1935 Charles F. Richter introduced his logarithmic Richter scale of magnitude, which was based on the amplitude recorded on a standard for the epoch seismometer, at a 100 Km distance from the epicentre. Table 1 depicts the effects caused by an earthquake according to the Richter scale magnitudes.

| **Magnitude (Richter)** | **Effect** | **Typical ground acceleration** |
|---|---|---|
| Up to 2.9 | Not felt by people | 1.7 – 14 mg |
| 3 – 3.9 | Felt. No damage | |
| 4 – 4.9 | Minor damage | |
| 5 – 5.9 | Some damage to structures | |
| 6 – 6.9 | Moderate damage | |
| 7 – 7.9 | Serious damage. Loss of life | |
| 8 and higher | Severe destruction. Loss of life | 0.65 – 1.24 g |

**Table 1** The Richter scale of earthquake magnitude

Seismographs are by default inertial systems and therefore their outputs are generally accelerometric. One exception is the geophone sensor, which converts the inertial motion into an electrical signal by means of a magnet within a moving coil, thus able to provide a direct velocimetric output. The conversion therefore of a signal acquired by a seismograph necessitates the single or double integration of the data depending on the sensor used in order to acquire a ground displacement over time trend. The cumulative effects of the integration process hugely exaggerate any errors in the data, and in combination with systematic errors, render earthquake data inaccurate to a degree which greatly affects our understanding of them and inevitably our efforts to better protect structures from their devastating effects.

The study of early (prior to 1960s) seismic data is often thwarted by errors, as most is derived from unevenly sampled and manually digitised records. Some early data was even segmented and recombined, giving rise to various erroneous post-integration artefacts and oscillations from abrupt changes in magnitude. Filtering and inappropriate decimation practices also gave rise to phase errors which manifested themselves as erroneous velocity and displacement phenomena.

Recent technological developments such as micromachining, precision low noise integrated circuits, and encapsulation techniques, have vastly improved the stability and operation of seismometers, however, due to many inherent physical and electronic limitations, much improvement is still necessary if such instruments are to yield useful near-true to the original earthquake displacement over time data.

A vast amount of more recent seismological data exists that has been acquired primarily with instruments utilising geophones and accelerometers since the 1960s. Since these instruments employ the aforementioned velocimetric or accelerometric sensors, time domain displacement data can only be acquired after one or two numerical integration processes respectively. The data acquired from such instruments inevitably contains cumulative integration errors resulting from various inaccuracies within the instrument, which together conspire to produce rather large errors in the displacement data trends, termed *baseline offset*.

It is not atypical for a seismic data displacement trend to show after-event displacement errors in the region of several meters, whilst in reality the end ground displacement has indeed been zero. These inaccuracies are predominately caused by the instrument's electronics practical limitations, but also due to internal to the sensor non-linearities, noise, and drifts, requiring rather involved calibration processes [1][2] [3] [4].

Current data processing methodologies necessitate the use of post-digitisation algorithms to reverse such displacement errors once the true end displacement is made known, usually via the Global Positioning System (GPS). By knowing the true end displacement of the trend, and assuming a zero averaged initial condition, a spline baseline correction can be imposed as shown in figure 1.

Recently, more involved speculative post-acquisition correction algorithms [5] and various complex digital signal processing and filtering methods, have also been used in an attempt to recover a displacement trend resembling the original time domain earthquake ground motion.

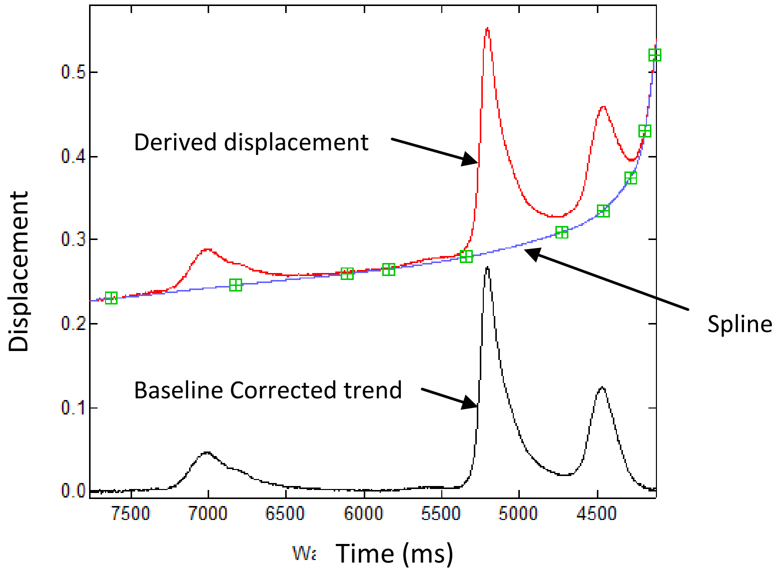

**Figure 1.2** Baseline spline correction example. (*public domain*)

Whilst these methods produce workable results, some necessitate the use of accurate GPS instrumentation with long term data averaging in order for precise end-displacement values to be acquired. More importantly, most methods assume a progressive and mathematically predictable ground motion, where in reality the true ground displacement can easily be masked within the usually exponential in nature baseline offset.

In addition to instrument based errors, external factors, other than temperature fluctuations, can also significantly interfere with the accurate acquisition of seismic data. Ground tilts and dynamic rotations occurring during strong near-field earthquakes have been shown to have a considerable effect on seismic instruments and therefore on the data derived by these [6], [7]. Although at first, correcting for such tilts and rotations may appear easily accomplishable, the fact that the centre of such rotations is not only unknown but also variable poses a rather difficult problem to solve.

It has been suggested that multi-sensor instruments could resolve rotational and translational motions simply by measuring the accelerations due to tilt motion of the instrument. Although this is theoretically possible, most methods conveniently assume a body-centric model (figure 1.3).

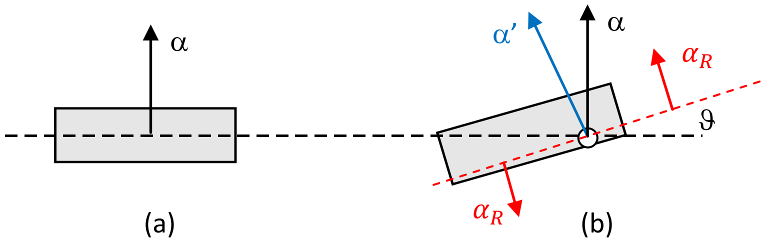

**Figure 1.3** Acceleration without rotational component (a), and with rotational component (b).

Figure 1.3(a) depicts the current use of sensors in the field, assuming a linear acceleration about the centre of the sensor (z-axis only shown here for clarity, but this holds true for all three axis x, y, and z). Current theory suggests that by utilising more sensors, such as accelerometers located at the periphery of the sensing instrument, differential accelerations marked as $\alpha_R$ in figure 1.3(b), would be detectable and therefore such motion could be mathematically describable. In real environments however, the rotational centre locations are unknown and are not body-centric. Assuming a centre of rotation a short distance away from the sensor, as shown in figure 1.4, one could argue that the acceleration difference between the resulting acceleration vectors $\alpha_n$ and $\alpha_f$ could indeed be used to estimate the rotational centre and therefore help describe the motion of the body in question. In practice however, this model does not scale up since as the centre of rotation moves further away from the body of the instrument, the smaller the acceleration differential between $\alpha_n$ and $\alpha_f$ becomes, and therefore only a matter of a short distance before this difference is within the noise floor of the instrument.

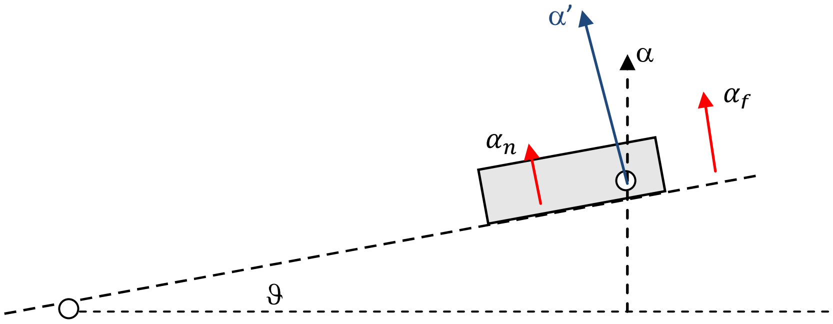

**Figure 1.4** Non sensor-concentric rotation due to acceleration.

The data corrupting effect of such tilts is of course due to the angular deviation of the sensing axis of the instrument with respect to the original frame of reference in all three dimensions. In this case, the true vertical acceleration $\alpha$ of the ground would be incorrectly measured as $\alpha'$ due to the angular displacement of the z sensing axis, where $\alpha' = \frac{\alpha}{\cos\vartheta}$ . Further, due to the rotational forces, radial accelerations will also manifest themselves as additional components on the other sensing axis, making the derivation of true motion a rather impossible task.

Seismological instruments in use to date do not have adequate, if any at all, correction abilities to address the above sources of error. Furthermore, although the necessity of recording seismic signals down to DC level has been recognised for many decades [8], due to the difficulties involved with the double integration process and initial conditions determination, some seismographs employ a High-Pass filter with a low -3dB cut off frequency of 0.1Hz or below, further adding to the distortion of the low frequency seismic waves [9].

Other effects, such as long term instrument inaccuracies due to component variations over time that can considerably add to the aforementioned errors, have also been ignored by seismic instrument manufacturers. In conclusion therefore, historic seismic records to date can be considered only as *approximations* to the original time domain seismic waves, since the data stored and processed is distorted in amplitude, phase, and sensitivity, resulting in displacement trends containing errors, sometimes in the order of several meters.

The complexity and magnitude of these errors pose a serious problem to the worldwide seismological societies attempting to analyse and understand the underlying mechanisms of earthquakes, and to those attempting to construct earthquake resistant structures.

The accurate acquisition of seismic data is essential to our understanding of earthquakes, which significantly impacts our decisions on the processes and materials used for the construction of safe buildings and public structures such as bridges. An instrument therefore capable of delivering precise seismic data could potentially provide for innovations in civil engineering and earthquake-proof structures, and even in the prediction of earthquakes, allowing for early warning systems for major catastrophic events such as tsunamis.

## 1.2 Inherent seismic sensor limitations

Modern inertial seismometers, of any physical scale, convert the motion of a point on the Earth's surface to a usable electrical signal, usually utilising a suspended inertial mass. This very principle of operation limits and distorts the true ground motion signal since the inertial mass requires to be kept in place via mechanical or electromagnetic means. Such instruments inadvertently result in an output which is dependent not only on the *amplitude* but also the *rate of change* of the input signal, therefore imposing a kind of mechanical filtering to the signal of interest.

Figure 1.5 below depicts the frequency response of a popular geophone. Geophones, although also based on the inescapable inertial mass-spring setup, unlike accelerometers, produce an output proportional to velocity rather than acceleration. The electromechanical arrangement is either a suspended moving coil arround a magnet or vice versa, resulting in a driven harmonic oscillator with an electromagnetically induced output voltage: $v \propto \frac{dx}{dt}$ where x is the displacement of the coil with reference to the magnet.

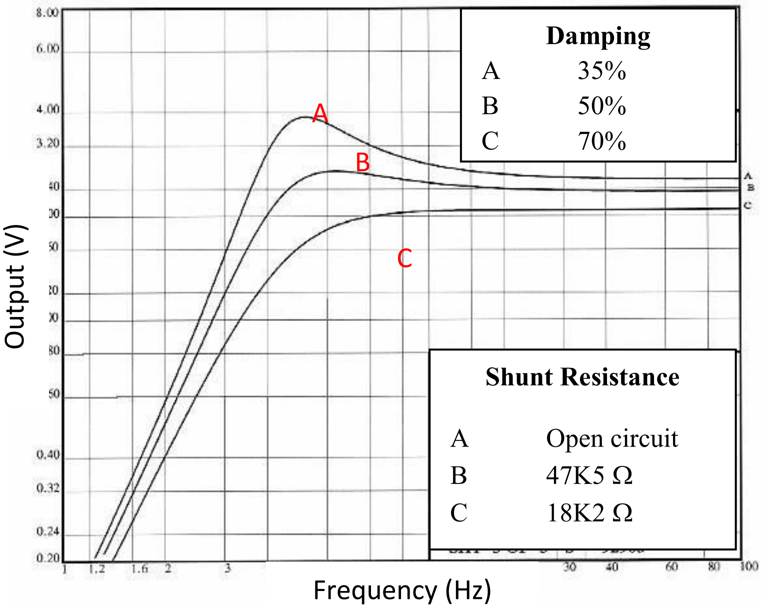

**Figure 1.5** Frequency response of a typical GS11D geophone by Geospace Technologies.

The output response of a typical geophone shown in figure 1.5 clearly indicates that although traditional geophones require a single integration in order to derive displacement data, even with corrective shunt resistors employed, their poor low frequency response deems them unusable for frequencies below 10Hz.

Micro Electro-Mechanical Sensors (MEMS) provide considerable improvement on resonance and sensitivity. The imperfect capacitance characteristics and mechanical limitations of the frequently used differential capacitance measurement mechanism however, tend to distort the signal. Inevitably, the driving electronics of the differential capacitance mechanism require an out of phase clock to be presented to the capacitor plates, which although rectified and filtered, is still present in the output signal. In addition, due to the small scale of the micro-machined inertial mass and polysilicon (Polycrystalline Silicon) springs, MEMS sensors suffer not only from Brownian and 1/f noise, but also from thermomechanical noise due to molecular agitation of the micro-scale inertial mass.

Figure 1.6 depicts the frequency spectrum of a typical unfiltered MEMS sensor output, showing both an 1/f characteristic and a near 50KHz internal clock feed-through.

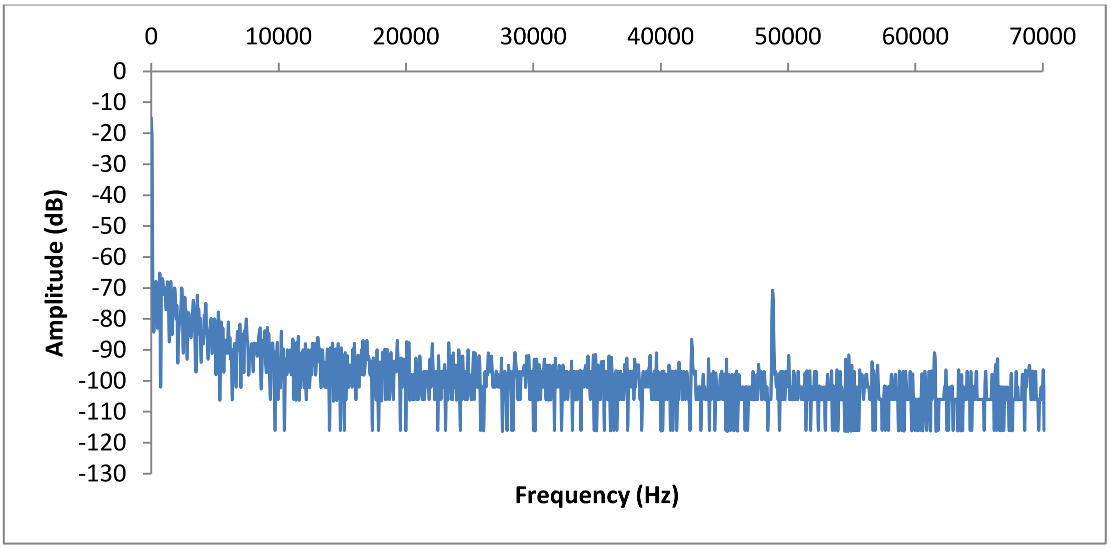

**Figure 1.6** Measured frequency spectrum of unfiltered MEMS accelerometer.

The physical constraints of such sensors along with the typical properties of systems on silicon further affect the response of such sensors yielding output non-linearity [10], temperature dependent effects on sensitivity [11], and various bias and cross-axis sensitivity related errors [12]. Even devices employing optical and mechanical-optical arrangements still suffer from these inherent errors due to the inescapable nature of the electromechanical arrangement [13] [14].

The necessary interfacing electronics are also subject to noise, drifts, and offsets, and the Analogue to Digital Conversion (ADC) process itself adds to the distortion of the original signal.

Digital Signal Processing (DSP) offers methods to model and represent these sensors effectively, but in truth, the practical difficulties of obtaining accurate impulse system response via electromechanical means and deriving representative transfer functions alone, make these methods far from mathematically exact. Although such algorithms perform relatively well, it is understood that they only operate inside a rather wide tolerance range, as the accuracy of the resulting response, even in the short term, is always only as accurate as the apparatus employed to derive it. It could be argued that if the provision of highly accurate mathematical models derived by testing in tightly controlled environments was realisable, accurate data from such sensors could then be recovered by direct de-convolution. Unfortunately however, such sensors suffer from a multitude of external dynamic interferences [15], internal drifts and changes, making their mathematical modelling very difficult if not impossible to construct with any accuracy. [16]

## 1.3 The need for an improved seismic sensor

The difficulty of precise seismic data recovery is of course due to the problem that a clear separation of the observer from the phenomenon observed cannot be readily accomplished, since the observer in this case is part of, resting on, the object of observation, namely the Earth. This has led to errors in the understanding of the behaviour of seismic waves which have in turn manifested themselves into instrument designs anticipating to measure such erroneous behaviour. One major such assumption has led to the design of only linear acceleration seismographs to this date, although dynamic ground tilts and rotations were observed and found to be of a large enough magnitude to distort the seismic data some decades ago. It is also becoming more evident that not only acute dynamic tilts are of importance during strong motion recordings, but post-event displacements and asymmetrical soil dynamics too can corrupt and impose hysteretic characteristics on the seismic data, as can very low frequency ground undulations. [17]

Many of the above sources of error conspire to give rise to the by far the most prominent observable effect of data corruption in the time domain, even with modern instruments; the "*runaway effect*" or "*Baseline Error*". This most frequently encountered error is characterised by erroneous linear velocity and exponential ground displacement trend offsets, derived from the original raw acceleration data via a numerical integration process. This baseline error completely invalidates the derived velocity and displacement trends, as assumptions to its nature are made in order to secure an artificial baseline of zero offset error. This is usually accomplished by the enforcement of a corrective spline to the derived data.

Various other methods including advanced calibration and DSP techniques such as Wavelet transformation, filtering, and post-digitisation and integration corrections, have all been, and still are, employed in an attempt to reconstruct a true seismic displacement trend. [18] [19] [20] [21]

The runaway, and other related phenomena have been the focus of numerous practical data recovery and research papers due to their prominence. It can be seen in figure 1.7, which is from one such paper [22] concerned with this very effect, that even after the first integration, the velocity data trend exhibits an unnatural but characteristic gradient, inevitably resulting in a rather large quadratic in nature displacement error after the second integration.

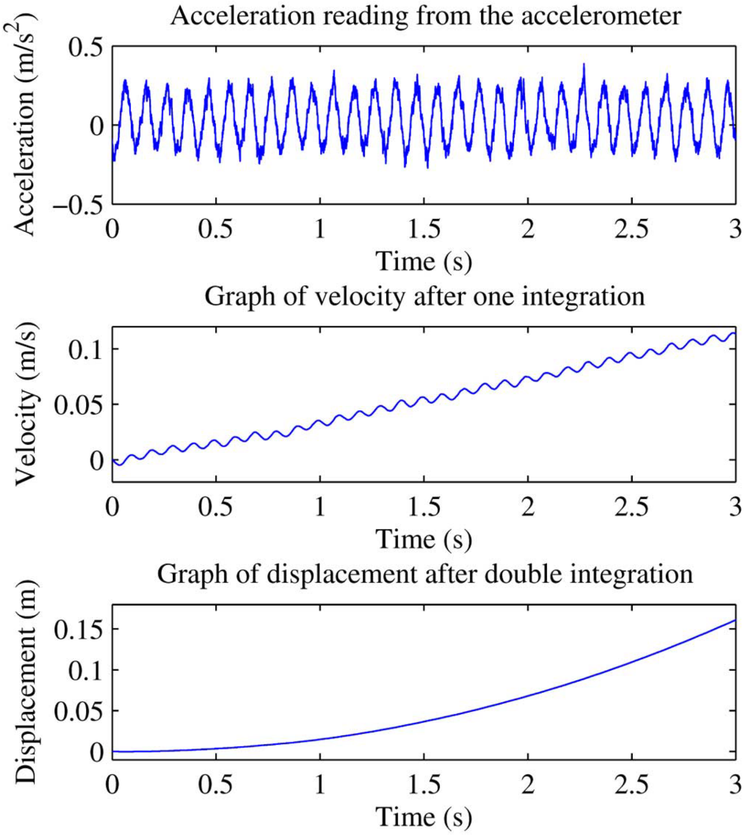

**Figure 1.7** Exemplification of baseline error [22].

It should be noted that the above trends are only of 3s in length, however in practical earthquake studies, seismic trends are normally 60s – 120s in length, resulting in much larger cumulative displacement errors in the order of several meters.

Although modern seismographs have much improved over that last decade, acceleration data derived from these is still at best difficult to work with, and at worst so erroneous, that its usefulness as a tool for the study and understanding of earthquakes can be considered at times very limited.

Much work has been done in the development of correction algorithms, filtering, calibration techniques [23] [24] [25] [26], and system models to address some of the problems associated with this type of data acquisition, but alas none of these methods addresses the root of these problems which is both time-variable and dynamic in nature. Such treatment of the effects rather than the causes tends to fail to produce consistent long term results in the complexity of real environments.

Further to the inherent electronic sources of error, mechanical constraints produce their own set of challenges when it comes to acquiring uncorrupted data, which are deeply rooted within the very construction of these instruments and their environment. Efforts to model or correct for these errors has proven of limited use due to the complexity of the real dynamic environment, where excitation is not only of linear, but also of rotational nature [27] [28] [29] [30] [31] [32] [33] [34], and the soil substrate is rarely a uniform and known quantity, therefore contributing its own asymmetrical and non-linear effects on the instrument [35].

Although it is essential to understand and attempt to correct the perceivable instrument errors [36] [37] [38] [39] [40] [41] [42], a close and in depth examination of the very sources of these errors is crucial in deriving robust solutions able to provide effective long term correction within real dynamic environments.

It is only by addressing the root of these problems rather than alleviating the symptoms, that an instrument able to recover long term accurate displacement seismic data can be constructed.

## 1.4 Motivation and project aims

Having spent my early childhood in a country prone to seismic activity, and having experienced a number of earthquakes of magnitude of over 5 in the Richter scale, I feel that I have a very personal connection with this area of research. However, it was not until few years ago – and after having acquired in depth knowledge in instrumentation - that I discovered the extent of the problems associated with the derivation of accurate seismic displacement trends from even the latest state-of-art seismometers. Many spurious artefacts in the derived displacement trends were associated with possible hysteretic instrument behaviour while others were linked to ground tilts, especially during large magnitude earthquakes. With the latter receiving much of the focus, this research originally intended to provide innovative solutions to the problems associated with dynamic and static tilts of seismic sensors in the near-field, however, during the initial research and experimental phase of this work, it became obvious that resolving the tilt problems alone would not yield any substantial improvement on the resulting data: The very significant contribution of the many overseen sensor and instrumentation error sources had to be predominantly addressed.

The objective of this work therefore is to research the multiple sources of error, internal to the instrument and external, and derive realisable solutions with the aim to create a High Precision Active Gyro-Stabilised (HPAGS) seismic sensor. The resulting six-degree-of-freedom MEMS-based seismic sensor should conceptually and experimentally prove beyond doubt, that the acquisition of highly accurate ground displacement data from accelerometric sensors is indeed a realisable possibility.

## 1.5 Novelty and contribution to knowledge

The majority of the content in Chapter 3 predominantly presents original theory and empirical evaluation of several novel methods and algorithms concerned with the correction or minimization of errors in current seismic sensing instruments. In particular: the method for the derivation of the dynamic response of a MEMS sensor, the direct generation of sensor signal dithering, the quality preservation sampling criterion, and the cross-axis sensitivity correction formulae, are all – to the author’s knowledge – both novel and a positive contribution to existing knowledge.

The realisation and experimental evaluation of the first six degree of freedom seismic sensor unit in Chapters 4 and 5, able to addresses the majority of the known and newly discovered via this research issues, also presents novel work which aims to inform the scientific society. Further, the auto-zero bias correction, and the auto gain correction circuits, along with their corresponding embedded algorithms, offer novel applications to classical feedback control and circuit theory.

Although literature which identifies some of the issues examined herein exists, there is no current literature that offers any effective solutions to these well defined problems, or indeed any literature which encompasses a unified sensor solution like the one presented in this thesis.

## 1.6 Thesis organisation

The rest of the work presented herein is organised as follows:

Chapter 2 presents an introduction to seismology and seismic waves along with the structure of the Earth in order to facilitate a basic understanding of the object of interest. It then continues with a review of seismic sensors starting with the early innovations of the recent past and onto the modern day accelerometers, analysing and discussing each with respect to their features and limitations. Sections on data acquisition, digitisation, and post-processing are also included in this chapter in order to give the reader a wider view of the current methods and technology employed in the acquisition of seismic data, from the sensor in the field, to the familiar trends on the computer screen.

Chapter 3 is partly dedicated to the description of a primary study which aims to experimentally demonstrate the magnitude of the problem regarding the baseline offset effect, and then proceeds with attempts to eliminate each of the primary sources of this error, by experimentally testing novel correction hypotheses and methodologies. The work in this chapter is presented in a logical signal progression manner: from the sensor, via the front-end electronics, to the digitising circuits.

Chapter 4 presents the physical design of the unified sensor electronics and mechanical components, and discusses the methods used to overcome the many difficulties encountered during the realisation of this type of instrument.

Chapter 5 presents experimental results which are used to substantiate conclusions on the effectiveness of the unified sensor employing the earlier conceived in this work novel hypotheses.

Chapters 6 and 7 consolidate the findings of chapters 3 to 5 into a general conclusion and propose future work to researchers wishing to continue to build upon the knowledge presented within this thesis.

# Chapter 2

## Principles of seismic data acquisition

### 2.1 Introduction to Seismology

Seismology is a rather recent science which has mainly been scientifically developed in the last century or so. Every day more than fifty earthquakes occur which are strong enough to be felt near their epicentres, and every month, some are large enough in magnitude to damage permanent structures. Several daily earthquakes occur which are not strong enough to be felt, but are able to be recorded by modern seismic instruments.

As a seismic event occurs, waves propagate from its epicentre and travel through and on the surface of the Earth. The study of the propagation of these waves has aided our understanding of the Earth's structure and has helped us identify the mechanisms of earthquake generation.

A good understanding of the nature of earthquakes is not only essential in geophysics and Earth sciences, but also in civil and structural engineering where the challenge to build earthquake-proof structures is all but too real in certain areas of the world.

Early treatment of earthquakes was understandably not very scientific and observations of volcanoes erupting whilst vibrations of the Earth were felt led to an incorrect connection between explosions and earthquakes. It wasn't until 1800 that Rayleigh, Poisson and others evolved the theory of elastic propagation which in turn determined the types of wave expected from seismic events. Compression and shear waves, termed body waves, are those that travel directly through the solid matter, where surface waves are those that travel on the surface of solids. Since compression waves travel faster than shear waves, they are usually referred to as Primary or P-Waves, whilst the slower shear waves are commonly referred to as Secondary or S-Waves.

The first noted attempt at observational seismology was in 1857, soon after a large earthquake just outside Naples attracted Irish engineer Robert Mallet to rush to Italy to record the destruction caused. He proposed that earthquakes radiate from a focal point, now termed the hypocentre, and that flowing this radial wave expansion backward one could calculate the exact geographical point of a seismic event. Mallet went on to conduct experiments using explosions to calculate wave velocities through the ground and suggested stations be constructed to monitor seismic activity.

### *2.1.1 Seismic Waves*

Seismic waves can be broadly divided into categories in accordance with their propagation properties, namely *Body* waves, which travel through solid matter, and *Surface* waves, which travel on body surfaces.

Body waves can then be subdivided into two further categories: *compression* waves, and *shear* waves. Figure 2 shows the propagation of a compression wave, where high compression regions travel through an elastic medium with areas of rarefaction (low compression regions) between them: a propagation model very analogous to sound waves in air. Compression waves are the fastest of the seismic waves and are therefore termed P-Waves or Primary Waves, since they are the first to be recorded on a seismogram and the first to be felt.

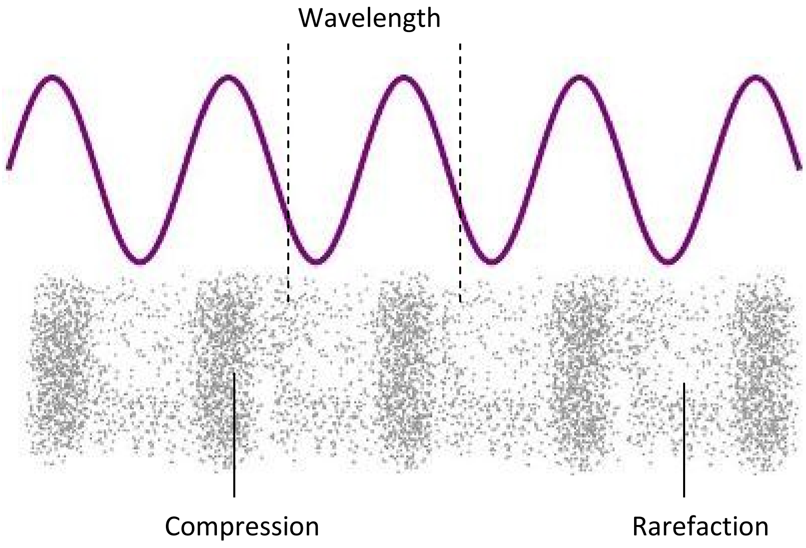

**Figure 2** The propagation of a compression wave

A Shear wave, being slower than the compression wave, oscillates perpendicularly to the direction of propagation, and due to its later arrival it is termed the S-Wave or Secondary Wave. Figure 2.1 shows the characteristic propagation of such a body wave. Although S-Waves are slower to propagate, they are usually larger in magnitude than P-Waves.

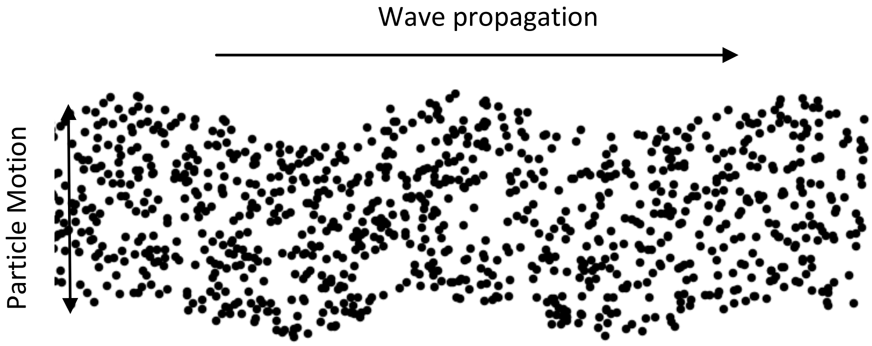

**Figure 2.1** The propagation of a shear wave

Surface waves can also be subdivided into different types of wave: *Love* waves, named after A. Love, a British mathematician who derived the mathematical model for this kind of wave in 1911, and *Rayleigh* waves, named after Lord Rayleigh who predicted their existence in 1885. Surface waves are in general larger in amplitude than body waves and in strong earthquakes can produce displacements of several centimetres.

Love waves are the fastest surface wave and move the ground from side-to-side, perpendicular to wave propagation, much like shear waves but confined on the surface, hence producing only horizontal motion. These transverse waves are typically the largest of all other seismic waves and although they quickly decay with depth, on the surface, they can travel vast distances as their amplitude decays only proportionally to $\frac{1}{\sqrt{r}}$ where r is the distance travelled. Due to this slow decay and large amplitude, Love waves are very destructive outside the immediate epicentre zone.

Rayleigh waves, unlike Love waves, include both longitudinal and transverse motions that decrease exponentially in amplitude as distance from the surface increases. Their decay on the surface is governed by the same physical laws as for the Love waves and therefore their slow decay and rolling motion also make them very destructive. Their nature makes them one of the most important waves in seismology and structural testing, as they tend to force surface particles into elliptical motion which is parallel to the direction of travel of the wave, but also with the major axis normal to the surface. Not only they displace in all directions, but they also "roll" and tilt the structures on the earth's surface, as shown in figure 2.2, and hence are termed *ground roll* in seismology.

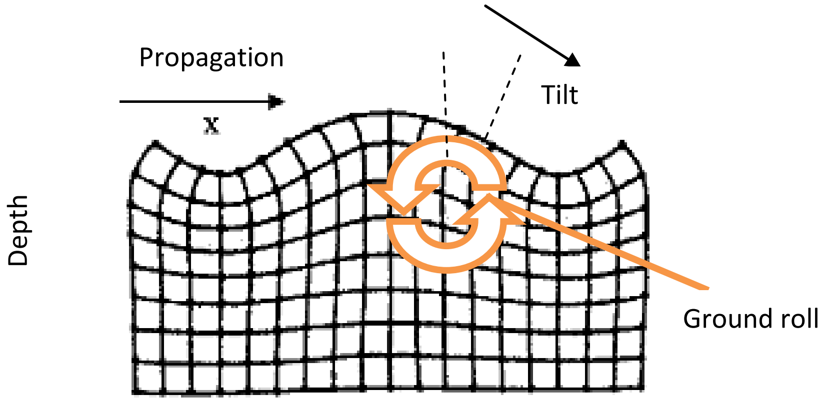

**Figure 2.2** Ground roll motion of Rayleigh waves

Figure 2.3 shows a typical seismic recording in which the comparatively different time of arrival and magnitudes of the above waves can be clearly distinguished. P-Waves arrive first, followed by similar magnitude S-Waves, and then the rather larger in magnitude Surface Waves arrive, composed of both Love and Rayleigh Waves. It should be noted that in the accelerograph of figure 2.3, time proceeds from left to right. Also, the Love and Rayleigh waves form different comparative amplitude waveforms in the Surface wave region of the response depending on the axis examined.

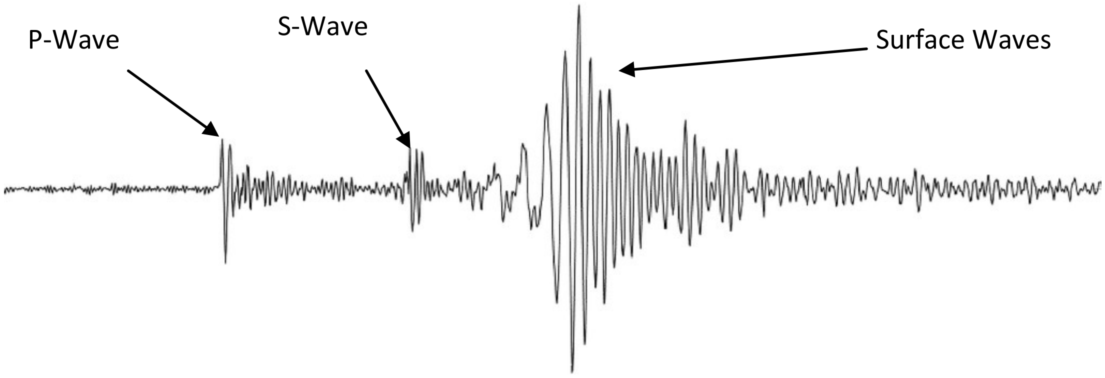

**Figure 2.3** A typical seismograph record of one axis

### *2.1.2 The Earth's structure*

A cross-section of the Earth is shown in figure 2.4 which can be broadly divided into the *crust*, the *mantle*, the *outer* core and the *inner* core. The thickness of the crust varies from 6 Km under the oceans, to 50 Km on the continents.

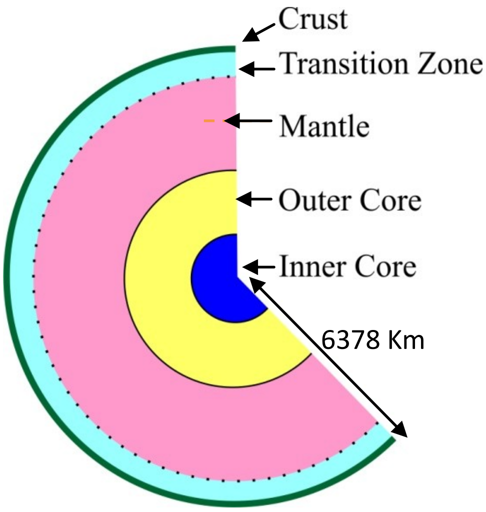

**Figure 2.4** Earth's structure

The mantle is a solid mass which constitutes nearly 84% of the Earth's volume. Seismic waves travelling through the mantle increase in velocity gradually with depth and in line with general expectation due to changes in temperature and pressure. This typical uniform substrate behaviour is generally observed within the mantle, with the exception of a region on the upper mantle termed the transition zone, located between 300 and 700 Km depth. Waves from the crust passing through this region experience a rather rapid velocity increase before entering the more uniform bulk of the mantle.

The outer core, which is liquid, encloses the solid inner core which is believed to be mainly composed of iron. P-Waves moving from the mantle to the outer core experience a sudden decrease in their velocity, before a steady increase occurs once again with increase of depth at a rate consistent of a homogeneous fluid. S-Wave velocity however, reduces to zero within the outer core as shear waves cannot propagate in liquids. It should be noted that seismic waves propagating through the Earth which is a medium of variable density and composition, exhibit typical wave behaviour such as refraction and reflection off the boundaries. This yields a much more complex seismic trend as multiple instances of the same wave can appear at different times depending on the length of the path travelled. This in combination with surface bound waves can indeed produce rather dynamic and unpredictable excitation stimuli to the seismic sensors on the crust.

### *2.1.3 Early seismographs*

Early seismographs were predominantly based on undamped pendulums unable to record time and unable to provide valid data for the length of the Earthquake. The first instrument able to record time was built by Filippo Cecchi in 1875, and soon after, many more improved versions made their appearance in Japan, including horizontal pendulums.

The first North American seismograph was installed in California near San Jose in 1897, which also recorded the 1906 San Francisco earthquake.

Due to the completely undamped nature of the pendulous sensors, early instruments would acquire resonance and distort the data shortly after the very few seconds of the event. It wasn't until 1898 when E. Wiechert introduced the first seismometer utilising viscous damping and therefore able to provide better quality data for the duration of the Earthquake.

It was not until the 1900's that B. Galitzen developed the first seismograph utilising electromagnetic induction via the pendulum arrangement, in order to produce a current in a coil proportional to the velocity component of the seismic event. Based on this revolutionary in its time approach, many seismographs were constructed and installed forming some of the first seismograph networks round the world. It was this sudden availability of seismograms that boosted experimental seismology with which by 1909 the identification of P and S waves, the presence of the Earth's core, and the existence of the transition zone were established. Continuous study of seismograms and earthquake locations lead to the discovery of plate tectonics in the 19060s and therefore the realisation of the primary mechanism of earthquake generation. The motion of the plates is of course what has and still is forming our planet, with the plates moving apart in the mid oceanic ridges causing continental drift, and being recycled back into the mantle in the subduction zones. In areas of shear faults, such as the San Andreas fault, the plate movement is transverse and a sudden release of built up pressure across the length of such a boundary can result in earthquakes of catastrophic magnitude.

A surge in funding for seismology followed the detection of a Russian nuclear bomb explosion by seismographs in 1949, and by 1961 the Worldwide Standardised

Seismograph Network (WWSSN) was in place comprising long and short period seismometers.

The 1960 great Chilean earthquake provided data able to establish for the first time the Earth’s natural resonance frequencies. It was found that the Earth can resonate for several days after a large magnitude earthquake. By 1972 the Apollo missions had placed seismometers on the lunar surface and the first moonquakes were recorded, whilst in 1976, Viking 2 placed a seismometer on Mars.

Various technologies have been employed to acquire both linear [43] [44] [45], and rotational [46] [47] [48] [49] [50] [51] [52] [53] [54] [55] [56] [57] seismic data, and even with the advent of newer technologies such as the Global Positioning System (GPS) [58], with the exception of very few [59], all are primarily based on the original inertial mass principle. Unlike some modern integrated sensors however, which due to their small size have also found other commercial applications [60] [61], early seismometers were large by comparison instruments. A typical mass spring inertial arrangement is shown in figure 2.5 below.

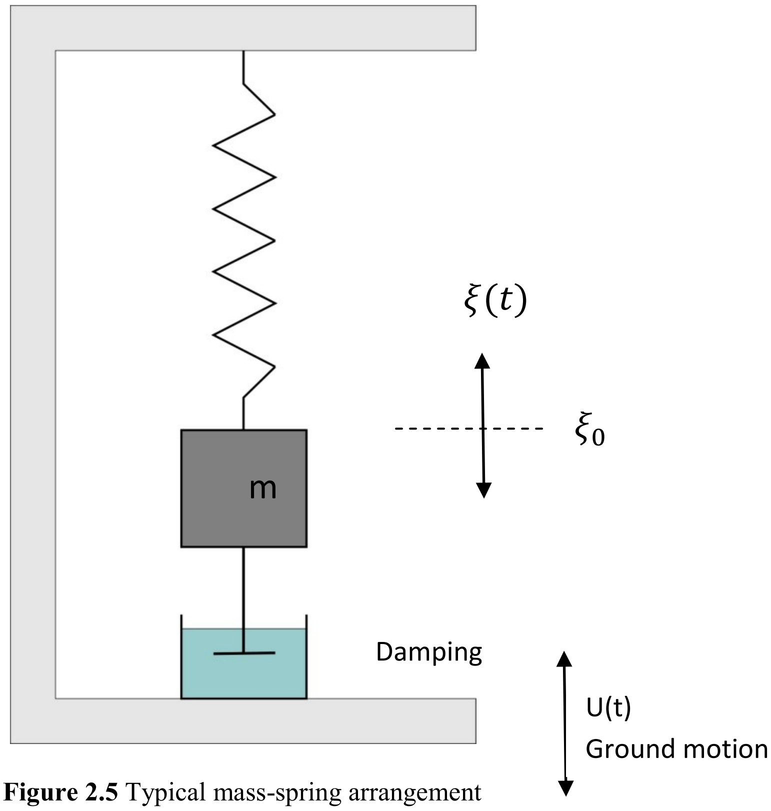

**Figure 2.5** Typical mass-spring arrangement

If just enough damping is provided by the damper in order to stop the mass oscillating excessively near its resonant frequency, then logically it can be deduced that the ground motion of the Earth u(t) can be described as a function of the motion of the mass $\xi(t)$. With the system initially at rest, a rapid upward movement of the Earth would result in the momentary extension of the spring, due to the mass' inertia, shortly followed by the acceleration and movement of the mass in the direction of the Earth's motion. With reference to the frame (which is the same as the ground) the mass initially appears to move downwards as the Earth moves upwards and therefore a phase difference must exist between the two. Extending this notion further, a high frequency sinusoidal ground motion would result in a stationery mass in space, achieving an opposite and proportional in amplitude movement to that of the Earth, in which case the seismometer would be recording true ground displacement with reference to the frame, and with a phase difference of $\pi$.

This is not however the case with low frequency ground motion, as the mass would be able to follow the motion of the ground closely resulting in very small relative mass movement and very little phase difference.

At a ground motion equal to the natural frequency of the system, maximum mass displacement would result and uncontrolled resonance if no damping was present. A critically damped system would therefore produce no resonant overshoot and near linear phase over the frequencies of interest.

If $\xi(t)$ is the displacement of the mass m with respect to the Earth, and $u(t)$ is the vertical Earth displacement, the absolute displacement of the mass is therefore:

$$\xi(t) + u(t) \tag{1}$$

The spring will exert an opposing force $F_s$ to the mass displacement in accordance to Hook's law:

$$F_s = -k\xi \tag{2}$$

where k is the spring constant, while the viscous dumper will exert a force $F_d$ proportional to the velocity of the mass:

$$F_s = -D\frac{d\xi}{dt} \tag{2.1}$$

where D is the dumping constant. Equating the forces using $F = ma$ we obtain;

$$-k\xi(t) - D\frac{d\xi(t)}{dt} = m\frac{d^2}{dt^2}[u(t) + \xi(t)] \tag{2.2}$$

Rearranging:

$$\ddot{\xi} + \frac{D}{m}\dot{\xi} + \frac{k}{m}\xi = -\ddot{u} \tag{2.3}$$

or

$$\ddot{\xi} + 2\epsilon\dot{\xi} + \omega_0^2\xi = -\ddot{u} \tag{2.4}$$

where the natural frequency of the undamped system (D=0) is $\omega_0 = \sqrt{\frac{k}{m}}$ , and the damping is described by $\epsilon = \frac{D}{2m}$ .

Examination of equation 2.4 confirms that for frequencies much higher than $\omega_0$, acceleration is high and therefore the term $\ddot{\xi}$ dominates the left hand side, therefore $\ddot{\xi} \cong -\ddot{u}$ and so the sensor responds to *displacement*. For frequencies lower than $\omega_0$, the term $\omega_0^2\xi$ dominates and therefore the sensor responds to *acceleration*, as $\xi \cong \frac{-\ddot{u}}{\omega_0^2}$

Based on the above mathematical relationships, equipping the mass with a simple stylus in a very low natural frequency system yields a simple seismograph, whilst a system with high natural frequency and means of measuring relative mass displacement yields an accelerometer. A moving coil attached to the mass over a stationery magnet on the other hand results in a velocity sensor. The characteristic of the sensor of course is also dependant on damping coefficient. Figure 2.6 depicts the response of such a second order system to a unity step input at different damping values varying from 0 to 1.4 in incremental steps of 0.2.

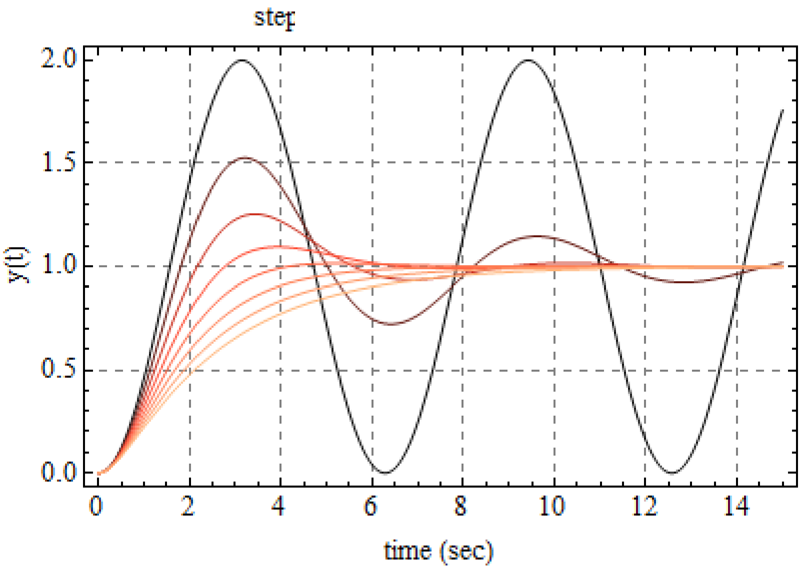

**Figure 2.6** Second order system response to a step function at various damping rates (public domain)

Since an arbitrary signal can be resolved into a sum of harmonics according to Fourier, we can generally assume a harmonic input ground motion signal $u(t) = e^{-i\omega t}$, where ω is the angular frequency, and assuming that the sensor is a linear system, the output should also be harmonic in the form $\xi(t) = X(\omega)e^{-i\omega t}$.

It then follows:

$$\ddot{u} = -\omega^2 e^{-i\omega t} \tag{2.5}$$

$$\dot{\xi} = -i\omega X(\omega)e^{-i\omega t} \tag{2.6}$$

$$\ddot{\xi} = -\omega^2 X(\omega)e^{-i\omega t} \tag{2.7}$$

Therefore:

$$\ddot{\xi} + 2\epsilon\dot{\xi} + \omega_0^2\xi = -\ddot{u} \implies -\omega^2 X(\omega)e^{-i\omega t} - 2\epsilon i\omega X(\omega)e^{-i\omega t} + \omega_0^2\, X(\omega)e^{-i\omega t} = \omega^2 e^{-i\omega t} \tag{2.8}$$

$$\Rightarrow X(\omega)(-\omega^2 - 2\epsilon i\omega + \omega_0^2)e^{-i\omega t} = \omega^2 e^{-i\omega t} \tag{2.9}$$

$$\therefore\ X(\omega) = \frac{-\omega^2}{\omega^2 - \omega_0^2 + 2\epsilon i\omega} \tag{2.10}$$

where $X(\omega)$ is the complex instrument response to a ground motion $e^{-i\omega t}$ which can be written in terms of amplitude and phase as follows:

$$X(\omega) = |X(\omega)|e^{i\varphi(\omega)} \tag{2.11}$$

where

$$|X(\omega)| = \frac{\omega^2}{\sqrt{[(\omega^2 - \omega_0^2)^2 + 4\epsilon^2\omega^2]}} \tag{2.12}$$

$$\varphi(\omega) = -\tan^{-1}\frac{2\epsilon\omega}{\omega^2 - \omega_0^2} + \pi \tag{2.13}$$

Figure 2.7 below shows graphically that resonance occurs as the frequency of the ground motion $\omega$ approaches the natural frequency of the system $\omega_0$ resulting in high amplitude response if the damping is sufficiently lower than critical.

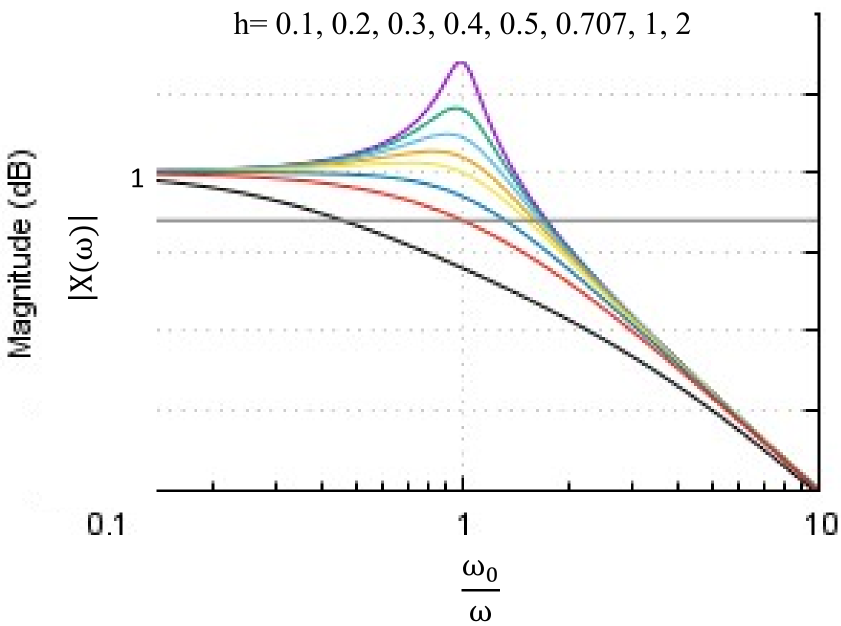

**Figure 2.7** Natural resonance of systems (public domain)

For frequencies much greater than the natural frequency $\omega \gg \omega_0$, the amplitude $|X(\omega)| \to 1$, and the phase $\varphi(\omega) \to \pi$, as seen in figure 2.8 below. The seismometer therefore responds to ground displacement, but with a phase shift of π.

For frequencies much less than the natural frequency, $\omega \ll \omega_0$, the amplitude $|X(\omega)| \to \frac{\omega^2}{\omega_0^2}$ , and the phase $\varphi(\omega) \to 0$, thus the seismometer responds to ground acceleration with zero phase. As mentioned earlier, the shape of the response depends on the damping coefficient represented by h, where $h = \frac{\epsilon}{\omega_0}$.

Evidently, both $\omega_0$ and h must be appropriately considered in order to create a useful instrument. So a purely mechanical seismometer utilising a stylus to record ground displacement requires a very low natural frequency, or in terms of actual construction, a very large mass needs to be suspended by very soft springs, which clearly presents huge practical limitations when considering low seismic frequencies in the order of 0.01Hz.

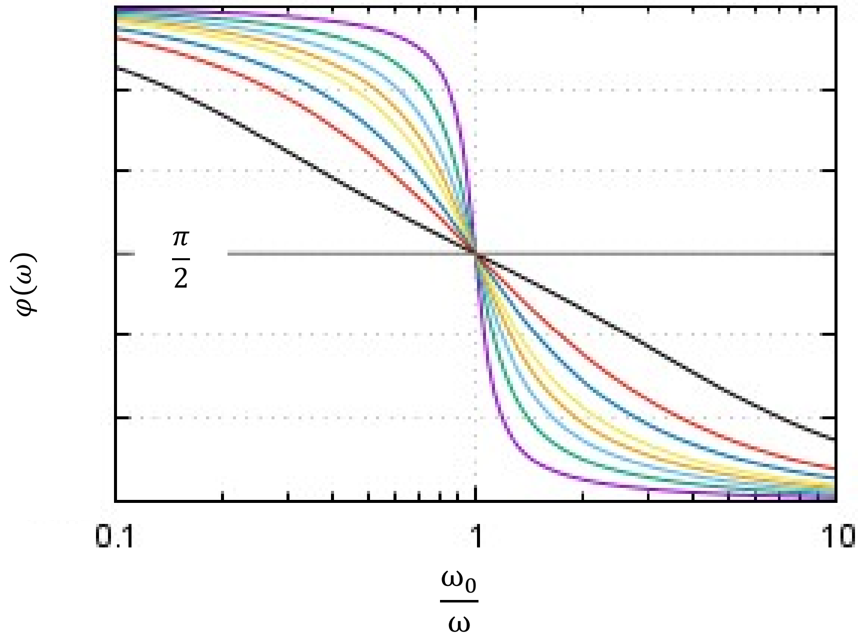

**Figure 2.8** Phase response of systems (public domain)

Similarly, a velocity meter constructed from a mechanical seismometer but with a moving coil round a stationary magnet, or vice versa, produces a voltage output proportional to the velocity of the inertial mass, and also suffers from the same practical limitations when considering the lower frequency seismic spectrum.

A diagrammatic velocity transducer arrangement is shown in figure 2.9 below.

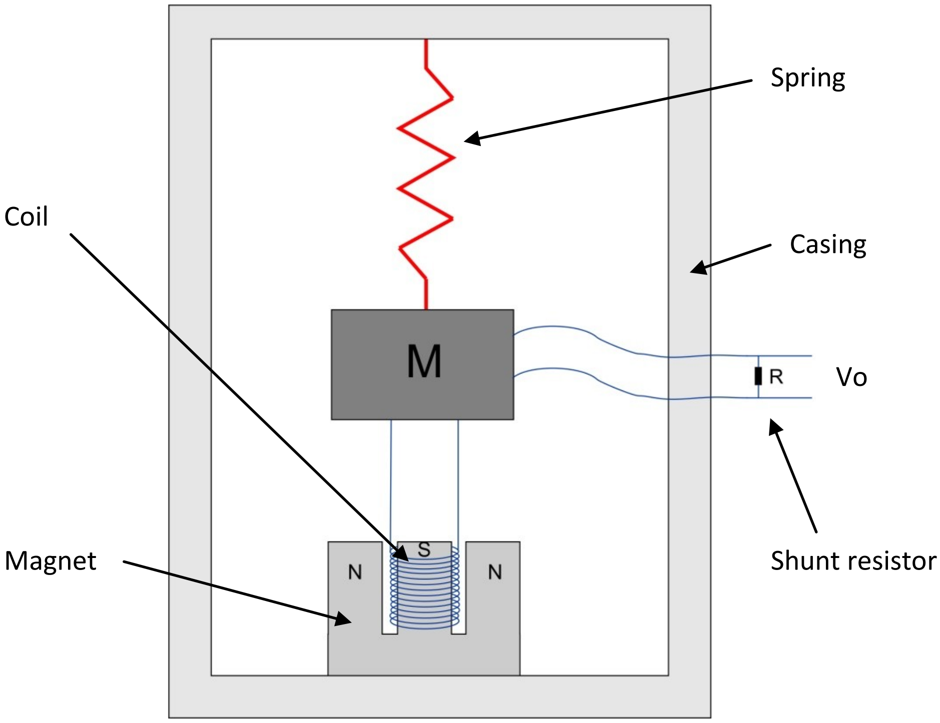

**Figure 2.9** Velocimeter arrangement

In such a transducer, damping can be simply achieved by loading the coil with a shunt resistor R in order to produce the desired response. Responses to different values of shunt resistance were shown in figure 1.3 for a typical geophone, which is of course a velocity sensor.

A true broadband sensor then can only be achieved by a high natural frequency accelerometer where $\omega_0 \gg \omega$.

The concluded responses of a mechanical sensor with $\omega_0 = 1Hz$, a mechanical sensor with velocity transducer also with $\omega_0 = 1Hz$, and an acceleration sensor with $\omega_0 = 100Hz$, are shown in figure 2.10 for clarity.

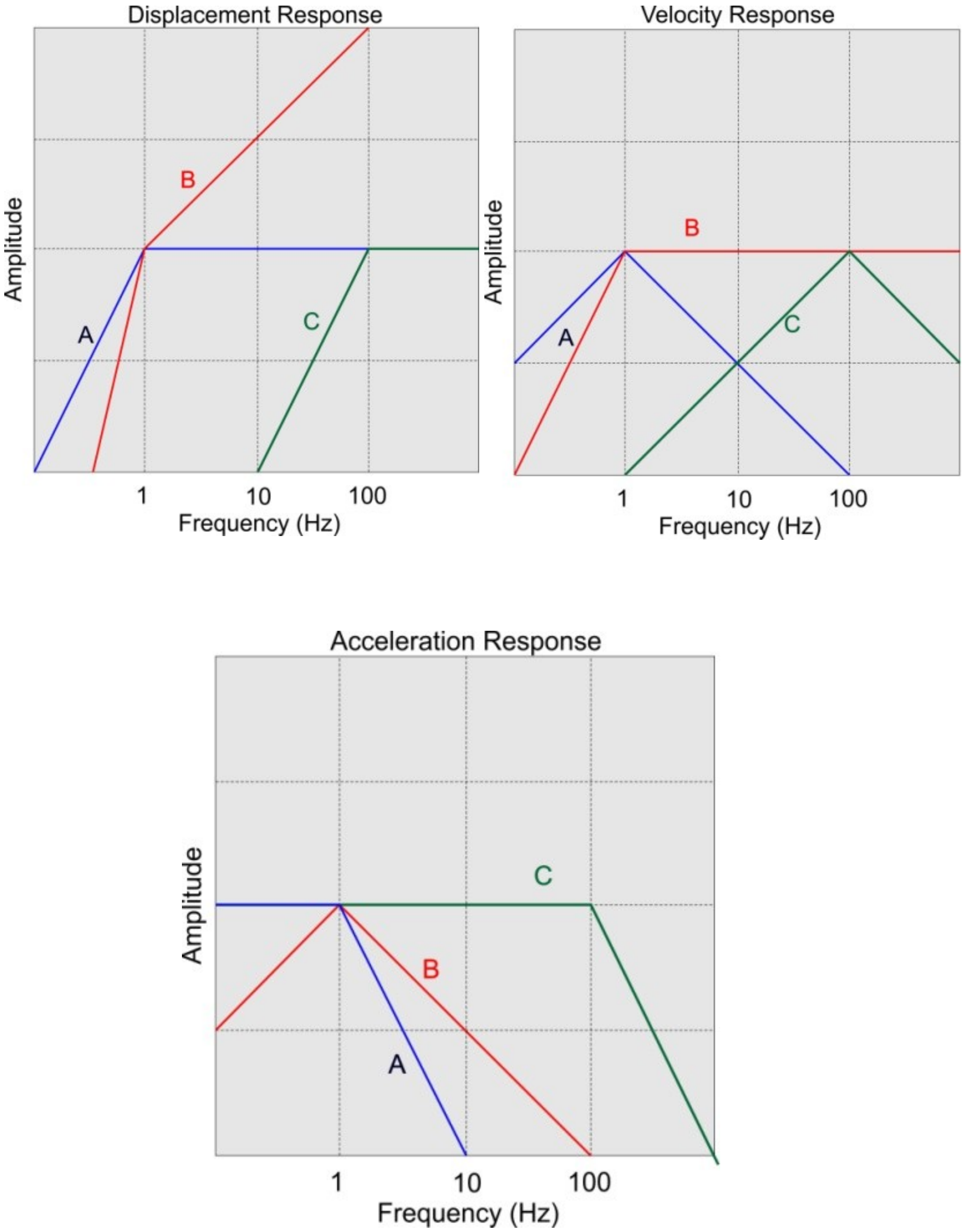

**Figure 2.10** Frequency, velocity and acceleration responses of **(***A) Mechanical Sensor: (B) Velocity Sensor: (C) Acceleration Sensor* (public domain)

Since the practical difficulties of producing low natural frequency sensors using a mass-spring arrangement were insurmountable, several designs focusing on pendulums and pendulums with springs evolved. When considering a pendulum, the natural frequency given by:

$$\omega_0 = \sqrt{\frac{g}{l}} \tag{2.14}$$

where g is the acceleration due to gravity, and l is the pendulum length. Whilst increasing the length would result in a smaller natural frequency, huge lengths would be required for achieving the lower frequencies of interest in seismology. However, reducing g, or more precisely, reducing the effect of g on the system, would also achieve a reduction of $\omega_0$. One such mechanical arrangement "the garden gate" for a horizontal seismometer is depicted in figure 2.11. In this arrangement the restoring force exerted on the near horizontal pendulum is $F \propto g \sin\alpha$ and therefore the natural frequency of the system is described by:

$$\omega_0 = \sqrt{\frac{g \sin\alpha}{l}} \tag{2.15}$$

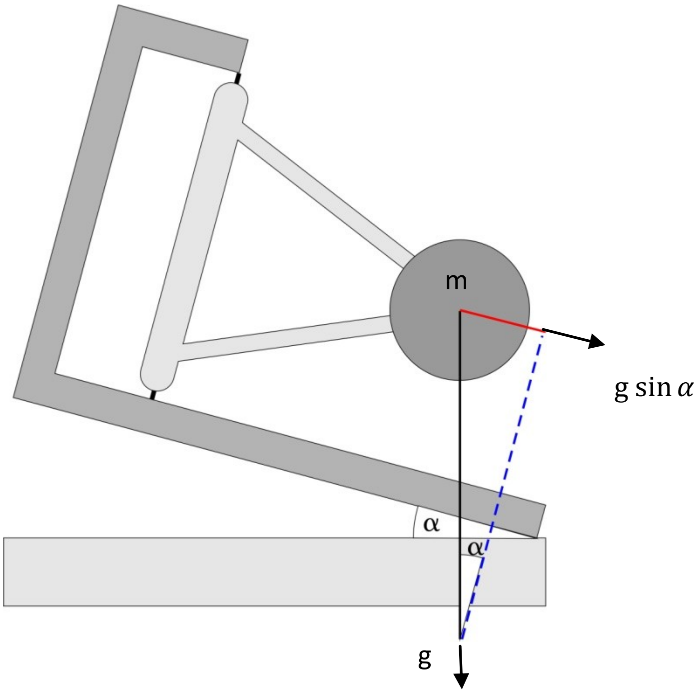

**Figure 2.11** The "Garden gate" arrangement

Garden gate seismometers have obtained in practice natural frequencies down to 0.05 Hz, however, as expected, these sensors are very susceptible to even the smallest changes of instrument tilt. Several of these very early type seismometers are still in use round the world.

Another early design was the "inverted pendulum" arrangement in which an inverted pendulum was held vertical by two opposing springs as depicted in figure 2.12 thus reducing the effect of g on the mass when off centre and resulting in a much smaller restoring force. Some very large scale instruments based on this design were built, with large masses as big as 1 ton and achieving natural frequencies down to 0.1 Hz.

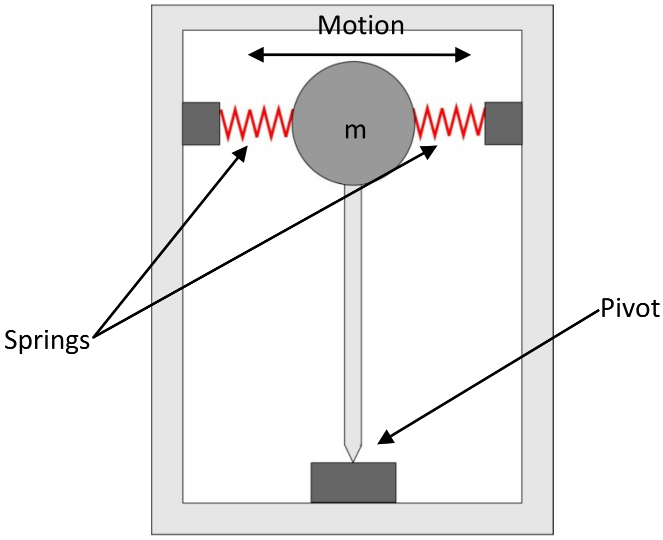

**Figure 2.12** Inverted pendulum arrangement

Inverted pendulum seismometers are reportedly the longest serving designs and many of these instruments are still in use worldwide to date.

In an effort to produce a low natural frequency sensor but for vertical motion, LaCoste invented the "LaCoste" seismometer in 1934 which in theory achieves an infinite natural period, in other words, the restoring force is zero at every point of its motion. The mechanical arrangement utilising a zero length spring is shown in figure 2.13.

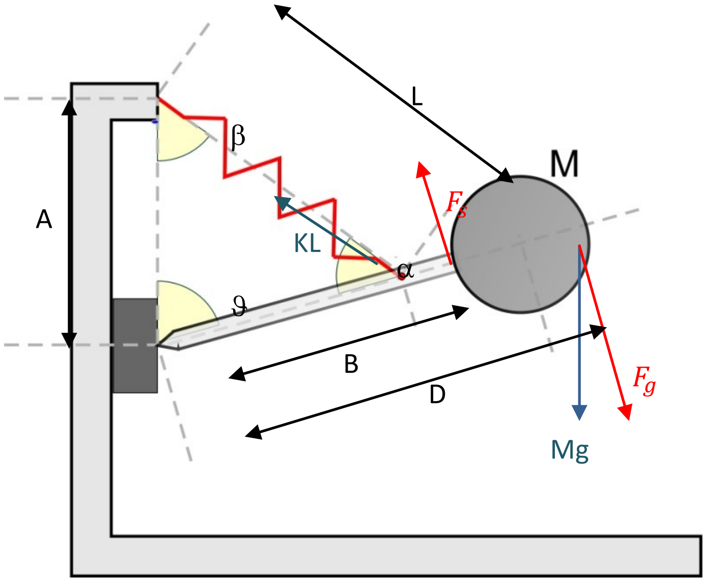

**Figure 2.13** The “LACoste” seismometer arrangement

The zero length spring is simply constructed as a normal spring but pre-tensioned such that in its un-stretched state, where the finite thicknesses of the spring wire loops touch each other thus not allowing the spring to contract any more, the tension is the same as if the spring was originally of zero length and was “stretched” to this physical length. In other words, if the spring was allowed to theoretically compress regardless of the thickness of the coils touching each other making this physically impossible, it would attain a zero length at zero tension. A zero length spring therefore has a tension proportional to its actual length.

Resolving the forces acting on the mass M, the torque due to gravity can be expressed as:

$$T_g = D[Mg\sin(\vartheta)] \tag{2.16}$$

and the torque due to the spring extended from its zero length to a length L can be found by:

$$F_s = KL\sin\alpha \tag{2.17}$$

$$\frac{L}{\sin\vartheta} = \frac{A}{\sin\alpha} \Longrightarrow L = \frac{A\sin\vartheta}{\sin\alpha} \tag{2.18}$$

$$F_s = KA\sin(\vartheta) \tag{2.19}$$

$$\therefore \; T_s = BKA\sin(\vartheta) \tag{2.19}$$

For mass stability at any angle $T_s = T_g$ and therefore:

$$BKA\sin(\vartheta) = D[Mg\sin(\vartheta)] \tag{2.20}$$

$$BKA = DMg \tag{2.21}$$

For a known mass M and spring constant K, as long as the relationship of the distances satisfies:

$$\frac{BA}{D} = \frac{Mg}{K} \tag{2.22}$$

the net force exerted on the pendulum will be zero, theoretically resulting in an infinite period. Much like the garden gate, this system does not work to the theoretical absolutes and inclining the vertical axis is necessary to provide stability and a non-infinite natural period. It is also extremely sensitive to small changes of inclination. A version of the LaCoste seismometer, utilising astatic leaf spring suspension, was also created as it was simpler to manufacture using a leaf spring to counterbalance the forces acting on the mass. Unfortunately this design suffers from similar drawbacks and it is in addition very sensitive to external disturbances.

Force Balance sensors, depicted in figure 2.14, evolved to compensate for some of the limitations of these purely mechanical sensors, were a closed loop electronic system generated a force via the means of a restoration coil on the mass equal to the force of the acceleration, in an attempt to keep the mass at a steady state. It is obvious that an error is required in the first place if a control system is to generate a restoring control effort, and therefore in practice the mass did indeed oscillate with small amplitudes. The measure of effort by the control system to keep the mass in steady state would be proportional to the acceleration sensed, usually a measure of current through the electromagnet actuator.

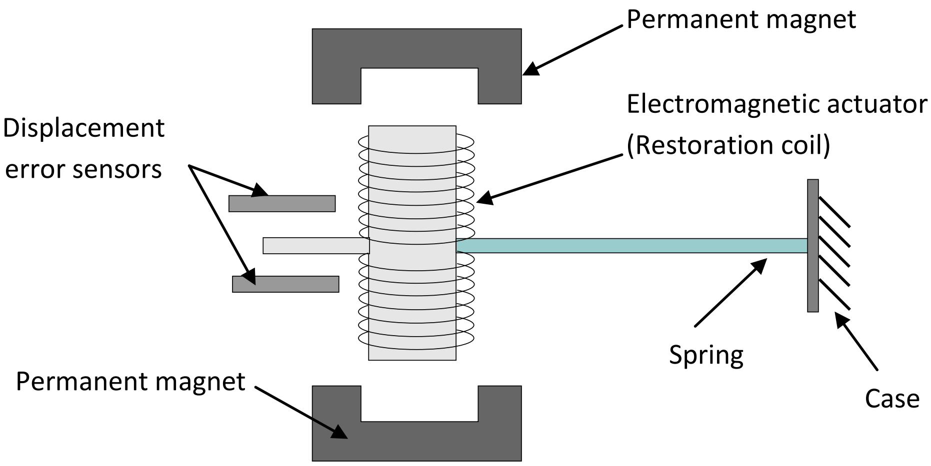

**Figure 2.14** Force balance sensor employing closed loop compensation

Such instruments have been, and still are widely used, with few manufacturers endlessly attempting to produce sensors with higher gains and higher natural frequencies, yet stable and sensitive enough to measure low level seismic tremors. These directly conflicting requirements have yielded numerous models, each suitable to specific bandwidths and with specific sensitivities.

Due to the impracticalities of direct displacement sensors, the other branch of evolution of seismometers, other than the Force Balance accelerometers, focussed on the moving coil velocity sensors yielding the much used over the years, geophone.

It should be noted that the words “seismograph” and “seismometer” have been and are still used interchangeably, however, many manufacturers, in order to avoid confusion, have categorised their products: “sensors”, “transducers”, or simply “Instruments”, meaning force feedback (balance), MEMS accelerometers, and Geophone type sensors; “digitizers”, or “data acquisition modules”, meaning digitization, filtering and general data acquisition modules able to accept inputs from such sensors.

To further add to the confusion, combined instruments with embedded sensors and data acquisition circuitry, are also marketed under the name “seismographs”.

All of the aforementioned instruments require direct or remote computer connectivity in order to further process and visually present the acquired data.

## 2.2 Modern seismographs

Although generally based on the early inertial mass-spring arm with stylus arrangement, modern seismometers utilise a variety of electronic sensors and can be categorised by the type of sensor used, their bandwidth capability, and their magnitude capability. Categorisation by sensor broadly results in velocimeters and accelerometers, the former utilising a geophone while the latter utilising an accelerometer as a sensor element. The bandwidth capability categorisation, which also depends on the type of sensor, results in Long Period (LP), Short Period (SP), Broadband (BB), and Very Broadband (VBB) seismometers, whilst their magnitude capability defines them as strong motion or otherwise.

By far good quality broadband instruments are currently the most utilised in local and global studies and these are the focus of this work. The challenge in designing these seismometers with good accuracy, linearity and low noise lies in the nature of the seismic signals which demand a sensor capable of large dynamic range capability. Table 2 below depicts the typical Earth bandwidth of interest according to source.

| Frequency | Source |
|---|---|
| 0.00001 – 0.0001 Hz | Earth tides |
| 0.0001 – 0.001 Hz | Earth free oscillation |
| 0.001 – 0.1 Hz | Seismic surface, P and S waves, of large magnitude earthquakes M> 6 |
| 0.1 – 1000 Hz | Seismic surface, P and S waves small magnitude earthquakes M< 2 |

**Table 2** Earth bandwidth of interest

It can be seen that the frequency range of Earth signals is very large ranging from 10 μHz to 1 KHz thus making great demands on the frequency response of the sensors, whilst an equally challenging amplitude range from 0.1nm to over 10m is also to be considered. These values are of course absolute extremes, and it is generally accepted that the frequency bandwidth of interest is from 0.01 to 100 Hz with good ground motion sensitivity in the order of nm. Although it is reasonably easy to band-limit the signal to 100 Hz in hardware, achieving the lower frequency cut off of 0.01 Hz or below without distorting the low frequency content of the seismic signal or losing it altogether in noise, is a an extremely challenging task.

### *2.2.1 Geophones*

Geophones are included in this section as they are still manufactured and used widely, and although they have been in existence for a very long time, modern geophones are the result of continuous improvement of the original mechanical seismometer with a coil sensor arrangement. A typical geophone is depicted in figure 2.15.

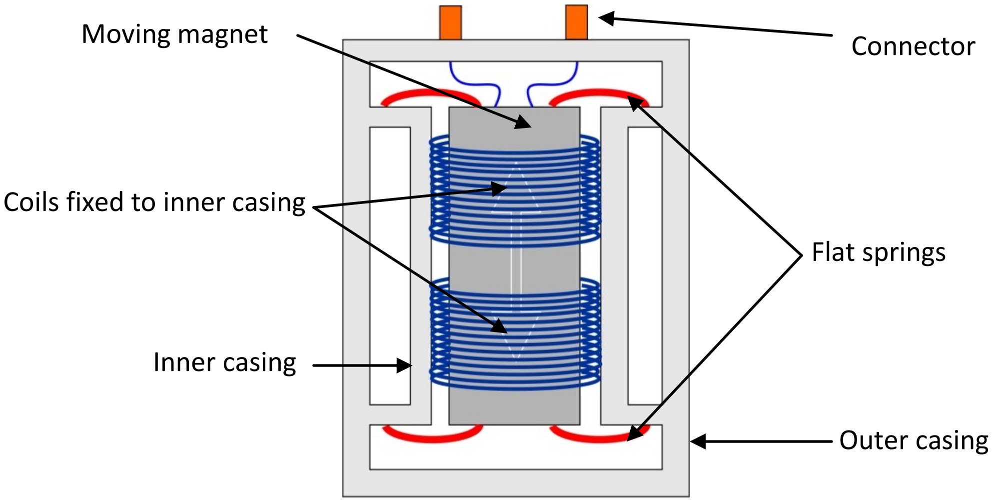

**Figure 2.15** A typical Geophone arrangement

Flat springs attached to the casing and the magnet allow for movement mostly in a single direction, whilst two stationary coils fixed to the inner casing are coupled differentially, in order to reduce noise. As seen earlier, these sensors suffer from poor low frequency performance and a limited movement range. Several attempts have been made to correct or improve the response of these instruments either by direct design or in the digital domain, however, the search for best performance has lead to theories of MEMS geophones constructed from MEMS accelerometer sensors [62]. Very few studies in existence propose the possibility of geophones performing better that accelerometers in strong motion events [63].

### *2.2.2 MEMS Accelerometers*

MEMS accelerometers are readily available in various specifications and technologies and can be broadly subdivided into several prominent types: thermal mass, piezoelectric, Piezoresistive, and capacitive accelerometers.

The “Piezo” group of accelerometers, which rely on the piezoresistive or piezoelectric effect, although high performing and rugged in construction, they simply do not operate efficiently at the lower frequencies required for seismology, typically failing to perform at frequencies below 1 to 2 Hz. Thermal mass accelerometers which utilise a heated gas as their inertial mass, perform very reliably down to DC level, but suffer from high noise floor. Most importantly however, they fail to perform reliably at higher frequencies, limiting their linear operation to only a few Hz.

Whilst each of the aforementioned accelerometers is unique in the principle of operation and provides certain characteristics desirable in certain situations, capacitive accelerometers possess wide bandwidth of operation down to DC, lowest noise floor, and in general they outperform all other types in almost every attribute, making them the focus of this work. The basic anatomy of a single axis capacitive MEMS accelerometer is shown in figure 2.16.

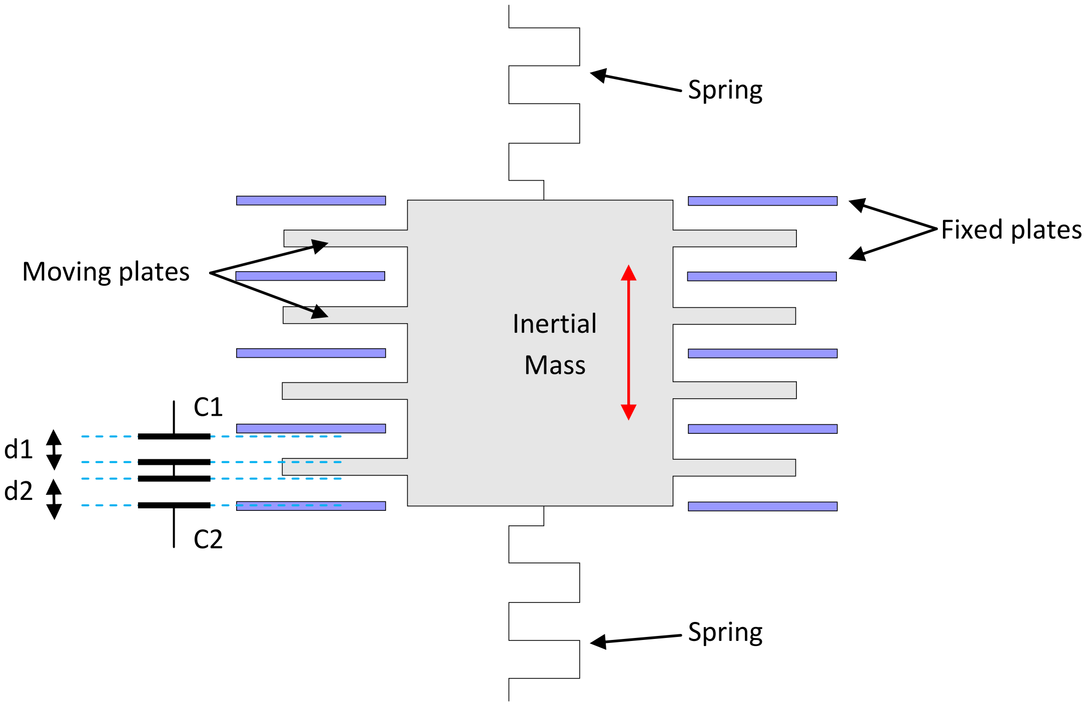

**Figure 2.16** An illustrational view of a MEMS accelerometer’s internal structure

Within the integrated circuit (IC), the inertial mass is suspended by polycrystalline silicon (polysilicon) springs such that the “fingers” protruding from it are central to the adjacent fixed plates at equal distances $d_1$ and $d_2$, thus creating capacitors $C_1$ and $C_2$. It should be noted that as with most configurations already discussed, this indeed is a miniaturised mass-spring system. With this in mind, it can be easily envisaged that any acceleration along the axis of sensitivity would result in displacement of the mass and an inevitable imbalance in the distances $d_1$ and $d_2$. As one distance increases, the other decreases in proportion, and since the resulting force due to the acceleration is proportional to the mass' displacement, measuring the displacement with high enough accuracy is all that is required to derive an output proportional to the acceleration experienced. This is normally achieved by an anti-phase excitation of the differential capacitive structure, as depicted in figure 2.17.

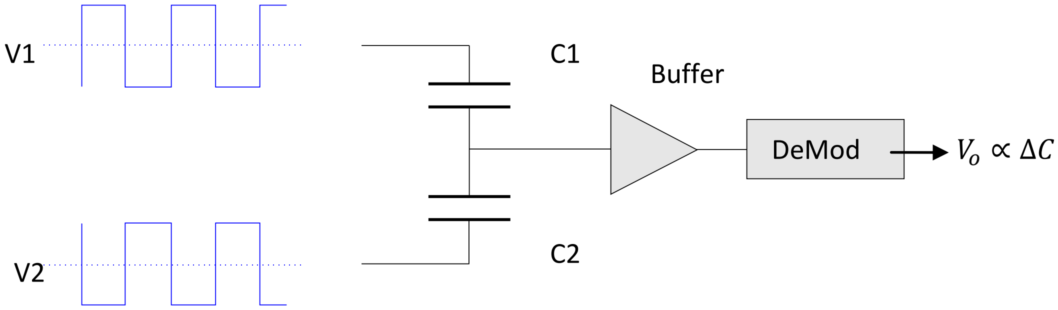

**Figure 2.17** Anti-phase excitation of differential capacitance structure

From elementary physics, the parallel plate model for a capacitor dictates that a capacitor's capacitance is proportional to the overlap area of the plates A, and inversely proportional to the distance d between them, as follows:

$$C = \varepsilon \frac{A}{d} \tag{2.23}$$

where $\varepsilon = \varepsilon_0 \varepsilon_r$, $\varepsilon_0$ is the permeability of free space, and $\varepsilon_r$ is the relative permeability of the dielectric. Also, the relation between the accumulated charge Q, and the capacitor's capacitance C when a voltage V is applied across it, is described as:

$$Q = CV \tag{2.24}$$

Assuming that the inertial mass is at rest and the voltages V1 and V2 are equal and opposite and of value $+V_s$ and $-V_s$ respectively; then capacitances $C_1$ and $C_2$ which are in series, would have a voltage of $2V_s$ across them, and would each accumulate a charge equal to the total charge $Q_T$ of the circuit, such that:

$$Q_T = Q_1 = Q_2 \tag{2.25}$$

where $Q_1$ and $Q_2$are the charges accumulated in capacitors $C_1$ and $C_2$ respectively. Since the total charge must be equal to the total capacitance times the voltage across the system, as dictated by equation 2.24:

$$Q_T = C_T V_T \tag{2.25}$$

where $V_T = 2V_s$ and $C_T = \frac{C_1 C_2}{C_1+C_2}$. It then follows that the total charge must be equal to

$$Q_T = \frac{C_1 C_2}{C_1 + C_2} 2V_s \tag{2.26}$$

The voltages $V_{c1}$ and $V_{c2}$ across each of the capacitors can therefore be describe by the following equations.

$$V_{c1} = \frac{Q_T}{C_1} = \frac{C_2}{C_1 + C_2} 2V_s \tag{2.27}$$

$$V_{c2} = \frac{Q_T}{C_2} = \frac{C_1}{C_1 + C_2} 2V_s \tag{2.28}$$

The voltage output $V_0$ from the differential capacitor arrangement and into the buffer can then be described as

$$V_0 = -V_s + V_{c2} = -V_s + \frac{C_1}{C_1 + C_2} 2V_s \tag{2.29}$$

but it can also be described as

$$V_0 = +V_s - V_{c1} = +V_s - \frac{C_2}{C_1 + C_2} 2V_s \tag{2.30}$$

$$\Rightarrow -V_s = -V_0 - \frac{C_2}{C_1 + C_2} 2V_s \tag{2.31}$$

Substituting for $-V_s$ into equation 2.29:

$$V_0 = -V_0 - \frac{C_2}{C_1 + C_2} 2V_s + \frac{C_1}{C_1 + C_2} 2V_s \tag{2.32}$$

$$\therefore\ V_0 = \frac{C_1 - C_2}{C_1 + C_2} V_s \tag{2.33}$$

It can therefore be seen that the voltage output is directly proportional to the difference of the capacitance value of the capacitors. Since the capacitance of each capacitor is inversely proportional to the distance between its plates, as shown in equation 2.23, and the capacitors of identical size exist within the same environment, it then follows:

$$V_0 = \frac{C_1 - C_2}{C_1 + C_2} V_s = \frac{\varepsilon \frac{A}{d_1} - \varepsilon \frac{A}{d_2}}{\varepsilon \frac{A}{d_1} + \varepsilon \frac{A}{d_2}} V_s \tag{2.34}$$

$$\therefore\ V_0 = \frac{d_2 - d_1}{d_1 + d_2} V_s \tag{2.35}$$

From the resulting equation 2.35, it can be seen that the net voltage output of the circuit is zero when the mass is at rest directly equidistant from the two adjacent fixed plates which form the differential capacitor pair $C_1$ and $C_2$. Any movement of the mass will also result in a differential change in the values of $C_1$ and $C_2$, which in turn will result in a positive or negative output depending on the direction of imbalance.

As explained earlier, a mass-spring system is governed by the physical equations:

$$d = \frac{F}{k} = \frac{ma}{k} \tag{2.36}$$

Where d is the displacement, k is the spring constant, and F is the force acting upon the mass m, resulting in an acceleration a.

$$d = \frac{a}{\omega_0^2} \tag{2.37}$$

From the equations it is evident that in order to be able to detect small displacements with a small mass, a very flexible structure is required, since a smaller mass also dictates a smaller displacement. Likewise, in order for the bandwidth of interest to be in the flat section of the second order response of such a system, a high resonant frequency $\omega_0$ is required, which dictates smaller displacements as a result of an acceleration acting upon the system.

The advancement of micromachined devices equipped with differential capacitance structures able to measure incredibly small changes in displacement, has made possible the fabrication of sensors with small inertial masses. The small mass attached with very flexible micro-springs is able to attain reasonably high resonant frequencies.

The excellent frequency response down to DC of the capacitive MEMS accelerometers has made them the sensor of preference for most modern seismographs. Able to match if not outperform their much more expensive and much larger macro equivalents [64], MEMS devices can also be altered on silicon to achieve more desirable characteristics for seismic and other specialist applications [65] [66] [67]. This rather expensive process however, requires the backing from a large commercial market sector in order to be thought attainable for niche sectors such as seismology.

As mentioned earlier, commercially available devices are rather adaptable and the technology can be easily integrated in to a variety of products allowing the exploration of different markets [68] [69] [70], albeit with some careful considerations on calibration [71] [72], noise, and the many aforementioned potential sources of error [73] [74] [75] [76].

In most MEMS accelerometers, measuring the displacement of the mass by measuring the difference in capacitance across the differential capacitor arrangement is typically achieved by a synchronous demodulation circuit as very diagrammatically depicted as part of figure 2.17. This technique is very effective in extracting low level signals buried within the noise floor whilst able to diminish any low frequency disturbances and close to DC effects. By effectively moving the measurement away from the low frequency, or other near in frequency sources, this technique improves the signal to noise ratio, making the sensing of weak signals possible. The modulation of the sensor signal to a higher frequency and its subsequent multiplication with an in-phase signal of the same frequency, results in the movement of the signal of interest back to DC, and the filtering of any other signals that are not synchronised with it. Assuming a modulating signal $V_1$, such that:

$$V_1 = A\sin(2\pi f t) \tag{2.38}$$

where A is the amplitude and f the frequency of the modulation signal; A subsequent multiplication of this modulating signal with another in-phase sinusoidal signal of the same frequency would result in a signal at DC, and another at twice the original frequency as shown in equation 2.39 below.

$$A\sin(2\pi f t) \times B\sin(2\pi f t) = \frac{1}{2}AB - \frac{1}{2}ABcos(2\pi 2 f t) \tag{2.39}$$

All other frequency noise and interference components would also be moved to other non-DC frequencies. A more detailed diagram of such a demodulator is shown in figure 2.18 below. The low pass filter removes all but the DC and bandwidth of interest, thus excluding any noise artefacts. With typical internal modulation frequencies in the range of 50KHz to 1MHz, and therefore comfortably outside of the bandwidth of interest, it is evident why these sensors by far outperform all other comparative technologies.

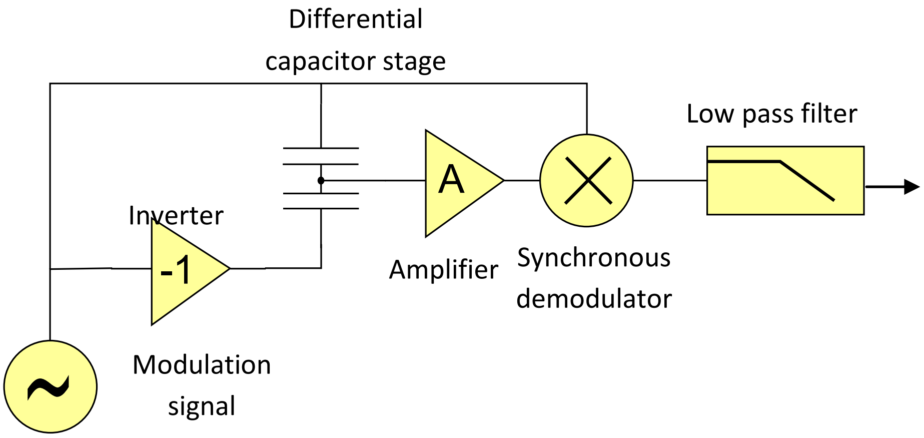

**Figure 2.18** Synchronous demodulator

Due to the simplicity of the circuit required, square waves are commonly used rather that sine waves for the modulation signals, and although adequate for the purpose, their noise rejection performance is by far inferior to systems utilising sine waves.

Since square waves can be thought to be constructed by the summation of their fundamental frequency and an infinite amount of odd harmonic sinusoids; multiplication of two square waves of the same frequency results in the multiplication of each sine component of the reference with each sine component of the modulated signal, in turn resulting in a DC component containing energy from each harmonic of the square wave. Filtering will thus be unable to filter out these higher frequency energy artefacts superimposed onto the DC signal, but depending on the harmonic, they will be rather small in magnitude. Modulation frequencies for such systems are therefore selected to be high and for their harmonics not to coincide with any known sources of noise, such as mains hum.

Careful selection of modulating frequency and the utilisation of a low noise amplifier layout tends to yield very simple circuits with very adequate performance, far superior to circuits attempting to directly measure DC voltages. Such a circuit with a lock-in amplifier for demodulation is depicted in figure 2.19

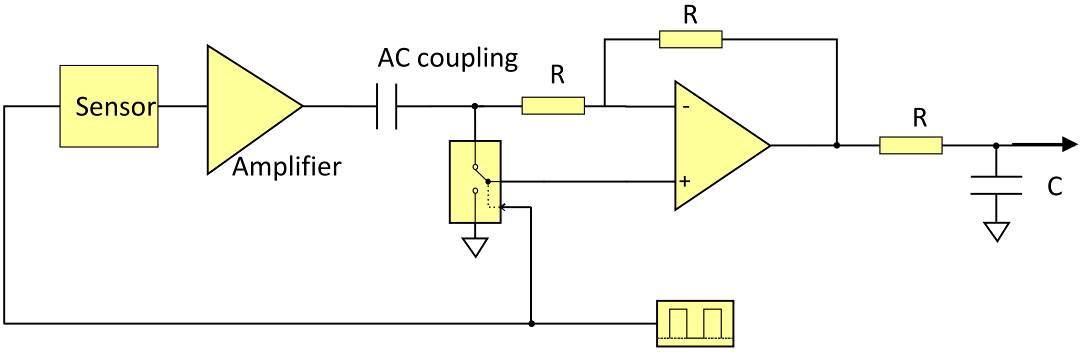

**Figure 2.19** Lock-in amplifier utilising square wave modulation

The modulating signal excites the sensor but also controls the switch to the non-inverting input of the amplifier. When the signal is positive, the switch sets the amplifier for a gain of +1. When the signal is negative, the switch sets the amplifier for gain of -1 resulting in a multiplication of the modulated sensor signal with the modulating reference square wave. The RC low pass filter on the output simply removes the unwanted higher frequency components.

Such a topology is easy to manufacture on-chip, and although any offsets, noise and $\frac{1}{f}$ characteristics are indeed diminished by this methodology, the noise and offsets of the end amplifier and filter are not. In addition, an output amplifier is also included with an internal in series resistor for short circuit protection, and to also allow for a single external capacitor to form a low pass filter without any other additional components.

### *2.2.3 Signal conditioning*

Once outside the MEMS, the sensor's raw analogue signal requires filtering, buffering, and usually amplification before digitisation. Typically a data acquisition system consists of the "front end" electronics, which their primary purpose is to interface the sensor to the digitising circuit by conditioning the raw signal appropriately. Such a typical system is shown in figure 2.20.

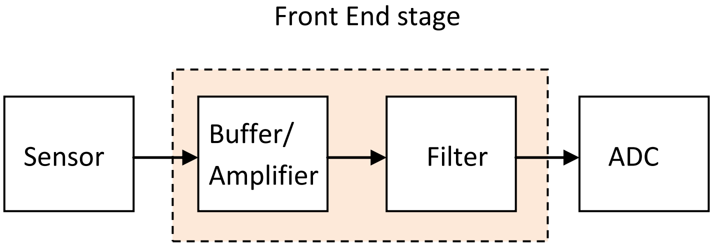

**Figure 2.20** A typical data acquisition system

Since the output of a MEMS accelerometer is DC biased even when no acceleration is taking place to a voltage level termed $V_{0g}$, any changes due to temperature, tilts, or ageing on this bias would also result in erroneous initial conditions and subsequent measurements. In order to eliminate this rather intricate problem, some seismograph manufacturers have opted for the low-tech approach of de-coupling the sensor signal with the aid of a large in-series capacitor, therefore eliminating any DC component and long term drifts of the baseline. This decoupling of course irreversibly distorts the signals below 1Hz which are of great interest in seismology [77] [78].

An additional issue caused by the large in value and high in tolerance internal to the sensor output resistor. With resistances typically in the region of 30K, the internal resistor immediately classifies a MEMS sensor as a high impedance source. Any coupling to this source therefore, capacitive or resistive, requires careful consideration across the frequency spectrum of interest.

An amplification stage within the instrument may or may not be employed depending on the sensor, the system topology, and the manufacturer, whilst the filtering stage is most often constructed using a simple RC filter stage in a low pass filter arrangement. Rarely, an additional switch capacitor filter is also employed to further ensure that frequencies above the Nyquist point are not present in the signal prior to digitisation, and to improve the overall amplitude and phase characteristics of the instrument.

In recent years, seismograph manufacturers have almost exclusively opted for the use of 24 bit ΣΔ analogue to digital converters, or compensators [79], in an attempt to provide high resolution seismic data. At these rather ambitious resolutions, extreme low noise design and very elaborate supply de-coupling is imperative if one is to attempt to capture acceleration data without flooding several least significant bits (LSbs) of the ADC with noise. Few, if any instruments, utilise multi-stage active filters in the front end electronics, as this initial front end filtering only viewed as means to narrow the bandwidth in preparation for digitisation. Further extensive filtering and processing is always performed after the digitisation of the analogue signal, in the digital domain.

Some more recent and rather unique seismographs, employ the averaging and active filtering of several sensor channels in order to minimise the noise content of the signal prior to final filtering and digitisation. Such a configuration is shown in figure 2.21 below.

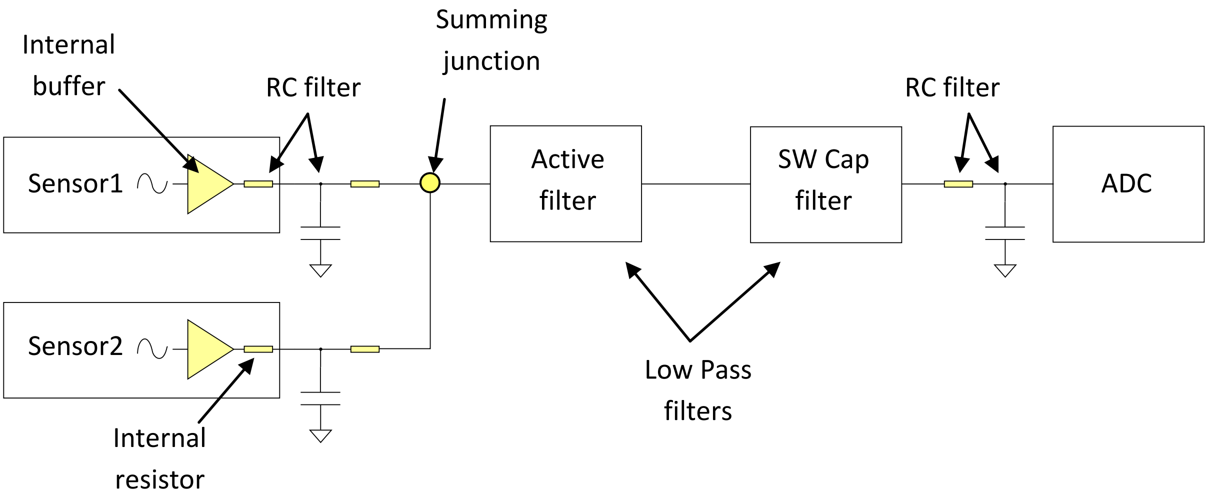

**Figure 2.21** Unique elaborate seismograph front end

Two or more axially aligned sensors are first band-limited by a low pass RC filter constructed by utilising the internal to the sensors resistors and external capacitors.

These filters have a rather high frequency cut-off as not to degrade the signal, and serve only as higher frequency noise reduction stages prior to the summing junction. In theory, the summation of two nearly identical signals containing random in nature noise would result in an output twice the signal magnitude with a much reduced in amplitude noise.

An active filter stage aids to provide a sharp cut-off and exclude the natural resonance frequency of the sensor from the signal, while a further Switched Capacitor (SW Cap) filter band limits the signal to within half the sampling rate of the ADC. The additional RC filter prior to the ADC is necessary in order to attenuate the inherent clock feed-through of the SW Cap filter.

It should be noted that this is a rather unique arrangement and typically only a simple RC filter is utilised for band limiting the sensor signal before digitisation in most instruments.

### *2.2.4 Signal conversion and storage*

Digitisation of the sensor signal is almost always accomplished by a 16 bit successive approximation, or more recently a 24 bit Sigma Delta (ΣΔ) analogue to digital converter (ADC). The sampling frequency can be selected by the user and rarely exceeds 40 KHz even in high performance models: higher sampling frequencies inevitably reduce the length of the data captured due to the finite amount of onboard memory.

The popularity of ΣΔ converters is due to a combination of low cost, high resolution, and high enough sampling frequencies to be able to digitise most seismic bandwidths of interest. The very nature of the converter, as suggested by its name, delta modulates the incoming signal to a much higher frequency resulting in the spreading of the quantisation noise via a technique known as oversampling. Although oversampling can clearly be achieved with any ADC, provided it is fast enough; a sigma delta converter also employs noise shaping which further moves the noise energy into the higher frequencies, which are in the end excluded by a low-pass filter. The current availability and technologies used within these converters clearly plays a crucial role to designing any sensor whose data is to be digitised and further processed in the digital domain.

From the block diagram of figure 2.22, a signal entering a sigma delta converter is first fed to a difference amplifier, hence the "Delta" in the name, before being integrated, or averaged over time in the Sigma part of its function. The Digital to Analogue Converter (DAC) on the feedback, is simply a switch that connects the inverting input of the ADC to either a positive or a negative reference voltage. The effect of the integrator is to average the error thus providing an averaging filtering effect to the signal whilst "pushing" the quantisation noise into higher frequencies. The overall effect on the signal once low-pass filtered and decimated is that of a high signal to noise ratio.

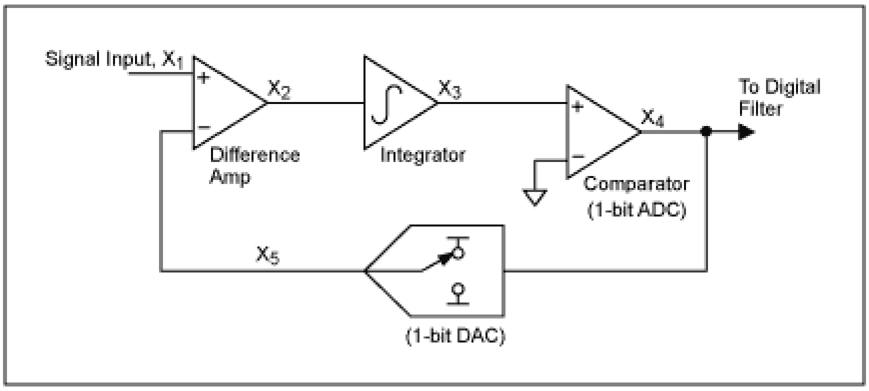

**Figure 2.22** Block diagram of Sigma Delta converter (Public domain)

Achieving high signal to noise ratios with more conventional ADCs also can be achieved by oversampling techniques and by the increase of the number of bits.

Although in most seismic instruments the digitising circuit is continuously active in order to constantly acquire pre-event data for a zero reference, a user adjustable vibration threshold (trigger level) above which an earthquake is deemed to be taking place is normally employed to trigger the instrument into digitising and storing seismic data. Such a trigger requires to be set to a "comfortable" margin above the noise level of the instrument and the background vibration noise of the particular location.

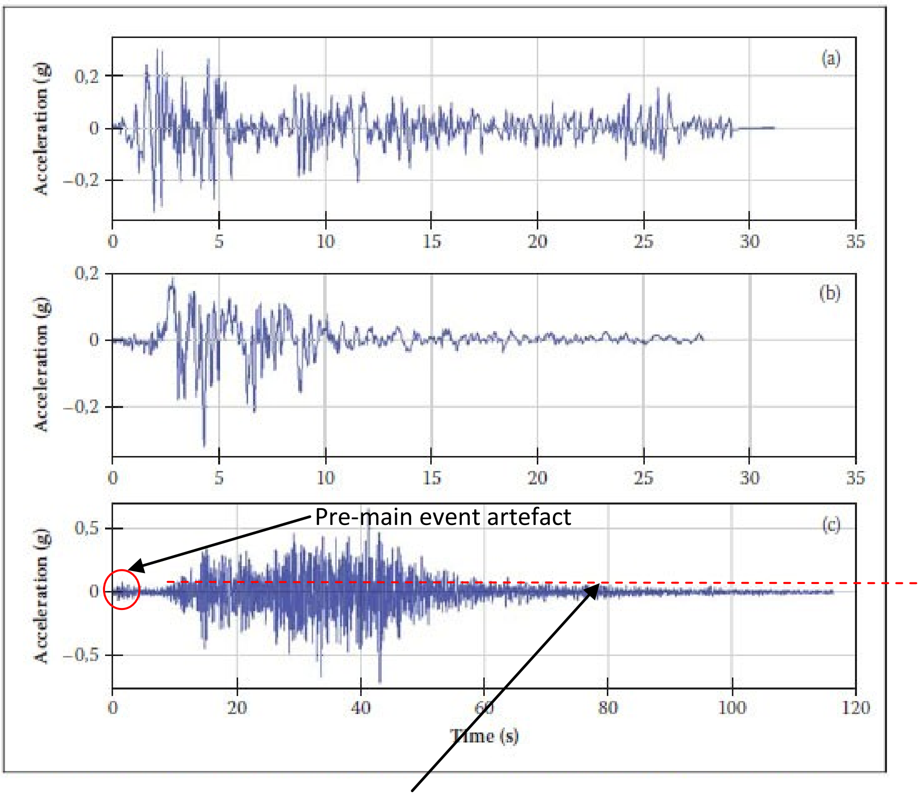

Pre-main event artefact

Trigger threshold level arbitrarily selected at approximately 0.08g

**Figure 2.23** Acceleration trends of (a) El Centro, (b) Northridge, and (c) Llolleo earthquakes (public domain)

Most earthquake accelerograms tend to follow recognised patterns in terms of primary and secondary wave arrivals, however each one does contain unique features when examined closely, as one would expect. Figure 2.23 depicts three different earthquake accelerograms from which the random nature of earthquakes can be clearly seen in the overall shape of each signal. The seismic trend from El Centro appears to have a steep but incremental onset, and also appears to contain some “ringing” before it finally subsides. The seismic trend from Northridge also shows a similar rapid and progressive onset, but tapers off smoothly after 10 seconds without any ringing artefacts. The seismic signal from Llolleo, which is plotted on a much longer timescale, exhibits a rather smoother onset and tail off and most interestingly at least one pre-main event artefact, which may or may not activate the triggering mechanism in this example. Such artefacts, especially low frequency adulations and low level tremors occurring many seconds before the main seismic event, could be missed thus yielding unrepresentative seismic data.

Once triggered, the instrument starts recording the seismic data for usually up to 120 seconds on its onboard memory, which is typically a of non-volatile type. Flash disks or cards of several Giga Bytes are usually employed.

## 2.3 Post-digitisation processing

Additional processing of the seismic data in the digital domain is essential in order to correct for inherent errors, further filter the digitised signal, and mathematically manipulate the data to yield a satisfactory displacement over time trend. Provided the data is derived using a modern instrument, it can be assumed that the sampling intervals are correct and the samples are of reasonable resolution. Since seismic instruments are event driven, the value of the trigger threshold must be of a value grater that the underline environmental and instrument noise. A value of 0.01g is usually attainable, however, pre-event data is typically lost within the averaging section of the accelerograph in an effort to determine a zero reference baseline. Since the baseline is mathematically transitioned in an attempt to provide a zero integral of the acceleration curve, errors are inevitably introduced, requiring the application of more precise baseline correction and de-trending methods, such as spline-fitting, and least squares regression trend subtraction from the accelerogram.

A seismograph, as a complete instrument, possesses its own dynamic response and therefore imparts an alteration to the signal recorded. The transfer function of the instrument, when known, is used in an attempt to reverse this distorting effect via de-convolution and derive more accurate seismic data.

Other more recent and involved methods use adaptive techniques and extract power spectra for the acquisition of a more complete picture of particular seismic events.

### *2.3.1 Digital filtering*

Although the acceleration data has already been band-limited by low-pass filtering onboard the instrument, further more aggressive filtering is always required in order to totally exclude higher frequency artefacts from inherent noise sources whilst retaining the accuracy of the data within the bandwidth of interest. Such digital filter invariably takes the form of an Infinite Impulse Response (IIR) filter, or a Finite Impulse Response (FIR). While FIR filters can be easily constructed to exhibit linear phase characteristics, FIR filters which are sometimes modelled on classical analogue counterparts such as Butterworth, Chebyshev and Elliptical, do not exhibit phase linearity and further digital manipulation is required to attain a zero phase output. As with other shape-critical data, the accuracy of the phase information in seismic trends needs to be retained without distortion, since it determines the location of peaks and other significant features within the trend.

Recently, more convoluted methods including least-squares adaptive techniques have been employed in an attempt to further improve the quality of the data [80] [81] [82] [83] [84] [85] [86].

### *2.3.2 Numerical integration*

Numerical integration is of course required to obtain seismic displacement trends from acceleration data, since displacement over time is indeed the second integral of acceleration over time. In principle, the initial conditions of velocity $v(t_0)$ and displacement $v(t_0)$ must be known in order for displacement over time to be derived by the double integration process. For example, deriving the velocity trend $v(t)$ by integrating the accelerogram $a(t)$,

$$v(t) = v(t_0) + \int_{t_0}^{t} a(t)dt \tag{2.40}$$

inevitably requires knowledge of the initial velocity term, which of course is not known. The only way to eliminate this difficulty is to assume both the initial velocity and initial displacement terms to be zero, which of course requires a very accurate estimation of the baseline of the accelerograph. A careful examination and estimation of the zero level instrument response is conducted almost exclusively via the use of pre event data capture. The averaging of this pre event data, which usually contains some noise and drifts, serves as the zero initial conditions for the integration process. As the trapezoid rule is most often utilised for the numerical integration for its computational simplicity, the accuracy of the integrals also depend on the sampling frequency and the resolution of the digitising ADC.

Despite the aforementioned assumptions and corrections, displacement data recovery from real signals is fraught with errors, and more intricate baseline correction [87] [88] [89] and de-trending and integration algorithms [90] [91] [92] [93] [94] [95] [96], still prove to be essential in the processing of seismic data.

It should be noted once more that geophones, unlike accelerometers, are velocimeters, and their output is proportional to the velocity, not the acceleration of the excitation signal, and hence require only a single integration for the derivation of displacement over time data. This could be viewed as a big advantage since a single integration would produce results with significantly reduced errors, however, their poor dynamic response, as seen earlier, prohibits their use where wide bandwidth accurate measurements are required.

## 2.4 Conclusion

Modern seismographs are evolving to take advantage of new and emerging sensing technologies in the quest to reproduce accurate displacement over time data. The use of MEMS silicon and servo accelerometers has been gaining momentum, and digitisation and post-digitisation techniques are constantly evolving in order to improve the quality of the resulting data.

Most modern seismographic instruments are compound units, comprising separate sensor and digitiser modules. The digitiser, being the central part of the device, can have inbuilt sensors, or it can typically provide multi-channel connectivity to several geophones and/or accelerometric sensors, as shown in figure 2.24 below. This type of setup is generally used for reflection seismometry, where the interest is in imaging what lies beneath the surface.

Clusters of seismic sensors are sometimes also used for specialist earthquake studies, however, earthquake monitoring typically requires sensors that are adequately geographically distributed at key locations several kilometres from each other.

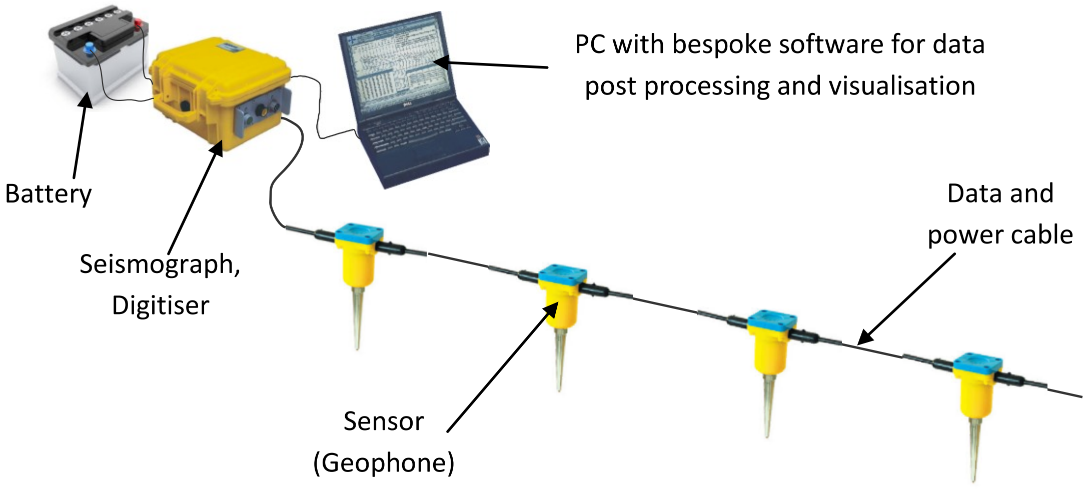

**Figure 2.24** Typical system installation

Other self-contained systems are neatly integrated into a single casing, utilising an onboard sensor, and are used for seismic motion monitoring rather than reflection imaging applications, like the one depicted in figure 2.25 below.

**Figure 2.25** A typical self contained seismograph

In order to appreciate the composition and performance of these modern instruments, a simplified list of technical characteristics of a modern and rather unique high performance state-of-the-art seismograph, is detailed in table 2.1 below

| *Sensor* | |
|---|---|
| Type | Tri-axial MEMs silicon accelerometers |
| Range | Type ± 5g (vertical axis 1 g offset) |
| Dynamic range | 91 dB 0.1-20 Hz<br>85 dB 0.1-80 Hz |
| Offset error | < ±1 % over operating temperature range |
| Linearity | < ±0.5% |

| | |
|---|---|
| Gain error | < ±1 % over operating temperature range |
| *A/D conversion* | |
| Sampling | Zero skew autonomous sampling 1ppm time-base (0-60ºC) |
| Anti-Alias | 1-pole RC filter (fc = 10kHz) |
| Input | 3 channels |
| Sensor data output rate | 50Hz, 100Hz, 200Hz. (500Hz factory option on request) |
| A/D type | 24-bit Σ-Δ A/D |
| Integral non-linearity | < 0.0006% (full range) |
| Resolution | 24 bits |
| SNR | 101 dB (200Hz) 104dB (100Hz) 107dB (50Hz) |
| *Signal Processing* | |
| Filtering | FIR digital anti-alias filter/decimator Linear phase |
| Measurement bandwidth | DC to 20, 40 or 80Hz |
| Recorded dynamic range | 130dB (80 Hz BW)<br>133dB (40 Hz BW)<br>136dB (20 Hz BW) |
| *Triggering* | |
| Pre-trigger filter options | 0.1 Hz high-pass<br>1 Hz high-pass<br>5 Hz low-pass<br>10 Hz low-pass<br>0.1 – 5 Hz band-pass<br>0.1 – 10 Hz band-pass<br>1 – 5 Hz band-pass<br>1 – 10 Hz band-pass |
| Absolute level | Independent thresholds on each channel<br>Selectable AND or OR triggering on each channel<br>Level from 0.1mg to 3 g in 0.1mg steps |
| Pre-event length | 10 to 120 seconds in 1-second steps |
| Post event length | 10 to 120 seconds in 1-second steps |
| *Storage* | |
| Storage time | 16 GB Flash disc (other options are available): |
| *Time stamping* | |
| Type | Low power GPS (standard) |
| Accuracy | Better than 10us of UTC with GPS lock |

**Table 2.1** Technical characteristics of a modern seismograph

This type of instrument has been used in the most demanding situations over the last decade due to its superior performance. It is not surprising that this calibre of instrument utilises triaxial MEMS sensor technology in order to benefit in size, performance, and cost. The now wide use of GPS technology enables seismographs to report not only exact location but also exact timing of events: a very important feature in the study of earthquakes and the propagation of seismic waves through the Earth.

# Chapter 3

## Non ideal instrument functionality

A block diagram of the processes involved from sensor through to the derivation of a displacement seismic trend is depicted in figure 3 below. In order to assess the possible sources of error, careful and methodical examination of each section of the signal path is essential.

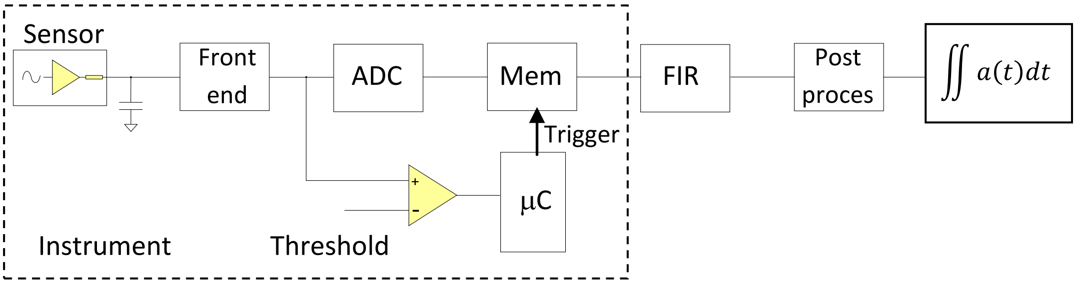

**Figure 3** Block diagram of sensor to displacement data process

Using the instrument specifications detailed in table 2.1 as a reference example of the current state-of-the-art, one can start to analytically conceive possible sources of error within the instrument itself.

A brief but more critical examination of the sensor section quickly reveals a potential for rather large offset and gain errors. For a typical sensor operating from a 3V supply, a 1% offset error is a substantial 30mV offset in magnitude. Similarly, a 1% gain error is more than adequate to irreversibly distort any precision measurement over the temperature range. It should be noted that although these offsets are specified over the temperature range, and some instruments also offer a temperature measurement for potential correction, they are not just affected by temperature alone. Ageing of components and other non-temperature related long term drifts, also significantly contribute to these sources of error.

In the A/D conversion section of the table, the actual sampling rate is not specified, but it could be assumed to be at least 20 KHz since the anti alias filter is specified to have a cut off frequency ($f_c$) of 10 KHz. For the given measurement bandwidth of

80 Hz, once reduced by the subsequent use of the FIR filter, a simple RC filter with an $f_c$ of 10 KHz will introduce nearly -0.5° of phase shift whilst maintaining a non attenuated signal throughout the bandwidth. It should be noted that since this phase shift originates from the anti-aliasing filter, the linear phase attributes of the digital FIR filter are not capable of recovering this phase shift. Further, should this RC filter be constructed utilising the internal to the MEMS output filter resistor as per manufacturer's recommendation, the rather large 15% tolerance of this resistor would certainly produce unexpected dynamic performance between instruments and between channels on the same instrument.

Recalling the noise frequency spectrum of figure 1.4 of a typical MEMS sensor, a noise component of -90dB is evident at the sampling frequency of 20 KHz, and -82dB at 10 KHz, whilst the peak-to-peak unfiltered noise amplitude of such a sensor is minimum 6 mV.

Considering a noise component of -85dB at the aliasing frequency of 15 KHz; once through the RC filter, the noise signal will be further attenuated by -5dB, a total of -90dB. The 24 bit ADC utilised in this instrument has a Least Significant bit (LSb) representative value of -144.5dB, and even after the noise shaping effect of the ΣΔ architecture, data and noise will still be aliased and phase shifted for frequencies greater than 10 KHz, creating error artefacts in the resulting sampled data which are irreversible by subsequent filtering or other digital processing techniques.

A much more detailed investigation of this instrument, representative of the latest manufacturing practices utilising MEMS technology, revealed the use of multiple sensors for each sensing axis in an attempt to diminish sensor noise by averaging several acceleration signal paths. Although in theory these signals could be averaged for noise reduction with the assumption that they are identical in nature, this is not the case in practice, and any precision factory calibration will not alleviate the fact that acquiring a signal in this manner can only result in signal "smoothing". This averaging technique achieves a reduction in noise at the expense of signal quality, since the output is simply the amalgamation of several different signals, of different amplitudes and phases. The notable manufacturer's design efforts however, highlight the importance of noise within seismic instruments [97].

Such pre-set techniques assume that there are no dynamic response differences between sensors and that all sensors will drift and age in a similar manner, making any possibility of reconstructing the original signal with any accuracy in the long term impossible. A component level evaluation of the circuit, conducted under a Non Disclosure Agreement (NDA), and therefore its details not reproduced in this work, showed phase errors in excess of over 11° over the 100Hz bandwidth in the primary filter stages, and a further 5° error in the secondary pre-Analogue to Digital Convertor (ADC) sections. Further, examination of the physical instrument assembly showed lack of adequate mechanical internal support, thus allowing the instrument to induce its own resonant interference onto the seismic signals.

The above assessment was conducted on an instrument deemed to be technologically advanced in order to reveal the sources of error commonly shared with many of the several types of seismograph in use to date. Although most other instruments do not employ multiple channel averaging techniques, further research revealed that simple RC filtering for sensor noise suppression is indeed very common if not standard practice.

Further errors can be reasonably expected to stem from cross-axis sensitivity, poor estimation of initial conditions, dynamic tilts, instrument long term drifts, gain errors, instrument dynamic response changes, and also integration errors, all leading to much altered and unrepresentative acquired seismic data.

Before embarking into detailed experimental investigation on the sources and effects of these errors, a primary experimental study of MEMS sensors typically used in seismological devices, was conducted in order to quantify the challenges of deriving displacement data from MEMS accelerometric sensors.

The primary electronic platform depicted in figure 3.1 was designed and fabricated to allow the experimental assessment of the sensor and the pre-amplification stages, both jointly and separately.

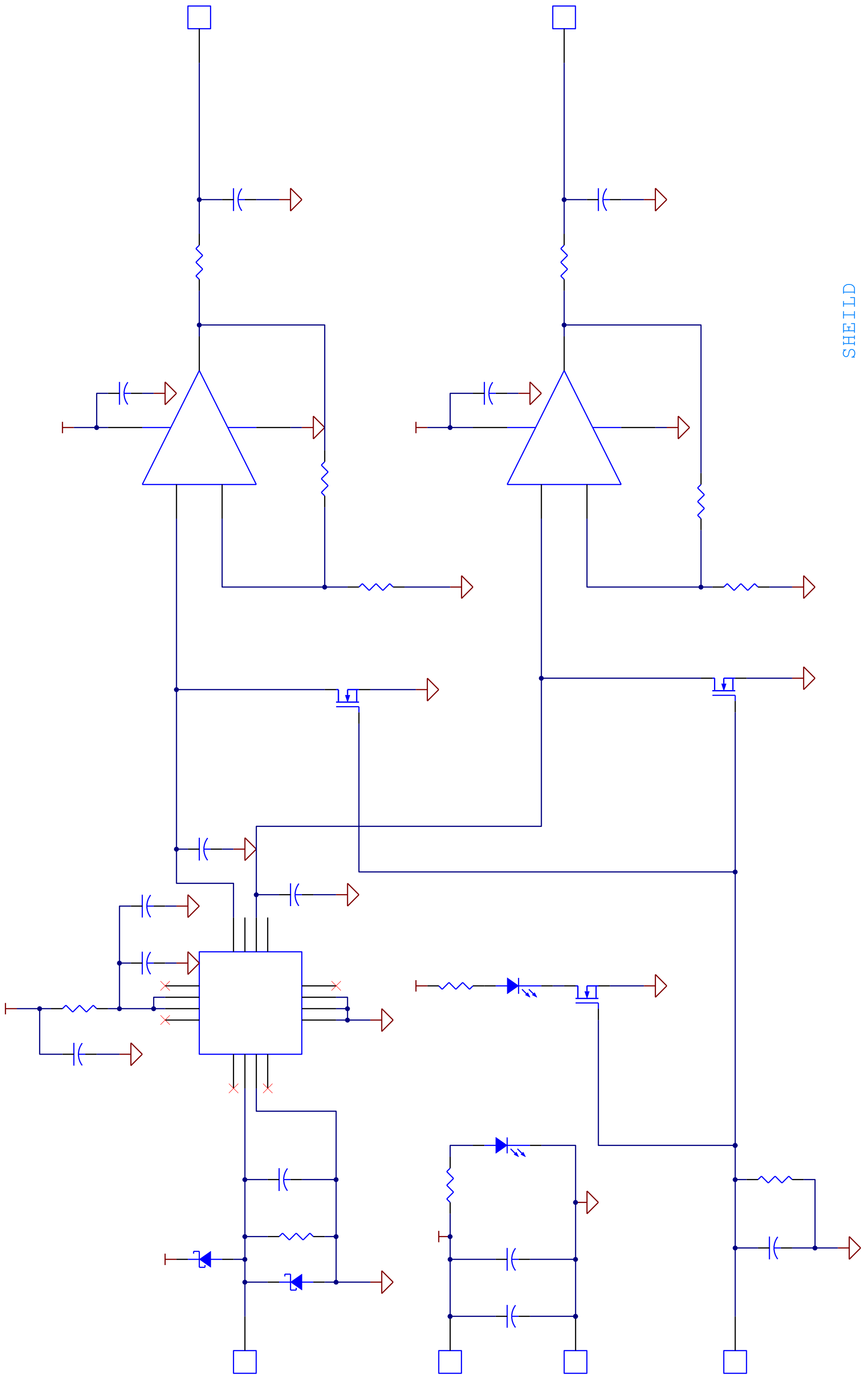

**Figure 3.1** The primary MEMS test platform

Frequency response results of the amplifier stage provided amplitude and phase distortion frequency figures in excess of 2MHz and 200KHz respectively, indicating that zero signal distortion within the 100Hz Bandwidth of interest could easily be accomplished with these or similar grade amplifiers.

To accurately study the response of MEMS sensors during the initial stages, a mechanical oscillator capable of pure sinusoidal excitation had to be constructed. It was deemed necessary for this mechanical oscillator to also be equipped with a sensor able to directly measure displacement over time with sub-millimetre resolution, and therefore serve as an electronic reference of the actuating mechanical excitation signal.

A non-contact sensor was thus designed and constructed able to meet the criteria set for the purpose of this primary study. A precision photocurrent-to-voltage convertor shown in figure 3.2, was fabricated with both amplifier and photodiode specifically selected for high speed operation. The Photodiode’s specification of rise and fall photocurrent times of 5ns, along with amplifier’s 63MHz Gain Bandwidth, and 17V/µs Slew Rate, were thought more than adequate for the intended purpose.

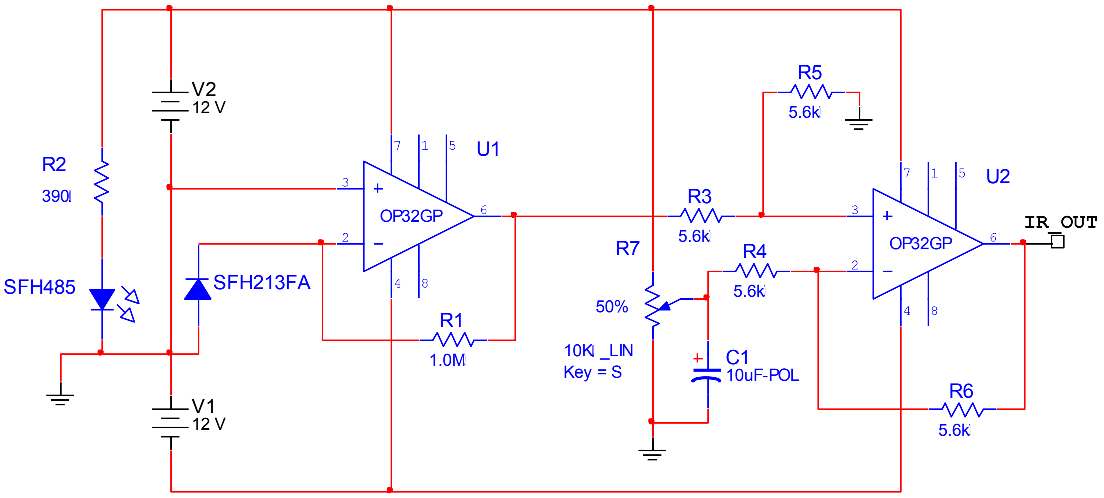

**Figure 3.2** Photocurrent to voltage convertor circuit

A second amplifier stage was also constructed to simply facilitate offset trimming of the output signal.

The physical assembly of the IR non-contact high speed range-finder is shown in figure 3.3. An opaque screen between the IR source and the sensing photodiode, helped prevent direct optical cross-coupling.

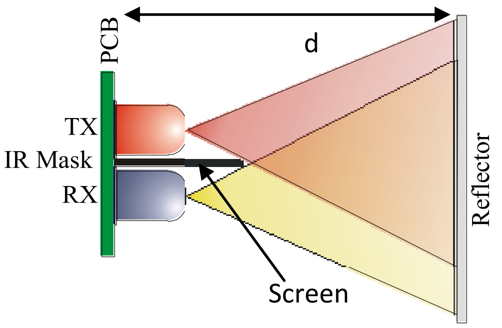

**Figure 3.3** Non-contact range finder optics arrangement

The distance d to the moving reflector was measured with the PCB's front face as a distance reference. The results of the sensor's output versus distance are shown in table 3, alongside the resultant curve's first differential $\frac{dV}{dd}$ , and a curve fit of the inverse square law such a system should theoretically obey.

| **Distance d (cm)** | **Sensor output (V)** | $\frac{dV}{dd}$ | $\frac{1}{d^2}$ (best fit) |
|---|---|---|---|
| 3 | 3 | | 3.483333333 |
| 3.5 | 2.7 | 0.6 | 2.598979592 |
| 4 | 2.2 | 1 | 2.025 |
| 4.5 | 1.75 | 0.9 | 1.631481481 |
| 5 | 1.4 | 0.7 | 1.35 |
| 6 | 1.04 | 0.36 | 0.983333333 |
| 7 | 0.8 | 0.24 | 0.762244898 |
| 8 | 0.65 | 0.15 | 0.61875 |
| 9 | 0.5 | 0.15 | 0.52037037 |
| 10 | 0.38 | 0.12 | 0.45 |
| 11 | 0.33 | 0.05 | 0.397933884 |

**Table 3** Non-contact range finder output, derivative and inverse square curve fit

Examination of the graphical representation of the results in figure 3.4 revealed that the non-contact range-finder did indeed follow the $\frac{1}{x^2}$ law, and therefore linearization of the output was necessary when the range of distances measured was greater than few millimetres.

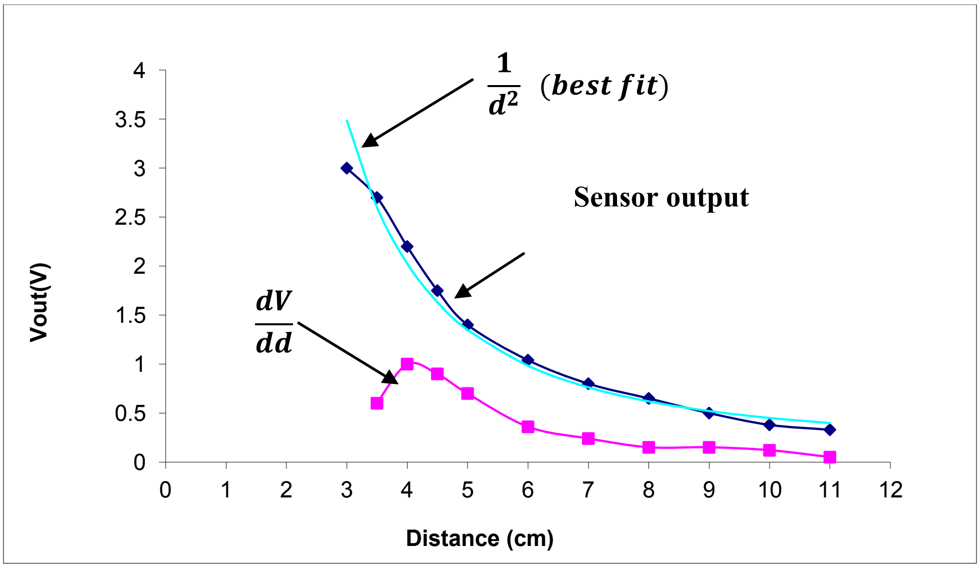

**Figure 3.4** Voltage to distance characteristic of the non-contact range finder

It was evident from the $\frac{dV}{dd}$ curve of figure 3.4 that the highest sensitivity of 100mV/mm was achieved at distances between 4 and 4.5cm, rendering this sensor suitable for this purpose in terms of both sensitivity and sub-millimetre resolution. It should be noted that the sigmoid appearance of the recorded voltage curve below 3.5cm was due to the screening of the receiver creating a shadow over the photodiode when the reflector was in very close proximity.

Evaluating the dynamic response of the sensor, took the form of imaging a reflector mounted on a leaf spring undergoing damped simple harmonic motion, as confirmed by the sensor results depicted in figure 3.5 below.

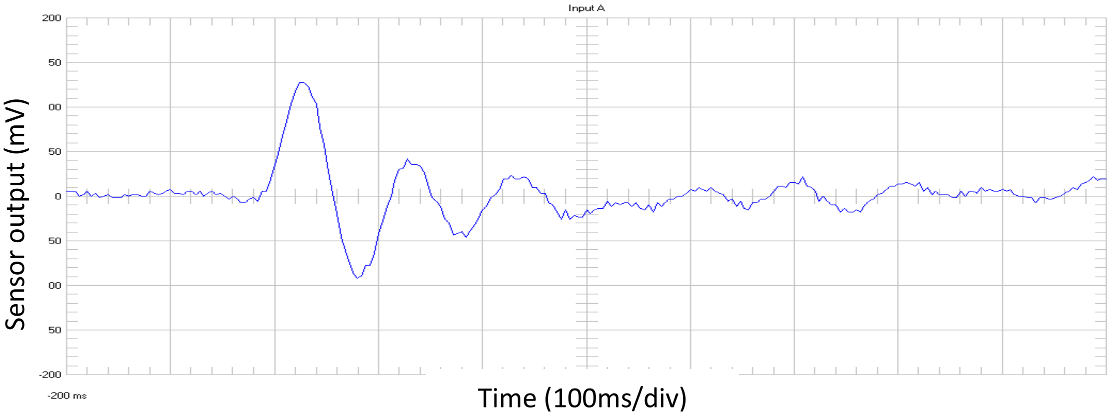

**Figure 3.5** Dynamic response of the non-contact rangefinder monitoring the vibration of a leaf spring

Figure 3.5 confirmed a good low noise dynamic performance in the lower frequencies in the order of 10Hz. Derivation of the dynamic capability of the sensor over the full 100Hz bandwidth, necessitated the use of a motorised optical chopper positioned between the reflector and the sensor. The high frequency pulse results are shown in figure 3.6 below.

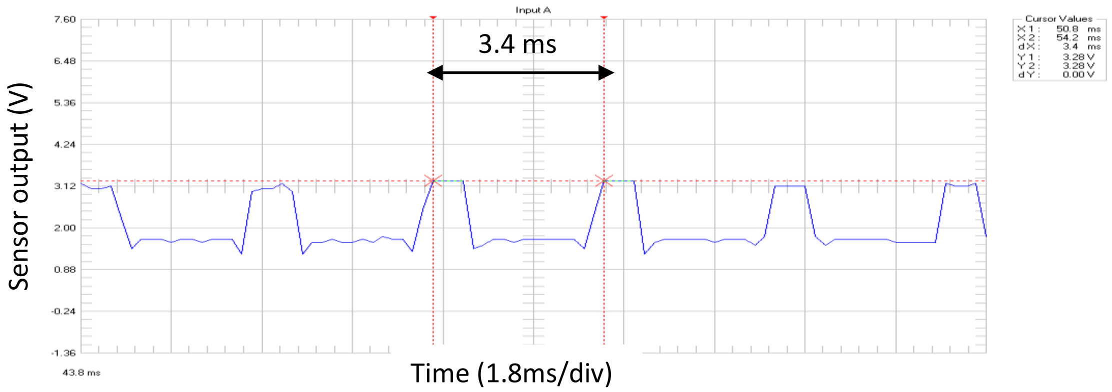

**Figure 3.6** Optical encoder induced rangefinder output

It should be noted that the trapezoidal appearance of the pulses in Fig 3.6 was not due to slew rate limitations, but due to the encoder's edges, creating a sharp but progressive non-binary change in reflectance, whilst the sharp spikes appearing below and above the cursor lines were due motor induced noise, as the supply was shared between the device and the driving DC motor. A period measurement revealed a response frequency of 294 Hz, which was almost three times the bandwidth of interest.

With the non-contact displacement sensor completed, a vibration platform able to provide sinusoidal excitation was constructed from aluminium machined to tight tolerances as diagrammatically depicted in figure 3.7. A cam-shaft arrangement was utilised to guarantee a pure sinusoidal mechanical actuation signal to the Device Under Test (DUT). A precision-machined steel shaft guided by two Teflon bearings served as means of communicating the cam-shaft's motion to the DUT. Amplitude of oscillation adjustment was accomplished by the use of an offset adjustable spindle, connecting the DC motor to the shaft. The platform was able to accomplish a full 100Hz operation at small amplitudes of oscillation.

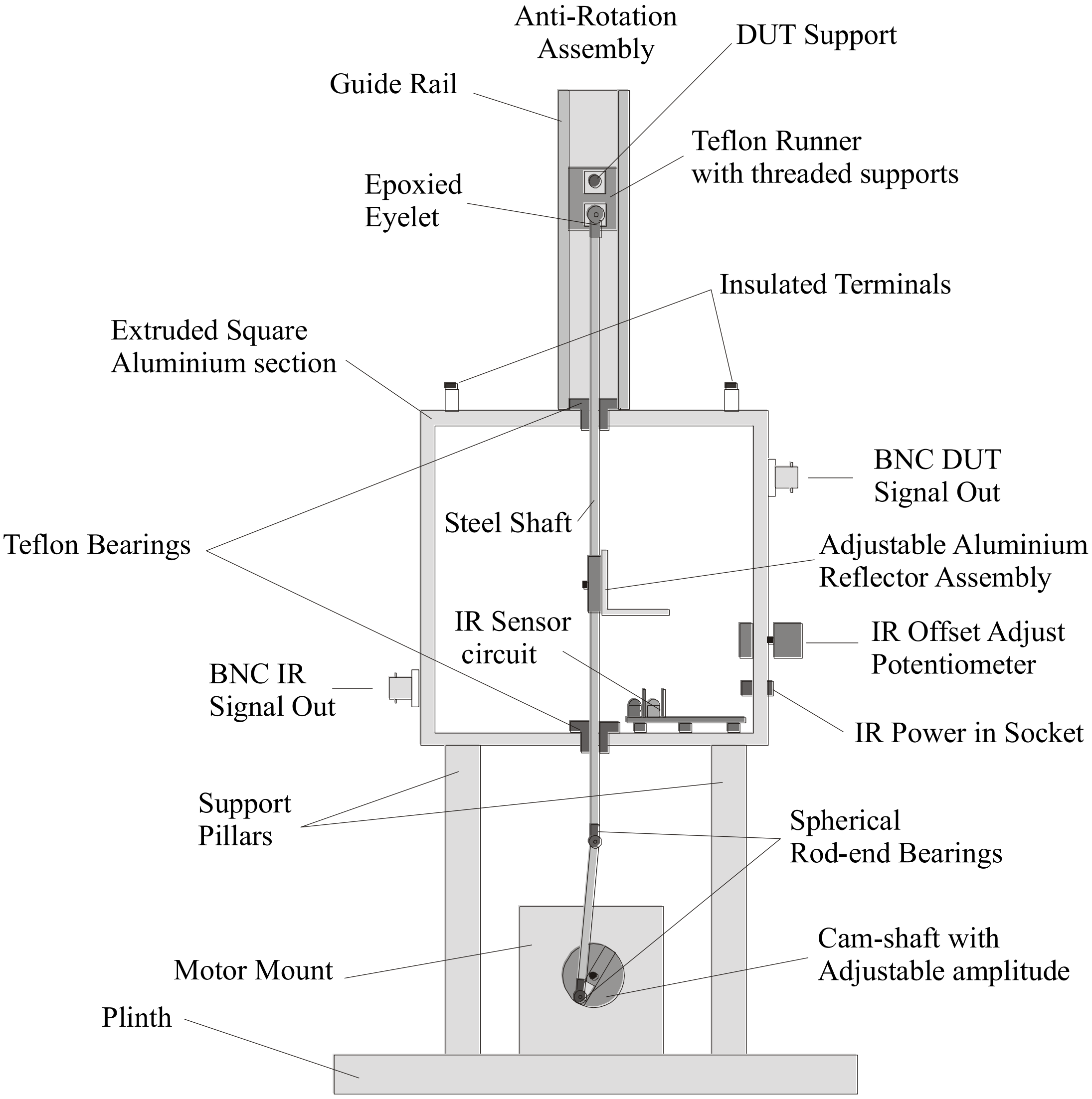

**Figure 3.7** The mechanical vibration platform

Using the vibration platform to excite the primary MEMS assembly shown in figure 3.1, without the output filtering sections populated, the first raw low frequency actuation results were obtained as shown in Figure 3.8 below.

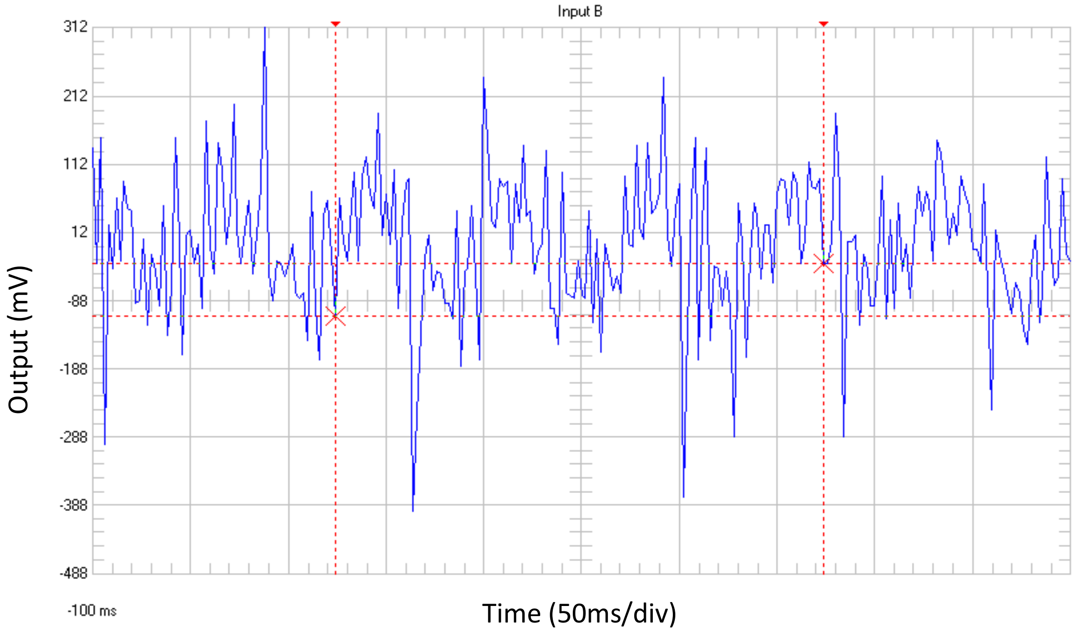

**Figure 3.8** First Primary MEMS platform raw vibration results

Although the rangefinder confirmed a pure mechanical sinusoidal motion, from the results of figure 3.8 it could be seen that the total absence of a band limiting capacitor on the output signal of the accelerometer, allowed for a rather large amount of noise to be present, making the sinusoidal function only just decipherable.

In order to investigate the effects of inter-structural resonance, an additional compact test-platform was constructed and attached directly to the lower section of the actuation shaft.

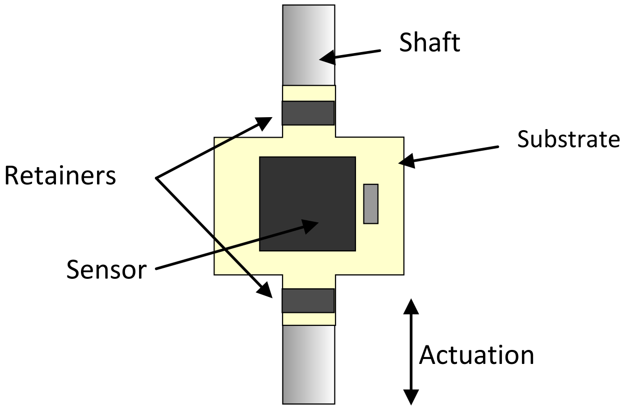

**Figure 3.9** Compact assembly directly bonded to the shaft

A MEMS accelerometer and an output filter capacitor were attached with resin to a Balsa substrate, and ultra-thin wires soldered directly to the pads of the MEMS IC as shown in figure 3.9.

Re-actuation of the compact assembly at an almost identical frequency showed a considerable improvement in the noise content of the signal, as depicted in figure 3.10, thus providing concrete evidence for the need of careful physical instrument assembly if inter-instrument resonance and structural vibration was to be avoided.

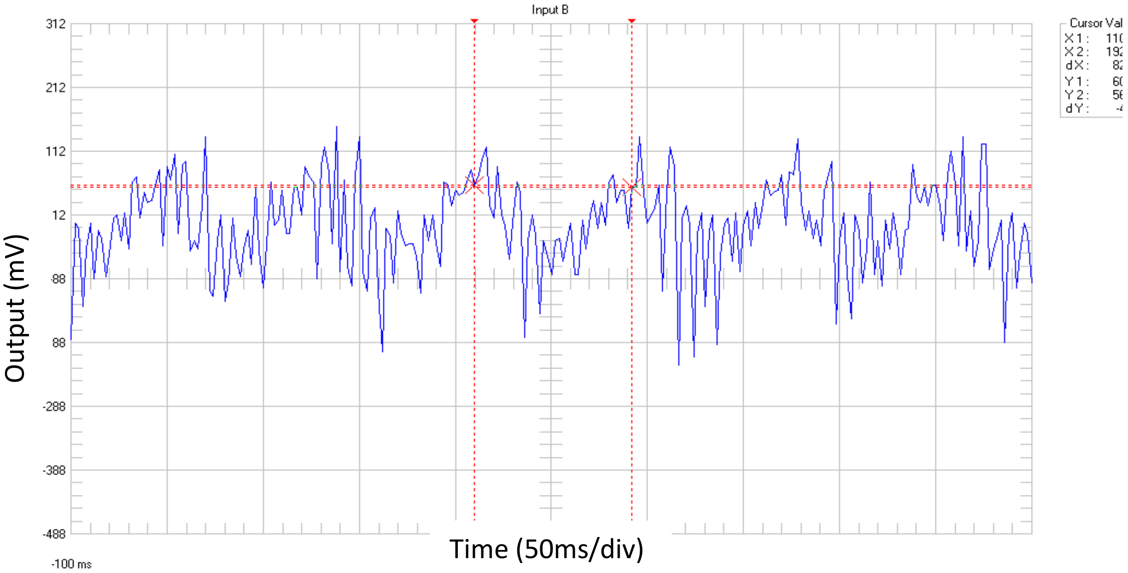

**Figure 3.10** Resin bonded compact assembly output with improved noise characteristics

Digitisation of the compact assembly’s raw and unfiltered data was digitised and an offset adjustment was mathematically applied in order to eliminate the zero-g baseline offset of the accelerometer’s DC-coupled output, as shown in figure 3.11 below. It should be noted that the units are irrelevant in figure 3.11, figure 3.12 and figure 3.13, as the axes values simply represent quantised and scaled output data with reference to scaled sample times.

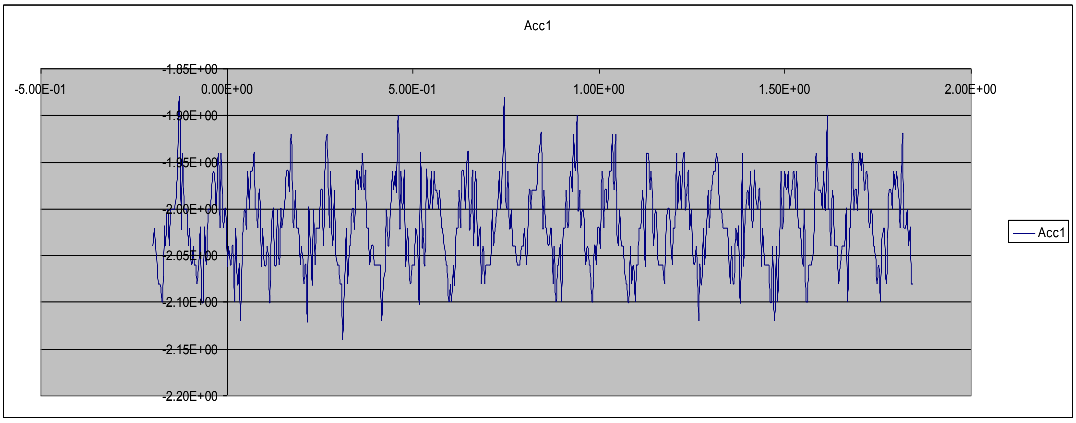

**Figure 3.11** Digitised and mathematically zero-g offset corrected raw accelerometer data

Numerical integration of the zero-g corrected accelerometer data yielded a representative velocity over time curve as shown in figure 3.12, where the effects of the cumulative nature of the integration process could already be seen. Various underlying sources of error, such as noise, non-linearities, and zero-g baseline misinterpretation, resulted in the magnification of errors yielding a rather unconvincing velocity trend.

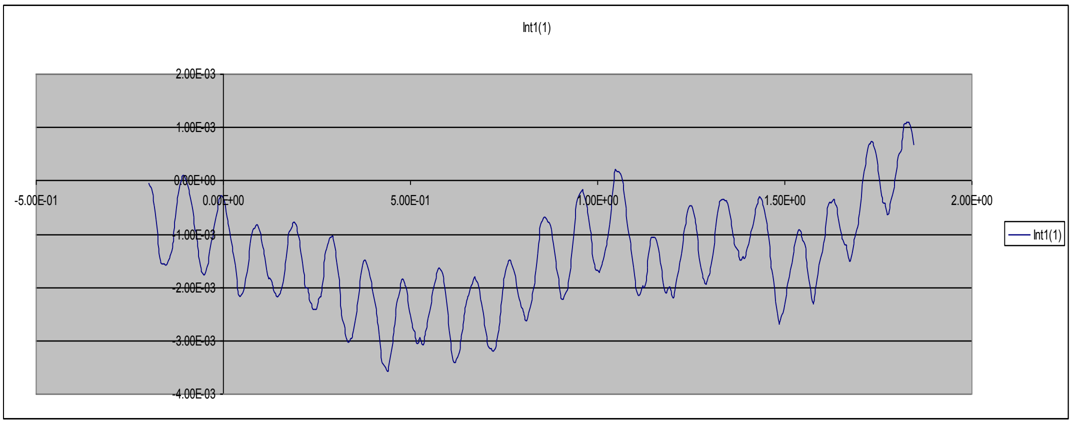

**Figure 3.12** First integral of the raw data representing velocity over time

Finally, deriving the second integral representing displacement over time is shown in figure 3.13, with the characteristic baseline offset that is most frequently observed in seismic data sourced from current seismographs, was experimentally and conclusively repeated.

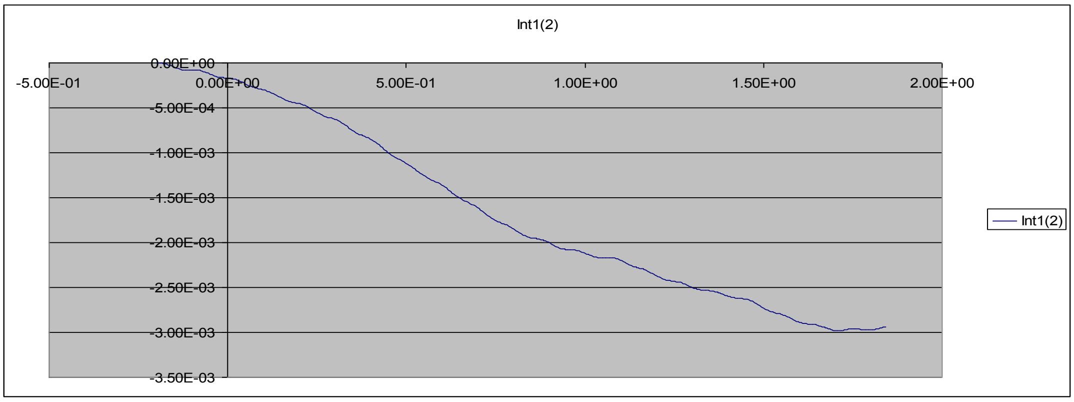

**Figure 3.13** Second integral of the raw data representing displacement over time with baseline error

Further tests showed that the baseline "runaway" phenomenon was reasonably consistent across all test vibration frequencies, with only mild improvement at the higher frequencies.

Duplicating the practices of the seismic instrument manufacturers, the output of the resin bonded test platform was AC-coupled and subsequently filtered with the aid of low pass RC filter with a 100Hz cut-off frequency. The much improved performance with regard to the baseline runaway is shown in figure 3.14, where the raw data and both the first and second integrals are depicted. Although this type of approach employed by few seismograph manufacturers to date appears to dramatically improve matters, it only bypasses the issue as it severely distorts the output across the bandwidth of interest, both in amplitude and phase. Such distortions, especially in the lower frequencies, result in the loss of valuable seismic data and produce various distortion artefacts in the higher frequencies.

Although heavily filtered and mathematically baseline offset corrected to six decimal places, the AC-coupled data with a length of only a few seconds, exhibited undulations in the displacement trend, proving an early departure from the ideal pure sinusoid expected.

The findings in this preliminary study which are fully in line with existing literature, provided clear evidence that current techniques, algorithms, and calibration models, operate within many constraints since they try to reverse effects of various errors with very limited quantitative access to their attributes. Although these correction techniques which often require several presumptions to be employed offer some aid towards the recovery of better seismic displacement data, an altogether new type of sensor arrangement able to target the very source of these errors is clearly required.

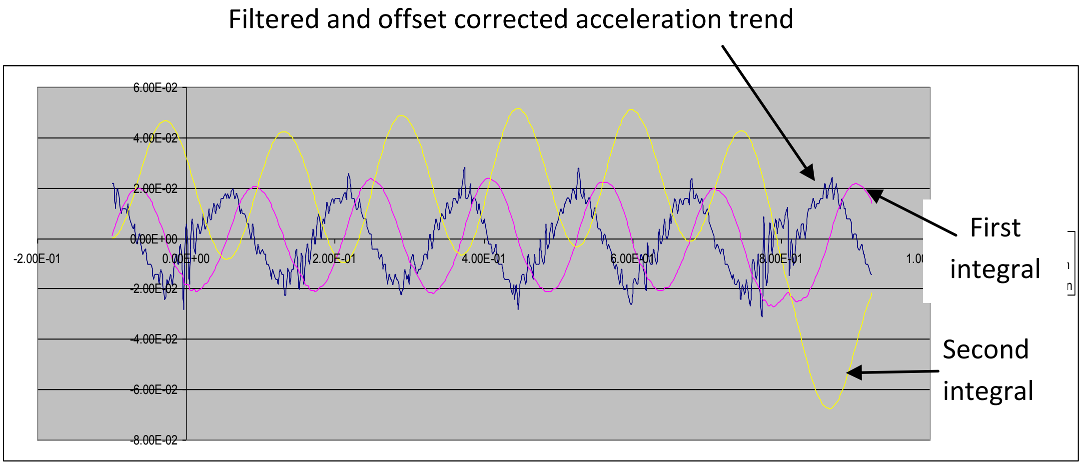

**Figure 3.14** Acceleration data, first and second integrals of filtered and AC coupled sensor

Further, long term instrument drifts, alterations in sensor response, and the dynamic environment presented by the very surface of the Earth, pose serious challenges to the acquisition of uncorrupted data, an issue this far completely unresolved by seismic instruments. An ideal sensor should therefore not only rely on preset factory calibration, mathematical correction and predictive schemes, but should be able to dynamically adapt to changes in order to respond to both internal and external interference in such a manner as to deliver long term undistorted data throughout its operational lifetime, and under all real environment conditions.

Both existing literature and the results of the primary experimental study suggest that the creation of an instrument capable of delivering long term near-uncorrupted and repeatable data should aim to rectify the effects of key error contributing sources as close as possible to their source, utilising quantitative techniques rather than exclusively relying in stochastic, pre-determined, or speculative post-processing methods. To this effect, the objective of this work is to identify, analyse, and provide novel solutions to these sources of error, with the aim to design, build, and experimentally evaluate a benchmark sensor arrangement.

The system diagram of figure 3 is repeated below in figure 3.15 with some of the most prominent sources of potential error identified.

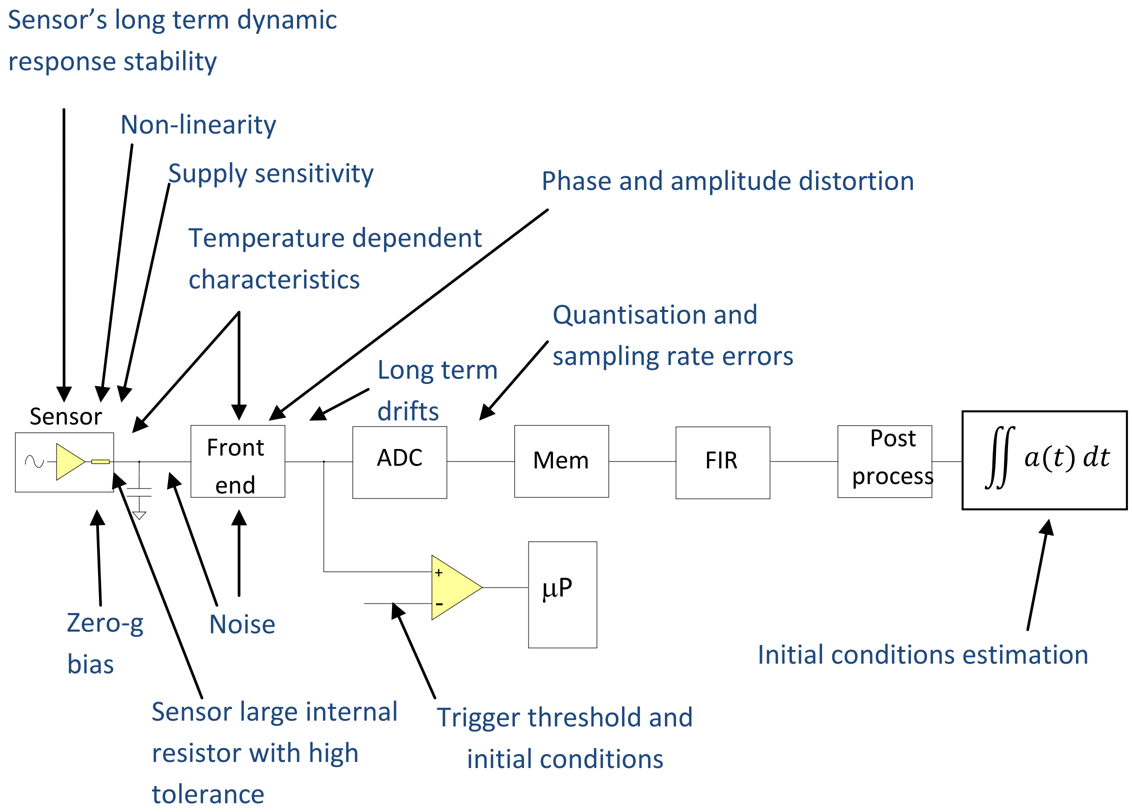

**Figure 3.15** Prominent sources of potential error identified by section

Since the intent of this work is to attempt the resolution of errors from their root, special attention is given to the investigation of the internal to the sensor potential sources of error, and the effects of the sensor to the original seismic signal in general.

## 3.1 Evaluation of the MEMS accelerometer sensor performance

Most research in the seismological arena has focussed on external to the MEMS issues whilst MEMS manufacturers understandably focus on commercially lucrative markets, which seismology unfortunately is not one of them. The need to understand how the current MEMS technology impacts seismic instruments is therefore rarely addressed as most researchers do not have the means to directly access or alter the internal micro structures within the MEMS devices.

Since the accelerometer data is the only means available in this case for deriving displacement over time trends, careful consideration should be given to the errors inherent to such a device, especially when the necessary double integration inevitably produces cumulative and exponential exaggeration of even the smallest of errors over time.

In an ideal system, the position (x) of a moving object at any time (t) can be calculated from its acceleration as follows;

$$x(t) = \iint_0^t a(t)dtdt + \int_0^t v_0(t)dt + x_0 \tag{3}$$

where $(a)$ is the acceleration, $v_0$ is the initial velocity and $x_0$ is the initial position of the object. The acceleration in terms of voltage output $(V_s)$ from the sensor can be simplified to;

$$V_s(t) = S(1 + \delta S)a(t) + V_{0g} + \delta V_{0g} \tag{3.1}$$

where $S$ is the sensitivity, $\delta S$ is the general sensitivity error incorporating temperature, cross-axial excitation, and ratiometric contributions. $V_{0g}$ is the zero-g voltage bias of the sensor and $\delta V_{0g}$ is the general voltage bias error, also incorporating contributions from temperature, misalignment and ratiometric artefacts. The derived acceleration $(a_m)$ by direct measurement of the sensor voltage output $(V_s)$ is therefore:

$$a_m(t) = \frac{V_s(t) - V_{0g}}{S} \tag{3.2}$$

Since the sensor voltage output contains errors as modelled above in equation 3.1,

$$a_m(t) = \frac{V_s(t) - V_{0g}}{S} = \frac{S(1 + \delta S)a(t) + V_{0g} + \delta V_{0g} - V_{0g}}{S}$$

$$\therefore\ a_m(t) = a(t) + \delta S a(t) + \frac{\delta V_{0g}}{S} \tag{3.3}$$

For zero initial conditions, $x_0 = v_0 = 0$, the derived position of an object by measurement can be represented as;

$$
\begin{aligned}
x_d(t) &= \iint_0^t a_m(t)dtdt \\
&= \iint_0^t a(t)dtdt + \delta S \iint_0^t a(t)dtdt + \frac{\delta V_{0g}}{S} \iint_0^t dtdt \qquad (3.4)
\end{aligned}
$$

From equation (3.4) it can be seen that a small error on the zero-g bias voltage can result in a rather large error, especially when several seconds of data is to be integrated. Since both the sensitivity and the zero-g bias level are ratiometric, they are also both influenced by any irregularities or noise on the supply rails.

The ADXL325 and ADXL327 MEMS accelerometer sensors have a typical zero-g bias level of 1.5V when the supply voltage is 3V, however, the newer ADXL327 offers superior performance in sensitivity and signal to noise ratio (SNR) and is therefore most suitable for this work. Although most appropriate for this study, an examination of the ADXL327 device's electrical characteristics revealed some of its more obvious inherent limitations.

According to the manufacturer, the package alignment error, that is the alignment error between the package and the sensing axis, and the cross-axis sensitivity are both specified to be at ±1°. While the package alignment error is of no consequence as it remains constant and can therefore easily be calibrated out, the cross-axis sensitivity, although also constant, would require a rather involved correction process if it was to be corrected for operation in a real three dimensional environment.

It should also be noted from the manufacturer's data, that both the sensitivity and the zero-g offset, that is the voltage output when no acceleration input is present, are temperature dependent. With a temperature effect on the zero-g bias voltage specified at ±1mg/°C, a temperature difference of just 10°C would result in a bias voltage error of 10mg, which in turn would result in an error contribution to the displacement trend of nearly 5cm in just one second of data. While temperature tends to alter slowly, and such changes in the zero-g bias could be taken into account during the zero bias derivation by pre-event data averaging; any change in the sensor's sensitivity due to change in temperature would irrecoverably contribute to erroneous measurements, unless an output temperature compensation scheme was employed.

Although both the ADXL325 and the ADXL327 sensors are indeed tri-axial, due to package limitations their z-axis is only able to achieve nearly half the bandwidth of the other two orthogonal sensing axes. A high performance tri-axial seismic instrument would therefore necessitate the utilisation of a separate MEMS sensor IC for the z-axis acceleration measurement in order to work around the rather poor inherent z-axis performance.

The internal to the sensors 32K output resistors, conceived by the manufacturer to offer short circuit protection and external filter design simplicity, could also present another potential source of error. The inclusion of these rather high in value resistors provides a rather inconvenient high impedance output with any benefit on filter design simplicity readily negated by their rather large ±15% tolerance. Figure 3.16 below shows a block diagram representation of the ADXL327 sensor.

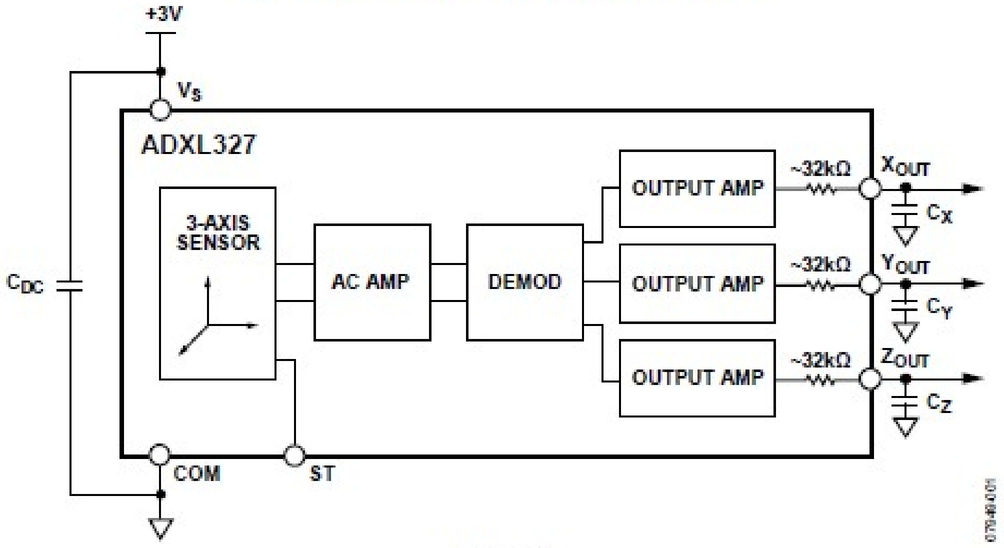

**Figure 3.16** Diagrammatic representation of the ADXL327 sensor (source: ADXL 327 datasheet)

Although the internal resistors may be beneficial in many non-precision applications such as smart phones, in seismic vibration sensing, coupling to the front end electronics requires their careful consideration.

Many other internal to the sensor sources of error required a rather deeper and experimental investigation in order to gain an adequate in-depth understanding of their nature and arrive at suitable correction methods.

### *3.1.1 MEMS Sensor noise experimental investigation*

Sensor noise is by far the most obvious and prominent source of error directly arising from the sensor's physical electromechanical properties.

A direct and unfiltered measurement of a MEMS ADXL327 sensor output, shown in figure 3.17, exhibited a typical 1/f characteristic and a rather prominent peak at just under 50 KHz matching the IC's internal clock frequency. This peak in the frequency however is both out of the 100Hz seismic bandwidth of interest, and at -72dB, of no real concern after low-pass filtering of the raw signal has taken place.

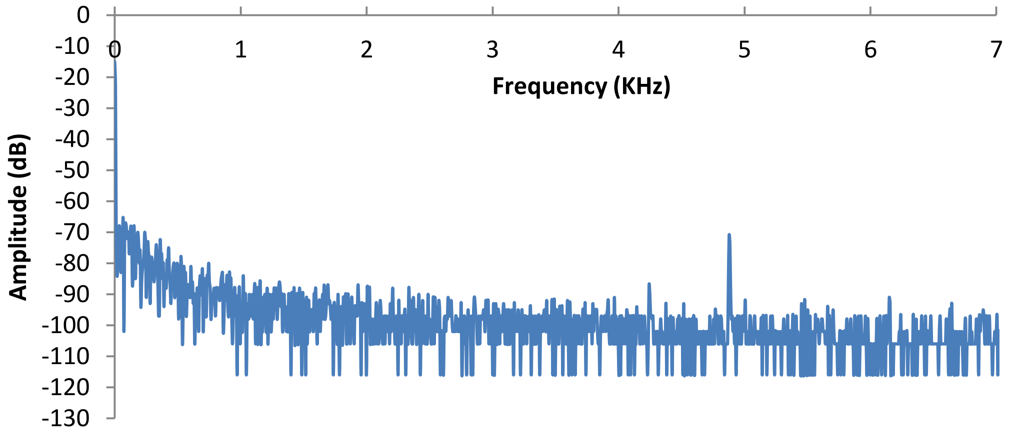

**Figure 3.17** Sensor noise frequency spectrum

The miniaturization of mechanical structures within these MEMS devices makes their moving parts very susceptible to mechanical noise resulting from molecular agitation. One, if not the main source of such noise, is Brownian motion where molecules of the surrounding mater and gas collide with the micro-structures to produce a random motion. Unlike traditional larger scale sensors where the noise floor is chiefly dictated by the amplification stage and the front end electronics, in MEMS accelerometers thermo-mechanical noise can be very prominent and in most cases the limiting factor in the resolution attainable.

Since many environmental factors within the device can be considered constant, such as the molecular densities of gas and silicon structures, the mechanical noise due to the agitation of molecules can be estimated by considering the effects of temperature on the mobility of the molecules.

As seen earlier, the arrangement of the moving parts within the accelerometer can be thought of as a mass (m) on a spring of constant (k) system, with mechanical damping (R). A fluctuating force $(f_n)$ would therefore result in a motion with displacement (z) as shown in equation (3.6) below.

$$f_n(R,t) = m\frac{d^2z}{dt^2} + R\frac{dz}{dt} + kz \tag{3.5}$$

The resistive force (R) on the system dictates that any motion of the mass will decay in time, but also necessitates that any movement of the surrounding structures or gases will also result in some motion of the sensor's inertial mass.

Considering the Equipartition theorem, the *average* kinetic energy of an atom at thermal equilibrium is equal to $\frac{3}{2}K_BT$, where (T) is the absolute temperature and ($K_B$ ) is the Boltzmann constant. Newtonian physics however, dictates that the kinetic energy of a mass (m) and velocity (v) is given by:

$$H_k = \frac{1}{2}m|v|^2 = \frac{1}{2}m\left(v_x^2 + v_y^2 + v_z^2\right) \tag{3.6}$$

where $v_x, v_y, v_z$ are the orthogonal velocity components, and each component must therefore contribute to the average kinetic energy by $\frac{1}{2}K_BT$.

From the potential energy of a mass-spring then, the mean square displacement resulting from thermal molecular agitation can be expressed as:

$$\frac{1}{2}k\langle x^2\rangle = \frac{1}{2}K_BT \quad [J] \tag{3.7}$$

where $\langle x^2\rangle$ represents the average spectral density of $x^2$ across all frequencies.

For any mechanical resistance, the spectral density of a fluctuating force, in accordance with Nyquist's Relation, can be shown to be:

$$F = \sqrt{4K_B TR} \quad [N/\sqrt{Hz}] \tag{3.8}$$

which is equivalent to the Johnson noise of a resistance created by the thermo-mechanical vibration of the medium interacting with the free electrons within the medium.

For the mass-spring system representation of the accelerometer, mathematical analysis of equation (3.8) yields a relationship between thermo-mechanical noise density ($ND_{th}$), resonant frequency (ω), mass (m), damping (Q) and temperature (T) of the sensor as follows:

$$ND_{th} = \frac{\sqrt{\frac{4K_B T\omega}{mQ}}}{g} \quad [g/\sqrt{Hz}] \tag{3.9}$$

$$\text{Where } Q = \frac{\omega m}{R} \text{ and } \omega = \sqrt{\frac{k}{m}} \tag{3.10}$$

It can be seen then from the above analysis that in a MEMS accelerometer sensor, most terms are pre-set by the fabrication process and the only variable available with regard to noise density contribution is temperature. Theoretically then, as the temperature approaches absolute zero the noise density should also tend towards zero in a non-linear fashion.

It is worth noting that a larger mass would then result in lower noise, pointing to the fact that bulk machined accelerometers have better noise characteristics than their surface machined counterparts. Altering other factors in order to increase Q would also benefit the signal to noise ratio at the expense of increased ringing at the resonant frequency.

### *3.1.1.1 Experimental investigation of temperature effects on sensor noise*

As the MEMS sensor noise is not only of thermomechanical origin, but also comprises Johnson noise, shot noise etc in the internal signal conditioning and sensing circuits, it cannot exclusively be defined by equation 3.9 alone. In order to experimentally asses the noise characteristics of the complete MEMS sensor over temperature, a test circuit was designed and fabricated as depicted in figures 3.18 and 3.19 below.

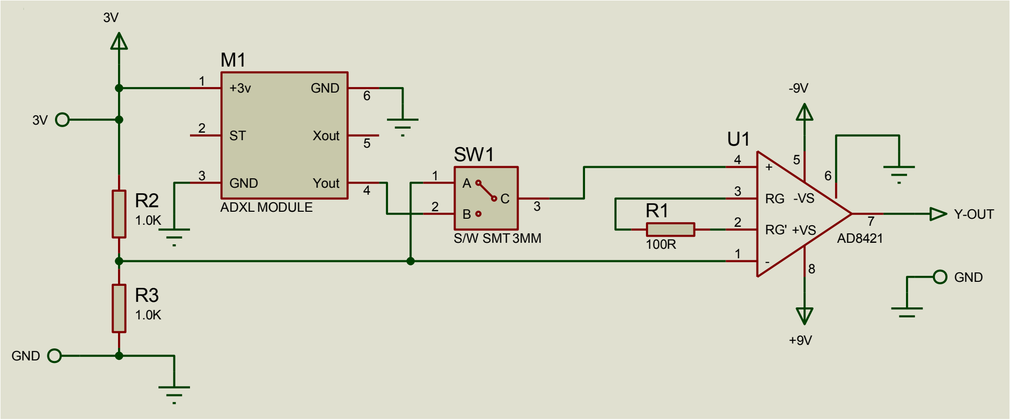

**Figure 3.18** Circuit diagram of sensor noise investigation circuit

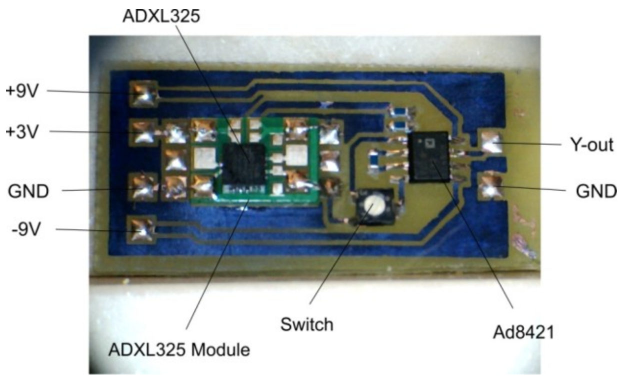

**Figure 3.19** Physical assembly of sensor noise investigation circuit

A quiet battery supply and a large amplification on the amplifier stage was thought essential in order for small variances in signal amplitude to be observable, however, exposure of the circuit to even unexceptional temperatures down to 5°C revealed rapid and exponential decrease in noise, albeit not readily evident by direct voltage output examination, as depicted in figure 3.20 below.

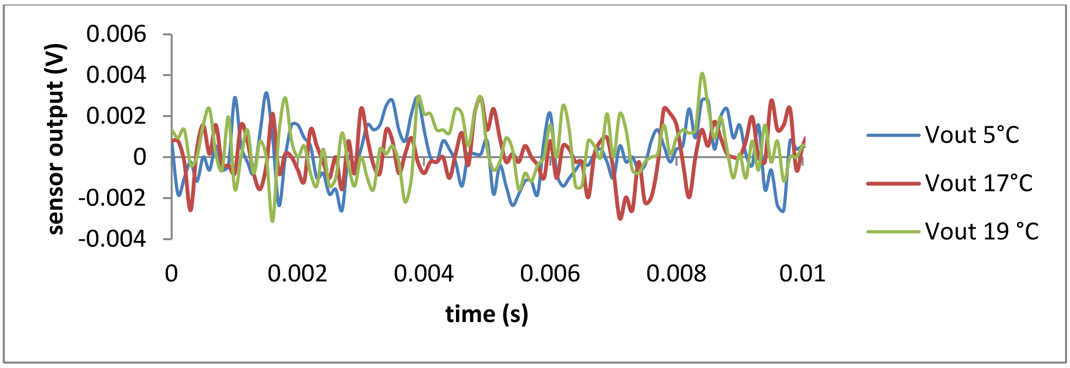

**Figure 3.20** direct sensor output at rest and at different temperatures

Statistical analysis however of the three voltage output trends of figure 3.20, yielded remarkable differences in the noise content of the signals over the three different temperatures.

| Statistical info | Vout 5°C | Vout 17°C | Vout 19°C |
|---|---|---|---|
| Standard Deviation | 0.0012389 | 0.001241625 | 0.001294403 |
| Range | 0.0070588 | 0.007215686 | 0.008235294 |
| Sample Variance | 1.535E-06 | 1.54163E-06 | 1.67548E-06 |

**Table 3.1** Statistical analysis of the output trends of Figure 3.20

Table 3.1 contains the results of the statistical analysis conducted on the voltage trends depicted in figure 3.20. The study revealed a standard deviation increase of 16.7%, which is representative of noise power; an increase of 9.2% in sample variance, and a 1.2mV pk-pk increase in the range of the signal, as the sensor temperature increased in temperature from 5°C to a 19°C ambient. Furthermore, the increase of both noise power and noise peak to peak voltage over temperature, exhibited a rather sharp exponential trend as shown in figures 3.21 and 3.22 respectively.

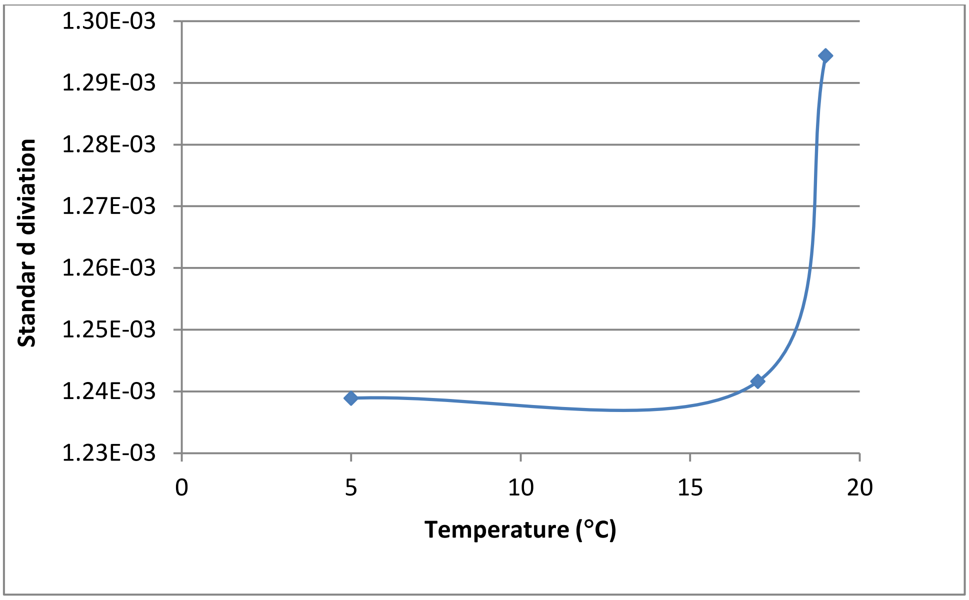

**Figure 3.21** Standard deviation of sensor noise over temperature

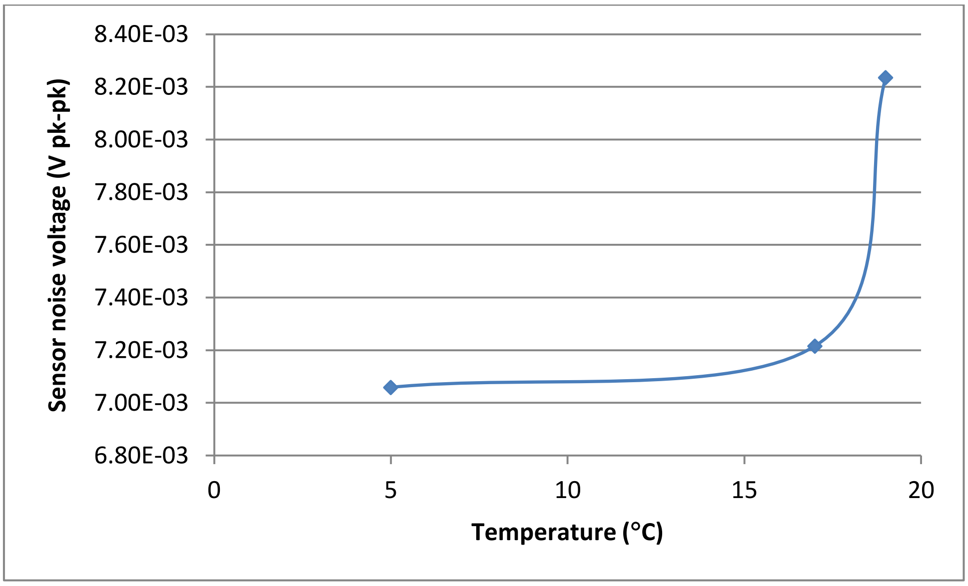

**Figure 3.22** Noise range over temperature

In instrumentation terms, if the sensor output was to be amplified and digitised by a 16 bit ADC over the range of ±10V, the noise increase in operation at 19°C by comparison to operation at 5°C, would be equivalent to sacrificing the 3 least significant bits (LSBs) to noise.

Operation at very low temperatures could therefore be an effective way of reducing the noise content of the signal directly from its source.

### *3.1.1.2 Experimental investigation of differential Bi-axial excitation for noise reduction.*

In an attempt to explore alternative additional methods of reducing noise at the output of the sensor, further experimental investigation and analysis of any potential relationship between the x and y outputs was conducted. Figures 3.23 and 3.24 show the unfiltered and simultaneously sampled x and y outputs of the sensor at rest, or zero acceleration input.

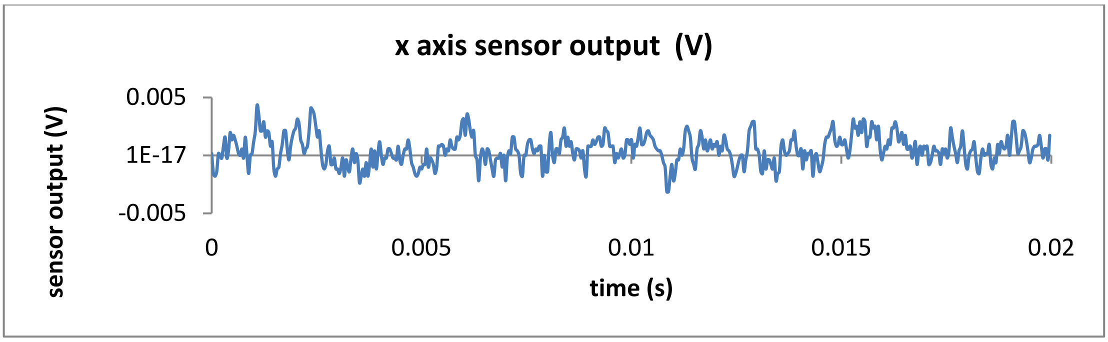

**Figure 3.23** x-axis sensor output at no excitation

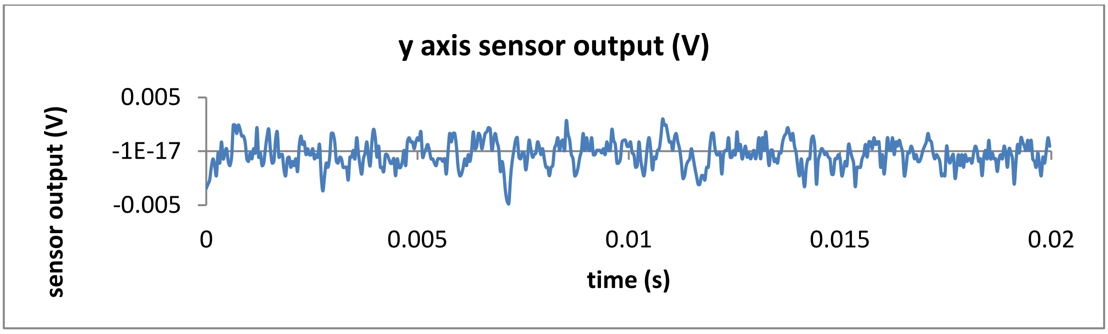

**Figure 3.24** y-axis sensor output at no excitation

The assumption behind this investigative approach presupposed that since the sensor benefited from a single wafer construction and the electronics of each channel were therefore in very close proximity, at least some proportion of the total noise, other than thermomechanical, should exhibit common mode characteristics. It should then follow that the utilisation of two channels at 45° to the direction of the acceleration vector should have resulted in a pseudo differential voltage output proportional to the acceleration, with the noise in common mode, as shown in figure 3.25 below.

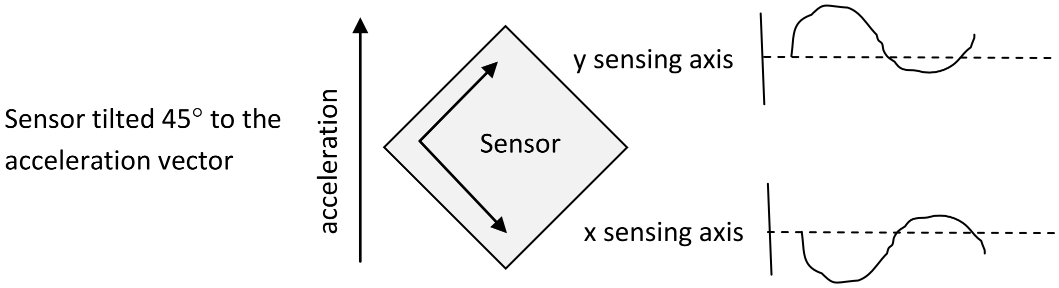

**Figure 3.25** Differential excitation of sensor axis

Standard differential signal handling should have therefore resulted in an amplified signal with much reduced noise content.

Although one sensor IC would have to be used for each instrument axis (2 sensor channels per instrument axis), the advantage of noise reduction at the source would by far outweigh the additional overhead in cost and complexity.

Some sections of the acquired sensor output signals are depicted in figures 3.23 and 3.24 did indeed appear very similar, especially when closely examined in segments, as depicted in figure 3.26. Casual assumptions of patterns, phase shifts and inversions observed could be easily made as follows;

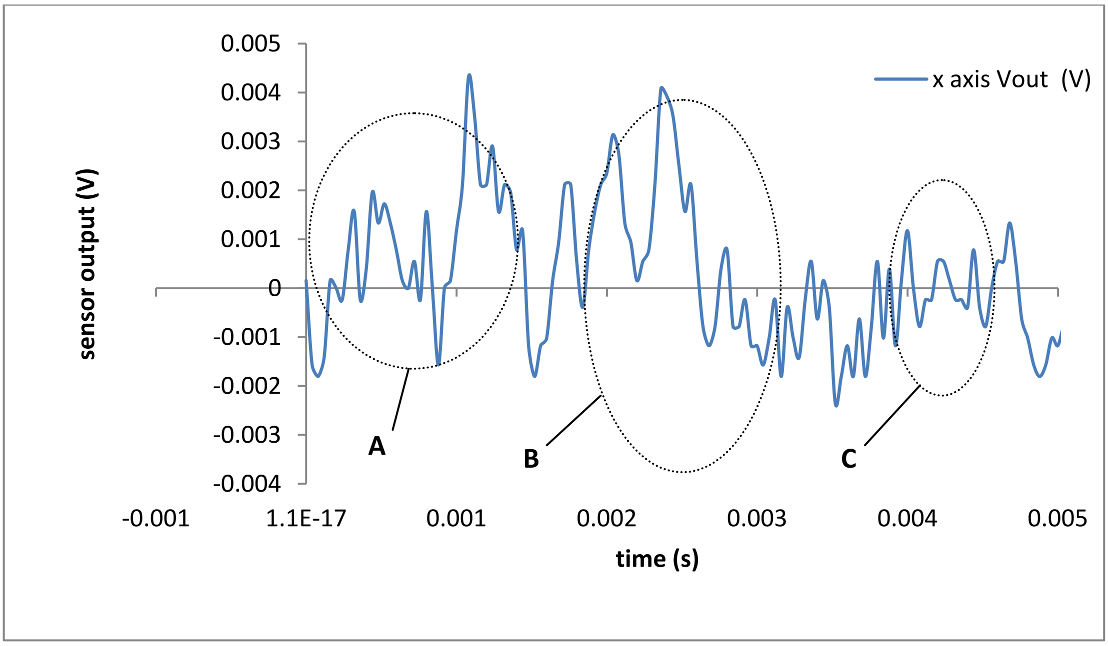

**Figure 3.26** x and y axis output segment comparison

Segment A could be interpreted as two signals with anti-phase low frequency content, but phase shifted high frequency common mode noise content, whilst segment B could indeed be interpreted as two signals where one is inverted and phase shifted, also implying common mode content. Segment C could be seen as two in-phase signals with much common mode content. Although all of the three aforementioned observations were frequently encountered within the output signals, there was no single effect dominance, necessitating the inevitable conclusion that *there was not any notable common mode content found between the x and y noise output signals of the sensor.* In addition, mathematical assessment via correlation of the two signals revealed a rather low consistent figure of -0.165 or below, further supporting the noise independence of the two signals and the little usefulness of the differential bi-axial excitation approach.

#### *3.1.1.3 Conclusion on sensor noise investigation*

As noise can be one of the main limiting factors of sensor performance, any methods employed to minimise the effects of noise on the signal are crucial. The experimental evaluation of sensor noise in this chapter has shown an exponential increase of noise with increase in ambient temperature, and a characteristic 1/f frequency response. Further, a peak at the internal clock frequency also became evident, albeit outside the bandwidth of interest.

Noise coupling from the power supply to the sensor can also produce a significant detrimental effect on the sensor signal, as the supply noise rejection of the MEMS sensors is rather limited by comparison to amplifier standards. Effective de-coupling of the supply rails and a quiet and stable power source are of extreme importance since the sensor output is ratiometric and therefore the accuracy of any acceleration measurement can be directly affected by any supply voltage irregularities.

### ***3.1.2 Experimental investigation of on- demand sensor dynamic response***

Any sensor or system employed to measure a physical property will be default impart some alteration to the original due to its inherent non-perfect response. Knowing the relationship between the input and the output of such a sensor or system is therefore essential if the original signal measured is to be correctly defined. Although the static or steady state performance of a system is incredibly important for accuracy and long term performance, when dealing with fast changing signals as is the case with seismic waves, the dynamic response of the system is also of vital importance to the quality of the data acquired with such a sensor.

The manufacturer's technical data offers very few clues as to the dynamic response of the MEMS sensors, but alludes to a flat frequency response from DC to 1.6KHz without the use of an external filter. It further states that this useful bandwidth can be reduced with an external capacitor to ground, forming a low-pass filter with the internal resistor, in order to benefit from the increased signal to noise ratio of the more restricted bandwidths. Acquisition of a sensor's dynamic response characteristics is typically conducted on a vibration platform able to sweep across frequencies in the bandwidth of interest, making the acquisition of this information by these means from a sensor in the field and on demand impossible.

#### *3.1.2.1 Sensor Frequency response acquisition via electrostatic frequency-sweep excitation*

Most MEMS accelerometers are equipped with a test pin which upon the application of a voltage, an electrostatic force is exerted onto the internal inertial mass, forcing it to deflect in a certain direction, thus producing a voltage output on all sensing axes. This test pin was experimentally found to be internally buffered with a comparator of threshold voltage a little below 2V, presumably to deliver a predictable response and avoid interference due to external spurious noise. It was empirically discovered however, that it was possible to excite the inertial mass via this pin, by applying a square wave of incremental frequencies, in order to attain a frequency response of the inertial mass-spring system. The resulting frequency response followed a typical mass-spring characteristic curve, as shown in figure 3.27, with the addition of an atypical dip between frequencies 1.5 KHz and 3 KHz. The otherwise perfect frequency response acquired by the excitation of the self test pin confirmed the fact that the internal interfacing electronics of the test pin did not limit the frequency of the input signal within the bandwidth of interest.

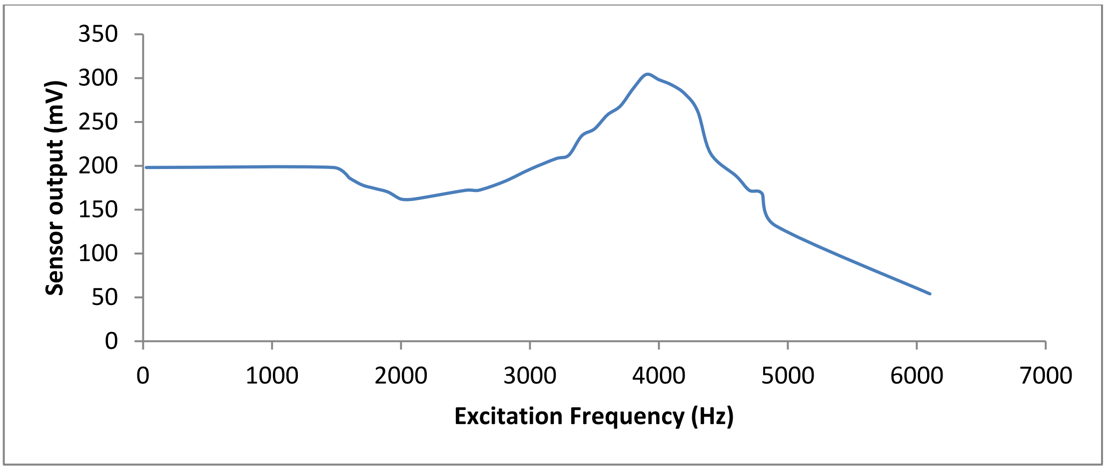

**Figure 3.27** Frequency response of sensor via electrostatic excitation utilising the test pin

From the experimental results of figure 3.27, a flat response from DC to 1.5 KHz was evident, followed by a characteristic resonant peak at 3.9 KHz. These findings, although very close to the manufacturer's claims of a useful unfiltered bandwidth from DC to 1.6 KHz, were neither uniform nor non-attenuated to 1.6KHz. In addition to the rather unexpected lower frequency response, a peak resonance was observed at 4.9 KHz, which was rather lower than the 5.5 KHz specified in the datasheet. Confronted with the above findings, the manufacturer has since confirmed that the internal conditioning electronics produce filtering of the output with a -3db at 1.6 KHz low pass characteristic, thus validating both the uncharacteristic dip observation and the shift of the resonance peak to a lower frequency.

It is conclusive from the above results that this input can be effectively utilised for the derivation of the frequency response of the sensor, and the wider electronic system, without the aid of a mechanical vibrator, in the field and on demand. The ability to acquire the system's frequency response means that in part at least, the validity of the instrument data can be guaranteed over long term.

### *3.1.2.2 Sensor output dithering via high frequency electrostatic excitation*

Further frequency response experiments showed that forcing the mass to oscillate at frequencies higher than 4.5 KHz resulted in regions of unstable behaviour, but still within the typical characteristic as depicted in fig 3.27. However, at a frequency of 6.1 KHz, the mass appeared to regain stability and the output exhibited a sinusoidal voltage of amplitude 54 mV peak to peak, with a mean DC offset of -86mV from the nominal no excitation zero g. While powered from a 3V supply and at a position orthogonal to the gravitational field, direct measurement of the sensor's zero g voltage output confirmed a value of 1.526V, which was within tolerance of the typical half the supply voltage level. A mean DC level of 1.44V was witnessed upon the subsequent application of a 6.1 KHz input signal to the test pin.

Since any mechanical excitation of the sensor can be thought of as a superimposition on the electrostatically induced 6.1 KHz signal, the 6.1 KHz signal could be successfully utilised as a form of dithering. However, since the typical sensor sensitivity of the ADXL325 is 175mV/g, the change in zero-g offset by -86mV due to the dithering signal equates to a loss of 0.49g in dynamic range. The superimposing effect of the electrostatically induced dithering on a mechanical vibration signal can be seen in figures 3.28 and 3.29 below, depicting a vibration signal with and without the dithering signal enabled respectively.

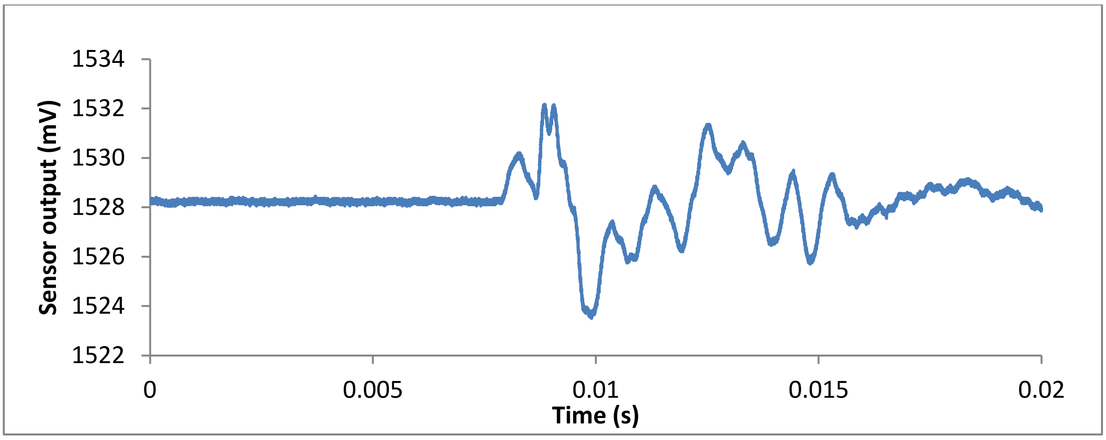

**Figure 3.28** Mechanical vibration without dithering enabled

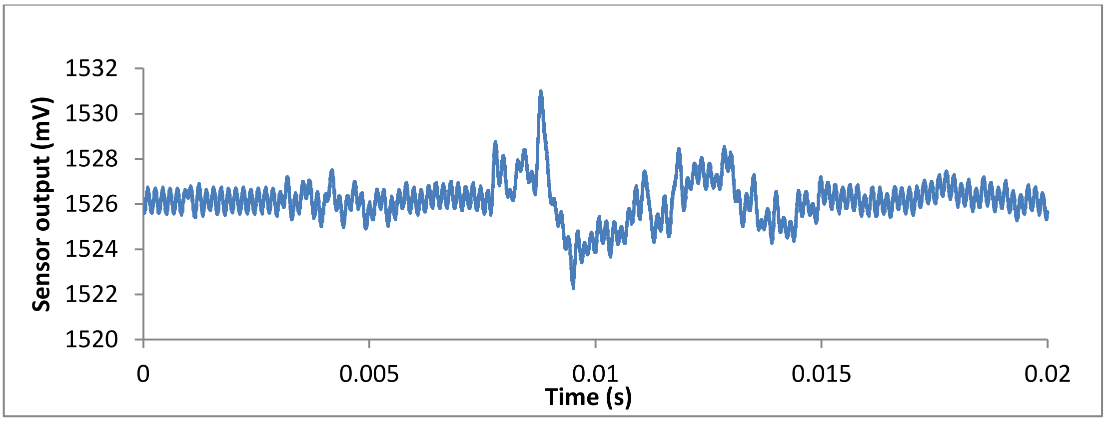

**Figure 3.29** Mechanical vibration with 6.1KHz dithering injected via the test pin

Such means of dithering can provide substantial benefits provided that the loss of dynamic range is acceptable for the intended application. Although the amplitude of the resulting dithering signal is larger than normal, it could be of benefit to the acquisition of seismic trends, especially in the capturing of the very low frequency, low amplitude adulations, sometimes present in seismic signals.

### *3.1.2.3 Sensor dynamic response acquisition via electrostatic impulse excitation*

It was envisaged, that an impulse response representing the characteristic behaviour of the device could be derived, if excitation of the test pin was achieved by a narrow enough pulse, approximating an impulse with respect to the system. Such a characteristic response should be similar to one acquired if the sensor was mechanically actuated.

Whilst a mechanically actuated response would suffer from various errors and inconsistencies, an electrically derived impulse response could provide a much more precise and stable characteristic. In addition, such direct derivation of the system's response could provide an on-demand system dynamic response characteristic in the field, without the need of any specialist laboratory equipment.

It is widely accepted that any linear system such as this, when within the linear range of operation, can be thought of as having an output y(n) which is the convolution of its input x(n) and its impulse response h(n) such that;

$$y(n) = h(n) \circledast x(n) = \sum_{k=-\infty}^{\infty} h(k)x(n-k) = \sum_{k=0}^{M-1} h(k)x(n-k) \qquad (3.11)$$

where $n = 0, 1 \ldots, M-1$; and $M = N_1 + N_2 - 1$ where $N_1\ and\ N_2$ are the lengths of the sequences $x(k) and\ h(k)$ respectively.

The ability to derive an on-demand the impulse response h(k) of the instrument, having acquired the device's output y(k) due to an unknown earthquake input signal x(k), could lead to a numerical derivation of the original earthquake signal x(k), containing minimal instrument distortion. The requirement of de-convolution of course presents a mathematical challenge which is better dealt with in the frequency domain. Representing both the instrument's impulse response h(k) and its output data y(k) in the frequency domain via the application of the Fast Fourier Transform

(FFT), de-convolution could then be performed by the direct division of $\frac{Y[K]}{H[K]}$ in the frequency domain: constituting de-convolution in the time domain. Subsequent application of the inverse FFT on the quotient should in theory result in an undistorted earthquake input signal x(k).

Extensive experimentation determined that a pulse of 3V, with a pulse-width of 20µs on the test pin, was optimum for the pulse to be assumed as an impulse by the sensor. The sensor output resulting from the application of such an impulse on the test pin, resulted in a typical impulse response characteristic as depicted in figure 3.30 below.

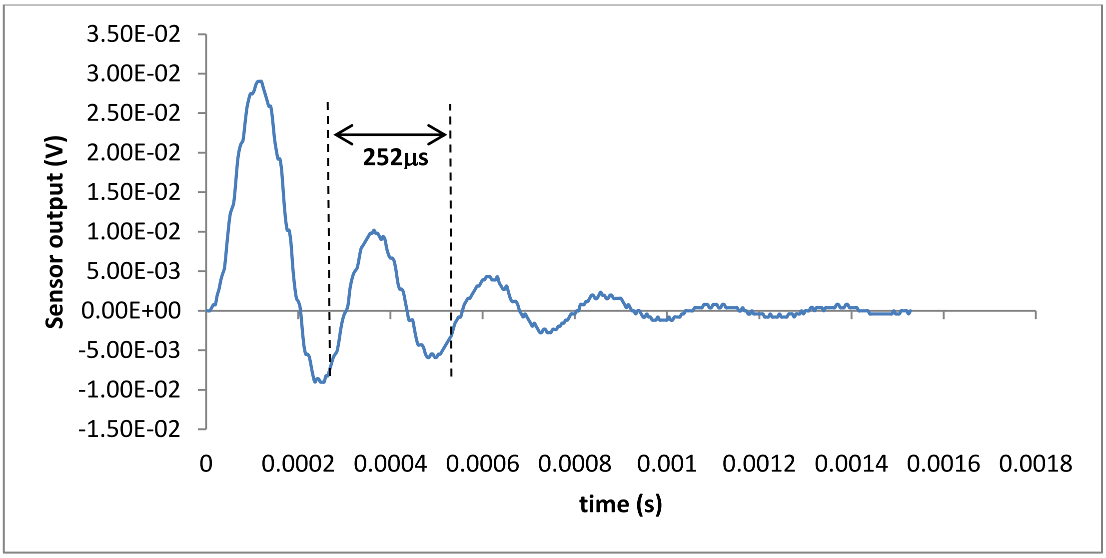

**Figure 3.30** Sensor impulse response via the use of the test pin

The successful and accurate in situ, and on demand derivation of the impulse response of the sensor and the wider system, is indeed incredibly valuable for the long term acquisition of undistorted data, especially from remote systems with potentially changing characteristics over time.

Further, the impulse response characteristic can be utilised to more accurately ascertain the resonant frequency of the sensor or system, as shown in figure 3.30. Direct calculation of the resonance period from the impulse response, 252µs in this case, resulted in a much more accurate figure of resonant frequency of 3.97 KHz.

In addition, further system evaluation or confirmation could be obtained from the sensor or system if required, by the acquisition of the step response derived by the integration of the impulse response, as depicted in figure 3.31.

Further, a frequency response could also be derived from the impulse response by acquiring its FFT, already depicted in figure 3.27, without the need to provide frequency sweep features within the instrument.

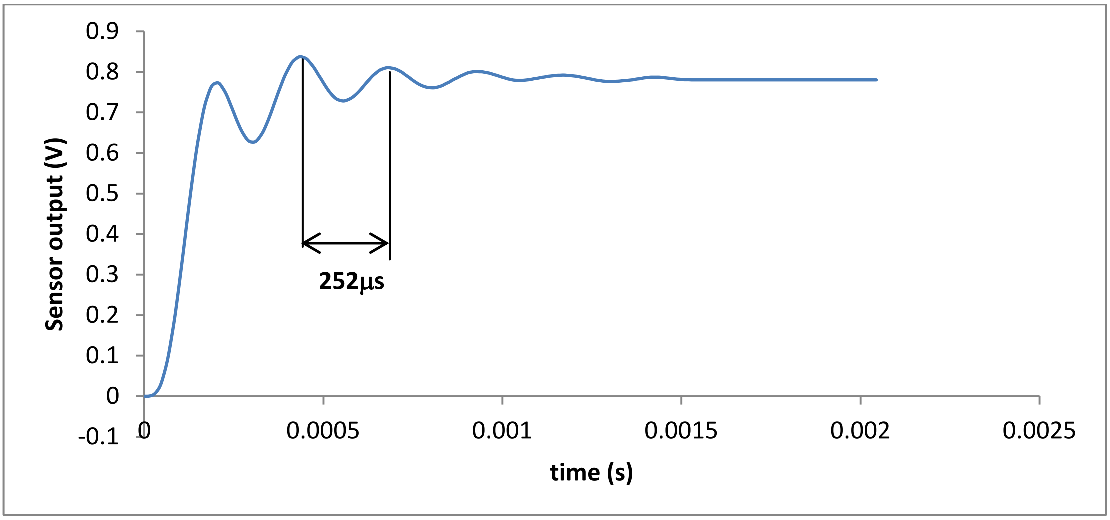

**Fig 3.31** Integral of sensor impulse response

It should be noted, that due to the unknown unit impulse function, which is proportional to the actual force exerted by the electronics onto the inertial mass within the IC, the step response could be used as a steady state reference to aid scaling.

### *3.1.2.4 Sensor phase response determination via frequency-sweep excitation*

Dynamic representation of any system also requires knowledge of its phase response, which is particularly important in seismic data as it eventually determines the location of important features on the seismogram. Fortunately, this can also be acquired via the electrostatic frequency-sweeping of the sensor’s test pin, and by measuring the comparative time delay between the input excitation signal and the sensor output.

Conversion of this delay to angle for every incremental frequency experimentally measured, yielded a logarithmic scale phase characteristic as depicted in figure 3.32

below. The most interesting aspect of the phase response characteristic acquired is of course the phase distortion within the 100Hz seismic bandwidth of interest. It is evident that any signal frequencies nearing the 100Hz point would incur a phase shift of as much as 1.58°. The fact that this phase characteristic is by no means linear is of no surprise, since the impulse response of the system derived earlier does not obey a left-right symmetry. However, a closer study of the phase shift within the seismic 100Hz bandwidth, figure 3.33, revealed a rather linear phase to frequency response within the bandwidth of interest, with the exception of a small anomaly possibly due to measurement tolerance.

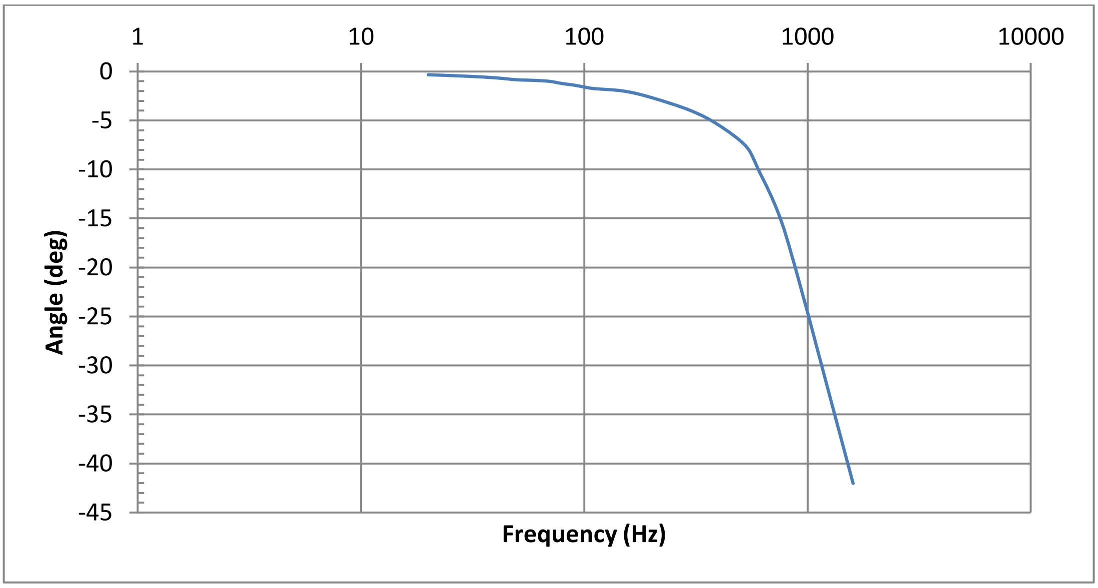

**Figure 3.32** Sensor phase response derived via test pin excitation

The discovery of the apparent phase linearity within the bandwidth of interest is of course of tremendous importance, since the only difference between a zero phase and a linear phase response is proportionality in delay. In terms of real data reconstruction therefore, the relative phase relationship within the signal, and therefore its shape and relevant time delays, are still accurately preserved.

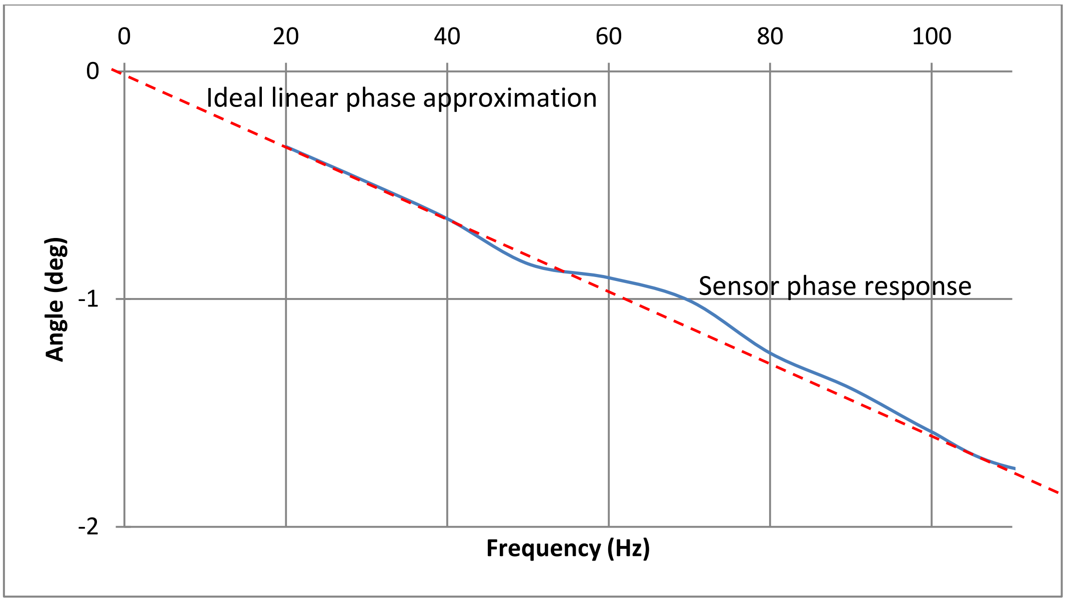

**Figure 3.33** Sensor phase response magnified segment

### *3.1.2.5 Sensor on demand dynamic response determination conclusion*

It has been shown that specific actuation of the sensor's self test pin, intended only for binary verification of operation by the manufacturer, can yield frequency sensor characteristics typical of a mass-spring system. It can therefore be assumed that this response is purely due to the internal mechanical structure of the sensor when operated within the 100Hz bandwidth, and partly due to the low-pass behaviour of the interfacing electronics that contribute to a flat response from DC to 1.5 KHz. The sensor's response at frequencies higher than this appears to be strongly dominated by the mechanical structures but also the internal electronics which further impart strong attenuation and phase effects to the sensor's output.

While high frequency excitation has proven to produce a suitable dithering effect on the sensor signal, albeit at the expense of dynamic range, impulse excitation has demonstrated that relatively accurate impulse and step responses could be obtained on demand. The latter of course is of great benefit since the sensor's and wider instrument's dynamic response can be accurately acquired, in situ and on-demand, in order to be used for the de-convolution of the acquired data, and therefore aid the reversal of any inevitable and undesirable effects imparted by the instrument on the original seismic signal.

### *3.1.3 Experimental investigation of non linear sensor response*

Other than the manufacturer specified non linear response, several other factors can influence the apparent linearity of the sensor, some stemming from manufacturing configurations whilst others can be dependent on environmental factors. In seismographic applications where accelerometers are used to acquire motion data, such small linearity errors or interferences can become rather prominent after the necessary double integration process, and usually manifest themselves as sizeable displacement offset errors.

#### *3.1.3.1 Experimental investigation of potential sensor hysteretic behaviour*

Any high accuracy sensor would not only possess phase linearity over frequency, but also inherent directional sensing linearity, as not to contaminate the pureness of the sensed signal with hysteretic or other non-linear behaviour. Testing for such behavioural attributes took the form of a high accuracy mechanical platform able to rotate the sensor noise investigation platform about an orthogonal to gravitation axis a full 360° as depicted in figure 3.34.

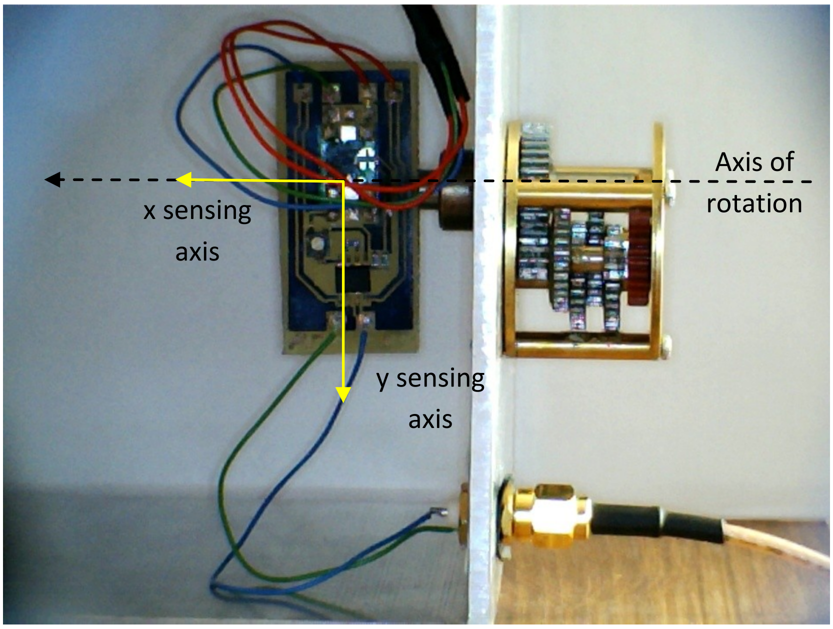

**Figure 3.34** Mechanical rotational platform

Accurate control over rotation was accomplished with a gear assembly with an input to output ratio of 1:250. Coincidental arrangement of the sensor's x axis with the axis of mechanical rotation, ensured minimal direct gravitational interference with the x axis output. Orthogonally to this, and in a rotational plane parallel to the gravitational field, the sensor's y and z axes served as the measurands over different angles of rotation.

Figure 3.16 below shows a diagrammatic representation of the sensor platform with the y axis at initial position of θ = 0. Rotation around the horizontal to the ground x-axis as indicated by the arrow is termed positive. It should be noted that in this configuration, since the x axis remained perpendicular to the gravitation vector, its output also remained at zero. Only the z and y axis were variably influenced by gravity depending on the angle of rotation. At the initial position therefore, both x and z axes were at zero g, while the y axis output was +1g.

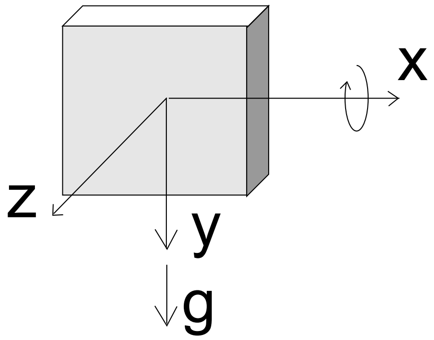

**Figure 3.35** Sensor on rotational platform a initial position

Rotating the platform such that the sensing y-axis spanned from 0° to 180° with reference to the gravitation vector caused the y-axis to experience an acceleration of +1g at the 0° position, and -1g at the 180° position. The graph in figure 3.17 below depicts the y-axis voltage output for a Clockwise (CW) rotation from 0° to 180° and the Counter Clockwise (CCW) rotation from 180° back to 0°. Whilst difficult to observe, the line in the following graph is not straight but bows towards the ends, hence exhibiting a non-linearity. This non-linear phenomenon however cannot be termed hysteretic since both the clockwise and counter clockwise resulting outputs are coincident.

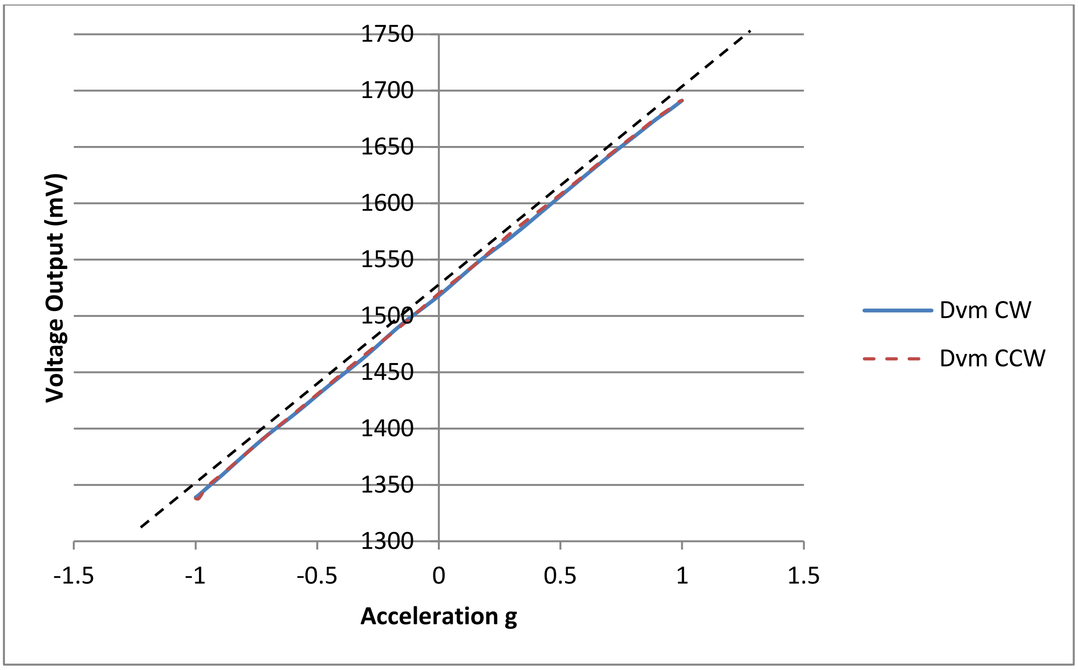

**Figure 3.36** y-axis voltage output for 0 - 180° rotation and back to zero

Repeating the experiment for a full 360° rotation first clockwise and then counter clockwise, yielded a y output sinusoidal in nature. The results of the y axis voltage output, for both CW and CCW directions, are shown in figure 3.18 below. Expectedly, a non hysteretic response can again be observed since both CW and CCW trends follow near identical paths.

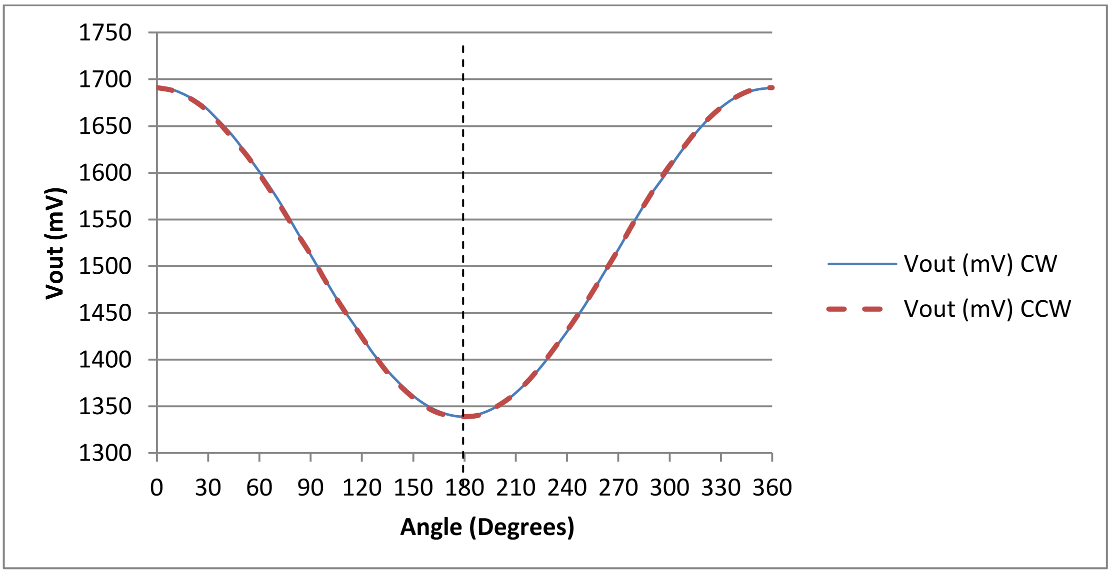

**Figure 3.37** y-axis voltage output for 0 - 3600° rotation and back to zero

### *3.1.3.2 Experimental investigation of sensor cross-axis interference*

Curiously however, there appears to be a lack of symmetry between the parts of the curve 0° to 180° and 180° to 360. This can be best seen by "folding" the curve along an imaginary vertical line at the 180° point, as shown in figure 3.19 below. The resulting sigmoid is evidently not due to hysteresis.

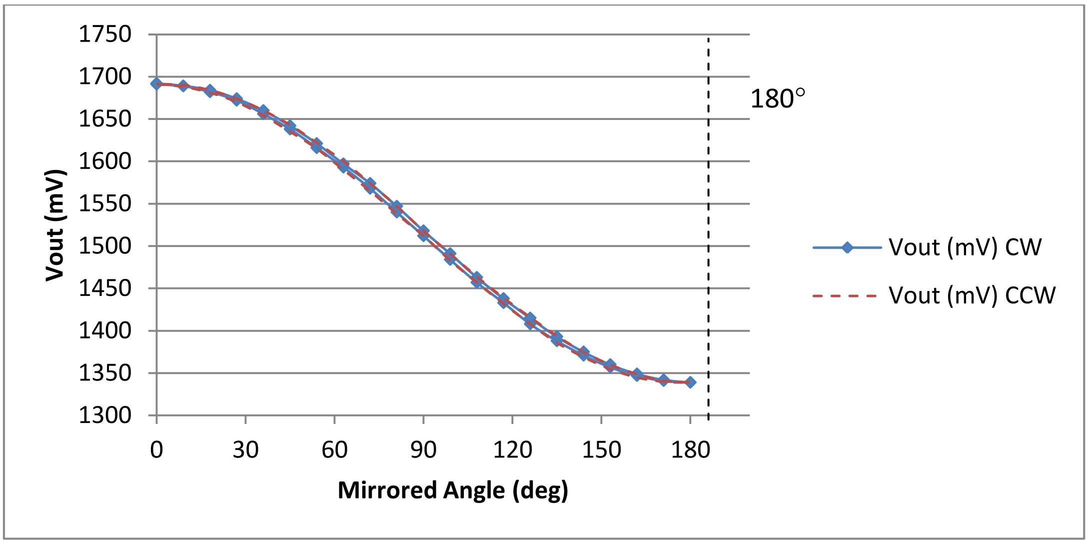

**Figure 3.38** Folded y-axis output along the 180° line

Further exemplification of this effect can be seen in figure 3.20 below where the y-axis voltage output is mapped across the acceleration due to gravity.

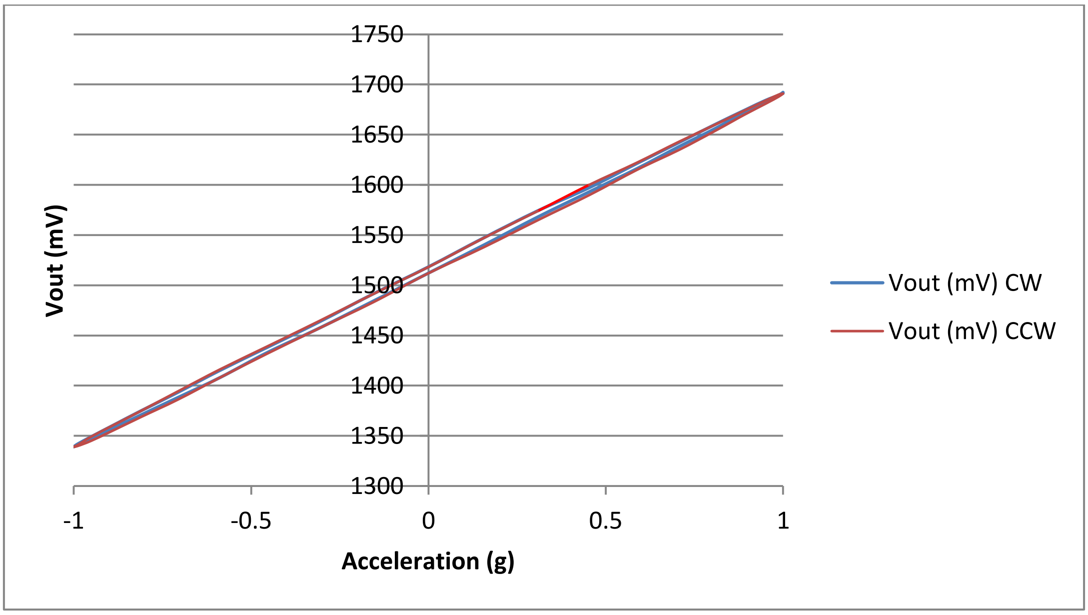

**Figure 3.39** Experimentally derived y-axis output with respect to g

The curve in figure 3.20 exhibits a consistent symmetric elliptical characteristic mostly exaggerated at y = 0 g. At these points of course, z = ±1 g depending on whether θ is 90° or 270°. Since the MEMS sensors considered in this work are fabricated using a single polysilicon micromachined structure, and the fact that manufacturer's data specifies the presence of cross-axis sensitivity even in single axis MEMS devices, the evidence strongly suggests that any cross-axis coupling would be chiefly mechanical in nature.

If the ideal y output was to be mathematically plotted over the 360° rotation and back, using the sensitivity derived from the experimental data, it would result in a straight line as shown figure 3.21 below.

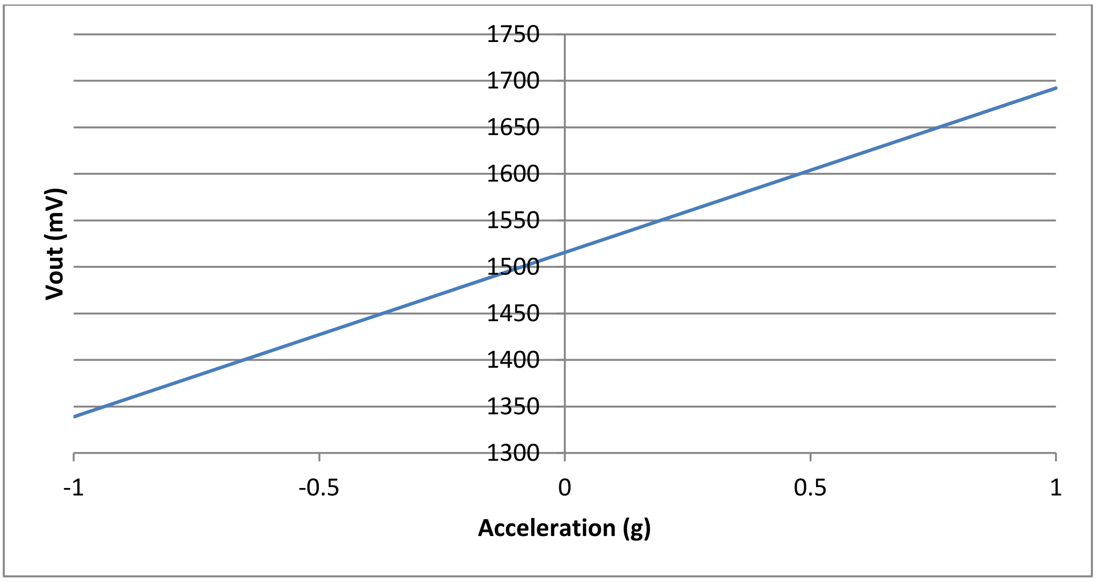

**Figure 3.40** Expected calculated output of y-axis over a 0 - 360° rotation and back

The manufacturer's datasheet states that the cross-axis sensitivity of the particular device is 1%. Calculating the 1% contribution of the z axis, which is 90° out of phase with y, over the same 360° and back rotation, and simply adding it to the ideal curve of figure 3.21, results in a curve depicted in figure 3.22. It is evident that the derived curve of figure 3.22 bears a distinct similarity to the experimentally derived curve of figure 3.20, albeit less elliptical in shape.

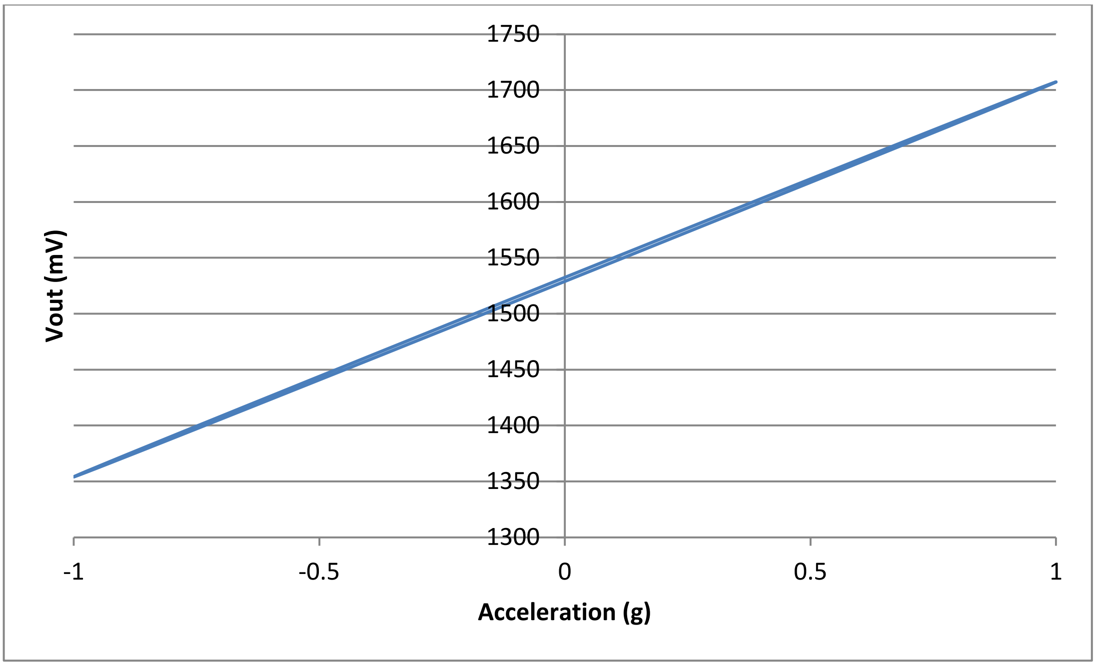

**Figure 3.41** Calculated output of y axis with the added z-axis 1% cross-axis contribution

Following the original concept however, that the cross-axis interference occurs at the seismic mass level, affecting the primary electronic interface circuitry within the MEMS IC, any output, z and y in this case, can be expressed as;

$$z_o, y_o = \cos(\theta)\,S + V_{0g} \tag{3.12}$$

Where S is sensitivity in mV/g, $V_{0g}$is the zero g bias voltage and θ is the deviation angle from the gravitational axis. The output at y with an added 1% contribution from z, can then be expressed as;

$$y_o = \cos(\theta)\,S_y + \frac{\cos(\theta + 90)\,S_y}{100} + \mathrm{V_{0g}} \tag{3.13}$$

It should be noted that only the y-axis sensitivity $S_y$ is considered, as the cross-axial coupling of z to y is considered to be purely mechanical. This mechanical coupling results in a displacement in the y axis, which in turn is added to the actual y axis displacement, and subsequently interpreted by the y axis electronics which employ the y axis sensitivity.

$$\Rightarrow y_o = \frac{[100\cos(\theta) + \cos\,(\theta + 90)]S_y}{100} + V_{0g} \tag{3.14}$$

It then follows that only the zero g bias voltage occurring at the y-axis output stage should be considered.

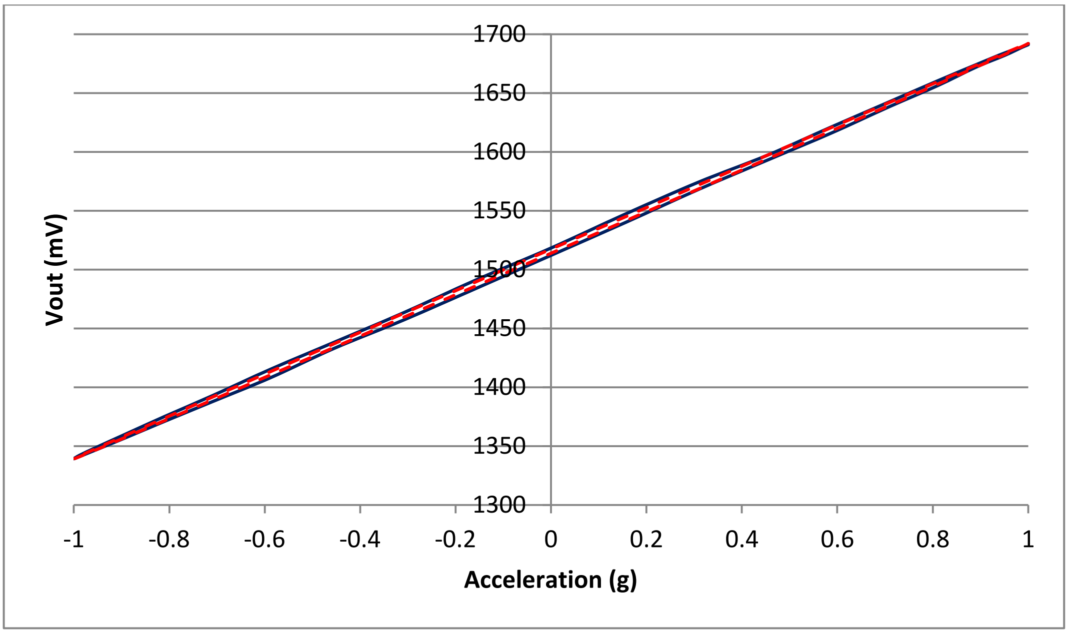

**Figure 3.42** Mathematically derived y-axis output compared with experimental results

The resulting graph of the mathematically derived y output utilising equation 3.14 is shown in figure 3.23 in dotted red, whilst for comparison, the actual experimental y output data is shown in solid blue. It can be observed that although the mathematically derived data is of appropriate shape, it yields a graph of narrower characteristic than the experimental data suggests. Increasing the cross-axis sensitivity of the theoretical model to 2% yields a graph which closely matches the experimental data, as depicted in figure 3.24 below.

It can therefore be concluded that the MEMS sensors considered for this work do not exhibit hysteretic or other classical non-linear behaviours, however they do appear to possess a cross-axial interference which manifests itself as a non-linear characteristic in a real three dimensional sensing environment. It is believed that the most likely cause for this phenomenon is small variations in the spring constants of the springs supporting the inertial mass into place as a result of the tolerances of the manufacturing process.

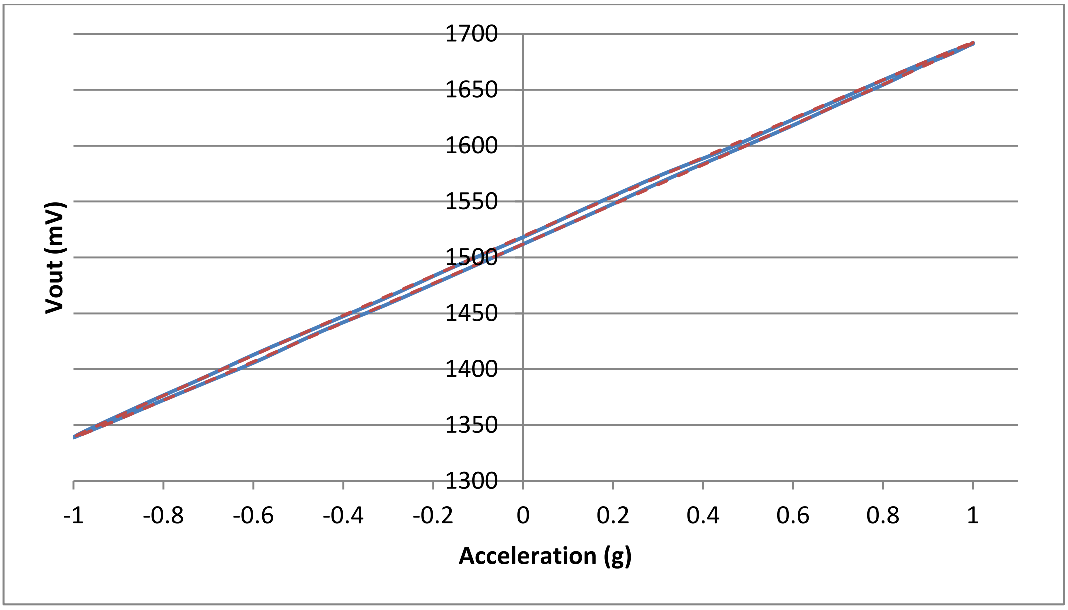

**Figure 3.43** Mathematically derived y-axis output with added 2% cross-axial sensitivity

### *3.1.3.3 Cross Axis interference theory development and experimental verification*

As depicted in figures 3.25 and 3.26 below, the MEMS springs are flat springs manufactured from polysilicon and therefore can produce both tensile and compressive forces during extension and compression respectively. Small differences in their spring constant will affect the motion of the inertial mass not only along the force axis, but also to a smaller extent laterally also.

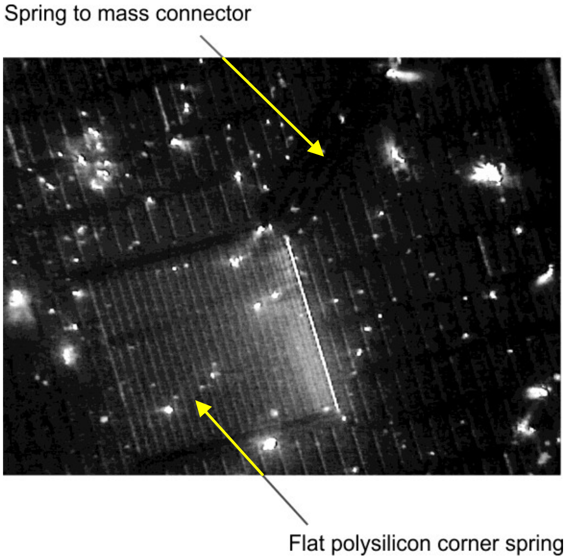

**Figure 3.44** Sliced MEMS IC under microscope showing corner spring structure

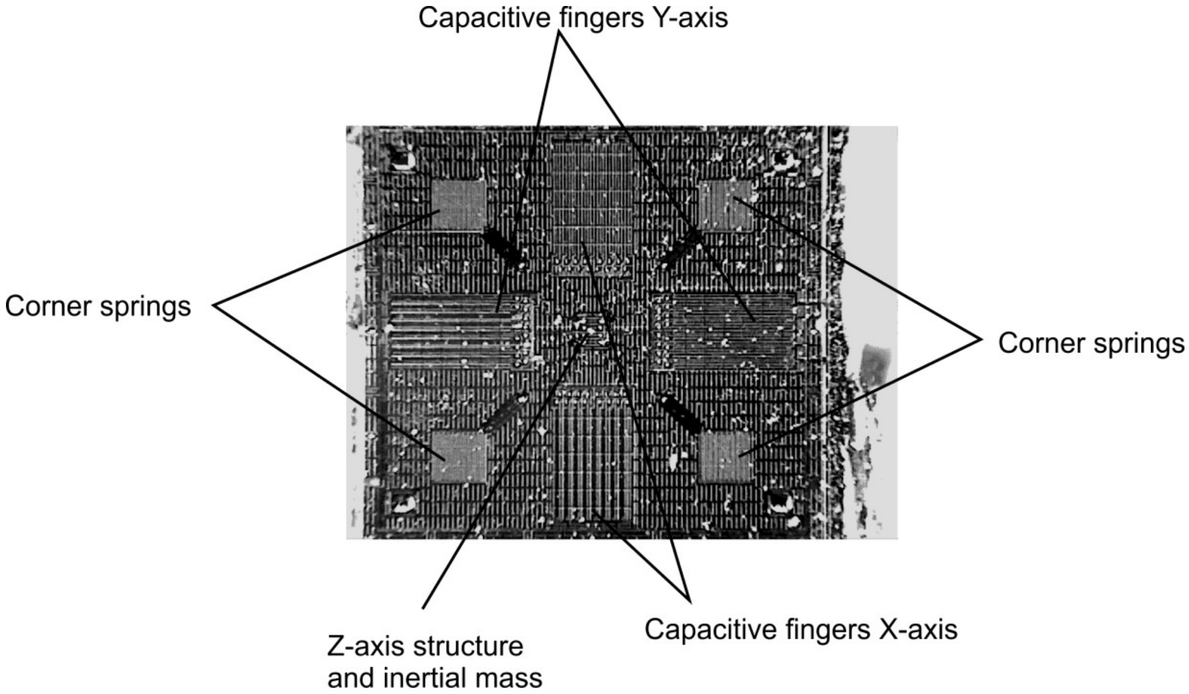

**Figure 3.45** Sliced MEMS IC under microscope showing inertial mass suspension structure

Figure 3.27 shows a typical simplified diagrammatical arrangement of a seismic mass M being suspended by four corner springs. The moving mass is able to create differential capacitor circuits with the fixed plates Cx, Cx', and Cy, Cy' in the x and y axis respectively. The orthogonal X, Y arrows indicate the direction of positive output with respect to linear displacement along that axis.

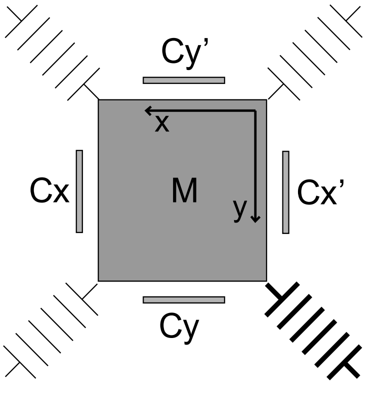

**Figure 3.46** Diagrammatic arrangement of inertial mass suspension

Assuming that due to etching a small inconsistency exists between the stiffness of the springs and therefore one of the springs, depicted with bold lines, is marginally stiffer than the other three. A force (a) applied in the direction of (y) would then not only correctly produce a movement in the (y) direction, but also a lateral displacement due to the opposition of the stiffer spring, thus resulting in a composite displacement along the vector (r) as shown in figure 3.28.

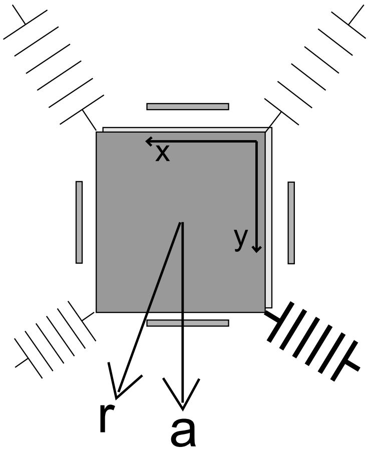

**Figure 3.47** Inertial mass displacement vector due to uneven spring compression

This lateral movement will inevitably manifest itself as a positive output on the x axis. Similarly, if the direction of the force (a) is reversed, the cross-coupling contribution due to the stiffer tension of the spring will produce an opposite lateral movement, and yield a phantom negative x axis output as shown in figure 3.29 below.

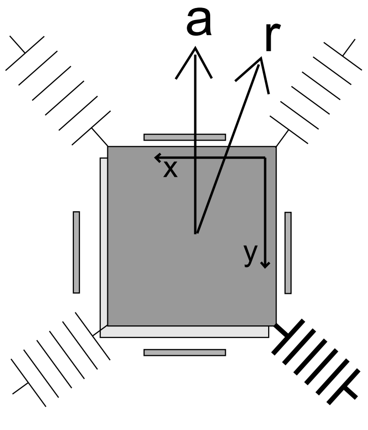

**Figure 3.48** Inertial mass displacement vector due to uneven spring tension

It is evident therefore that any random mismatch in the constants of the suspension springs will always result in a lateral movement of the seismic mass, and therefore cross-axis sensitivity will always exist in all current real non-ideal sensors, regardless of how many axis they are capable of measuring.

Since the output of any axis is proportional to the acceleration acting upon that axis and shows no hysteretic behaviour, calibrating out this effect should then be possible by simply evaluating the amount of cross-axial coupling and the sensitivity for each axis. The voltage output of the x and y axis can therefore be represented as follows:

$$x_o = S_x A_x + S_x A_y C_{yx} + V_{0gx} \tag{3.15}$$

$$y_o = S_y A_y + S_y A_x C_{xy} + V_{0gy} \tag{3.16}$$

Where $S_x , S_y$ are the sensitivities of x and y axis respectively in mV/g, and $A_x, A_y$ are the actual accelerations experienced by the sensing axis x and y respectively in g. The terms $V_{0gx}, V_{0gy}$ are the zero acceleration bias voltages on the x and y outputs, and the letter C denotes Cross-Axial Contribution constant with the first subscript letter defining the contributing axis whilst the second the affected axis. For example $C_{zy}$ is the contribution that z has on y; a value of 2% or 0.02 in the case of the graph in figure 3.24. The simultaneous equations 3.15 and 3.16 can then be simply solved in order to obtain actual acceleration values on each axis based on the voltage outputs measured. For example, the acceleration along the x-axis can be derived as follows;

$$\therefore\ A_x = \frac{S_x C_{yx}\left(y_o - V_{0gy}\right) + S_y\left(V_{0gx} - x_o\right)}{S_x S_y \left(C_{yx} C x_y - 1\right)} \tag{3.17}$$

In a real seismic wave acquisition application however, one would of course need to consider the effect on all three dimensional components. Describing each output in terms of the other two yields three interdependent equations describing the voltage outputs of each axis as follows;

$$x_o = A_x S_x + V_{0gx} + C_{yx} A_y S_x + C_{zx} A_z S_x \tag{3.18}$$

$$y_o = A_y S_y + V_{0gy} + C_{xy} A_x S_y + C_{zy} A_z S_y \tag{3.19}$$

$$z_o = A_z S_z + V_{0gz} + C_{xz} A_x S_z + C_{yz} A_y S_z \tag{3.20}$$

Since the earlier experimental arrangement isolated the x-axis in a plane perpendicular to the gravitational vector, $A_x$ can only acquire the value of zero. Furthermore, acceleration $A_z$ can be readily calculated from the known deviation angle of the z-axis to the gravitational vector and its sensitivity for every equivalent measurement of y. It then follows that that equation 3.19 expressing $y_o$ can be simplified to yield;

$$y_o = A_y S_y + V_{0gy} + C_{zy} A_z S_y \tag{3.21}$$

The corrected output $y_{oc}$ of $y_o$, with any cross-axis coupling removed, should then be the measured $y_o$ output minus the calculated cross axial interference term of the z axis $C_{zy} A_z S_y$ imposed on the y axis, as follows:

$$y_{oc} = y_o - C_{zy} A_z S_y \tag{3.22}$$

Applying equation 3.22 to every point of measurement of the earlier experimentally derived y-axis output data $y_o$ (figure 3.20), the calculated z axis acceleration $A_z$, and setting $C_{zy}$ to an accurately measured value of 1.8, yields a y axis corrected voltage output $y_{oc}$ exhibiting an excellent linear response as shown in figure 3.30 below.

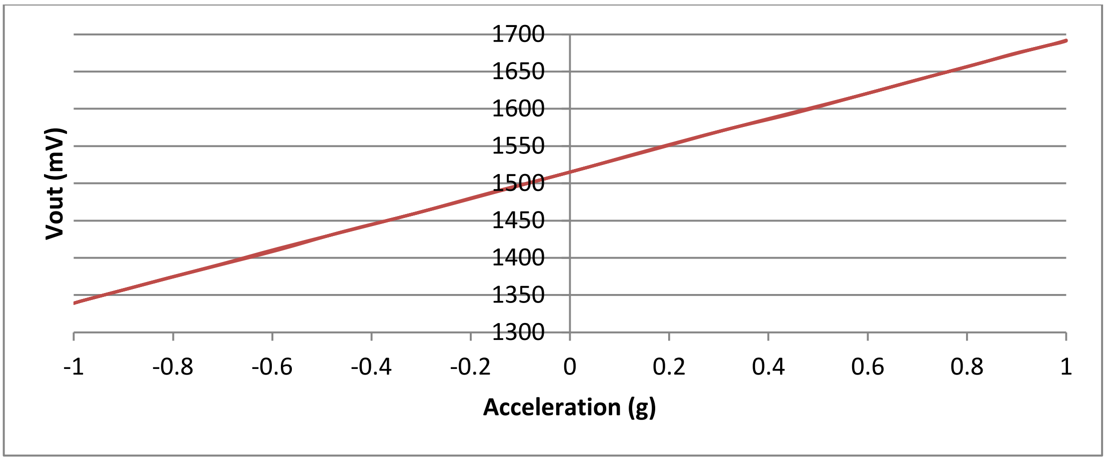

**Figure 3.49** Mathematically corrected experimental y-axis output using equation 3.22

Having derived a mathematical model representing the voltage outputs of each axis, and having proven by experiment that the model can indeed be used to reverse the cross axial interference on each output, acquiring the true acceleration experienced by the y axis in this case, could then simply be done by rearranging equation 3.21 as follows:

$$A_y = \frac{y_o - V_{0gy} - C_{zy}A_zS_y}{S_y} \tag{3.23}$$

Examination of equation 3.23 reveals that the true acceleration $A_y$ experienced by the sensor in the y direction, can easily be derived as all the terms on the right hand side can be known. $V_{0gy}$, $S_y$, and $C_{zy}$ can all be readily measured, whilst $A_z$ can be derived from the measured $Z_0$ data. It should be stressed that although the equation for $Z_0$ contains the term $A_y$ and hence the very acceleration to be derived, cross-axial interference is primarily mechanical in nature and therefore it is only the force created by the external acceleration that creates the cross axis interference phenomenon in all axis; therefore the acceleration on each axis is only a result of this external force. In other words, the acceleration experienced by each axis has as a common source the external acceleration, and therefore the acceleration experienced by each axis does not endlessly cross-couple with the other two axis thus creating more inertial mass displacements in an infinite ever increasing loop. This very fact deems the simultaneous equations solvable and valid by experiment.

Extending this idea to a three dimensional space, expressions for acceleration experienced by each of the three axes can then be derived by simply rewriting the three initial equations 3.18, 3.19 and 3.20 as follows:

$$A_x = X - C_{yx}A_y - C_{zx}A_z \tag{3.24}$$

$$A_y = Y - C_{xy}A_x - C_{zy}A_z \tag{3.25}$$

$$A_z = Z - C_{xz}A_x - C_{yz}A_y \tag{3.26}$$

where $X = \left(\frac{x_o - V_{0gx}}{S_x}\right)$, $Y = \left(\frac{y_o - V_{0gy}}{S_y}\right)$ and $Z = \left(\frac{z_o - V_{0gz}}{S_z}\right)$

It follows then that the acceleration acting on each axis $A_x$, $A_y$ and $A_z$ can be calculated by the derived linear correction formulae 3.27, 3.28 and 3.29 below.

$$A_y = \frac{X\left(C_{zy}C_{xz} - C_{xy}\right) + Y(1 - C_{zx}C_{xz}) + Z(C_{zx}C_{xy} - C_{zy})}{1 - C_{zx}C_{xz} + C_{zx}C_{yz} + C_{yx}C_{zy}C_{xz} - C_{yx}C_{xy}} \tag{3.27}$$

$$A_x = \frac{A_y\left(C_{zx}C_{yz} - C_{yx}\right) - ZC_{zx} + X}{1 - C_{zx}C_{xz}} \tag{3.28}$$

$$A_z = Z - C_{xz}A_x - C_{yz}A_y \tag{3.29}$$

### *3.1.3.4 Sensor Cross Axis interference conclusion*

Experimental investigation into the sensor's linearity has shown substantial evidence to support that the cross-axis interference is indeed the chief source of non-linearity. Unlike previous research [98], the results presented herein demonstrate no evidence of any hysteretic or otherwise classical non-linear behaviour exhibited by the sensor.

Due to the ability to directly measure the axes' sensitivities and their equivalent cross-axis sensitivities, the mathematical correction formulae derived are of significant importance when attempting to reconstruct true acceleration data trends from sensor measurements acquired in a real three dimensional environment, where cross axial coupling to strong orthogonal components is prevalent.

### *3.1.4 Temperature related errors*

In addition to having a direct effect on sensor noise as described earlier, temperature variation contributes adversely to other crucial characteristics of sensor performance [99] [100], such as the zero g bias voltage output of the sensor, when no acceleration forces are acting upon it. As shown in figure 3.32 extracted from the manufacturer's datasheet, the zero bias voltage of the x axis significantly decreases with an increase in temperature.

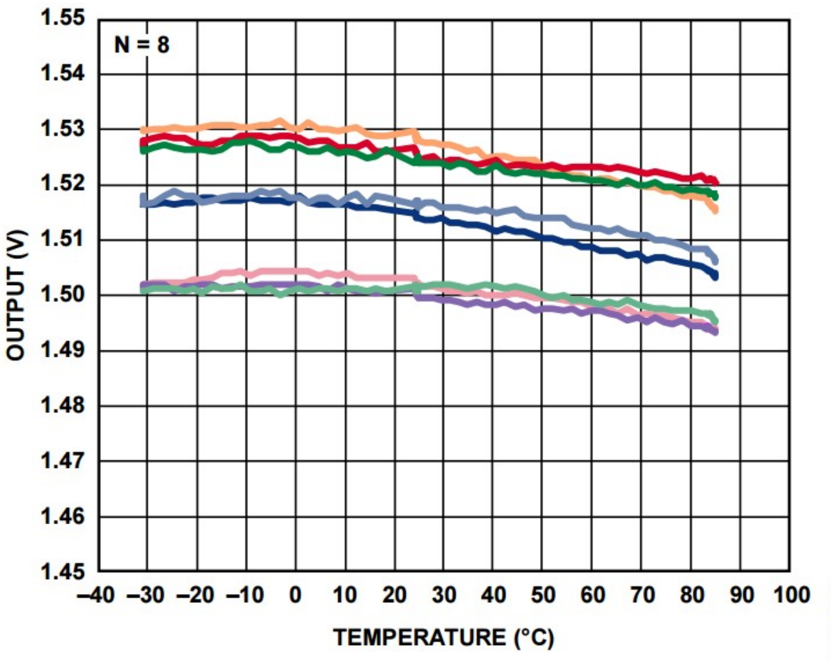

**Figure 3.50** Voltage output over temperature (source: ADXL 327 datasheet)

Typically, within the range of 0 °C to 50 °C, a 7 mV decrease of $V_{0g}$ is evident over the eight devices tested and their outputs depicted in figure 3.32 above. It should be noted that the y axis zero g bias voltage $V_{0gy}$, exhibits an inverse characteristic to that of the x axis, showing an equivalent increase in voltage with increase in temperature.

Pre-event trend averaging and AC coupling employed by some seismographs, tend to eradicate this issue, especially as temperature changes are slow to occur, however, other temperature related errors are much harder to manage, in particular sensor sensitivity changes. The manufacturer states a change in sensitivity of ±0.01 % per °C, therefore a feasible 50 °C temperature change in the operating environment of a seismic instrument, equates to a ±0.5 % change. The sensitivity of a typical sensor could therefore change as much as nearly ±1 mV/g over the modest 50 °C operating temperature range considered, potentially resulting in significantly erroneous data.

#### *3.1.4.1 Temperature related errors conclusion*

Although zero g bias drifts tend to be crudely alleviated by some seismic instrument manufactures via the utilisation of AC coupling and therefore the creation of unreliability of low frequency data, others employ a 60 second averaging of pre-event data to derive a bias reference. The latter of course also diminishes any low frequency adulations often present in seismic signals, or small immediate pre-event seismic artefacts below the trigger threshold, which inevitably get averaged to produce an erroneous zero bias reference. Any deviation from the true zero bias reference would of course result in an exponential error due to the double numerical integration necessary to derive displacement over time data.

Temperature compensation could be utilised, but the unknown and unpredictable true nature of the effect of temperature on the bias and the sensitivity of the sensor, would make this inappropriate for high accuracy measurements in the field.

### ***3.1.5 Investigation of Fabrication based errors***

Package misalignment, that is the alignment error between the IC package and the sensitive axis on the silicon die, is quoted by the manufacturer to be in the region of ±1°. Small as this might appear, this inherent to the fabrication process misalignment can produce significant errors in measurement due to the resultant dynamic coupling between the axis, which cannot be readily resolved by simple instrument calibration.

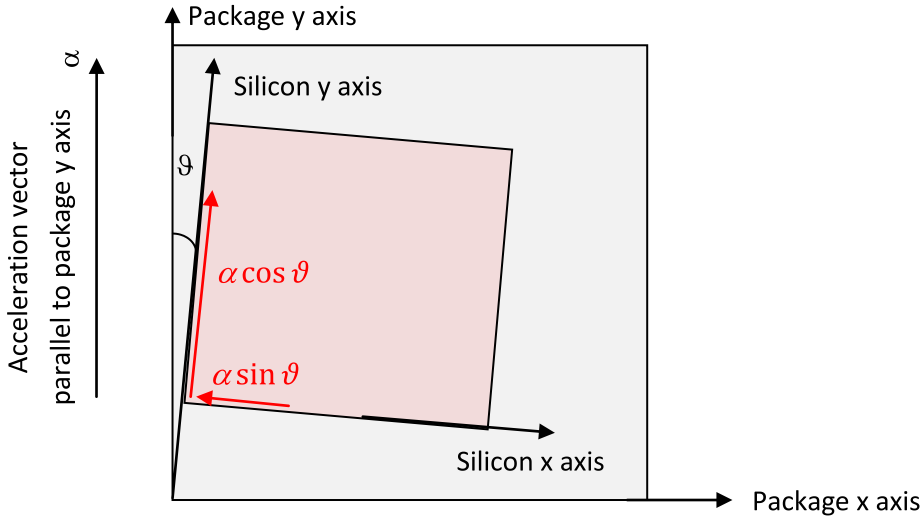

**Figure 3.51** MEMS package to silicon die misalignment

Figure 3.33 depicts such a misalignment in a single plane, with the angle of misalignment $\vartheta$ exaggerated for clarity. An acceleration vector α in parallel with the package's y axis, will result in a voltage on the y output of the sensor proportional to $\alpha\cos\vartheta$, and similarly, an x voltage output proportional to $-\alpha\sin\vartheta$. Such an inconsistency could be thought to be easily resolved by calibration, given a simple coplanar model such as this, however, extrapolation of this model to three dimensions, and consideration of the complex nature of seismic waves, exhibiting both linear and rotational motion, would indeed result in a mathematical impossibility, since linear and rotational components cannot be mathematically separated. In addition, other cross-axis effects, such as the cross axial interference reviewed earlier, would further add to the complexity of any model rendering any attempt on cross-axis coupling calibration simply not feasible.

### *3.1.5.1 Fabrication based errors conclusion*

Consideration of a complex motion containing both linear and rotational components even in two dimensions should very quickly indicate that since a rotational motion can generate parasitic linear motion artefacts, as discussed in the introduction of this work, distinction between true linear and linear artefacts caused by rotations proves impossible. The addition of multiple sensors, or even the addition of rotational sensors such as MEMS gyros, would be of limited use as a correction methodology. The rather small distance between sensors within the instrument would by comparison to the potential distance of the instrument form the centre of rotation be far too small to produce results of any practical use. Minimising this effect from the outset is therefore crucial for the acquisition of accurate seismic measurements.

## 3.2 Analytical evaluation of front end electronics

### *3.2.1 Filter phase and attenuation investigation*

As briefly discussed in the beginning of this section, the necessity of an anti-aliasing filter prior to the digitization of the sensor signal could present hidden artefacts in the digital data if not thought out carefully. Classical electronics theory dictates a minimum sampling frequency of twice the maximum frequency content of the signal of interest, however this Nyquist point, is a minimum.

As most, if not all seismic instruments, utilise a simple RC filter for anti-aliasing purposes, the rather slow roll-off of the skirt presents an issue with the low attenuation of the unwanted frequencies. More so, the use of this type of filter tends to push the -3dB cut off frequency $f_c$ to several times the bandwidth of interest in an attempt to minimise the adverse effects of phase distortion within the 100Hz bandwidth. Although a filter can be easily designed by defining a minimal distortion in the attenuation of the signal over the 100Hz bandwidth, satisfying the low phase distortion requirement is much harder.

A low-pass RC filter with a cut-off frequency of 100Hz attenuates the signal by -3dB by design, however it imparts an impressive -45° phase shift to the signal. The design of the front end filter therefore should be predominantly governed by phase and sampling rate criteria.

Figure 3.34 shows that in order for the filter to exhibit a good phase characteristic of just -0.5° in the 100Hz bandwidth, it requires a cut off frequency of 10KHz, as utilised by the exceptional seismic instrument detailed in section 2.4.

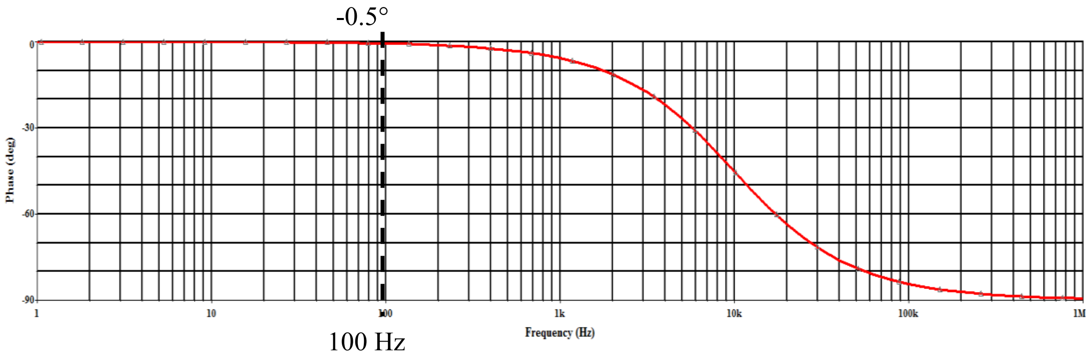

**Figure 3.52** RC filter phase over frequency characteristic

Although such a cut off frequency is perfectly reasonable, digitisation of the sensor signal using a 24 bit ADC, would require noise frequency clearance down to an LSb of -144dB.

$$20 \times log\left(\frac{1}{2^{24}-1}\right) \cong -144\ dB \tag{3.30}$$

However, the RC filter's amplitude roll-off attains a value of -140 dB at 100 GHz. This of course does not directly necessitate a sampling frequency of 200 GHz, as it would assume very high frequency noise of full scale to be present in the signal, but serves as a good indication that a considerably higher sampling frequency than the one dictated by Nyquist would be required when digitising signals from sensors such as MEMS accelerometers, which inherently exhibit a white Gaussian noise characteristic, contributing equally to all frequencies.

#### *3.2.1.1 Filter phase and attenuation conclusion*

The simplicity of an RC filter as means of band-limiting the sensor signal may indeed appeal to many instrument manufacturers, however the limitations of such filters when solely employed for bandwidth limitation prior to digitisation make them inadequate for the acquisition of high quality, high resolution seismic data.

Although many modern instruments boast 24 bit resolution and wide frequency bandwidths, the employment of RC filtering at the first stages of the front end electronics aids to only corrupt the sensor signal irreversibly, rendering any subsequent active and digital filtering ineffective for the provision of high quality undistorted seismic data.

### *3.2.2 Investigation of offsets and drifts in the front end electronics*

Voltage offsets in the amplifier stages of seismic instruments, be it for active filtering or simply for buffering the signal to the ADC, are largely dealt with by seismograph manufacturers via the utilisation of highest precision components. While this is indeed a significant step towards the acquisition of accurate and long term stable data, the limitations of even the highest precision amplifiers prove to be simply inadequate for the high resolution data required by seismic instrumentation.

Typically, precision amplifiers have an input offset voltage in the region of 25 to 500μV. Special zero drift devices with internal chopper architectures boast offset voltages down to 1μV.

Whilst this is a superbly low offset for an amplifier, consideration of the requirements of a typical seismic instrument could prove challenging.

Assuming the use of a MEMS sensor powered by a 3V stable source, without any requirement for amplification; an ADC resolution of 24 bits would dictate a Least Significant bit (LSb) of 0.18μV, a figure nearly a tenth of the best offset achievable by any amplifier. Assuming a reasonable amplification of the signal in order to provide an input of 10V maximum to the ADC, would increase the LSb of the ADC to a 0.6μV, and still below the best offset provided by specialist amplifiers. Similarly, a boost of the sensor signal to 20V, which is very much the limit of 24 bit ADCs, would imply an LSb of just over 1μV. Although the latter might initially appear as a rather appropriate solution, in order for the signal to be amplified from a 3V to a 20V useful range, an amplification of at least six times would be required. As this amplification can only be provided by an amplifier, a six-fold increase of the amplifier's offset voltage would also be present on its output, resulting in an offset of at least 6μV at the ADC, which of course is six times larger than the ADC's LSb.

Further, ageing effects of the amplifiers and the passive components utilised can produce long term drift effects in the range of several tens of micro Volts in the useful lifetime of the instrument. In addition, temperature changes would also impart drifts in the values of the analogue components, making any attempt to zero the offsets by calibration inadequate in the long term.

Any gains within the analogue front end will also be affected by drifts and changes of the passive components, a feature which would directly affect measurement precision.

#### *3.2.2.1 Investigation of offsets and drifts in the front end conclusion*

An analysis of the requirements and challenges presented by modern seismological instruments has revealed that simply relying on best components and practices in order to achieve high resolution and long term stable measurements is indeed of limited use. Even though instrument calibration could help minimise offsets in the front end, the continuous alterations that take place due to ageing and due to environmental factors such as temperature and humidity, make the suppression of these sources of error by calibration alone unattainable.

## 3.3 Evaluation of digitisation errors

Quantisation and aliasing errors although important and should be carefully considered in any digital system design, are indeed very well documented and extensively considered by instrument designers. As detailed earlier, most seismographic digitisers almost always employ a 24 bit ADC. Similarly, sampling frequencies are normally chosen to be several times the Nyquist criterion, with typically five times to be an accepted standard for good quality signal reproduction in the digital domain. A sinusoidal signal therefore, sampled seven times its own frequency, as shown in fig 3.34, would be expected to be adequately reproduced in the digital domain.

Although true according to Nyquist in terms of shape retention and absence of aliasing, a periodic pattern however is evident on the amplitudes of the peaks of the sampled sinusoid.

The graph in figure 3.34 is arranged such that the minor grid lines on the y-axis represent the quantisation level of the ADC, while the minor lines on the x-axis represent the sampling period, in this case 250 Hz. Since the signal depicted here is a real sinusoid of frequency 34.7 Hz, its period of 0.02881 is marked by vertical dashed lines in red. Red circles on some of the peaks indicate the highest sampled values, which appear to occur every fifth cycle. The amplitude difference between the highest and the lowest peaks is many orders of magnitude greater than the quantisation level, therefore this phenomenon cannot be related to ADC resolution.

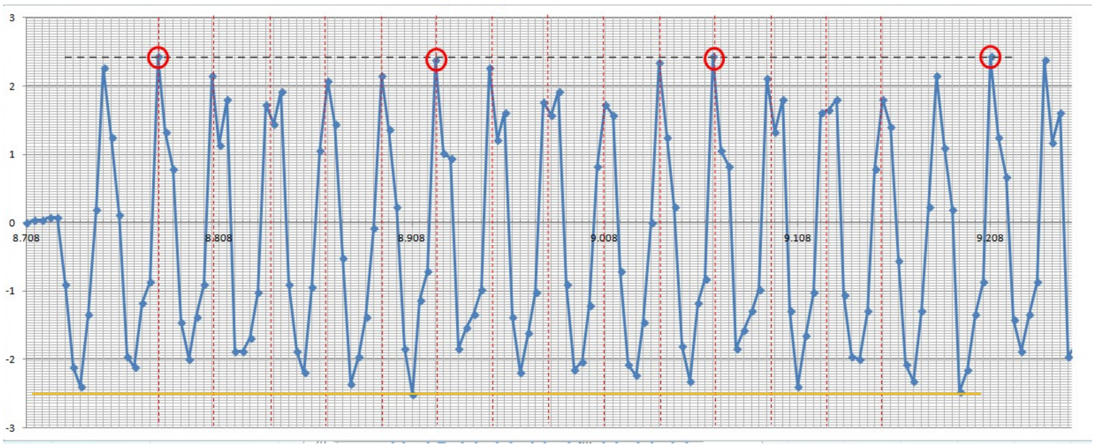

**Figure 3.53** Sampled signal exhibiting digitisation errors

Considering the relation between the signal’s period of 0.02881s and the sampling period of 0.004s; the signal period is 7.2 times greater than that of the sampling clock. Although this dictates that no aliasing should be present, it also dictates that if both the sampling clock and the signal were coincident, such that at time zero the sampled data was that of the absolute peak of the signal, the next peak of the signal would not be sampled at its maximum value as it would occur 0.2x0.004s after its nearest sample. Similarly, the following peak would occur 0.4x0.004s after its nearest sample and so forth, until near coincidence would be achieved on the 5th peak of the signal. Since both the signal and the sampling clock are periodic, the resulting phenomenon is also periodic, producing peaks in the sampled data every 5th cycle.

Although this occurrence is clearly demonstrated by the digitisation of a single frequency sinusoidal, a complex signal would almost certainly mask its existence. It is evident from the above, that a seismic accelerograph, sampled several times its maximum frequency in order to satisfy the Nyquist criterion, could still undergo sampling distortions, which depending on the start and end points of digitization, would most certainly produce exponential errors in the resulting displacement trend.

### *3.3.1 The Quality Preservation Sampling (QPS) criterion*

Considering a perfect sinusoid of the form

$$y = Asin(2\pi ft) \tag{3.31}$$

where A is the signal amplitude and f is the frequency. Utilising an ADC of N bits resolution, with voltage reference span of $V_{ref}$ volts to digitise this signal, would dictate an LSb of the ADC as follows

$$LSb = \frac{V_{ref}}{2^N - 1}\ Volts \tag{3.32}$$

The differential of the signal would of course yield a cosine with a maximum at t=0, indicating a maximum rate of change of the signal at t=0. At the point therefore that the signal's amplitude transverses the LSb level:

$$y = Asin(2\pi ft) = LSb \tag{3.33}$$

yielding a minimum *Quality Preservation Sampling* criterion time of

$$t_{QPS} = \sin^{-1}\left(\frac{LSb}{2A\pi f}\right) \tag{3.34}$$

It can then be concluded, that in order for a signal to retain its absolute fidelity, the sampling frequency must be at minimum

$$f_{QPS} = \frac{1}{t_{QPS}} \tag{3.35}$$

Application of the QPS criterion requires only an estimate of the highest frequency and amplitude of the signal, since the ADC resolution and voltage references are usually pre-defined or constrained by design and availability.

The signal of figure 3.34 which was sampled with an 8 bit ADC over a voltage reference range of 10V, would therefore require a sampling frequency in excess of 14 KHz in accordance with the QPS criterion for its characteristics to be preserved.

## 3.4 Soil dynamic effects

Up to recently, seismology was concerned with the effects of linear motion along the three orthogonal components, x or East-West, y or North-South, and z or Up and Down. Soil however is not a uniform medium nor is it constant. Its properties of elasticity for example depend on moisture, and its dynamic response to vibration depends on consistency and frequency of vibration.

Liquefaction is such one extreme dynamic characteristic of saturated soil, where under certain circumstances it behaves like a liquid during an earthquake, thus allowing any structures upon it to rapidly sink into it.

### *3.4.1 Dynamic and static tilts*

Since surface waves can be of large amplitude with wavelengths spanning to several tens of meters or more, it is only logical to accept that the very surface of the Earth not only undergoes linear displacements due to seismic wave propagation through it, but also experiences tilts between the troughs and peaks of the resonance. In high magnitude earthquakes, near field instruments can be significantly affected by these dynamic tilts to produce rather inaccurate seismic data [101] [102]. Furthermore, local after-event tilts could be permanent due to the actual displacement of soil mass in the area where the instrument is located, thus causing a permanent misalignment of the instrument.

Since surface waves tend to mainly cause rotations on the surface of the soil, very much like water waves do on water, it is assumed that the z axis of the instrument therefore would be most affected. Evidence however suggests that relatively large rotations can also be experienced on the plane parallel to the ground, as shown in figure 3.35 below.

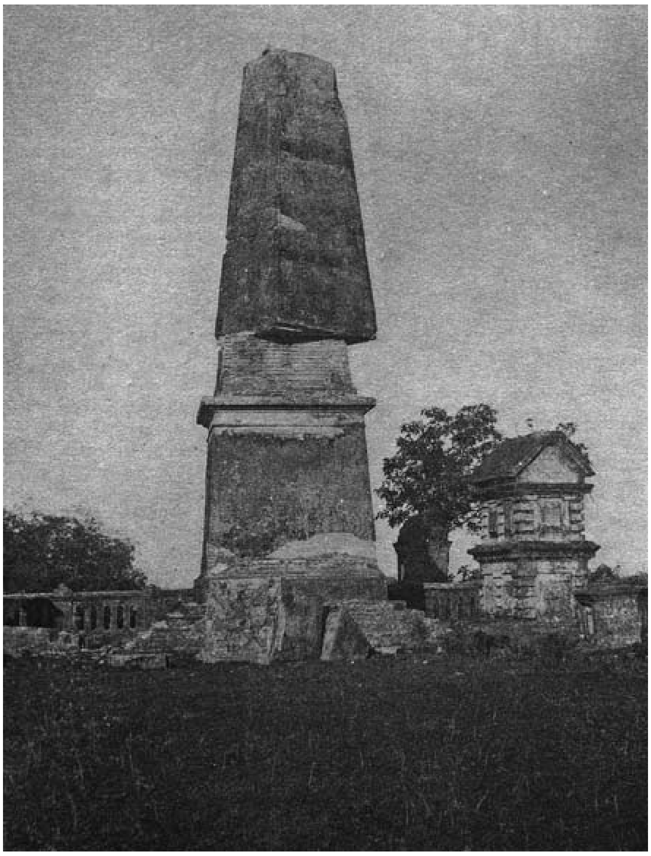

**Figure 3.54** Rotation of obelisk after the 1897 Great Shillong Earthquake (Source: Report on the Great Earthquake of 12th June 1897. Mem. Geol. Survey India, vol. 29. (from figure 1)).

Although one might correctly assume that rotations round the z axis are no different to rotations around the x or y axis coplanar to the ground; with respect to the sensor, these can indeed be perceived rather differently.

Figure 3.36 below depicts a sensor with two sensing axis x and z at rest at an angle of $\vartheta$ to the vertical z reference.

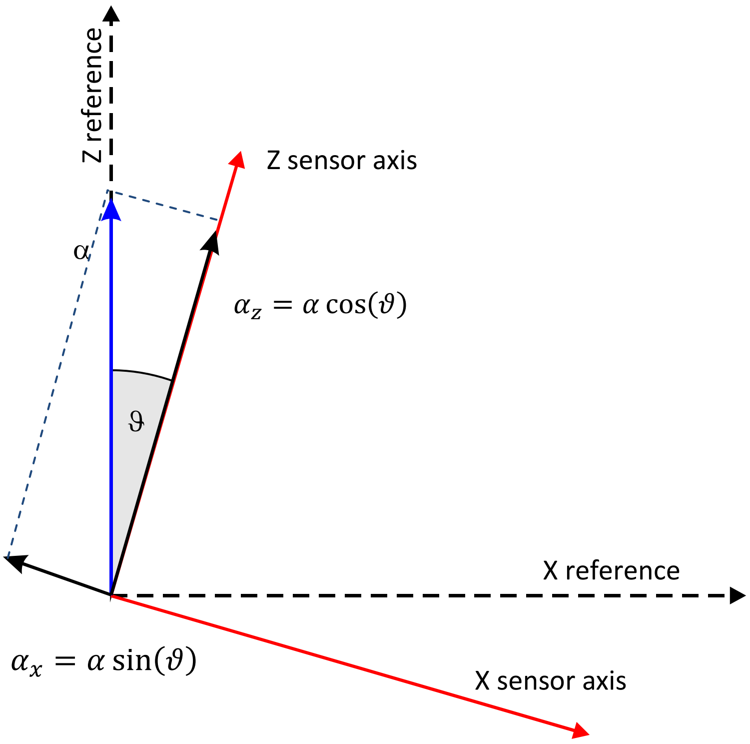

**Figure 3.55** Vertically misaligned sensor

An acceleration α applied along the vertical reference would be interpreted by the sensing axis of the sensor as two orthogonal components $\alpha_x$ and $\alpha_z$ which from basic trigonometry equate to:

$$\cos(\vartheta) = \frac{\alpha_z}{\alpha} \Rightarrow \alpha_z = \alpha\cos(\vartheta) \tag{3.36}$$

$$\sin(\vartheta) = \frac{\alpha_x}{\alpha} \Rightarrow \alpha_x = \alpha\sin(\vartheta) \tag{3.37}$$

The obvious result bears no surprises, however it dictates that tilts on the z axis are by far less corruptive to the z sensing axis signal than they are to the x or the y axis signals. In order to quickly and visually quantify this, fig 3.37 below depicts the standard sine and cosine graphs. A sensor at rest and in perfect alignment with the vertical reference would therefore be experiencing a zero degree tilt. Any tilt causing deviation from the zero axis of reference would as discussed cause an alteration to the sensing sensitivity of the axis.

It can be seen from the graphs below, that any small deviation about the zero angle of reference produces dramatically different changes to the sensitivity between the sin(x) and cos(x) dependent axes, which clearly indicates that the z axis is rather tolerant, while the x and y axes are considerably sensitive to even small tilts.

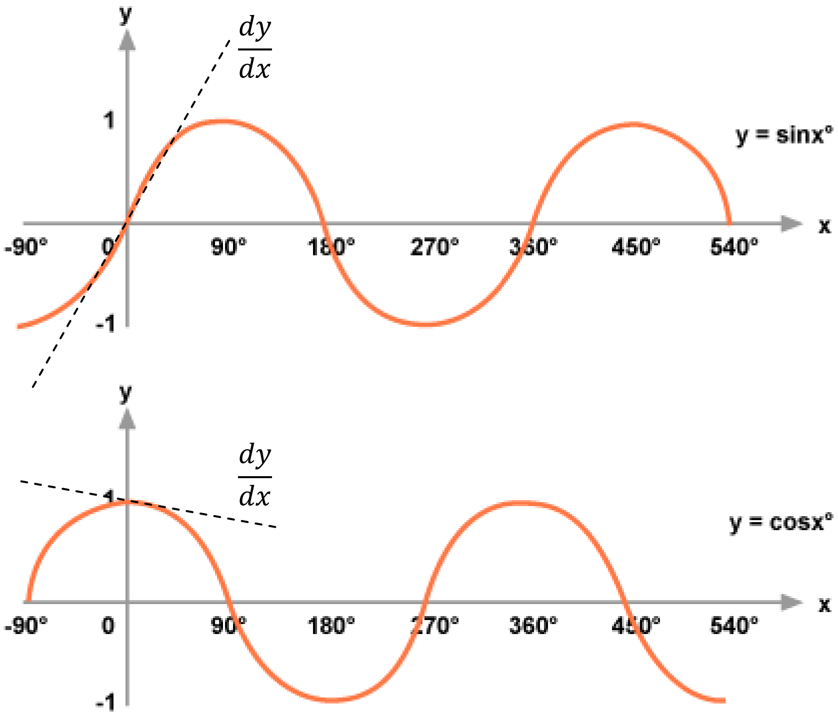

**Figure 3.56** Gradients around 0° of Sine and Cosine graphs

### *3.4.1.1 Dynamic and static tilts conclusion*

As reviewed earlier in this work, there are no means of calculating and excluding the effect of tilts in order to derive pure linear tri-axial seismic data. The complexity of motion alongside the restrictions of the instruments does not allow for the resolution between linear and rotational components.

Another factor to be considered is the asymmetrical behaviour of the ground. Since soil is a non-uniform mixture, seismic waves travelling across underground rock formations or sand deposits will behave differently to when travelling across a more uniform clay substrate [103] [104]. Sensors therefore positioned near underground boundaries could in theory experience an asymmetric oscillation dependant on the direction of the waves with respect to the position of the sensor and the boundary.

Considering for simplicity a vertical oscillation of a sensor near an underground boundary, as shown in figure 3.38 below:

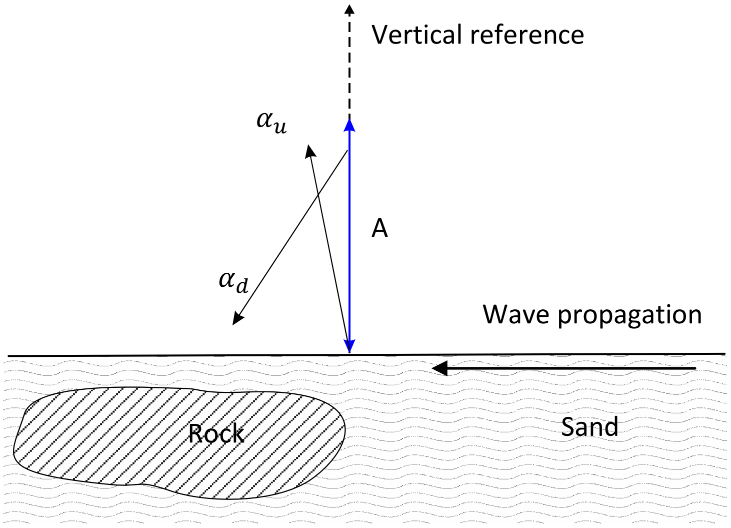

**Figure 3.57** Sensor near underground boundary

With a seismic wave propagating from sandy to rocky soil, a change in the shape of the wave would be expected amongst other artefacts such as reflections etc. Very much like a water wave reaching the shallows, an increase in amplitude over the rocky subsoil would create a non uniform vertical motion for the sensor. On the arrival of the wave-front, the sensor would be accelerated upwards and tilted by the smaller in amplitude surface wave describing a motion represented by vector $\alpha_u$. Once the wave-front is over the rocky substrate, its increase in amplitude would create a sharper wave edge on the downward motion thus creating a larger tilt during the negative acceleration part of the sensors motion, as represented by vector $\alpha_d$.

The above phenomenon would inevitably introduce a non-linearity in the form of mechanical hysteresis as it would consistently generate larger upward than downward acceleration readings, leading to sizeable offsets in the velocity and displacement trends post numerical integration.

In conclusion, tilts can and do play an important role in seismic error generation in more ways than originally anticipated. Their measurement and consequent corruption of seismic data has been known for over a decade, however, no methods exist to date enabling their isolation or their useful integration into the seismic data.

## 3.5 Conclusion

The identified possible sources of error were both mathematically and experimentally examined in this chapter. With the utilisation of the primary MEMS circuit and the precision sinusoidal vibration platform, it was confirmed that the direct use of a MEMS acceleration sensor for the measurement of seismic data, with or without primary filtering, inevitably results in erroneous displacement data after the necessary double numerical integration.

A detailed examination of the sensor itself identified numerous sources of error able to corrupt the seismic signal before it even exits the MEMS IC.

Sensor noise is by far one of the most obvious causes of error and sensor resolution limitations. It exhibits a Brownian noise characteristic spanning the entire spectrum and contains some artefacts from the internal clock albeit significantly attenuated and at frequencies beyond the bandwidth of interest. Sensor noise dependency to temperature, although widely documented and mathematically evaluated herein, did not reveal the true magnitude of this dependency until experimental investigation revealed a sharp exponential increase of sensor noise relating to increase in temperature.

An attempt to attenuate the sensor noise by utilising common mode rejection in the form of bi-axial differential excitation proved that although some noise should be common due to the shared wafer between the channel electronics, the non-common mode micromechanical noise by far exceeds any common mode noise content that might be present.

The test pin, present on most MEMS accelerometer sensors for the binary confirmation of their operation, was successfully utilised to gain vital sensor dynamic response information, enabling the in-situ and on-demand acquisition of the frequency, impulse, step, and even phase response of not only the sensor, but the wider instrument. Such information of course can be used to reverse the effects of the instrument’s electromechanical dynamic characteristics on the measured signal by means of de-convolution in the frequency domain.

Further use of the test pin also showed the ability to dither the output signal with some loss of dynamic range, should it be necessary to monitor very low frequency and amplitude adulations which may cause errors in the zero g bias voltage evaluation.

Experimental investigation on the sensor's linearity did not show any signs of hysteretic behaviour, however, it revealed a non-linear effect stemming from cross-axis sensitivity due to mechanical coupling between the channels. The extensive mathematical evaluation and the subsequent derivation of formulae for the correction of this phenomenon were experimentally proven in their ability to derive true and uncorrupted by this effect acceleration data from each channel.

Further, sensor limitations were investigated, such as the effects of temperature fluctuations on sensitivity and zero g bias voltage. It was shown that the zero g bias was quite susceptible to variations in temperature in a non-linear fashion and in different polarities between channels, making its removal by calibration rather inefficient. The sensitivity change due to a variation in temperature could be one of the several key sources of hidden error as it directly impacts the precision of the acceleration measurements.

Finally, sensor die to package misalignment was examined to reveal that correct sensor to instrument alignment from the outset is vital to acquiring uncorrupted data.

The front-end electronics also contribute to potential errors in the form of amplifier offset errors, component ageing, and thermal drifts. An examination of these sources of error revealed that current common practice and the utilisation of best available components is simply not adequate for the attainment of error-free seismic data.

Environmental factors other than temperature and humidity also influence the accuracy of data, and the much discussed issue of dynamic and static ground tilts during a seismic event was investigated to show that not only it affects the direct accuracy of the readings, but it also affects different channels in different ways, depending on their orientation. It was further shown that non-uniformity in soil composition could produce a hysteretic behaviour due to the alteration of the shape of the surface waves across underground boundaries. Such non-linear effects of course contribute to asymmetrical data, which in turn results in exponential displacement trend errors due to the cumulative effect of the integration process.

In conclusion, manufacturers have been attempting to produce 24-bit resolution, high accuracy seismic instruments, by solely depending on the quality of the components used and the refinement of data by subsequent linear FIR filtering, whist completely ignoring the very prominent sources of error stemming from within the sensor itself.

Although few seismic instrument manufacturers have employed more effective front-end electronic solutions, such as active filtering and even multi channel averaging, the latter only aid to “smooth over” the fundamental sources of error, which left uncorrected from the source, cannot be corrected by any means further down the dada acquisition line. This study clearly identifies the rather prominent shortcomings of current seismic instruments and proposes methods for the improvement of acquisition of seismic data.

To this effect, this study serves as a guideline of specifications demanded of a novel benchmark seismic instrument, with the ability to acquire precise and repeatable data in a real environment, and over very long operating periods.

# Chapter 4

## Realisation of the HPAGS sensor

In the previous section of this work, an in-depth investigation of the challenges encountered by the accurate measurement of ground acceleration data and its subsequent processing to precision ground displacement over time, highlighted several sources of error currently not tackled by current seismic sensor technology. It was shown that these range from internal to the MEMS package drifts, misalignments and non-linearity, to the challenges of the front-end electronics in terms of noise reduction, filtering, signal preservation, and long term stability.

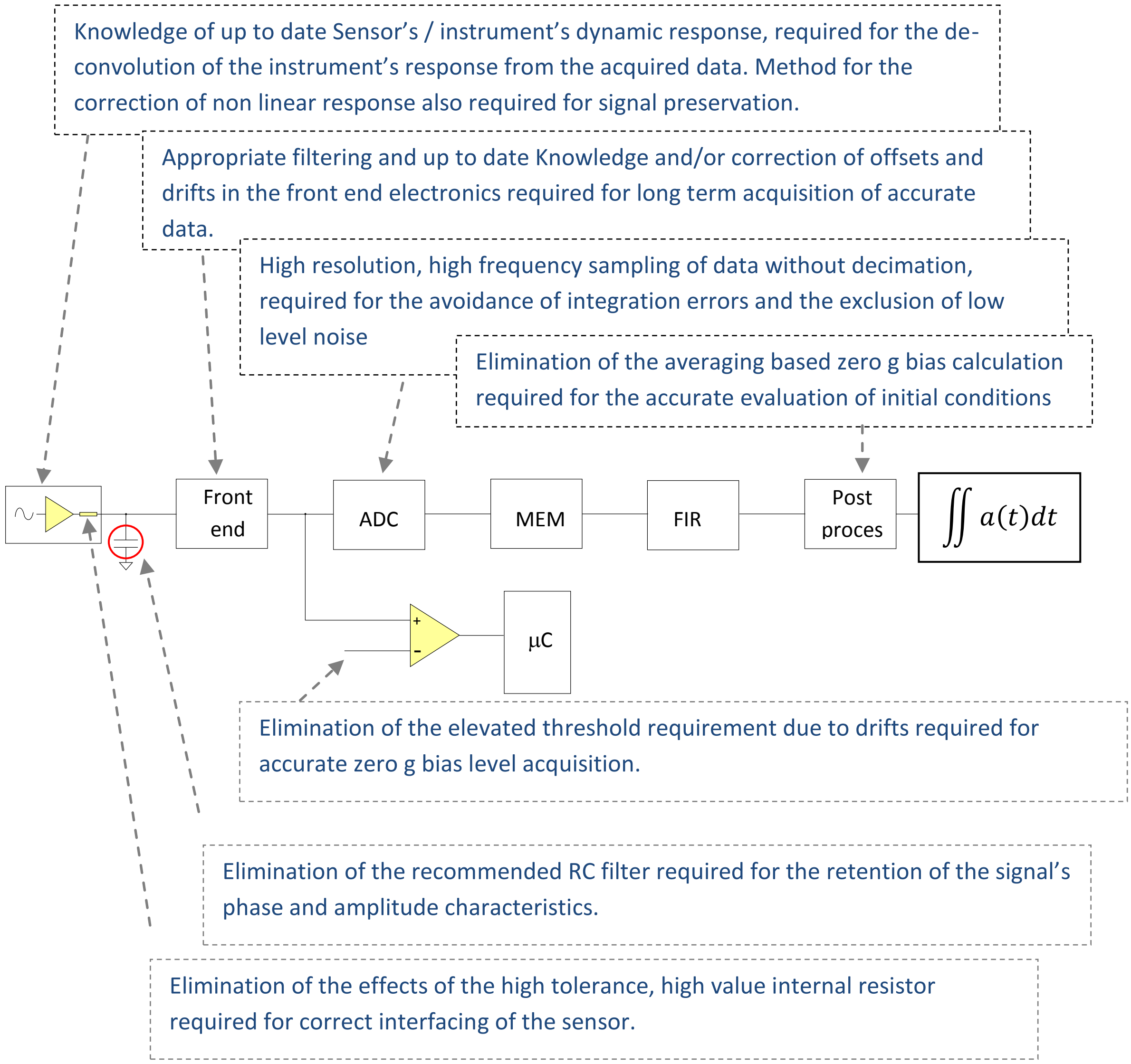
Knowledge of up to date Sensor's / instrument's dynamic response, required for the de-convolution of the instrument's response from the acquired data. Method for the correction of non linear response also required for signal preservation.

Appropriate filtering and up to date Knowledge and/or correction of offsets and drifts in the front end electronics required for long term acquisition of accurate data.

High resolution, high frequency sampling of data without decimation, required for the avoidance of integration errors and the exclusion of low level noise

Elimination of the averaging based zero g bias calculation required for the accurate evaluation of initial conditions

Elimination of the elevated threshold requirement due to drifts required for accurate zero g bias level acquisition.

Elimination of the recommended RC filter required for the retention of the signal's phase and amplitude characteristics.

Elimination of the effects of the high tolerance, high value internal resistor required for correct interfacing of the sensor.

**Figure 4** Specification diagram of HPAGS sensor base on error analysis

A careful re-evaluation of these errors served as an accurate specification model for a high precision instrument, for which a system level diagram is shown in figure 4.

In addition to the error sources depicted in the requirements system diagram above, environmental factors such as temperature and soil dynamics had to also be considered in the design of a high precision instrument.

## 4.1 Electronic Systems

The HPAGS sensor is intended to be a smart and active seismic sensor unit able to interface with a variety of digitisers for the acquisition of undistorted seismic data. To this effect, the device considered herein, does not encompass circuits and methods for the digitisation of the signal, however, as seen earlier, novel correction algorithms and linear FIR filtering of the data is provided for the correction, derivation, and evaluation of accurate displacement trends.

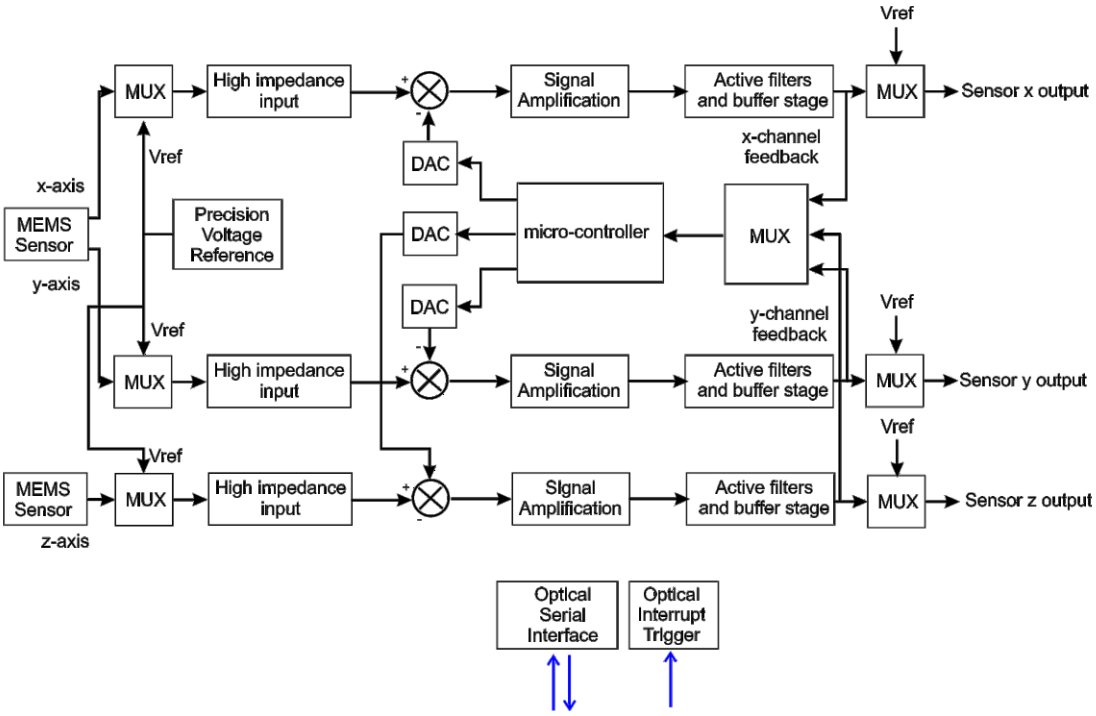

**Figure 4.1** HPAGS system level diagram

A top level system diagram of the HPAGS sensor electronics is presented in figure 4.1, believed to present a set of realisable novel solutions to the challenging problems identified in this work.

All control signals between the micro-controller and appropriate peripheral devices such multiplexers, DACs, sensor electrostatic excitation, and interfacing electronics, have been omitted for clarity.

With the sources of error identified throughout this work in mind, this novel sensor topology aimed to systematically address them all in the hope of acquiring superior quality seismic data.

HPAGS sensor electronics comprised two MEMS accelerometers, one for the x and y sensing axes, and a separate one for the z-axis. Although the ADXL327 is a tri-axial device, the manufacturing constraints and consequently the inferior performance of the z-axis of the MEMS sensor, made the use of an additional sensor essential. Vertical mounting of the additional MEMS allowed for its x or y sensing axis to be used for z-axis acceleration measurement.

The front end electronics were arranged as to eliminate the use of an external capacitor in conjunction with the internal to the MEMS resistor, by providing a very high impedance interface. This served to neutralise the effects of a high impedance source and also allowed the instrument to be unaffected by any changes in the high tolerance source resistor. Instead, a two-stage bespoke Bessel-Thompson active filter circuit aided to attenuate high frequency noise whilst accurately retained the signal's amplitude and phase characteristics.

As the front end electronics were inevitably going to be subject to component changes due to ageing and environmental variation, closed loop correction and evaluation systems were devised in order to ascertain the instrument's accuracy over its lifetime.

For any electronic circuit comprising active components which introduce gain, the knowledge of the precise value of gain and offset at the time of the acquisition of data is essential. Simply measuring the output of a channel as means of deriving offset might appear a sensible approach, and indeed most manufacturers do just that, however the output of each channel is a product of both gains and offsets, and the two cannot be considered as a unified offset error. While true offsets arising from the active components of the instrument could simply be negated post-data acquisition, changes in gain in the front-end electronics directly affect the sensitivity of the instrument, and can lead to serious misinterpretation of data. For example, the ADXL with a typical sensitivity of 420mV/g coupled to a circuit with a gain of 3.3 would yield an instrument sensitivity of 1.386V/g. With the most accurate available resistors of 0.01% tolerance used for the design, a gain error of 139μV/g would still be possible from the outset, and subject to unpredictable variations over time.

In order to put this into perspective, the digitisation of the HPAGS sensor output, digitised by a 24 bit Sigma-Delta convertor over a 10V output range, would have an LSb and therefore a resolution of nearly 60μV, which is already half of the gain error. Multiple gain stages within the instrument would of course add to this error and multiply it yielding an error in the evaluation of the seismic signal.

The electronics of the HPAGS sensor incorporated an accurate voltage reference, which with the aid of a multiplexer (MUX), this reference voltage could be switched through the front end electronics instead of the MEMS output, thus allowing for its measurement and therefore the determination of the overall gain of the front-end electronics. A problem however can arise when one considers that even the precision reference itself has a voltage variation and tolerance greater than the required resolution of the instrument. This issue was successfully resolved by a further MUX on the output of the instrument, by which the voltage from the reference could be directly connected to the output of the instrument and therefore a direct comparison could be made between the actual voltage from the reference and the voltage resulting from the reference being fed through the front end electronics.

In most standard instruments, the offset arising from the MEMS accelerometer and further exaggerated by the front end electronics, is dealt with in the digital domain. As reviewed in earlier sections, an average of pre-event data is collected and averaged for the derivation of a bias reference. This reference is then subtracted from the signal. This approach provides for the allowance of errors, both from any pre-event artefacts and from possible quantisation errors prior to a double integration able to exponentially exaggerate even the smallest of offsets. Further, allowing the true voltage bias in the analogue front-end to be offset in either positive or negative direction, significantly reduces the dynamic range of the instrument as saturation could be reached in either direction by a strong motion event. To this effect, the HPAGS sensor design incorporated a closed loop high gain system and offset circuitry allowing for the precise setting of the bias voltage to zero in each of the three channels. This allowed for maximum dynamic gain and a trigger threshold able to be set at very low levels, without the fear of false triggering due to drifts. This method had the additional major advantage of allowing for true zero bias, not requiring the use of pre-event data or its averaging, thus eliminating any potential errors associated with pre-event artefacts and erroneous initial conditions of integration, known to majorly contribute to the exponential errors so frequently encountered in seismic data trends.

It was envisaged that the complete HPAGS sensor would in future be fabricated on silicon and encapsulated alongside the MEMS to provide an integrated solution on chip. As such, the electromechanical design could be significantly scaled down via the use of micro-bearings and micro-actuators, resulting in a unified novel electromechanical seismic sensor, complete with thermoelectric cooling for the significant reduction of noise and the avoidance all errors associated with temperature of drifts.

On the system level, the HPAGS sensor was designed to provide three precision output channels of analogue acceleration data, while rejecting and eliminating environmental and internal sources of error via active electronic and electromechanical circuits. Due to the smart and active nature of the sensor, a requirement for communication with the data acquisition system and wider seismographic instrument existed, which was fulfilled by means of Infrared (IR) and visible optical transceivers. A full IR RS232 serial link was included for the direct communication to the embedded micro-controller, and a binary visible range sensor, for the signalling of a seismic event. The optical nature of the transmission of data was dictated by the restrictions posed by the mechanical structure requiring six degrees of freedom without the obstruction of cables.

The circuit of the HPAGS sensor, with only one channel shown for clarity, is depicted in figure 4.2 below. The other two channels are identical in design.

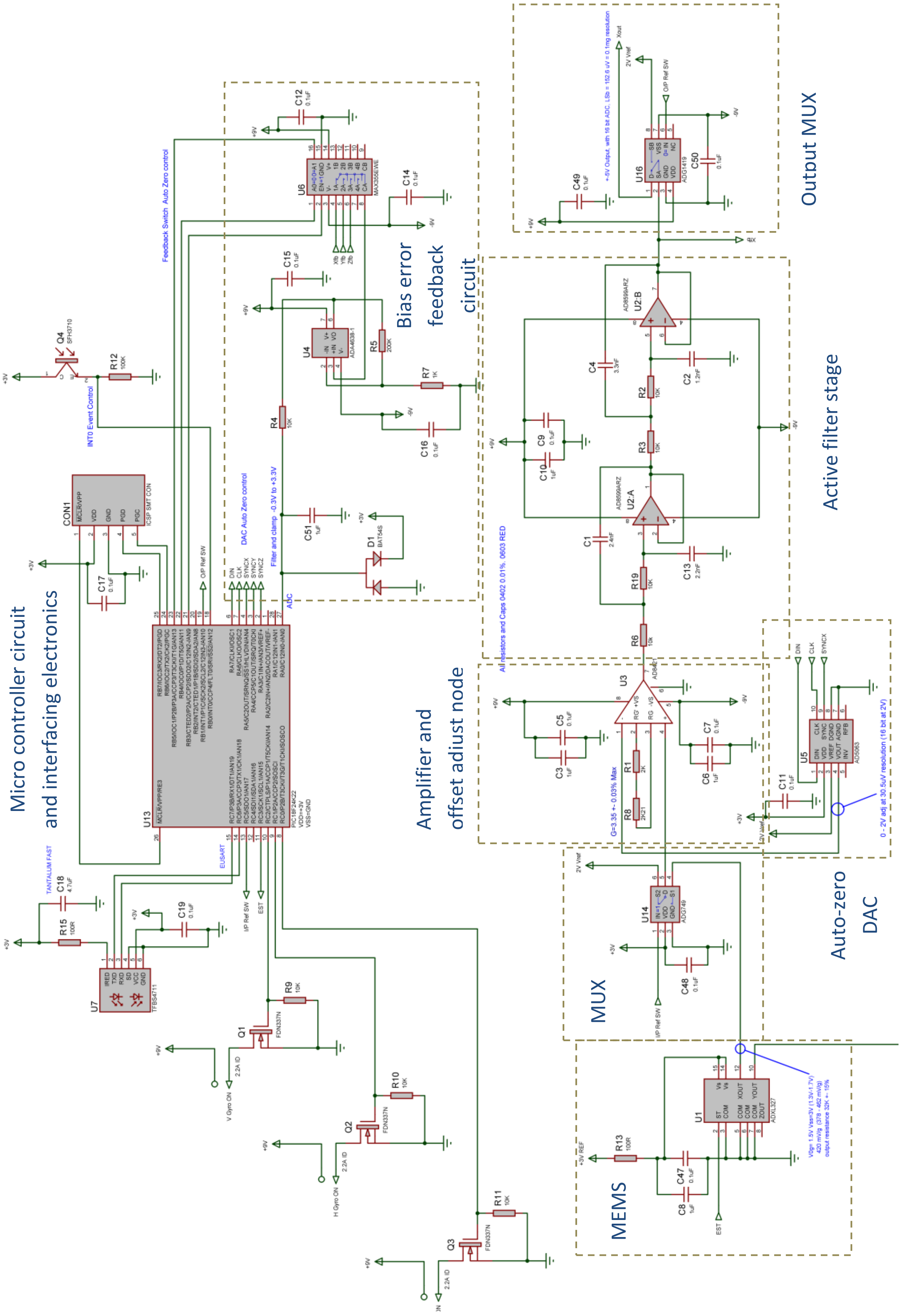

**Figure 4.2** HPAGS circuit with only one out of the three channels depicted

The signal channel electronics of figure 4.2 were divided in functional sections enclosed in dashed rectangles to aid their functionality description. The remaining not enclosed circuit, comprises the micro-controller with the interfacing electronics to the channels, the electromechanical components, and the optical communication ports.

Following the circuit in a logical order from sensor to the sensor's output, the MEMS section of the circuit is depicted in more detail in figure 4.3. It is worth noting that the Self Test pin 2 of the accelerometer was made available for connection to the micro-controller for dynamic response evaluation of the system.

In addition to the power decoupling capacitors C8 and C47, an in series with the supply resistor R13 was included in order to filter out any spurious noise that might be present near in frequency to the 5 KHz clock, or any of its harmonics. Since the output of the MEMS accelerometer is ratiometric with respect to its supply, any noise or variation to the power supply could cause errors to the acceleration measured.

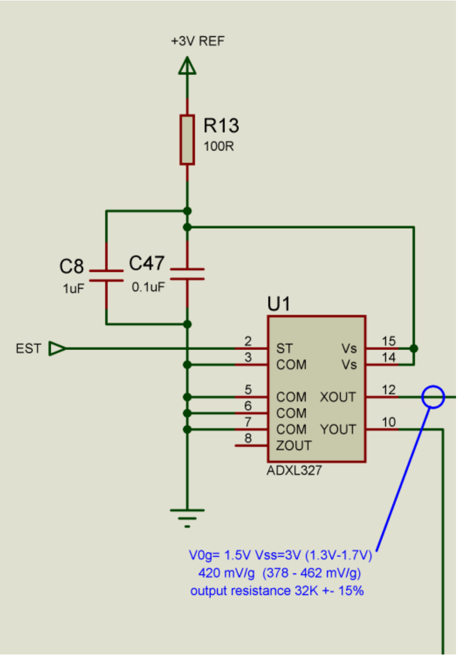

**Figure 4.3** Detail of MEMS circuit

The low pass RC filter created simply aided the attenuation of any frequencies above 1.45 KHz present in the power source.

The MEMS device, as other critical components of the circuit, was powered by a very stable 3V reference source, generated by a high precision reference U8 as shown in figure 4.4 below. It should be noted that a 2V precision reference U9 was also used to provide accurate voltage references to the ADCs and to the output channels. Both voltage references allowed for an initial ±3mV accuracy, very low drift, and exceptional noise characteristics. Unlike the low power requirement of the 2V reference, the 3V reference served as a precision reference and as a power supply, and was therefore buffered by a unity gain stable power amplifier U25 of matching characteristics in precision.

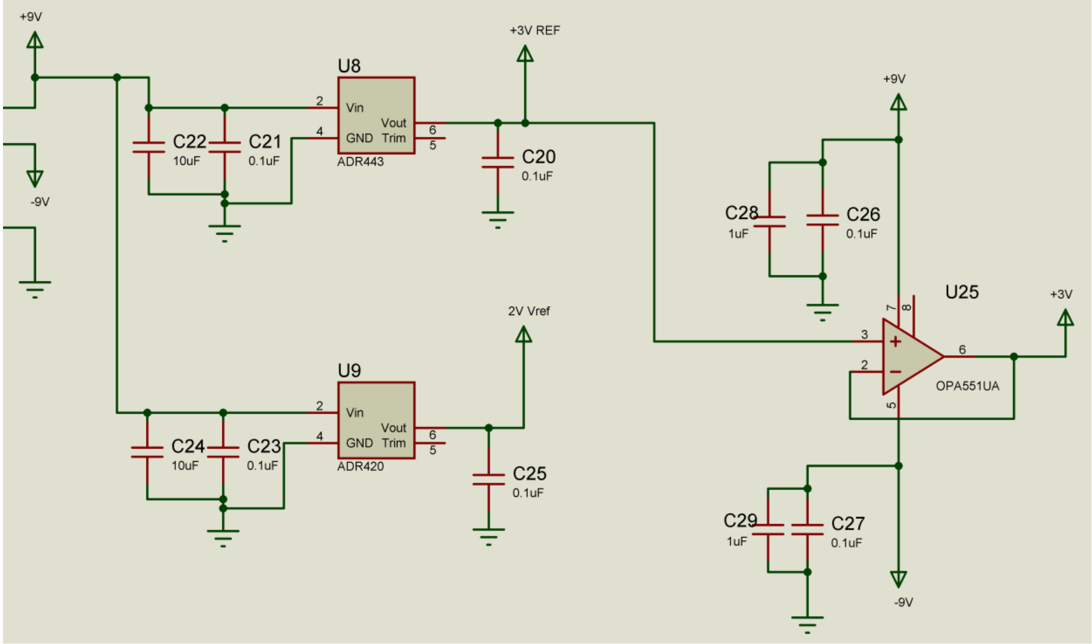

**Figure 4.4** HPAGS sensor power supply and precision reference circuit detail

Although the reference's initial error and the amplifier's could combine to give rise to a larger offset, the 3V supply only powered devices not sensitive to variations in supply voltage, whilst the sensitive MEMS sensors were powered directly from the reference source. The 3V reference voltage was made available for precise measurement to the wider instrument, as it could in theory drift enough to effect the validity of acceleration measurements.

The MEMS sensor's manufacturer provides three data points as to hint to the device's sensitivity dependency on supply voltage, which are reproduced in a graphical format in figure 4.5 below, verifying a true linear dependency. The derivative of this curve provides a value of sensitivity change due to supply voltage change of 131mV/g/V. This rather large alteration in sensitivity indicates how great data errors from current seismological instruments can be, as they do not employ any form of analogue level correction methods.

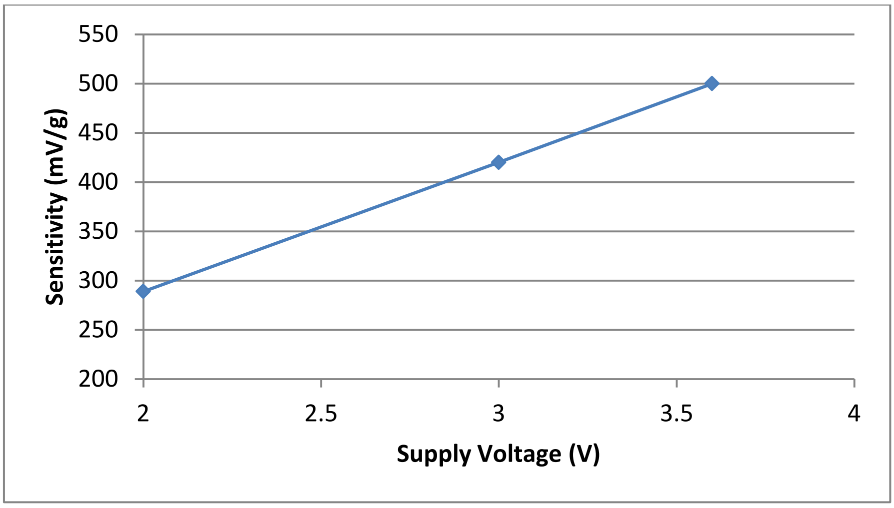

**Figure 4.5** MEMS sensitivity drift due to supply voltage change

Although the ADC reference within the micro-controller was also supplied via the 3V rail, a small change in the absolute precision of the measured analogue value due to any voltage alteration would not be of significance due to the exceptionally high amplification of the signal prior to its input to the ADC.

The 2V reference rail could also undergo small variations in its value, and although it was used to supply the voltage references of the DACs, this variation was of no consequence since an absolute value was not required due to the closed loop nature of the zero-g bias voltage correction system, discussed in detail later in this section.

Following the signal path through the channel, the output of the accelerometer was fed to a MUX simply serving the purpose of switching either the signal or the 2V reference to the input of the channel. The amplification and offset node was accomplished by the use of an instrumentation amplifier configured for a gain of 3.35. It should be noted that any offsets in any of the amplifier stages through the channels were simply zeroed by the zero-g bias offset closed correction loop and therefore of no importance. The gain of the amplifier stage was set by high precision 0.01% resistors R8 and R7, in order to reduce gain variation in the channel. However, since even such small variations could impact the precision of the overall instrument, a gain evaluation circuit discussed later in this section, was employed to ascertain the absolute accuracy of the sensor.

The ±9V supply throughout the circuit was derived from a battery source ensuring very low noise. Any variation in the battery voltage would not cause any adverse effects to the instrument as long as it remained within the normal operating limits of the electronics.

The design of the active filter section detailed in figure 4.6, was also of crucial importance since it could impart unrecoverable errors on the accelerometer's signal, both in amplitude and phase.

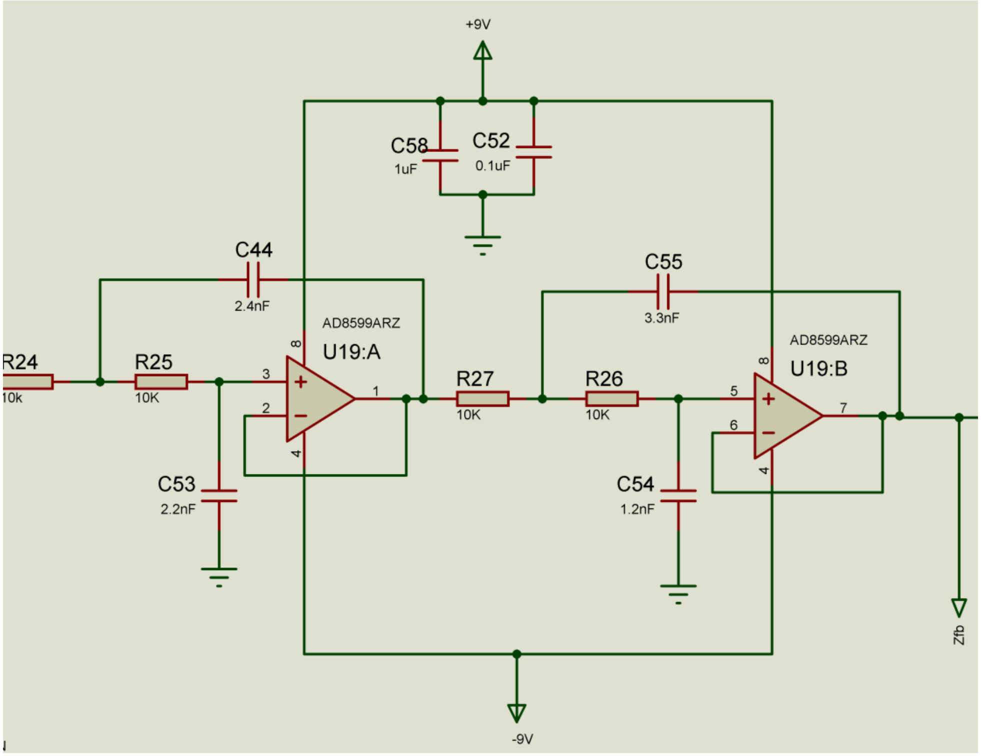

**Figure 4.6** Active filter circuit detail

The two-stage active filter constructed using ultra low noise and ultra low distortion dual amplifier AD8599ARZ, labelled in circuit as U19:A and U19:B in the channel in question, ensured the highest signal fidelity. The hardwired unity topology of the filter further aided the avoidance of any gain-based error distortion.

In order to preserve the vital phase characteristics of the seismic signal, a Bessel-Thomson configuration with a cut-off frequency of 6 KHz was selected.

A direct comparison between the characteristics achieved by the RC filter utilised in the current state of the art instrument, and the active filter used in the HPAGS sensor, can be seen in figures 4.7 and 4.8 below.

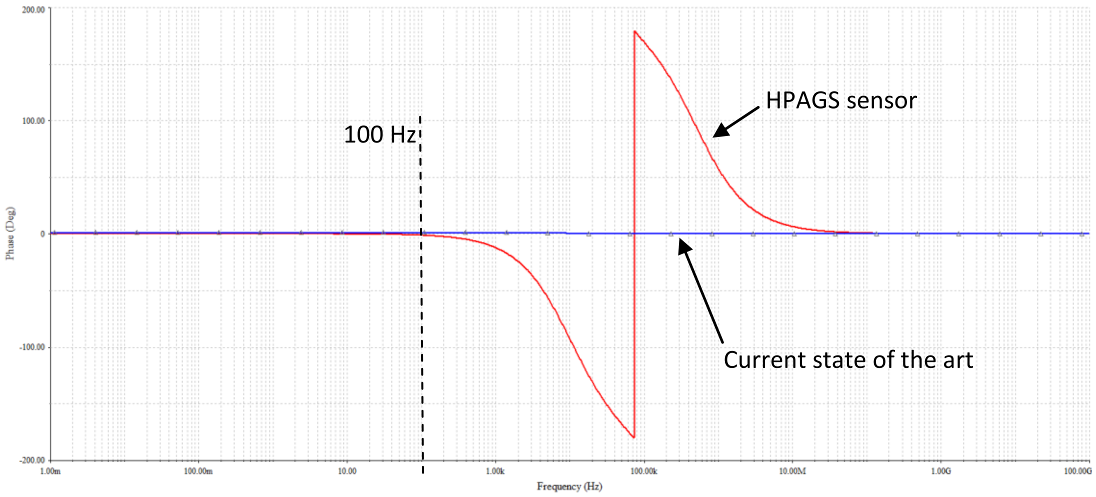

**Figure 4.7** Phase comparison between HPAGS active filters and current state of the art instrument

The phase characteristics shown in figure 4.7 are indeed very similar in both the active and passive RC filter cases, indicating that the design was predominantly governed by the phase response. However, a comparison of their resulting amplitude responses, as shown in figure 4.8, clearly demonstrates the advantage the HPAGS sensor presents in terms of noise rejection.

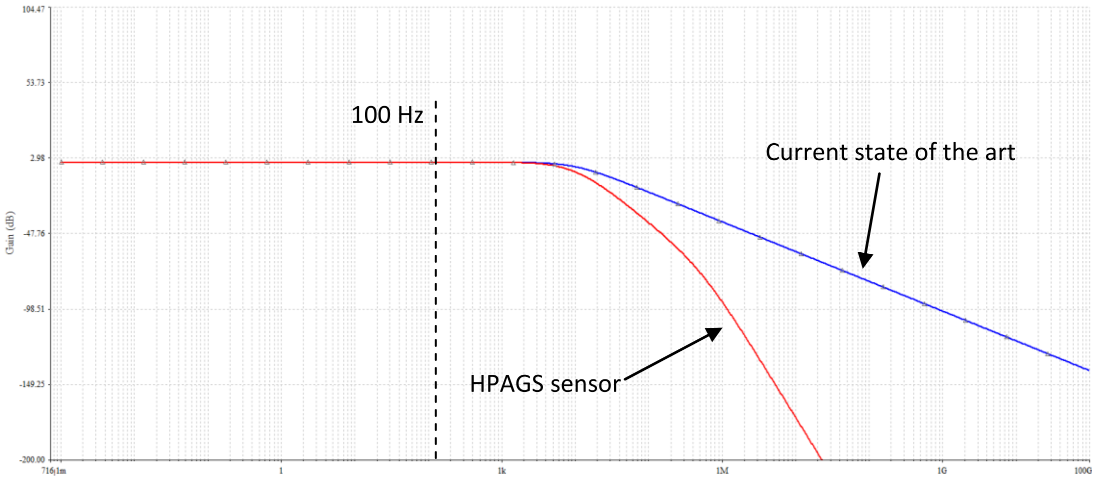

**Figure 4.8** Amplitude comparison between HPAGS and current state of the art instrument filters

The output MUX positioned after the last filter amplifier and buffer, enabled the selective connection of either the seismic signal or the 2V reference voltage to the output. All the switching and multiplexing devices used in the circuit were specifically chosen as not to impart any distortions to the signal via attenuation or via stray capacitance.

It is important to note that there was an additional connection made available to the filtered output signal from the active filter section, which served as the feedback signal for the auto zero-g bias correction loop. The auto zero offset bias circuit adjusted the output of the HPAGS sensor to true zero voltage throughout the channels, representing a zero acceleration sensed by the device. The feedback loop comprised the micro-controller, which upon reception of an instruction via the optical port, acquired the voltage of an output channel through the Bias feedback error block, shown in figure 4.9 below.

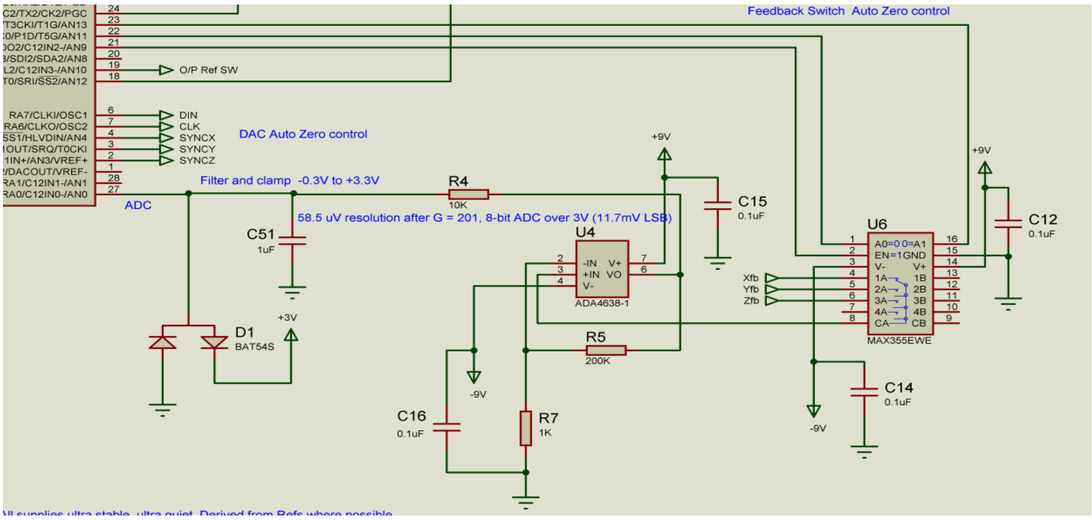

**Figure 4.9** Auto-zero correction feedback loop detail

In this section a multiplexer U6 switched the output of the appropriate channel, under the control of the micro U13, through a very high gain amplifier U4, to the micro-controller's pin 27, which was configured as an ADC input. The high gain of 201 of the amplifier, amplified the error of the sensor's output, by comparison to zero, thus providing a resolution of 15µV to the 10 bit ADC within the micro-controller, which is better than half the LSb of a 24 bit ADC that may be used to acquire the HPAGS sensor's data.

An input protection circuit D1, coupled to an RC low-pass filter, protected the micro-controller's ADC input pin from over voltage whilst removing any high frequency content allowing for an accurate measurement. If the sensor voltage was not zero, and error existed and the micro increased the voltage to the offset adjustment node U3, in order to reduce the error in a closed loop control fashion. This was accomplished by the micro-controller by serially transmitting successive correction values to the Auto-zero DAC U5, which in turn fed a representative voltage to the offset adjustment amplifier U3. This operation continued until the output voltage of the selected channel was zero.

Since the zero-g offset correction loop is a high gain closed loop control system, instability was prevented by a two-stage incremental proportional control algorithm within the micro-controller, which allowed adequate settling time between control steps before re-sampling the error.

The action of the zero-g bias correction circuit and control algorithm revealed a rapid 0.8V/s correction rate as depicted in figure 4.10 below.

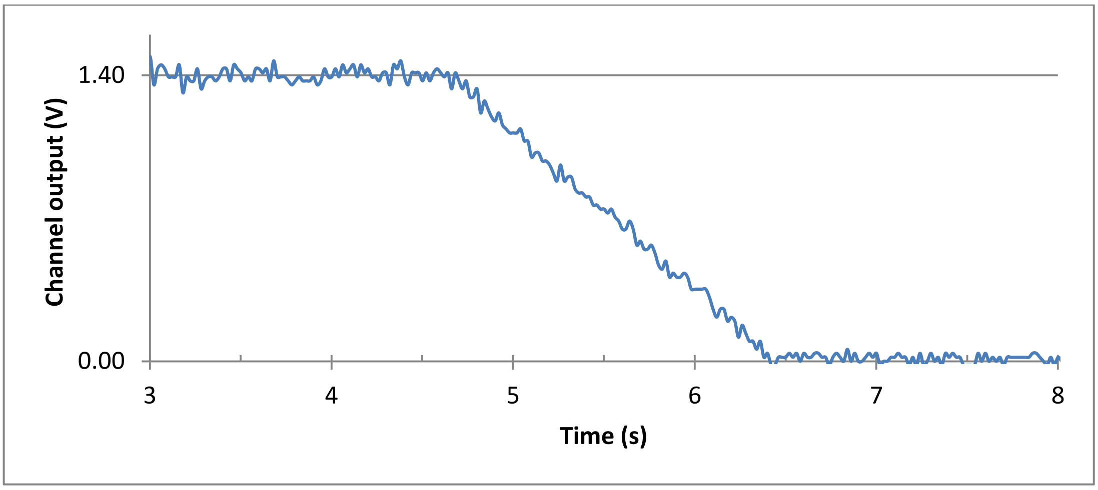

**Figure 4.10** Action of HPAGS sensor's Auto-Zero correction circuit and algorithm

The gain error measurement circuit elaborated on earlier in this section was implemented through the control of the input and output multiplexers of each channel, U5 and U16 for the channel examined here. The switching enabled a direct comparison between the 2V reference voltage, and the voltage output of the channel as a response to a 2V reference input.

Referring to the circuit in figure 4.2, communications were served by the optical IR device U7, connected to the serial port of the micro-controller, while the visible light phototransitor, was connected to the micro-controller's high priority interrupt, allowing for a quick response to an event trigger from the wider instrument.

The power control of the gyro motors and gimbal brakes were switched by MOSFETs Q1, Q2, and Q3. Connector CONN1 was an onboard programming port allowing for in-circuit reprogramming of the micro-controller as necessary.

The dynamic response of the HPAGS sensor unit was accomplished via electrostatic excitation by the application of an impulse or a variable frequency square wave voltage to the self test pin of the sensor. Pin 11 of the micro-controller was connected to the pins of both MEMS accelerometer sensors' self test pins, enabling simultaneous and equal excitation of all three x, y and z channels of the instrument. The impulse response of HPAGS sensor's x channel is shown in figure 4.11.

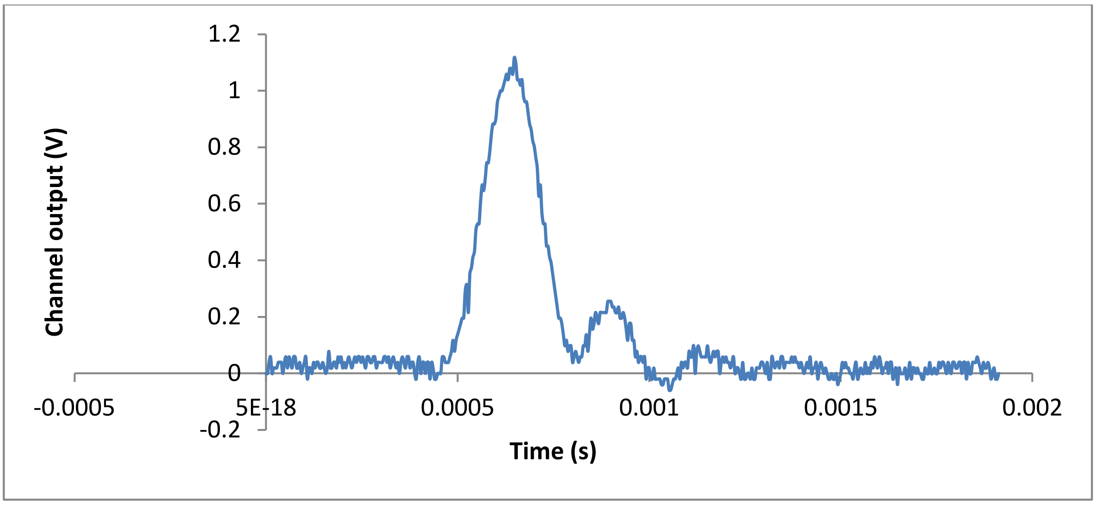

**Figure 4.11** Impulse response of x-channel derived by electrostatic excitation

It should be appreciated that this is the impulse response of the whole channel inclusive of active filters, and not just of the sensor.

## 4.2 The physical layout

The physical implementation of the HPAGS sensor electronics took the form of an ultra thin 0.5 mm 4 layer printed circuit board (PCB) as shown in figure 4.12.

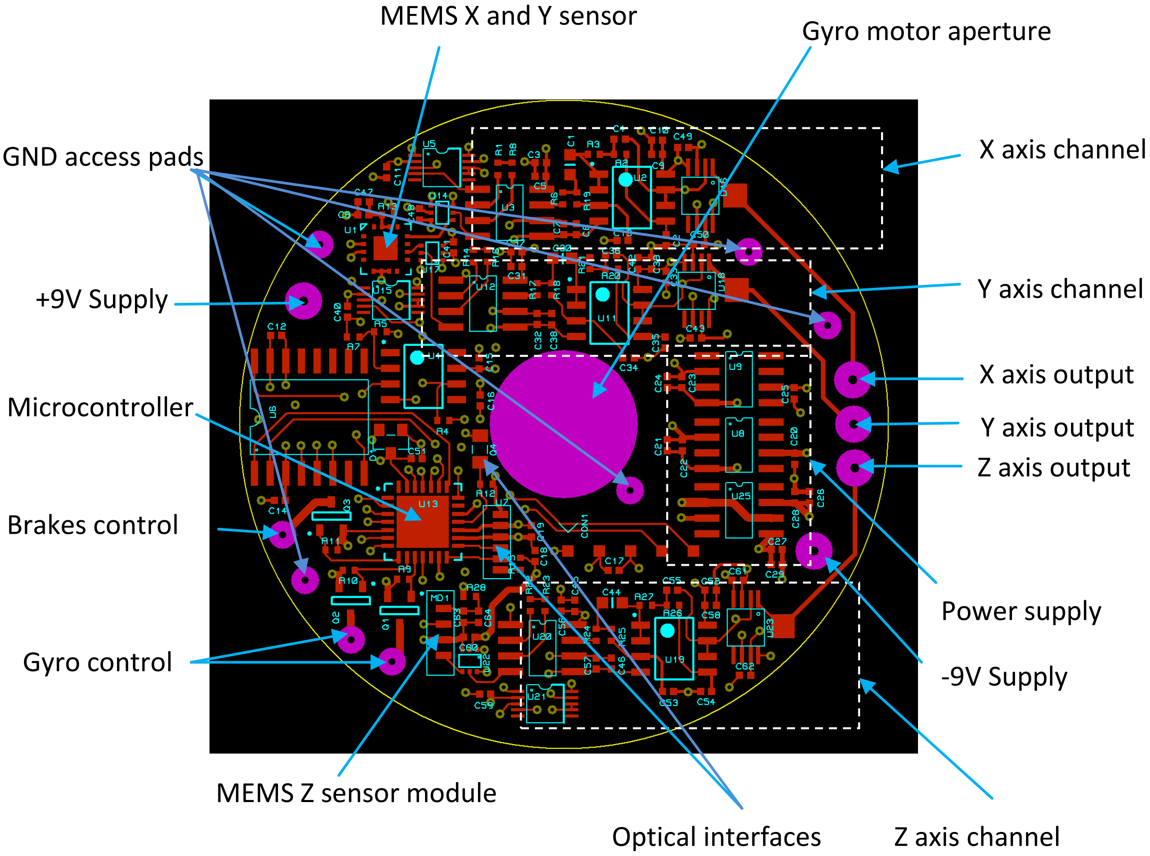

**Figure 4.12** HPAGS sensor's electronics physical layout

The highly compact design enabled for low noise interference and a small mechanical gimbal assembly. The thinness of the board allowed for its easy insertion into the inner gimbal's recess, and a further reduction in the weight of the overall platform load.

## 4.3 The electromechanical assembly

The custom-designed electromechanical assembly, precision machined to 0.1mm tolerance out of aluminium and brass, as pictured in figure 4.13, allowed the sensor electronics a three dimensional rotational decoupling from the measurement surface. The gyros oriented in a perpendicular to each other arrangement, actively stabilised the platform to a fixed celestial point thus allowing for the decoupling of any rotational seismic motion from the otherwise linear ground acceleration motion vectors. (Detailed mechanical diagrams of the assembly can be found in appendix D).

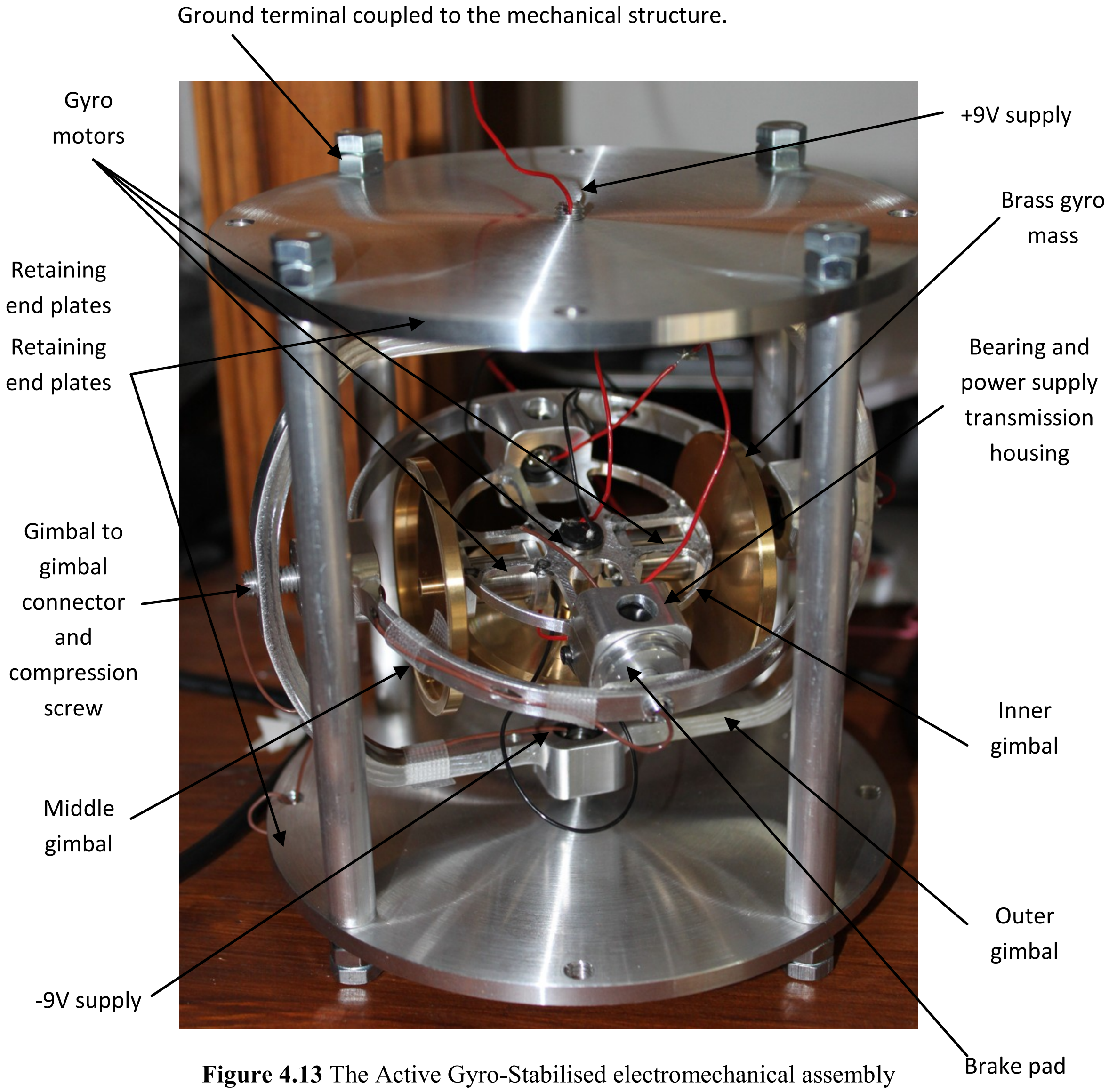

**Figure 4.13** The Active Gyro-Stabilised electromechanical assembly

### *4.3.1 The gyro stabilisation system*

Gyro stabilisation in itself is not a new concept since it has been in use for decades in various formats for the aid of gyroscopic navigation instruments. Unlike these instruments however, the gyro stabilised platform requirements for the HPAGS sensor makes it a rather unique undertaking.

Gyro instruments can be broadly divided into compasses, where gravitational biasing forces North to South alignment by means of regression, and gyro stabilisers, mainly used in camera stabilisation units. Much larger gyro stabilisation platforms exist, as those used in ships for the damping of the wave induced rocking motion.

In all of the above applications, the gyroscopic platform's characteristics other than its ability to reasonably quietly provide enough angular momentum are of little importance, provided that its size is also appropriate. In HPAGS however, its most important characteristic had by default to be its ability to provide reasonable short term stability, adequate for the duration of an earthquake, without producing any at all vibration interference to the ultra sensitive sensing elements onboard. Originally therefore, a smooth electromagnetic, liquid gyro drive was proposed for the purpose of stabilisation of the HPAGS sensor electronics. The proposed gyro would have utilised mercury as its rotating mass, and would have been driven by high current injectors, acting perpendicular to strong permanent magnetic fields, thus imparting a resultant torque onto the conductive liquid.

The stringent health and safety regulations in UK universities and industry requiring rather elaborate measures to be taken for the handling of mercury, unfortunately prevented the construction and test of such an apparatus, therefore allowing only for the use of conventional motors for actuation.

Conventional motors however, generate enough vibration during operation able to interfere with the very sensitive sensing electronics of the HPAGS platform. The solution sought therefore, was the design of a motorised gimballed platform employing high speed motors and light enough rotational masses, in an attempt to push the frequency of the inevitable motor vibration outside the 100Hz bandwidth of interest. Although such a construction was counter-intuitive in terms of angular momentum, and therefore at the expense of long term gyro stability, it was thought the only way available, adequate enough for the purpose of proof of the overall concept.

The inner gimbal, encompassing the gyro assembly, is depicted in figure 4.14.

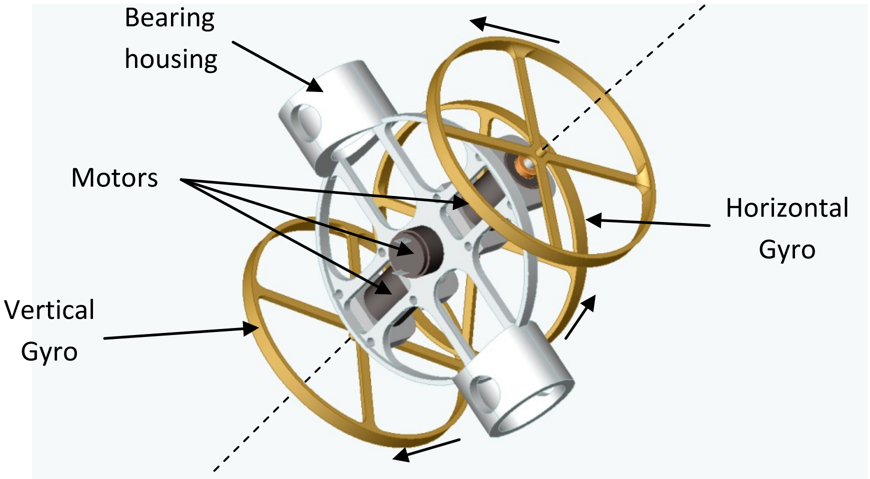

**Figure 4.14** Gyro assembly detail

The gyro assembly was constructed in such a way as to have a centre of mass below its rotational axis, thus able to self acquire the vertical gravitation vector without the need of any active components. Further, the positive gravitational biasing would enable the true North alignment of the platform via the operation of the vertical gyros alone.

The opposing nature of the vertical gyros enabled the cancelation of their starting torque, whilst it helped oppose the respective starting torque of the secondly energised horizontal gyro. Since the low centre of gravity aided the platforms vertical stabilisation passively, only a single gyro was deemed necessary to avoid oscillation.

In order to gain as much mechanical advantage, the gimbal arrangement was constructed from lightweight aluminium, while the high speed gyro masses were machined out of brass.

### *4.3.2 The power commutation system*

Resolving the mechanical problems however required a way of conveying power to the very centre of the gimballed platform without impeding on its free movement.

A through bearing power transfer method was conceived and fabricated as shown in an exploded view in figure 4.15 below.

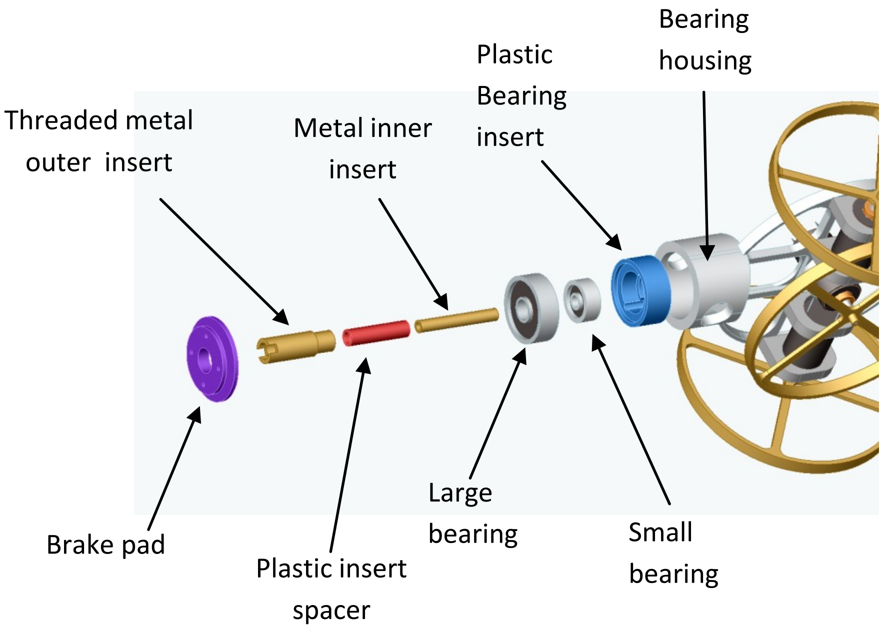

**Figure 4.15** Through-bearing power commutation detail

An assembled cross-sectional view of the through-bearing power commutation assembly is shown in figure 4.16.

The metal outer insert served electrically as a ground connection to the casing and mechanically as a brake pad holder, but more importantly as means of applying a compressive force on the opposing bearings in order to eliminate any vibration due to internal relative movement.

The metal inner insert was used to covey power through to the small bearing, providing a fully flexible means of power transfer without inhibiting the rotational movement of the gimballed platform. The plastic inner and the plastic bearing insert allowed complete insulation from ground.

The large bearing being in tight contact with the casing ensured a good ground connection, while the bearing insert was manufactured with a 1mm rim, in order to ascertain the electrical separation between the large and small bearings, and therefore between ground and power respectively.

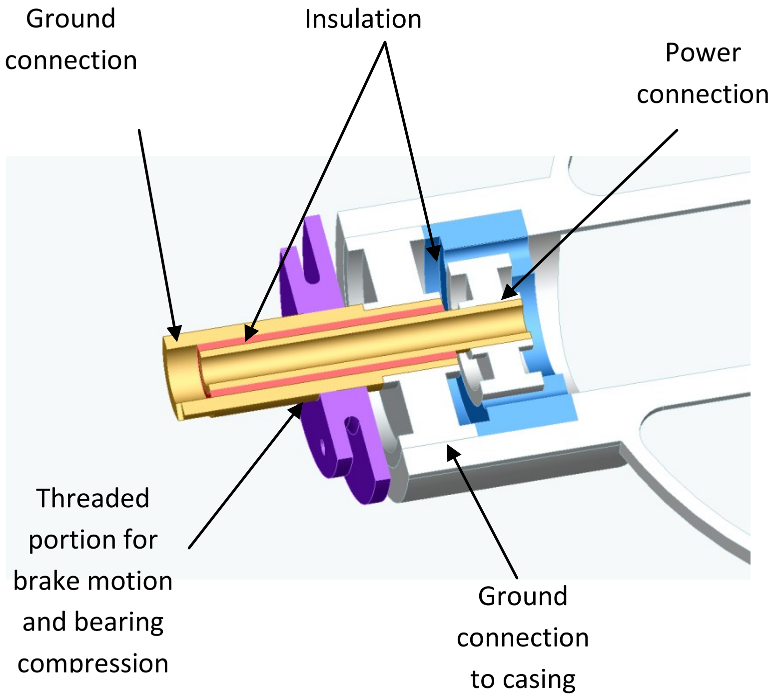

**Figure 4.16** Assembled bearing and commutator detail

The threaded portion of the outer insert allowed for the circular operation of the brake pad, actuated via means of a shape memory alloy. Tethering holes on its inner ring allowed for both the mechanical connection to the pad but also the electrical connection to ground. A small current passed through the shape memory alloy would increase its temperature and force it to rapidly return to its shorter in length original shape, thus forcing the pad to rotate and tighten against the bearing housing. Removal of the current would allow the alloy to relax and stretch under the tension of an opposing spring acting upon the pad, thus releasing the brake.

### *4.3.3 The six degree of freedom assembly*

The assembled gimballed gyro system is depicted in figure 4.17. The mechanical arrangement allowed for the isolation of any rotational motion around the x, y, and z axes, whilst directly mechanically coupling of the sensing electronics, residing on the inner gimbal, to any acceleration stimuli along these axes, namely $\alpha_x$, $\alpha_y$, and $\alpha_z$.

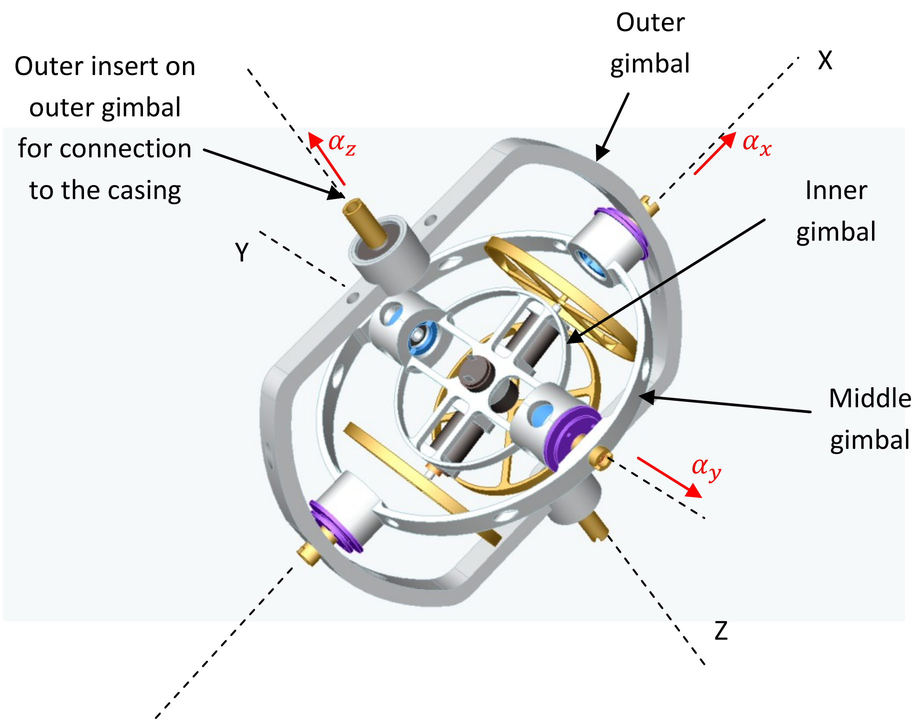

**Figure 4.17** Six degrees of freedom gimbal assembly

The gyroscopic force created by the gyros was indeed adequate for short periods of time, however, longer term drifts and mechanical biases would eventually interfere with the system, returning its attitude to a preferred state relative to the casing rather than the celestial space. This was no doubt due to the rotational mass size compromise made during the design phase in order to try and push the vibration noise of the platform to a higher frequency than that of the bandwidth of interest.

## 4.4 Control and embedded software

The HPAGS being a micro-controlled sensor, appropriate code was required for the onboard micro-controller in order for the various correction and actuation algorithms to be implemented. Further, Windows-based control software was also required in order to remotely communicate with the sensor, thus allowing for the emulation of a complete seismographic system.

### *4.4.1 PC Host Instrument Control Software*

The host software developed allowed the remote control of the sensor, as if incorporated into a complete seismograph solution. To this end, the control software was able to instruct the sensor to activate the gyros, auto-calibrate for bias error on all axis, activate and release brakes, and switch the references through the channels, and directly to the outputs, for gain verification and correction.

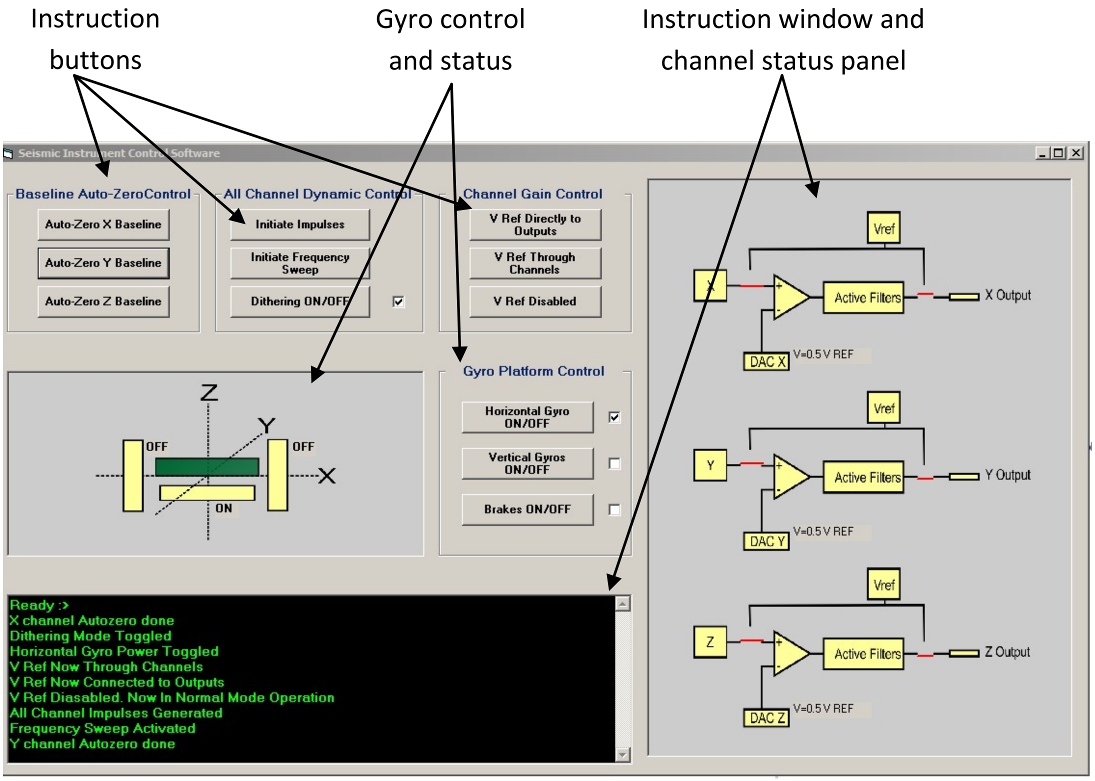

```
Ready :>
X channel Autozero done
Dithering Mode Toggled
Horizontal Gyro Power Toggled
V Ref Now Through Channels
V Ref Now Connected to Outputs
V Ref Diasabled. Now In Normal Mode Operation
All Channel Impulses Generated
Frequency Sweep Activated
Y channel Autozero done
```

**Figure 4.18** Bespoke Windows based host instrument control software

A screen-shot of the windows based control software is shown in figure 4.18.

In addition to status indication boxes, the user interface also incorporated a full commented instruction response window for clarity of operation. Further, an active diagrammatic channel-status panel was also included, in order to provide clear indication of input and output MUX status and DAC programmed voltage outputs at any given time.

An additional indication panel was also incorporated into the General User Interface (GUI), which allowed for the status of the gyros to be viewed at a glance, thus providing a full overall remote control system for the HPAGS sensor.

The control software was developed to take advantage of the available USB connectivity by utilising a Virtual Com Port (VCP) driver for windows, thus creating a "handle" to the port hardware. The use of a USB to Serial IC enabled the serial communication between the Windows control software and the embedded microcontroller onboard the HPAGS sensor, either optically, or via a two wire connection.

The instruction protocol developed was based on the ASCII character instruction set, where each character would correspond to an individual instruction. The symbolic representation of the characters was therefore easily handled by the high level windows software, while their numeric representation enabled the easier creation of an instruction decoder on the HPAGS sensor's embedded microcontroller.

The code listing for the control software, excluding objects and controls, is included in Appendix A.

### *4.4.2 Embedded Software*

The embedded software was developed in assembler and in a manner that allowed the HPAGS sensor to function as a real-time system. A simplified flowchart of the code is shown in figure 4.19 below.

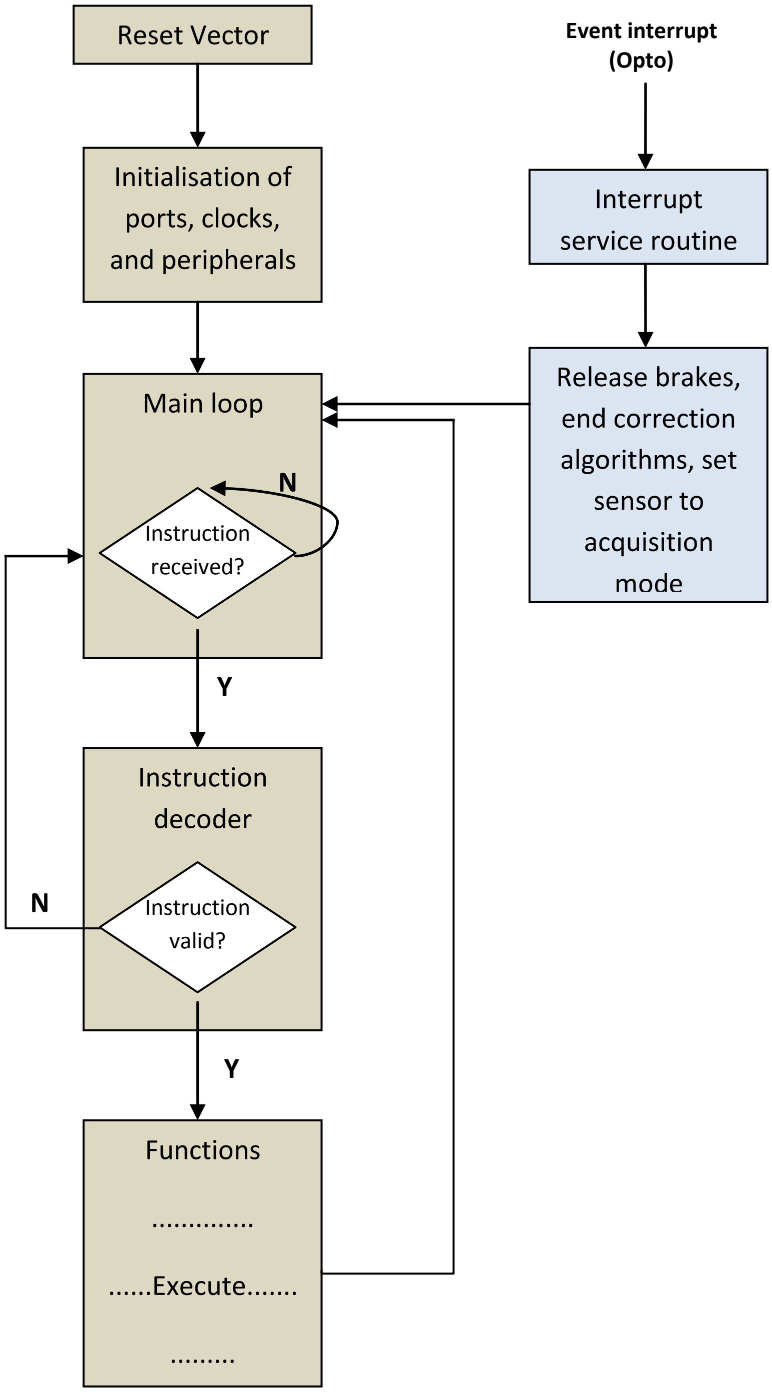

**Figure 4.19** HPAGS sensor embedded software flowchart

On reset, or power up, the initialisation routine was designed to quickly configure the digital input/output (I/O) ports and set up the analogue channels and their connections to the internal ADC. The internal clock speed was selected for fast code execution (4 MHz) and serial port compatibility, set to a speed of 9600 bits per second. The HPAGS sensor was capable of entering the “ready” state within the main loop in under 11μs from reset, where it awaited for further instruction from the wider system. Upon a valid instruction received, verified by the Instruction Decoder section, the appropriate function was called and the instruction executed before returning to the ready state.

Most open-loop instructions were decoded and executed within micro seconds. Closed-loop instructions however, such as auto-zero axis corrections necessitated hardware settling time allowance for stability, and therefore required few seconds to complete.

The optically coupled event interrupt was designed to rapidly set the HPAGS sensor in a normal acquisition mode, in the very unlikely event that an earthquake occurred whilst the sensor was executing a correction algorithm.

The embedded test code developed is listed in appendix B, containing the core functionality and function holders where necessary, as described by the flowchart in figure 4.19.

# Chapter 5

## HPAGS tests and results

Experimental validation of some of the new correction methods developed was demonstrated in chapter 3 and this chapter should therefore be viewed as an extension to those results. Correction methods only theoretically derived, or requiring the use of the full HPAGS sensor electronic hardware, embedded software, and post digitisation mathematical correction, are experimentally evaluated and presented in this chapter.

The requirement for the following experiments to deduce the new sensor's effectiveness in improving the accuracy of seismic data, as well as to compare with traditional and current state of the art instruments, could only be met by the methodical evaluation of the HPAGS sensor's correction principles.

### 5.1 Sensor calibration process

A calibration process for the derivation of the sensor's fundamental characteristics is of course crucial to the acquisition of any precision measurements, since it quantifies the sensor's performance parameters, including axial and cross-axis sensitivity.

Experimental derivation of these parameters required that the sensor and front-end electronics underwent testing in four specific spatial orientations as shown in figure 5 below. The directions indicated by the arrows denote the sensing axes' positive acceleration vectors.

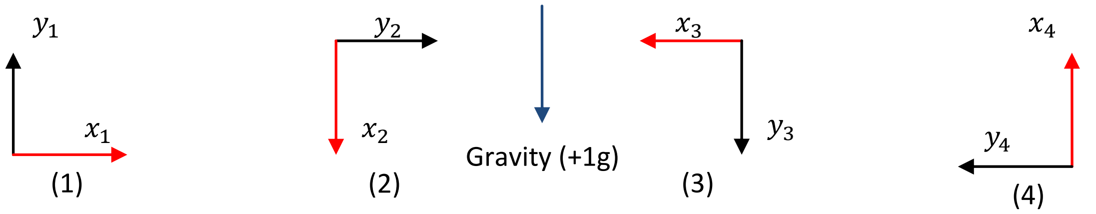

**Figure 5** Spatial orientations for calibration

The orientations depicted in figure 5 ensured that two out of the three sensing axes experienced zero acceleration, while the third axis experienced a +1g or a -1g accelerations. It should be noted that due to the perpendicular to the page's surface z-axis orientation, the z-axis did not experience any alteration in its zero acceleration state in any of the four orientations presented.

The precise rotational positioning required by the calibration process necessitated the modification of the high accuracy mechanical platform of figure 3.34 in a manner as to accommodate the HPAGS sensor's electronics in a vertical plane, as shown in figure 5.1 below.

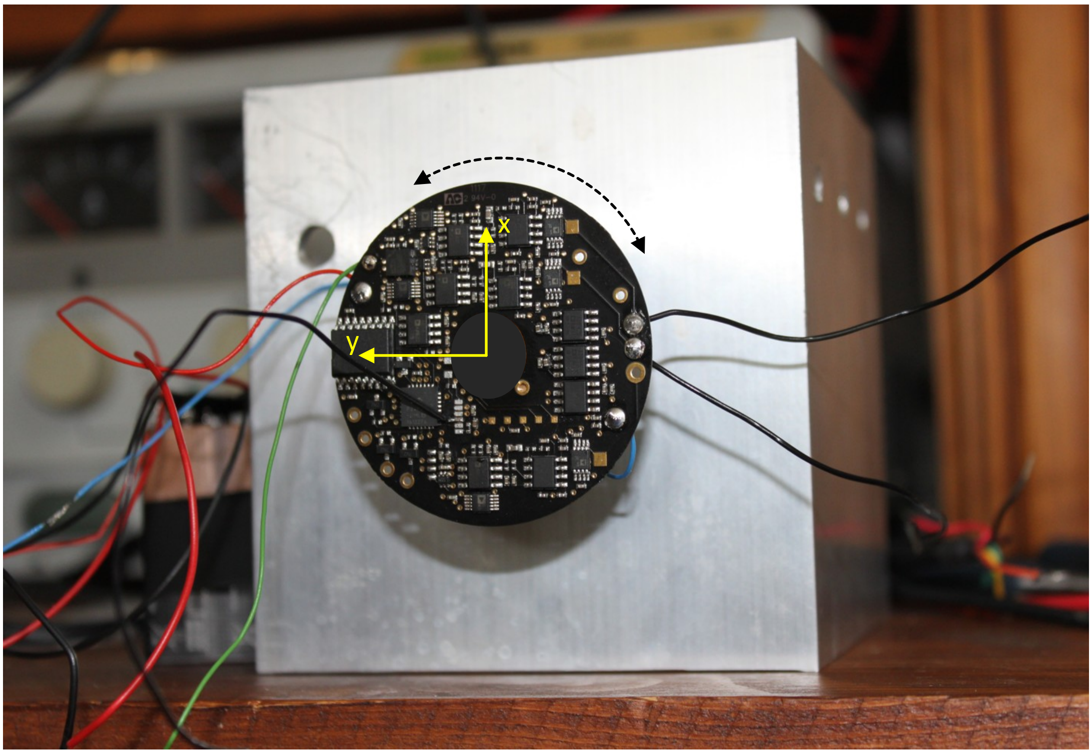

**Figure 5.1** High accuracy rotational platform

Mathematical representations for the x and y outputs for the general calibration setup could then be derived via the use of the earlier derived equations 3.18 and 3.19, reproduced below for clarity.

$$x_o = A_x S_x + V_{0gx} + C_{yx} A_y S_x + C_{zx} A_z S_x \tag{3.18}$$

$$y_o = A_y S_y + V_{0gy} + C_{xy} A_x S_y + C_{zy} A_z S_y \tag{3.19}$$

By elimination of the terms containing z-axis acceleration due to the z-axis perpendicular to the gravitation vector orientation:

$$x_o = A_x S_x + V_{0gx} + C_{yx} A_y S_x \tag{5}$$

$$y_o = A_y S_y + V_{0gy} + C_{xy} A_x S_y \tag{5.1}$$

Whilst the above equations would have been correct for outputs derived directly from the sensor, the front end electronics of the HPAGS sensor introduced a -1V bias offset to the sensor signal at the summing junction, and subsequently, a gain $G_A$=3.35, thus necessitated the alteration of equations 5 and 5.1 in order to correctly represent the HPAGS sensor unit as follows:

$$x_o = [(A_x S_x + V_{0gx} + C_{yx} A_y S_x) - 1]G_A \tag{5.2}$$

$$y_o = [(A_y S_y + V_{0gy} + C_{xy} A_x S_y) - 1]G_A \tag{5.3}$$

In orientation 1 of figure 5, $A_x = 0$ and $A_{y=} - 1$ therefore the representation of the y-axis output in this orientation:

$$y_1 = \ [(-S_y + V_{0gy}) - 1]G_A \tag{5.4}$$

Similarly, in orientation 3, $A_x = 0$ and $A_{y=} + 1$, and therefore the y output in orientation 3:

$$y_3 = \ [(S_y + V_{0gy}) - 1]G_A \tag{5.5}$$

Direct measurement of outputs $y_1$ and $y_3$, revealed values of 0.140V and 2.88V respectively. From equations 5.4 and 5.3 therefore:

$$y_1 = \ \left[\left(-S_y + V_{0gy}\right) - 1\right]G_A = 0.140\ (V) \tag{5.6}$$

$$y_3 = \ \left[\left(S_y + V_{0gy}\right) - 1\right]G_A = 2.88\ (V) \tag{5.7}$$

Solving the simultaneous equations by first equating each to the common term $V_{0gy}$

$$V_{0gy} = \frac{y_1}{G_A} + 1 + S_y \tag{5.8}$$

$$V_{0gy} = \frac{y_3}{G_A} + 1 - S_y \tag{5.9}$$

and subsequently to each other:

$$S_y = \frac{y_3 - y_1}{2G_A} = 0.409\ \ (V/g) \tag{5.10}$$

The zero-g bias voltage of the y axis $V_{0gy}$ could therefore be directly calculated from equation 5.6:

$$V_{0gy} = 1.4507\ (V) \tag{5.11}$$

Derivation of equations for $x_1$ and $x_3$ for orientations 1 and 3 respectively, using direct measurements of the x-axis outputs, resulted in:

$$x_1 = \left[\left(V_{0gx} - C_{yx}S_x\right) - 1\right]G_A = 1.45\ (V) \tag{5.12}$$

since $A_x = 0$ and $A_{y=} - 1$

$$x_3 = \left[\left(V_{0gx} + C_{yx}S_x\right) - 1\right]G_A = 1.54\ (V) \tag{5.13}$$

Similarly, orientations 2 and 4 yielded:

$$x_2 = \left[\left(S_x + V_{0gx}\right) - 1\right]G_A = 2.88\ (V) \tag{5.14}$$

$$x_4 = \left[\left(-S_x + V_{0gx}\right) - 1\right]G_A = 0.164\ (V) \tag{5.15}$$

$$\therefore\ S_x = 0.405\ \ (V/g) \tag{5.16}$$

$$\Rightarrow\ V_{0gx} = 1.455\ (V) \tag{5.17}$$

Therefore

$$C_{yx} = 0.05473 \tag{5 .18}$$

Equally, direct measurement of the y output in orientations 2 and 4 provided the following mathematical representations of the outputs:

$$y_2 = \ \left[\left(V_{0gy} + C_{xy}S_y\right) - 1\right]G_A = 1.53\ (V) \tag{5.19}$$

$$y_4 = \ \left[\left(V_{0gy} - C_{xy}S_y\right) - 1\right]G_A = 1.49\ (V) \tag{5.20}$$

$$\therefore\ C_{xy} = 0.01471 \tag{5.21}$$

Experimental determination of the sensor's parameters during calibration was conducted at an ambient temperature of 20°C, and with a supply of ±9V. Since many of the sensor's parameters are mainly affected by temperature and supply voltage variations, all experiments were conducted at the same temperature and at the same supply voltage. All subsequent experiments were also conducted in similar environments and therefore utilised the correction coefficients derived in this section.

## 5.2 FIR Low-Pass 100Hz Filter design

In order to retain the amplitude and phase qualities of the original signal, the HPAGS sensor's active filters were tuned to provide a frequency cut-off at 5KHz. To further band-limit the acquired data, in the digital domain, to the seismic 100Hz bandwidth, a Finite Impulse Response Filter (FIR) was designed and implemented.

The filter requirements of sharp 100Hz cut-off with high attenuation in the stop band and linear phase response were satisfied by a Kaiser window implementation. The amplitude response of the filter shown in Figure 5.2 below, exhibited no ripple in the pass-band, and attenuation in excess of -120dB in the 102Hz stop-band.

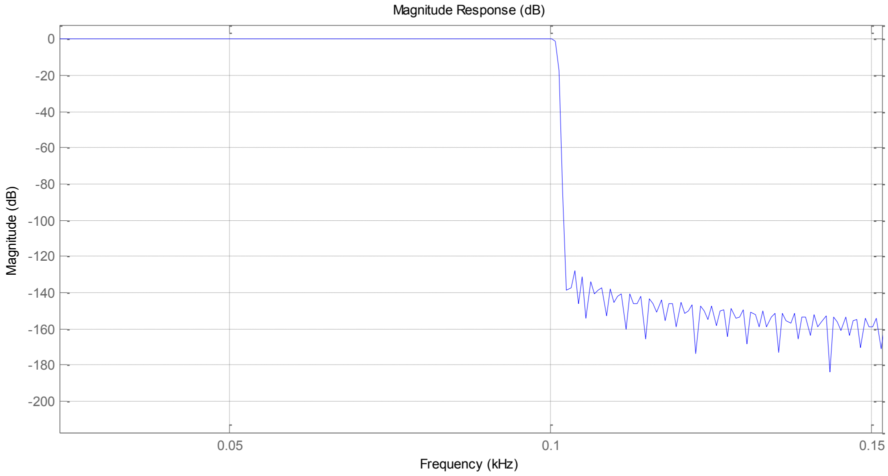

**Figure 5.2** Kaiser Window amplitude response (fc=100Hz, fp=102 Hz)

The phase response of the filter, as depicted in figure 5.3, also demonstrated a good linear phase characteristic, therefore retaining the original signal's characteristics without distortion.

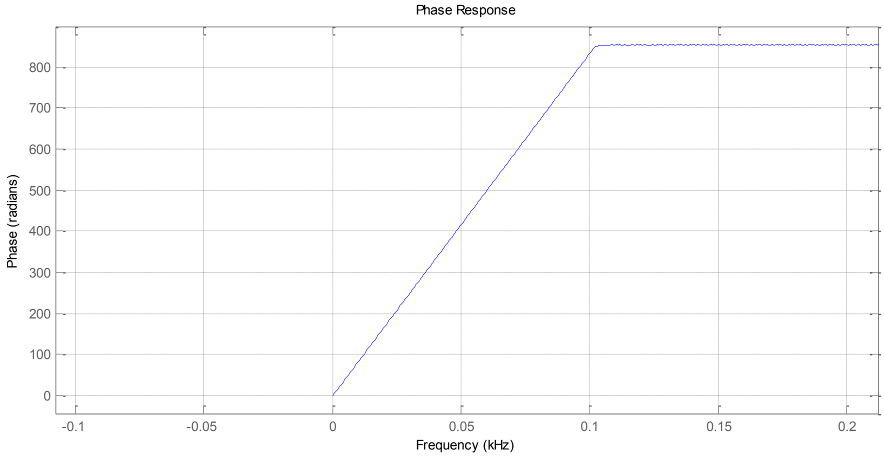

**Figure 5.3** Kaiser Window phase response (fc=100Hz, fp=102 Hz)

The impulse response of the filter characterised by its coefficients shown in figure 5.4 below, exhibited a right-to-left symmetry, characteristic of a phase-linear system.

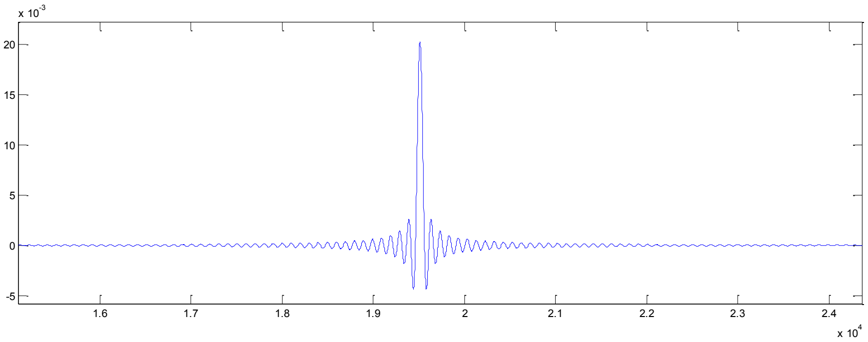

**Figure 5.4** Kaiser Window impulse response (fc=100Hz, fp=102 Hz)

## 5.3 Setting the assessment standards

Direct comparison between existing instruments and the HPAGS sensor proved to be rather more intricate than originally anticipated, since the comparative instrument references established were:

1. Conventional instruments with RC filtering, representing over 95% of the instruments utilised to date.
2. State-of-the art instruments of higher sampling frequency, RC and active filtering, representing a very small minority used for specialist applications.

Since the more complex HPAGS sensor, employed a much higher sampling frequency, active filters only, and several new correction methodologies and circuits, namely:

1. Sampling at QPS criterion for undistorted digitization of data.
2. Active zero offset calibration
3. Active gain error correction
4. Cross-axis interference correction
5. Impulse de-convolution correction
6. Active gyro tilt correction

direct comparison of results between instruments therefore, based solely on the amount of drift of the baseline in their equivalent derived displacement data, was deemed to be an unreliable measure of instrument performance.

It could be argued that the displacement baseline error over a specific period of time could be used as a direct comparative measure of quality between current technology and the HPAGS sensor, however, due to the multi-variable environment affecting the deviation of the displacement baseline, such a simplistic comparative method would result in inequitable comparisons.

For example; most instruments utilise 60 seconds of pre-event data to derive the average bias level, and 60 seconds of event data to capture the event. A conventional sensor sampling at a rate of 500Hz, would acquire 30,000 samples of pre-event, and event data, where the HPAGS sensor sampling at 250KHz would acquire 15,000,000 samples of respective data. Clearly therefore, if an improvement was to be shown in the displacement baseline offset of the HPAGS sensor results in the 60 second period, it could not be known whether this improvement was due to the correction methods employed, or simply due to the higher resolution of the signal, or indeed due to both. Further, since integration is a cumulative mathematical process, the higher sampling rate would yield a superior accuracy in terms of area calculation, while it would also yield an exaggeration of any small remaining errors due to the disproportionate increase of summations for a given time.

A comparison of equal lengths of data, in terms of number of samples, would appear to be a fairer comparison, since both offsets and the integration process act upon individual samples, however, the peak adulations observed in lower frequency sampled data were best examined over much longer trends, as the output could in some circumstances depend on the start and end points of the acquired data.

While the *effect* of displacement baseline error is indeed an *indication* of overall error, it is *not* in itself an error that could be directly addressed, since its origins were shown to be a multitude of *primary* underlying errors. Baseline error is therefore *the result of the cumulative effect of several primary errors*, and consequently it is the correction of these primary errors that the HPAGS sensor should be addressing directly, and be evaluated upon thoroughly.

It is widely accepted, and shown within this work, that conventional and state-of-the-art technologies are undoubtedly unable to provide accurate seismic data. Further, the effects of sampling rates much below the QPS criterion where also shown to produce notable errors on higher frequency digitised data. It was therefore concluded that experimentation utilising typical lower sampling frequencies with sinusoidal mechanical stimuli in the higher end of the 100Hz bandwidth, would only provide information already derived earlier in this work, and data which is widely accepted as inaccurate. Further, the utilisation of a higher non-distorting sampling rate, would allow for the use of shorter in time trends, since the envelope formation due to inadequate sampling would no longer be an issue. Any other primary error should however be clearly evident within the very first few cycles of an oscillation. Reduction of the data size would also serve to speed up calculations in mathematical software without the loss of fidelity, since all results could be extrapolated to the full 60 second timeframe for comparison where necessary.

The experimental setup used for the evaluation of the HPAGS sensor's effectiveness, requiring a frequency variable sinusoidal input, is shown in figure 5.5.

The vibration platform benefited from near-pure primary sinusoidal mechanical excitation verified by the reference displacement signal derived by the IR sensor, as discussed earlier in this work. Since the actual amplitude of mechanical oscillation was able to be determined by direct measurement on the excitation platform, and the phase linearity of the HPAGS sensor was already evaluated in chapter 3, the IR signal served only as a visual assurance of sinusoidal fidelity, and therefore deemed surplus to requirement in the following experimental evaluation. The HPAGS electronics were mounted on the mechanical vibration platform, with the x-axis in the vertical plane, and the y-axis in the horizontal plane.

Direct comparative analysis of experimental results was conducted by the systematic evaluation of each of HPAGS sensor's corrective algorithms and circuits.

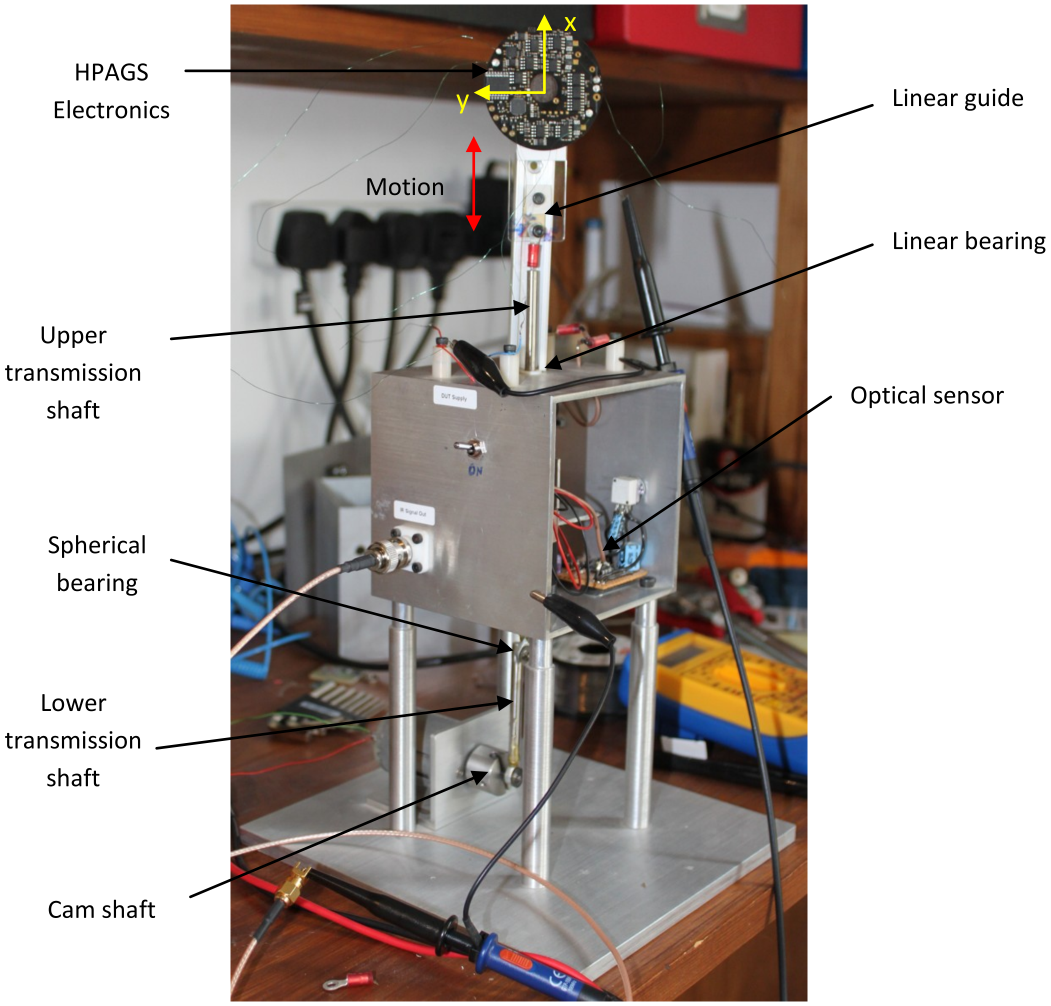

**Figure 5.5** Mechanical vibration platform with HPAGS electronics affixed to the excitation shaft

The unfiltered IR output of the displacement sensor, confirming the sinusoidal action of the mechanical vibrator, is shown in figure 5.6 below.

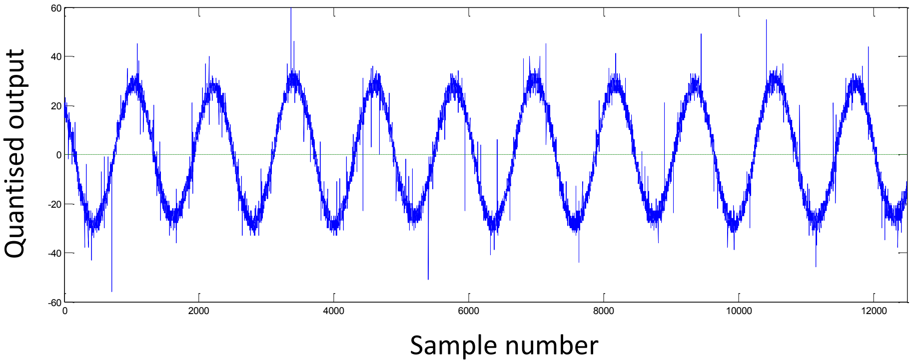

**Figure 5.6** Unfiltered IR displacement sensor data

## 5.4 HPAGS Auto-zero bias correction assessment

The Quality Preservation Sampling (QPS) criterion derived earlier in this work, does not only aid the retention of signal integrity but also the measurement accuracy of digitised data. According to the QPS criterion therefore, the HPAGS sensor's x-axis output required sampling time period, was derived as follows;

$$t_{QPS} = \sin^{-1}\left(\frac{LSb}{2A\pi f}\right) \tag{5.22}$$

$$t_{QPS} = \sin^{-1}\left(\frac{153 \times 10^{-6}}{2 \times 1.3 \times \pi \times 5 \times 10^{3}}\right) \tag{5.23}$$

$$t_{QPS} = 3.74\mu s \tag{5.24}$$

In the above calculation, the LSb figure was based on a 16 bit ADC used for the digitisation of the signal over a 10V reference range, and a peak signal amplitude of 1.3V at a maximum frequency of 5KHz. The 5KHz frequency limit was of course imposed by the cut-off frequency of the active filters in each channel on the HPAGS sensor electronics.

An indicative sampling frequency of 267KHz was therefore required in order to preserve the data quality of the signal, but also the measurement of the error voltage on the feedback loop of the auto-zero bias correction circuit onboard the HPAGS sensor.

In the following experimental assessment, the Auto-zero bias circuit was remotely activated by the host Windows software, and served as the only means of bias offset correction of one set of acceleration data, whilst the other set of data was corrected using the conventional average subtraction method.

Both sets of data were acquired using the same sampling frequency, under the same conditions, resulting in the same number of samples, thus providing for a direct comparison between the conventional, and the advanced auto-zero method utilised by the HPAGS sensor.

### *5.4.1 Results*

The unfiltered, auto-zero corrected acceleration data, and the conventionally corrected acceleration data, both sampled at a more convenient, but close to the QPS derived, frequency of 250KHz, is shown in figure 5.7 below.

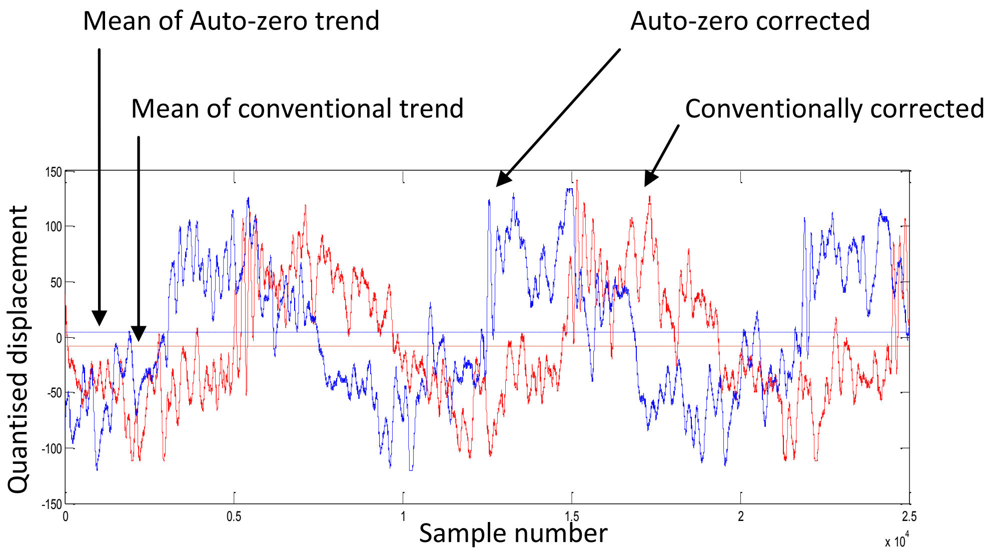

**Figure 5.7** Auto-zero versus conventionally average-subtraction corrected acceleration trends

The resulting error of interest is of course the distance between the mean value of each trend and the absolute zero reference line of the x-axis. It was observed that the Auto-zero method provided superior performance in terms of baseline correction of the acceleration data.

Filtering of both the bias-corrected sets of data, and subsequently double-integrating them, resulted in expected bias-deviating displacement trends due to the initial offset errors. The best-fit linear lines of both the auto-zero corrected and conventional data sets, are shown if figure 5.8, where the considerable improvement resulting from the auto-zero corrected data can be clearly seen.

It should be evident however, that due to the small error in the auto-zero corrected acceleration trend, the resulting displacement trend exhibited a slight baseline offset, albeit not very significant by comparison to that of the conventionally corrected data.

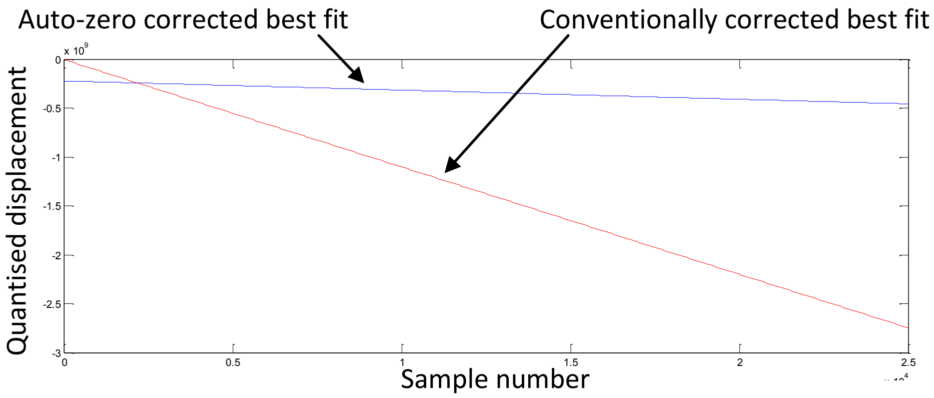

**Figure 5.8** Auto-zero, and conventionally corrected best-fit linear displacement trends

A block diagram of the Auto-zero correction circuit is shown in figure 5.9, with circuit diagram references corresponding to the circuit of figure 4.2.

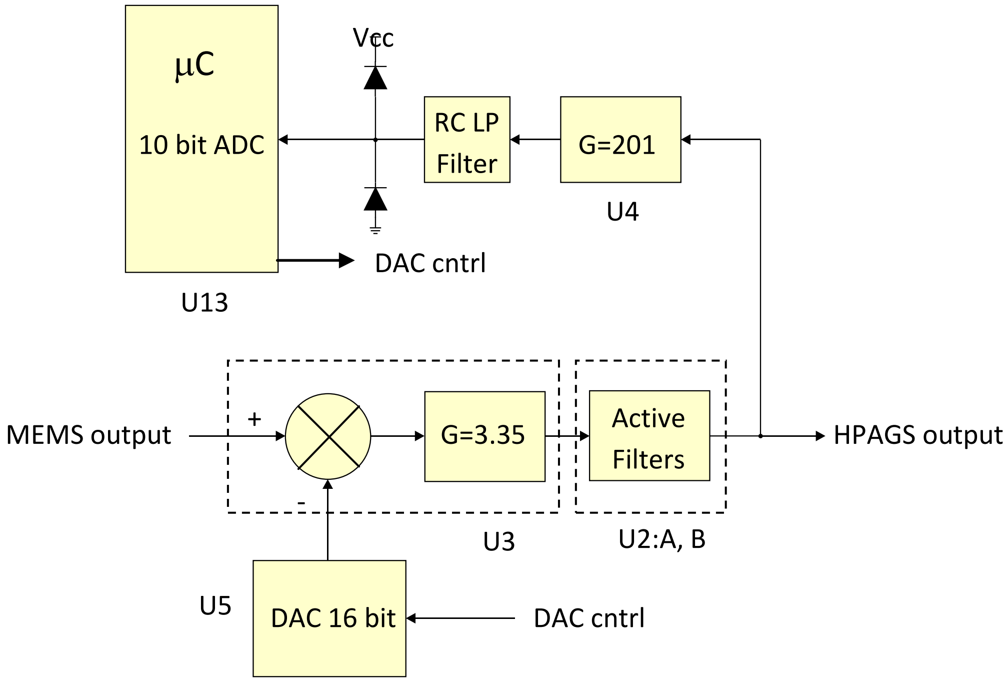

**Figure 5.9** Auto-zero bias correction system block diagram

The theoretical error of the correction loop can be calculated by analysing the resolution and the gains throughout the loop.

The correction applied to the loop via the micro-controller is directly fed to the 16 bit DAC (U5). With the DAC's reference at 2V, the resolution of each corrective step can be shown as

$$\frac{2}{2^{16}-1} = 30.5\,\mu V \tag{5.25}$$

However, U3 further amplifies this corrective step by 3.35 times, resulting in a step of 102µV at the HPAGS channel output.

In turn, U4 amplifies the absolute value of the output by 201 times, therefore increasing the step voltage to 20.5mV at the ADC input. The ADC within the micro-controller shares the 3V supply as a reference and therefore achieves a resolution over 10 bits of 2.9mV.

A worst case scenario would therefore produce a correction overshoot of 20.5-2.9=17.6mV at the ADC, equivalent to an actual maximum bias error of only 87µV on the HPAGS sensor's channel output. However, the quantised output of the mean resulting from the Auto-zero correction on the waveform in figure 5.7, was indeed many times the magnitude of the maximum calculated error.

Direct measurement of the signal at the ADC input, after Auto-zero, revealed a high noise level content, as shown in figure 5.10.

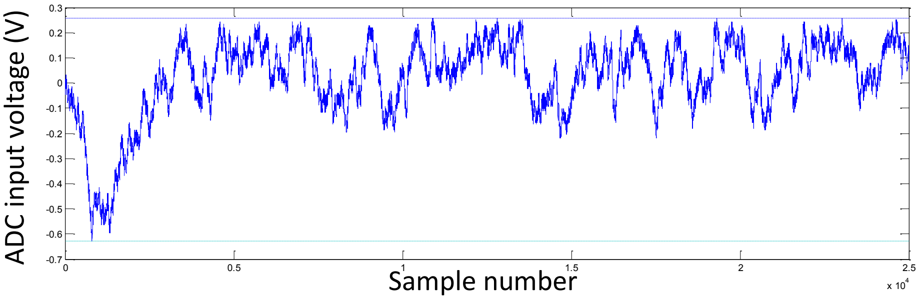

**Figure 5.10** Voltage at ADC input

The high gain of amplifier U4 resulted in noise content higher than the RC filter was able to attenuate efficiently, thus creating a feedback signal of undetermined and variable amplitude.

An increase of the filter capacitor to 10μF and the increase of a settling time delay in the micro-controller Auto-zero code, resulted in an improved HPAGS Auto-zero system, able to further reduce the offset error. A comparison of the means of the bias-corrected acceleration output signals derived are shown in figure 5.11.

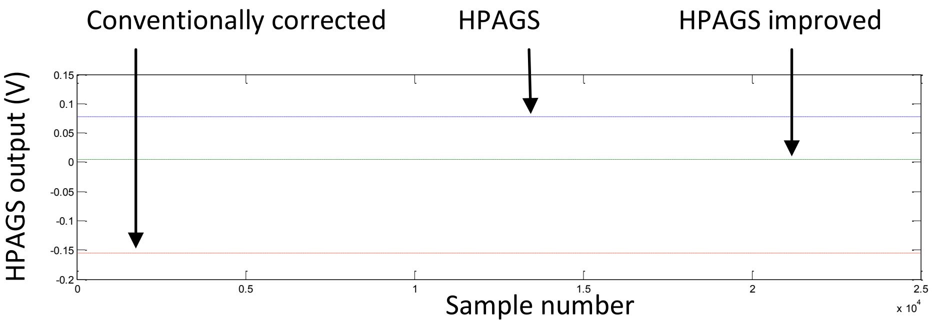

**Figure 5.11** Means of Conventionally, HPAGS, and HPAGS improved bias corrected signals

The resulting displacement best-fit lines are shown in figure 5.12 below, with the improved correction system producing a displacement baseline significantly closer to the zero x-axis level.

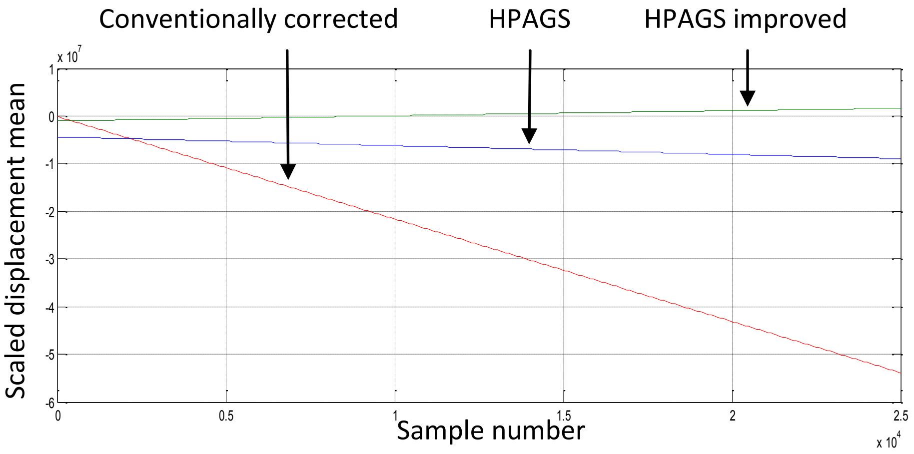

**Figure 5.12** Displacement best-fit lines of Conventionally, HPAGS, and HPAGS improved corrected signals

Quantification of the best-fit lines revealed that for a seismic signal acquired over a 60 second period, sampled at the HPAGS sensor's QPS frequency of 250KHz, a conventionally bias corrected signal by average subtraction, would result in a displacement error of over 13 cm, where an HPAGS bias corrected signal utilising the improved system, would result in a displacement error of only just over 3 cm.

Averaging of the feedback signal in the micro-controller as means of deriving an even more superior accuracy of data was not possible with the HPAGS sensor circuit since the ADC within the micro was unidirectional.

From this point onwards in this work, any reference to the Auto-zero correction mechanism should be regarded as a reference to the improved version of the algorithm and circuit as detailed above, unless otherwise explicitly stated.

### *5.4.2 Conclusion*

The comparative experimental assessment between Auto-zero corrected and traditional bias subtraction corrected data, proved that although the data in both experiments was acquired at an increased sampling rate of 250 KHz, much higher than any conventional or even state-of-the-art instruments, the resulting auto-zeroed displacement trends demonstrated major improvement in terms of accuracy.

Although the Auto-zero correction mechanism still produced an offset error in the acceleration trends higher than the theoretical ideal, the validity of the method as means of significantly reducing the offset error was undoubtedly demonstrated.

It can therefore be concluded that the novel auto-zero bias correction algorithm and circuit employed by the HPAGS sensor does provide for a dramatic improvement to the accuracy of displacement trends derived by the numerical integration of acceleration data. Furthermore, the action of the Auto-zeroing improves the dynamic range of the sensor by centring its output on the zero volt reference.

## 5.5 HPAGS input re-composition by impulse de-convolution

Utilisation of the MEMS accelerometer's test pin to acquire the MEMS sensor's and the wider HPAGS instrument's response, as previously discussed, allowed for the reduction of any sensor-related variations to the original signal. According to classical Digital Signal Processing (DSP) theory, the acquired acceleration data from the sensor can be thought of as the convolution of the actual mechanical acceleration experienced by the sensor and its impulse response. De-convolving the impulse response from the output data of the sensor, should therefore in theory provide accurate reconstruction of the mechanical actuation signal.

Convolution being a complex operation between data sets renders the application of direct de-convolution of the resulting data mathematically impossible for most real applications. Since however convolution in the time domain is equivalent to multiplication in the frequency domain, the process of de-convolution in the time domain simply becomes a division in the frequency domain, posing fewer, but still some implementation challenges.

### *5.5.1 Results*

Figure 5.13 below shows auto-zeroed and FIR filtered acceleration data acquired from the HPAGS instrument, excited by the sinusoidal mechanical vibration platform.

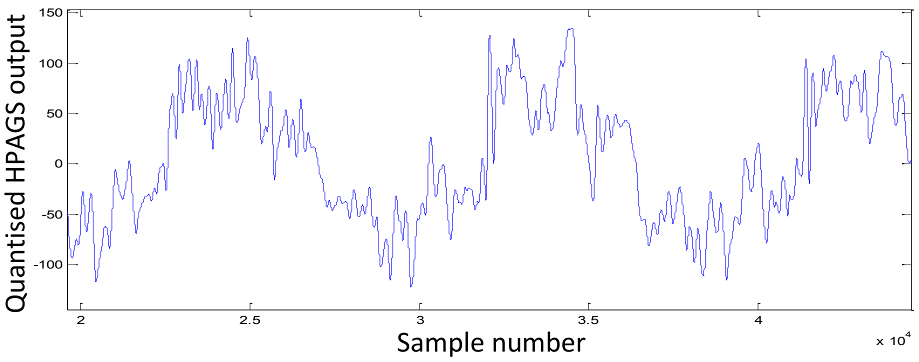

**Figure 5.13** Auto-zero corrected and filtered acceleration trend

An impulse remotely initiated by the host software and digitised immediately after the acquisition of the acceleration data is shown in figure 5.14 below.

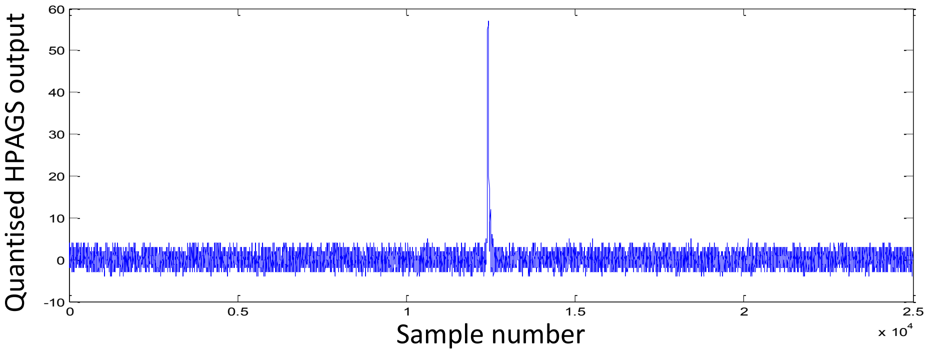

**Figure 5.14** Electrostatically triggered Impulse response

It should be noted that the horizontal positioning of the impulse peak in figure 5.14 appears central only due to the digitizer's settings. Any horizontal shift to the impulse response does not alter the system's characteristics other than the phase relationship in terms of delay between the input and the output data sets. It was already shown earlier in this work that the HPAGS sensor exhibited linear phase characteristics and therefore a shift of the impulse peak to sample zero was deemed appropriate if representative data was to be acquired, as shown in figure 5.15 below.

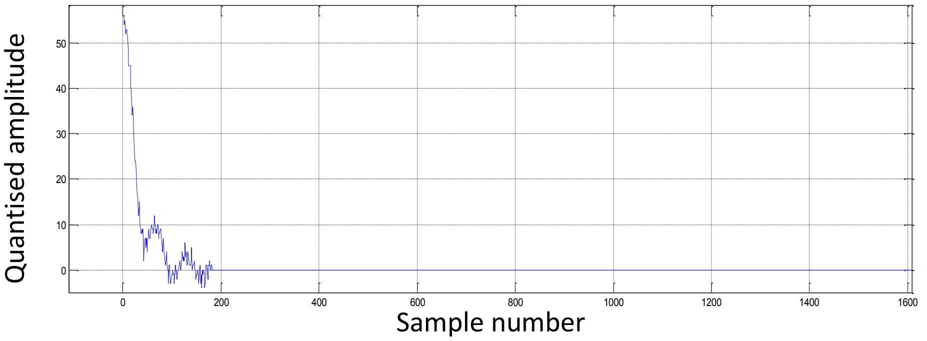

**Figure 5.15** Impulse response of x-axis channel

The shifted representation of the impulse response of figure 5.15 is contained only within the first 182 samples of data. The rest of the data set comprises zero padding of an appropriate length for the enablement of a point by point division of the sensor output and impulse response frequency spectra.

Close examination of figure 5.15 also reveals the presence of noise on the impulse response signal which was originally thought detrimental to the data recovered by de-convolution, however, experiments showed that although smoothing the impulse response by averaging yielded a smoother in appearance response, it created abrupt changes in the magnitude of the data, which in turn generated their own frequency content yielding a much noisier result.

The frequency spectrum of the impulse response is depicted in figure 5.16 below.

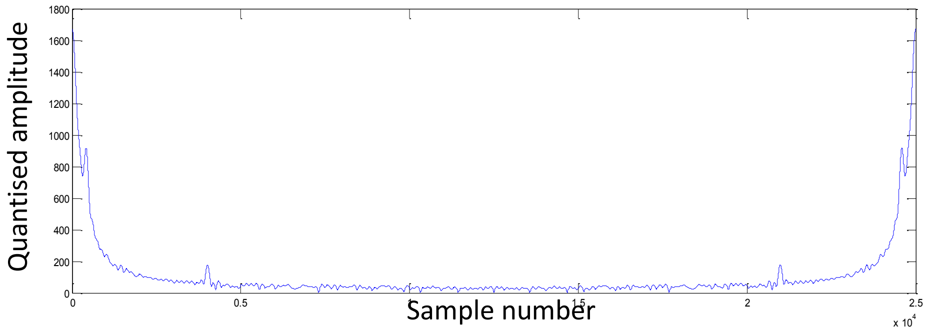

**Figure 5.16** Frequency spectrum of x-axis impulse response

It should be noted that the impulse response was digitised at the same sampling frequency as the HPAGS output signal, allowing for best de-convolution results.

The frequency spectrum of the HPAGS output, is shown in figure 5.17 for reference. It can be readily envisaged that the spectra division would yield a magnification of any noise artefacts in the regions where the impulse response frequency data approaches near zero values, thus necessitating the use of an FIR filter to recover the de-convoluted data.

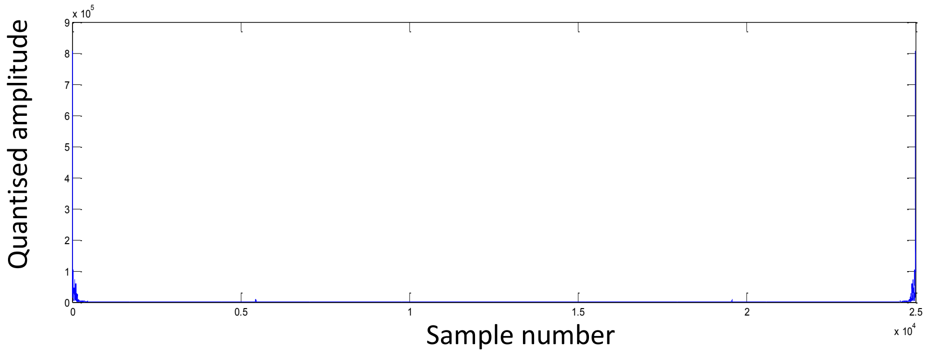

**Figure 5.17** Frequency spectrum of HPAGS x-axis output.

The resulting spectrum of the division of the two frequency characteristics is shown in figure 5.18 below, exhibiting the anticipated increase in noise in the near zero regions of the impulse response frequency data.

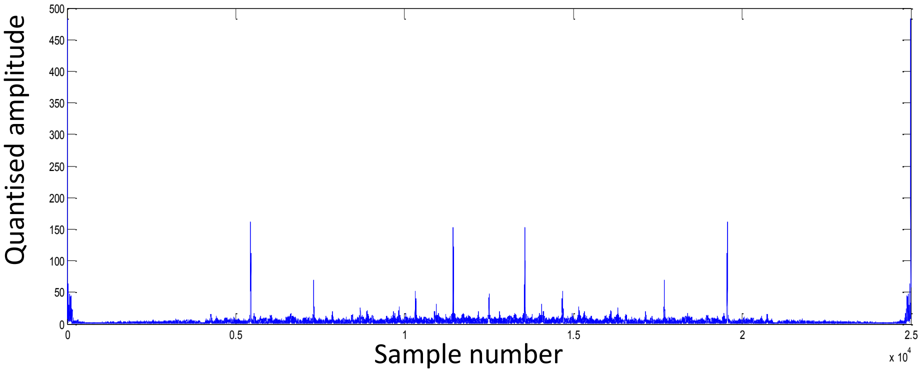

**Figure 5.18** Frequency spectrum of the division of the acceleration and impulse response spectra

Since figure 5.18 depicts the frequency spectrum of the quotient of the HPAGS output and impulse response spectra, it should also mathematically represent the spectrum of the de-convolved mechanical input stimulus. The derivation of the mechanical acceleration input to the HPAGS sensor, shown in figure 5.19, was therefore accomplished by the application of the inverse FFT (IFFT) to the quotient spectra, and by subsequent FIR filtering in order to remove the residual high frequency noise.

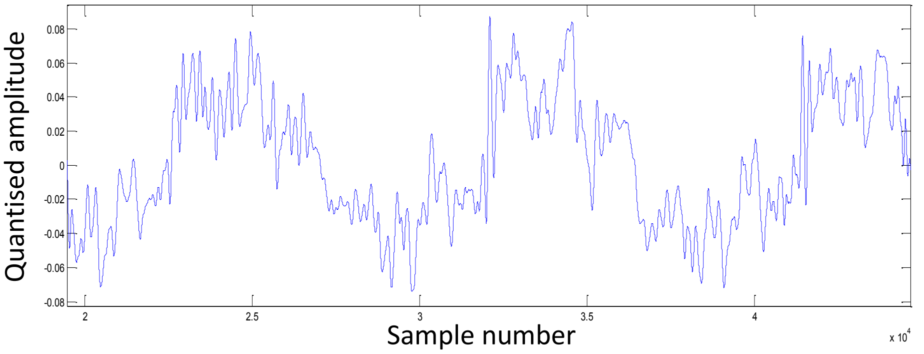

**Figure 5.19** mechanical input derived by the IFFT of the acceleration and impulse spectra

The resulting mechanical actuation trend of figure 5.19 was found to be of the expected form with regard to shape and phase, representing the mechanical acceleration input to the sensor. Since the HPAGS sensor was specifically designed to impart low noise, minimal phase, and minimal attenuation to signals within the 100Hz bandwidth of interest, the resulting impulse de-convoluted acceleration input, as expected, did not exhibit any notable differences by comparison to the output sensor data of figure 5.13. In fact, other than magnitude scaling, the impulse de-convoluted input was found to be nearly point to point identical to the output of the sensor.

Derivation of displacement trends by double integration of the HPAGS output data and the impulse de-convolution derived data, yielded nearly identical results, thus further proving the transparency of the sensor to in-bandwidth data. The displacement trends of the direct output and the de-convolution computed input, are depicted in figure 5.20 below, scaled appropriately for direct comparison.

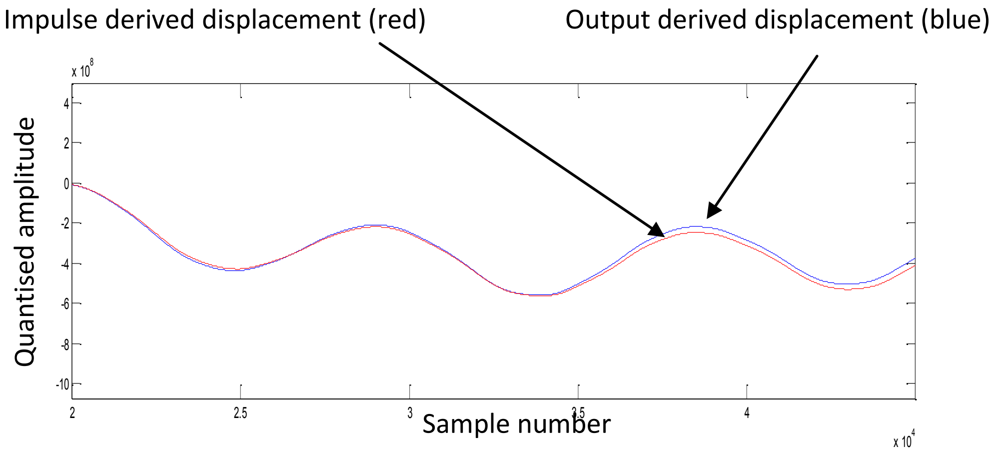

**Figure 5.20** Displacement trends of impulse derived and direct output accelerations

In order to further confirm the transparency of the instrument and the accuracy of the impulse response model, a sinusoidal of frequency 1.5 KHz, and therefore within the HPAGS sensor's 5KHz active filter bandwidth, corrupted by an out of band 7.5 KHz noise, was synthesised and presented as an input to the model. This high frequency input was constructed by the addition of two digitised sinusoids of different amplitudes as shown in Figure 5.21

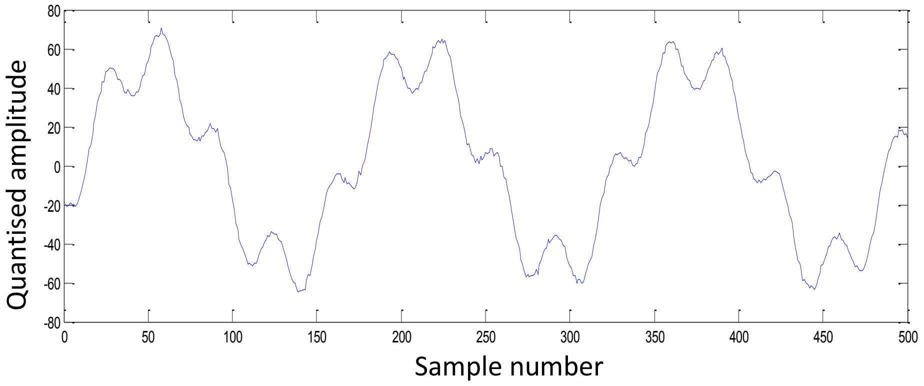

**Figure 5.21** Synthesised high frequency input

Convolution of the synthesised input with the sensor's impulse response, yielded an output with the high frequency 7.5 KHz "noise" component lying outside the designed 5KHz bandwidth, highly attenuated, as shown in figure 5.22

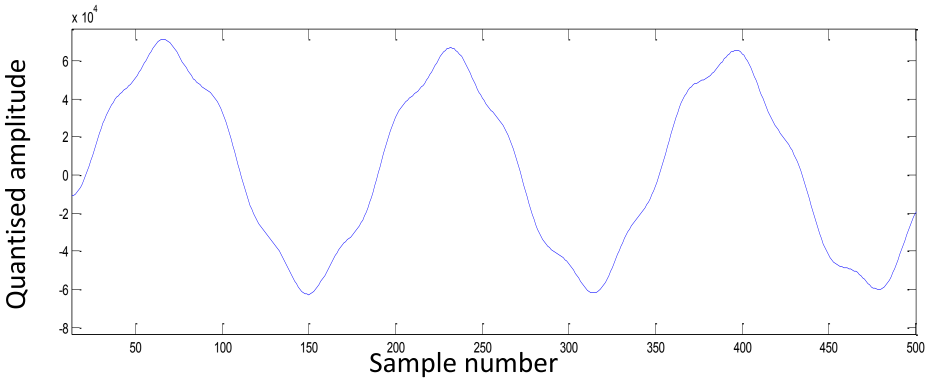

**Figure 5.22** Evaluated output by convolution of high frequency input and Impulse response

The results depicted in figure 5.22 provided further experimental proof of the validity of the impulse response acquisition and dynamic modelling of the HPAGS sensor via the direct impulse excitation of the MEMS' self test pin.

### *5.5.2 Conclusion*

The recovery of the mechanical acceleration stimulus was shown possible via the electrostatic excitation of the inertial mass via the self test pin on the MEMS sensor.

The input acceleration data obtained by the de-convolution of the experimental HPAGS sensor impulse response from the digitised output, resulted in near identical data to the digitised output, thus strongly supporting of the original design claim of the sensor's minimal distortion to in-band signals. In addition, out of band interference signals were also shown to be successfully attenuated as a result of their direct convolution with the experimentally derived impulse response, providing further evidence of the validity of the impulse response derivation method onboard the HPAGS sensor.

The ability to acquire in-situ, direct dynamic characteristics of the sensor, was shown to provide good means of on-demand system response evaluation, and therefore long term output data correction as required.

## 5.6 HPAGS gain error correction assessment

Drifts in the front-end electronics due to environmental factors and due to the ageing of components can impact the accuracy of the sensor in terms of offset but also in terms of gain. Whilst the offset was shown to be significantly rectified via the use of the auto-zero bias correction mechanism, gain drift would require physical component alteration for its correction, or direct measurement and post digitisation scaling of the data.

The gain correction circuit onboard the HPAGS sensor provided for the direct measurement of each channel's gain and therefore enabled the correction of any such drifts in the front-end electronics.

### *5.6.1 Results*

With reference to Figure 4.2, the gain correction methodology was based around a direct comparison principle, which although not perfect, it was believed to offer an excellent accuracy to circuit complexity ratio.

By switching the input MUX (U14) such that the input to the front-end electronics was provided by the 2V reference instead of the MEMS accelerometer, and with the DAC (U15) output set to zero; the output of the HPAGS sensor channel $V_o$ attained a value of 6.53V

The through-channel voltage output can be described as:

$$V_o = \left(V_{Ref} + V_{ios1}\right)A + V_{ios2} \qquad (5.25\ )$$

Therefore gain:

$$A = \frac{V_o - V_{ios2}}{\left(V_{Ref} + V_{ios1}\right)} \qquad (\ 5.26)$$

Where A is the channel gain, $V_o$ is the channel output, $V_{Ref}$ is the voltage reference voltage, $V_{ios1}$ is the input voltage offset of the instrumentation amplifier (U3), and $V_{ios2}$ is the input voltage offset of the filter section (U2:A and U2:B).

Subsequent switching of the output MUX (U16) such that the HPAGS sensor output was directly coupled to the 2V reference indicated an actual reference voltage $V_{Ref}$ of 1.96V.

Quantification of the input offset parameters of the amplifier stages, as specified by the manufacturers:

$$V_{ios2} = 240\mu V \max \; (20\mu V \; typ)$$

$$V_{ios1} = 25\mu V \; max$$

confirmed a *maximum* gain measurement error of 0.005%, and a *typical* error of only 0.0015%; a gain accuracy improvement of 20 to 67 times respectively.

Substitution of the typical values in equation 5.26 indicated a gain of 3.33 rather than the 3.35 expected by design.

A comparison of acceleration trends obtained with and without the HPAGS sensor's gain correction circuit utilisation is shown in figure 5.23 as a *difference* in data amplitude, representative of the gain output error.

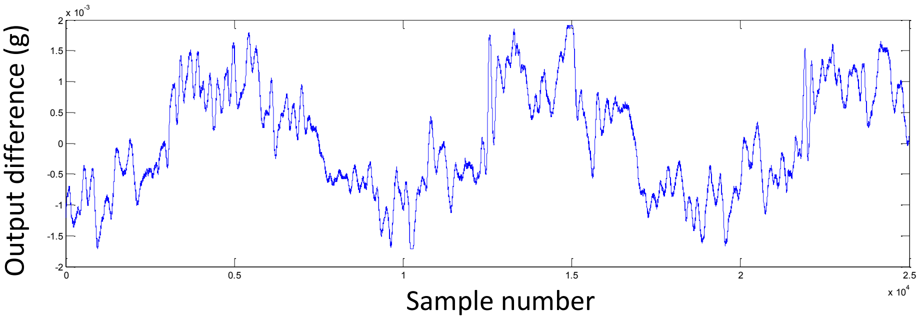

**Figure 5.23** Output difference between expected and gain-corrected trends

### *5.6.2 Conclusion*

It was shown that the gain correction circuit employed by the HPAGS sensor aided to significantly reduce the errors resulting from component drifts in the front-end electronics.

The ability of the circuit to provide gain correction functionality on-demand and in situ allowed for the reduction of gain errors in acquired data without the improbable requirement of long term stability of components. The great benefit behind this correction methodology designed in the HPAGS sensor, is the acquisition of correctly dimensioned output data, as gain errors directly affect the sensitivity and therefore the accuracy of the instrument.

The inclusion of the gain correction circuit on the HPAGS sensor was deemed to provide exceptional gain correction and a superior benefit to data accuracy by comparison to the increased complexity and cost of the overall instrument.

## 5.7 HPAGS Cross-axis sensitivity correction assessment

The cross-axis sensitivity assessment, conducted in section 3.1.3, and subsequent correction formulae, were experimentally and thoroughly proven in a sample-by-sample steady state fashion. An experimental re-assessment utilising the mechanical vibration platform allowed for the application of the correction formulae to dynamic and more realistic data sets.

### *5.7.1 Results*

After auto-zeroing, with the HPAGS sensor mounted on the vibration platform, as in the previous experiments (figure 5.6), with the x-axis oriented in the vertical plane and the y-axis in the horizontal plane; a horizontal "disturbance" was induced by means of mechanical displacement of the whole vibration platform along the y-axis. This y-axis induced disturbance, along with the affected x-axis' vertical sinusoidal cycle were digitised for analysis. Sections of the x and y-axis acceleration outputs of the HPAGS sensor, focussing on the disturbance event, are shown in the figures 5.24 and 5.25 respectively.

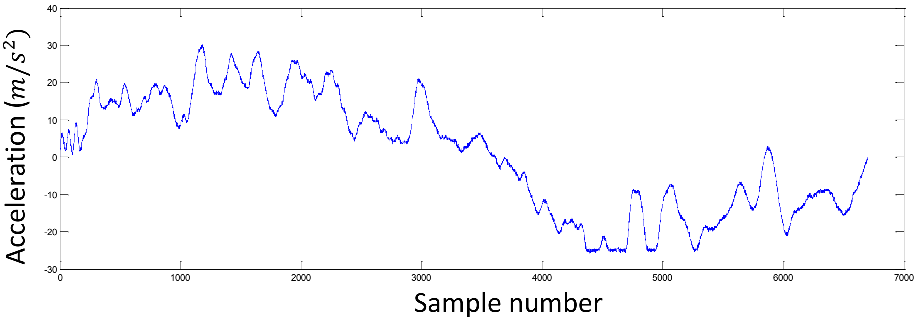

**Figure 5.24** Acceleration trend of x-axis output

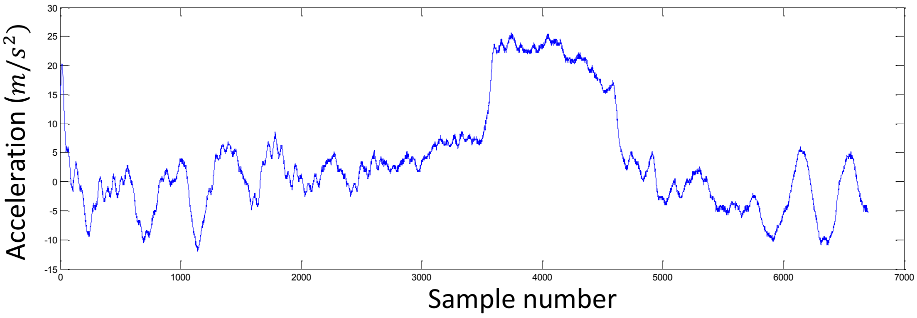

**Figure 5.25** Acceleration trend of y-axis output

The single x-axis acceleration cycle affected by the horizontal disturbance is shown in figure 5.24, corresponding to a vertical motion of the HPAGS sensor from the lowest to the highest point of oscillation.

Figure 5.26 depicts the x-axis, x-axis cross-axis sensitivity corrected, and the y-axis data trends.

The general correction equations 3.27 and 3.28 were rearranged for use with the discrete x and y-axis acceleration data, with all z-axis terms excluded, as follows:

$$A_y[n] = \frac{-X(C_{xy}) + Y}{1 - C_{yx}C_{xy}} \tag{5.27}$$

$$A_x[n] = \frac{A_y[n](-C_{yx}) + X}{1} \tag{5.28}$$

where $X = \left(\frac{x_o}{S_x}\right)$, and $Y = \left(\frac{y_o}{S_y}\right)$, since both channels were auto-zeroed and therefore the term $V_{0gx}$was deemed to be zero. Also, the cross-axis sensitivities were set to $C_{yx} = C_{xy} = 0.02$; the channel sensitivities $S_x = S_y = 0.405$ V/g; and the channel gains were set to 3.33, based on values derived experimentally. The Matlab script for the cross-axis sensitivity and gain correction of the x and y channels is included in Appendix C.

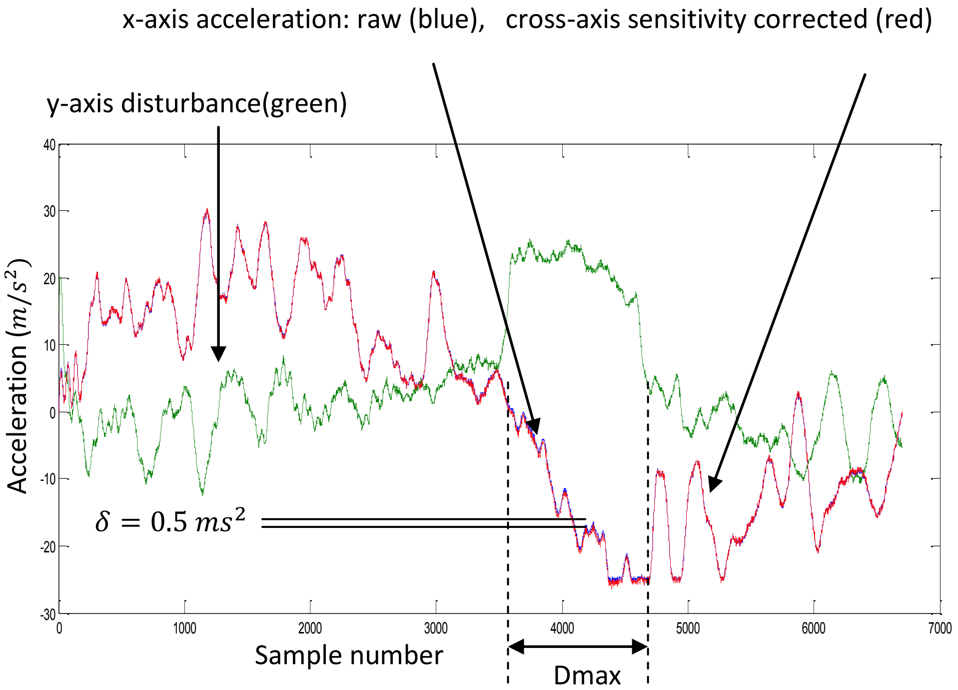

**Figure 5.26** Comparison between x-axis raw, cross-axis corrected, and y-axis data

The *Dmax* region in figure 5.26 denotes a region of greatest difference between the raw x-axis acceleration in blue, and the cross-axis sensitivity corrected acceleration in red, as indicated by the subtle visibility of the blue trend just above the red, otherwise nearly coincident and therefore invisible outside this region. This segment of maximum deviation coincided with the peak y-axis disturbance, as dictated by the correction formulae of section 3.1.3, which were based on the already proven steady-state experimental results.

### *5.7.2 Conclusion*

The maximum difference of $0.5\, ms^2$ between the cross-axis corrected and the uncorrected x-axis acceleration data observed in figure 5.28, poses little threat to the accuracy of accelerograms as presented in this experiment under laboratory controlled conditions. However, had this error been due to a more realistic, non-uniform excitation, or a due to a permanent event-induced tilt, it could have been the cause of a significant baseline error of up to 0.9m over a standard seismograph event-recording period of 60 seconds. Figure 5.27 graphically depicts the displacement error of the data segment examined.

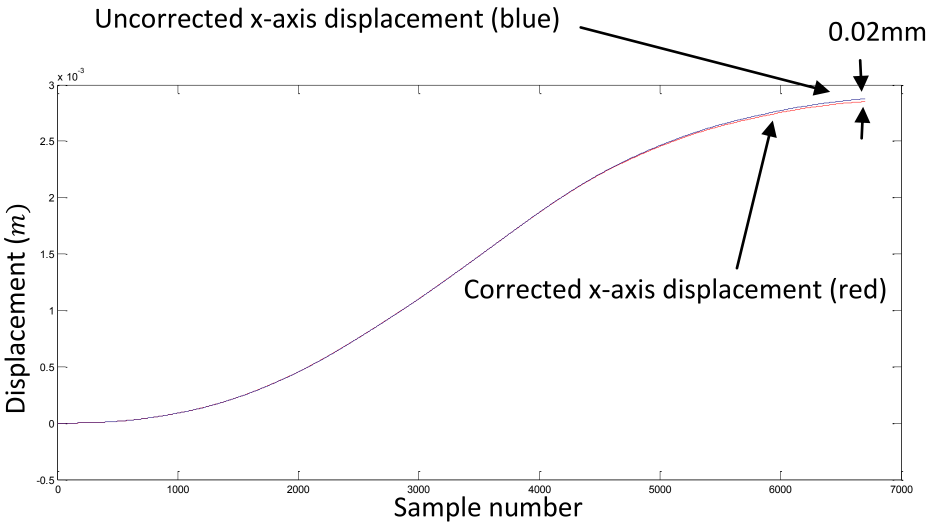

**Figure 5.27** x-axis displacement data; uncorrected, and cross-axis corrected.

The general cross-axis sensitivity correction formulae derived in section 3.1.3, were therefore shown to provide essential correction to realistic dynamic data derived from the HPAGS sensor, and thus able to minimise baseline offset errors due to cross-axial coupling effects on seismic data trends.

## 5.8 HPAGS Gyro stabilisation module assessment

The restrictions imposed on experimentation with the intended mercury liquid drives, inevitably lead to the use of DC motors for the gyro stabilisation module and therefore the injection of vibration noise into the HPAGS signal. Due to small asymmetries within the DC motors inescapable by construction, some vibration noise will always be present in any platform utilising them for actuation.

### *5.8.1 Static evaluation of gyro motor noise*

Before any experimentation could be conducted, an accurate evaluation of the noise interference the gyro motors induced to the sensor's outputs was conducted.

Activation of the vertical gyros, on the otherwise stationary HPAGS sensor platform, showed excessive high frequency vibration noise content in its outputs as shown in figure 5.28 below.

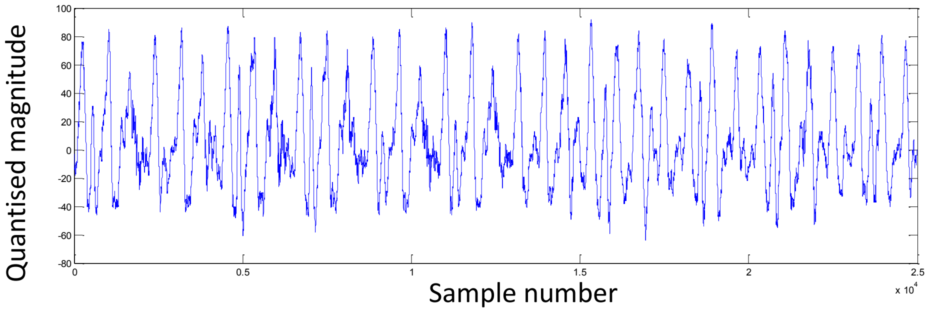

**Figure 5.28** HPAGS x-axis output with vertical gyros on.

While every attempt was made during the design phase to restrict the loading on the motors in order to achieve high speed operation, this method of forcing vibration noise outside the 100Hz bandwidth of interest was inevitably at the expense of maximum angular momentum attained.

Frequency analysis of the resulting noisy signal output of the sensor revealed a spectrum with peaks at 175Hz and higher, as depicted in figure 5.29.

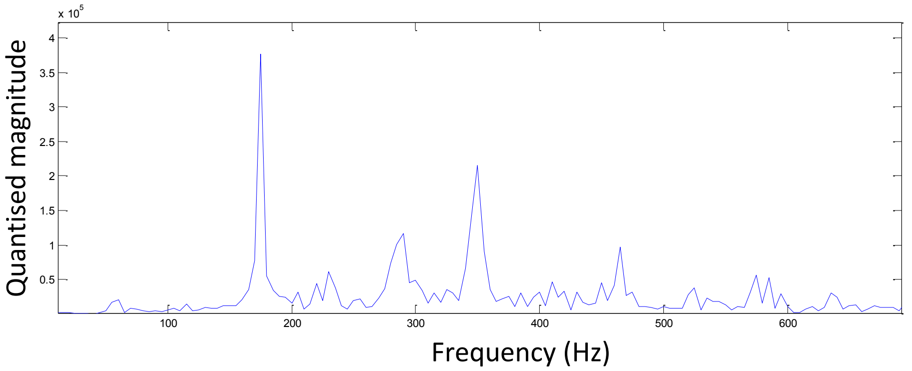

**Figure 5.29** Frequency spectrum of the HPAGS x-axis output with vertical gyros on.

With the 100Hz bandwidth mainly unaffected by the gyro motor noise, as intended by design, the rather high amplitude noise residing just outside the pass-band required the re-design of the original FIR low-pass filter used this far, in order to adequately attenuate this higher in magnitude noise. The effectiveness of this higher order FIR filter is shown in figure 5.30, where the original unfiltered signal spectrum is compared with the spectrum of the signal post-filtering.

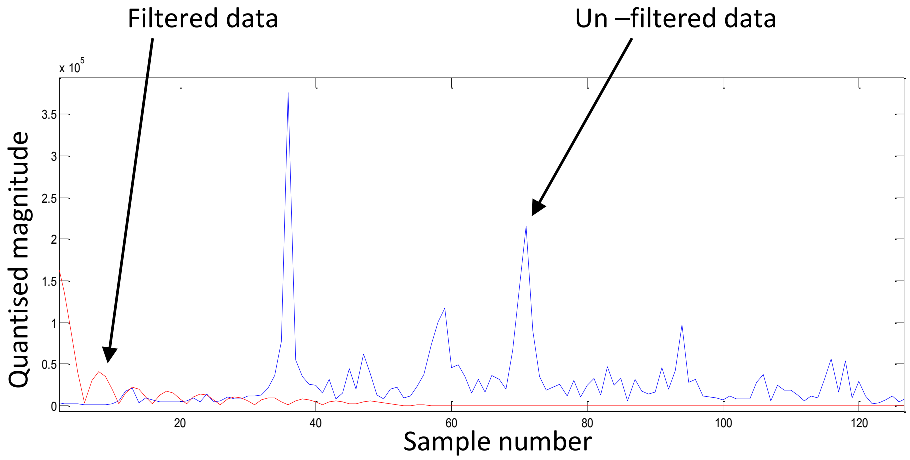

**Figure 5.30** Spectrum comparison between unfiltered (blue) and filtered sensor outputs (red).

It can be seen from the results depicted in figure 5.30 that the motor-induced noise was satisfactorily attenuated by the higher order FIR filter, allowing the extraction of the signal of interest.

### *5.8.2 HPAGS active gyro correction assessment*

As detailed earlier, the unavoidable use of DC gyro motors, and the need to force the inevitable vibration noise to high frequencies outside the 100HZ bandwidth, resulted in lower angular momentum produced by the gyros, rendering the gimballed platform incapable of very long term gyro stabilisation. While the platform responded exceptionally well to angular accelerations on all three axes, it was not able to retain a long term fixed celestial orientation. This unavoidable consequence also impacted on the platform's ability to auto-align with true north by precession.

Although the obligatory use of DC motors for the actuation of the gyros did not entirely fulfil the long term requirements of the HPAGS sensor, it still enabled the provision of proof of concept in support of gyro-stabilisation of seismic sensors via alternative low-vibration technologies, such as the mercury liquid drive discussed earlier in this work.

With all the correction circuits, algorithms, and formulae employed by the HPAGS sensor sufficiently proven throughout this work, an in-depth assessment of the corrective action of the active gyro stabilised platform on seismic data acquisition was conducted. This assessment necessitated a more involved experimental setup allowing for a complex but predictable motion. A Computer Numerical Control (CNC) machine, with its cutting tools disabled, was used for the provision of accurate two dimensional displacement.

Figure 5.31 shows the HPAGS sensor platform on the CNC machine bed with power, computer control, and signal cables attached.

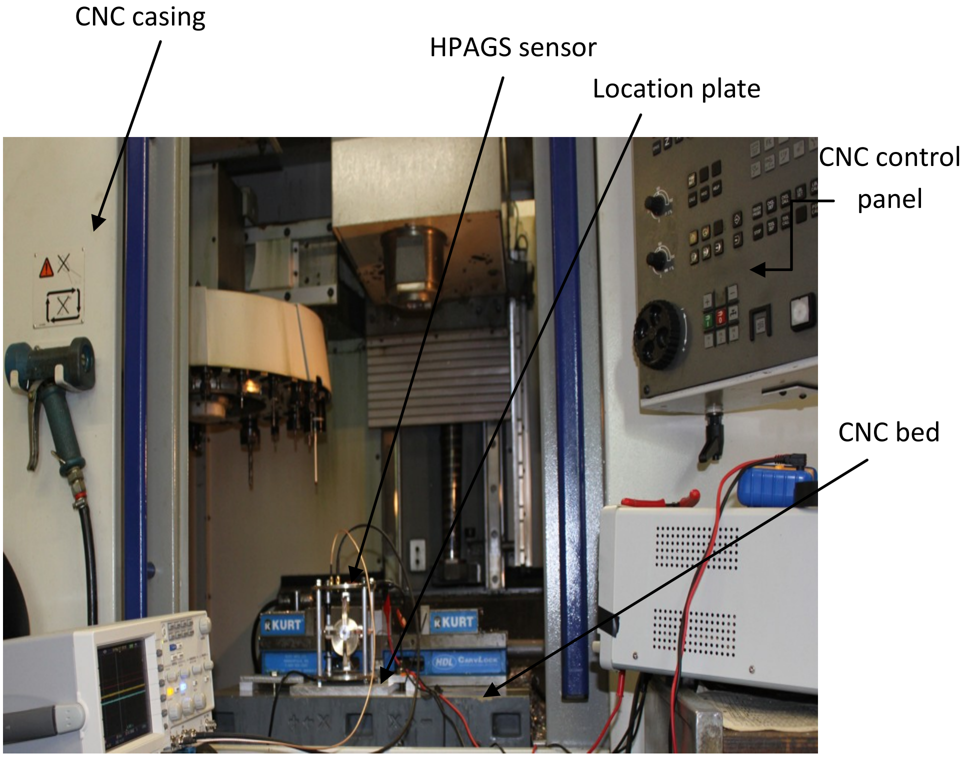

**Figure 5.31** The HPAGS sensor attached onto the CNC machine

In order to also induce rotation, a flat metal plate with a location hole was machined allowing the HPAGS sensor to both pivot and slide. The location metal plate, with a single locating hole, was securely fixed to on a CNC Mikron C500 machine bed, capable of precision two dimensional linear motion. The HPAGS sensor was placed onto the metal plate and pivoted off-centre via the insertion of a metal pin through the sensor's body and into the locating hole of the metal plate below. A non-elastic tether, attached to the opposite end of the sensor's body, allowed for its tethering to a fixed non-movable datum, thus enabling the generation of a complex linear and simultaneous rotational motion.

A detailed view of the HPAGS sensor's attachment to the CNC machine's movable bed is depicted in figure 5.32 below.

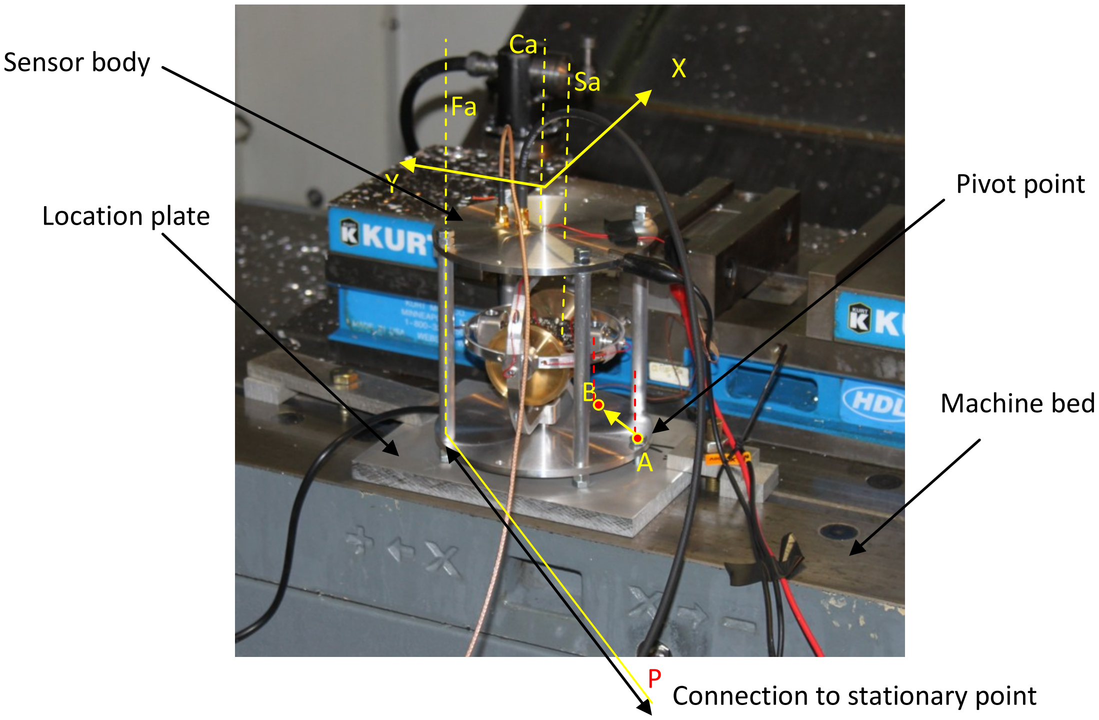

**Figure 5.32** HPAGS sensor attachment to the CNC bed detail

The sensor's body was connected via a steel pin which located into a receiving hole on the location plate beneath, thus creating a pivot point at point A. The location plate in turn was securely fastened to the CNC machine's bed. A tethering point on the base of the sensor's body, perpendicular to the Fa axis, allowed for a connection to a fixed datum point P on the casing of the machine (tether not shown in figure 5.32).

While the sensor electronics were concentric with the mechanical rotational centre of the gimballed assembly along axis Ca, the MEMS accelerometer itself resided offset from this axis on the PCB as indicated by the location axis Sa, having its sensing axis as indicated by the x and y arrows in figure 5.32. It should be noted for clarity that the CNC machine's x-axis was coincident with the HPAGS sensor's y-axis, and similarly, the machine's y-axis was coincident with the sensor's x-axis.

The CNC machine was programmed to move the bed in a 45° diagonal motion, thus forcing the pivoting pin, and the sensor body, to move 10mm in both x and y direction, from position A to position B at a maximum speed determined by the machine's control system. The tethering connected to the sensor's body, as indicated by the intersection of location axis Fa and the sensor's base, opposed this linear movement, thus causing a rotation of the HPAGS sensor about the pivot point.

It is important to consider, that although the pivot point was the point of rotation between the locating plate and the HPAGS sensor, this was not the inertial centre of rotation of the HPAGS sensor with respect to the fixed reference plane containing point P.

In order to exemplify the complex motion of the sensor and the attitude of the sensing axes within the gimballed mechanical arrangement, a top view diagram of the HPAGS sensor is depicted in figure 5.33 at the initial position A. The points of importance correspond to those of figure 5.32, with Ca denoting the body centre of the sensor and electronics, Fa denoting the tethering point, and Sa the MEMS sensor's centre on the PCB. The direction of MEMS sensing axes is shown by the x and y arrows respectively.

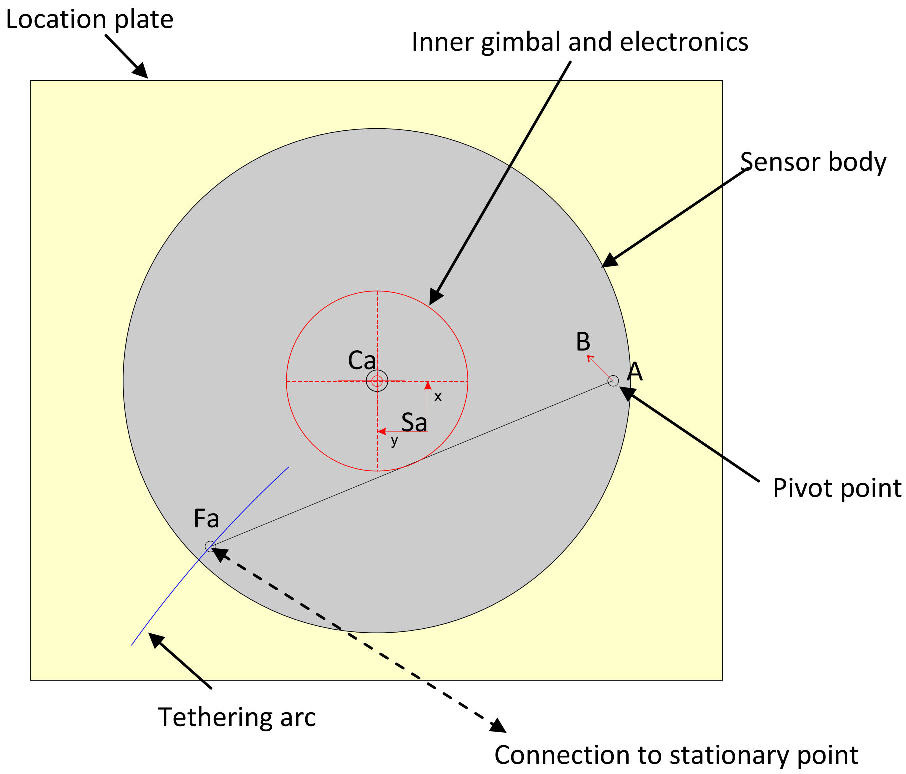

**Figure 5.33** HPAGS sensor on CNC bed top view diagram

It is important to envisage that as the bed, and the location plate, move from point A to B, the pivot point on the HPAGS sensor's body is forced to coincide with this linear motion, however, the tethering point Fa is restricted in distance by the fixed reference point and is therefore free to only describe a motion along a tethering arc, as indicated in figure 5.33. The combined effect of the bed's diagonal motion and the enforcement of the tethering arc on point Fa, would yield a non sensor-centric rotational motion.

### *5.8.3 Results*

In order to confirm the validity of acquired data prior to engaging in complex rotational and translational measurements, the HPAGS sensor was initially firmly clamped to the machine's bed with its gimbals locked, and the sensor and machine axes aligned, in the x-to-y corresponding configuration as mentioned earlier.

In this configuration, the sensor was forced to follow the bed's x-y motion without any rotations introduced, thus enabling the acquisition of reference acceleration, velocity, and displacement data, used to verify the accuracy and calibration of the instrument before proceeding to the more complex experimental stages.

The acceleration data for the x and y instrument axes is shown in figure 5.34

.

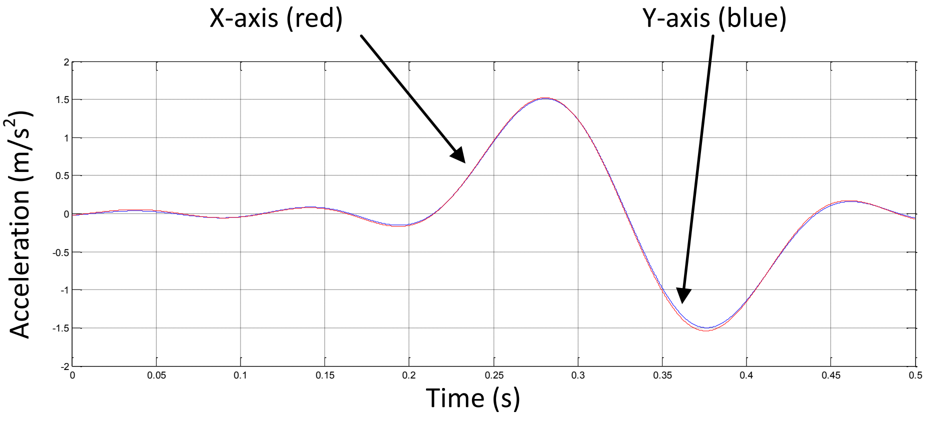

**Figure 5.34** HPAGS x and y-axis acceleration data of machine bed

As it was hoped, both channels exhibited near-identical acceleration trends, which in turn corresponded to similarly-performing velocity and displacement data, as depicted in figures 5.35 and 5.36 respectively.

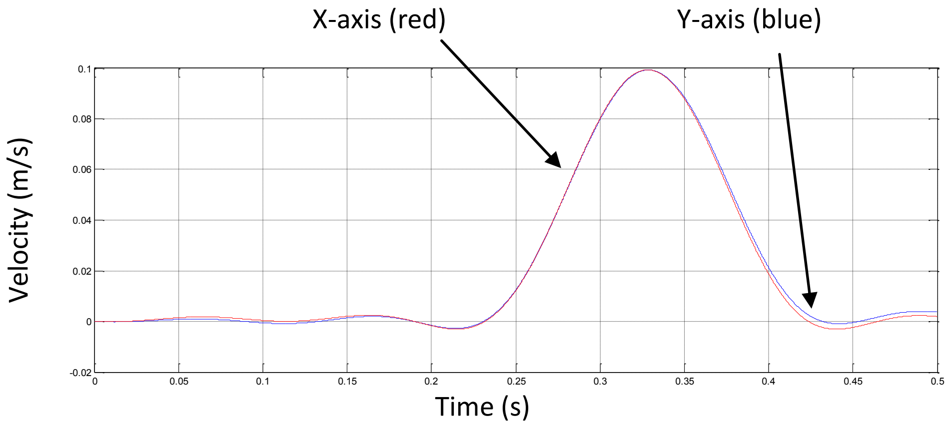

**Figure 5.35** HPAGS x and y-axis velocity data of machine bed

It should be noted that the total displacement attained by the sensor and therefore the bed from the experimental results of figure 5.36, match the programmed 10mm displacement of the CNC machine.

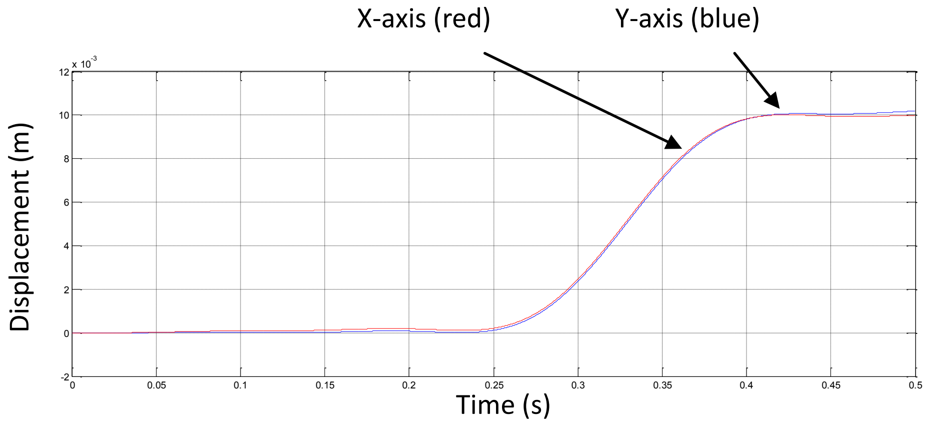

**Figure 5.36** HPAGS x and y-axis displacement data of machine bed

Following the very satisfactory results obtained by the machine-bed motion experiment, the HPAGS sensor was placed on the location plate and secure only via the locating metal pin, and tethered to the fixed point, as in figure 5.32, allowing it to rotate and translate accordingly. In order to compare conventional rigid sensor performance with that of the gyro stabilised HPAGS platform, experiments were conducted with all the gimbal brakes on, thus emulating conventional rigid sensor behaviour, and then repeated in gyro-stabilised enabled mode, with the gimbal brakes off and gyros active.

During all the gyro evaluation experiments that focused solely on the ability of the HPAGS sensor to provide superior translation data when exposed to concurrent rotational motion in comparison to conventional rigid sensors, the sensor's auto-zero bias, gain, and sensitivity correction systems and algorithms were enabled.

The x and y-axis acceleration data of the HPAGS sensor, having undergone an A to B motion in rigid mode (all brakes locked) is shown in figure 5.37.

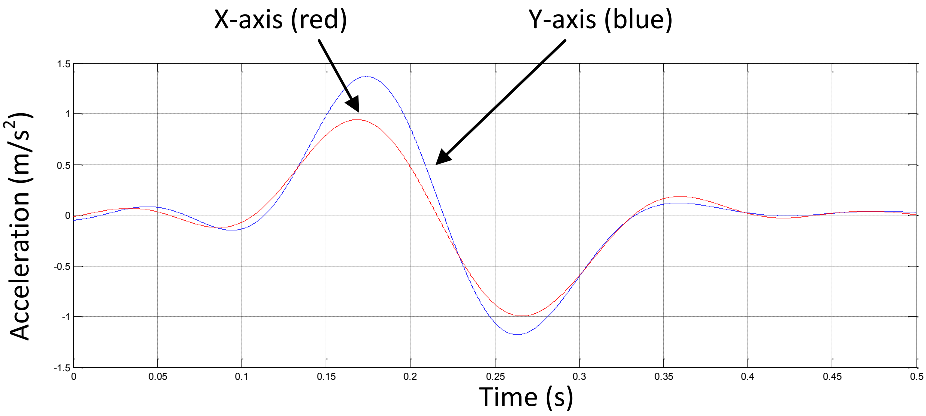

**Figure 5.37** HPAGS x and y-axis acceleration data in rigid mode.

Unlike the coincident x and y-axes acceleration trends acquired by measuring the linear motion of the machine bed, shown in figure 5.34, the results obtained by the complex rotational and translational motion, shown in figure 5.37, indicated lower acceleration values in the x-axis, by comparison to those in the y-axis. This of course yielded corresponding results in the velocity and displacement data, as depicted in figures 5.38 and 5.39 respectively.

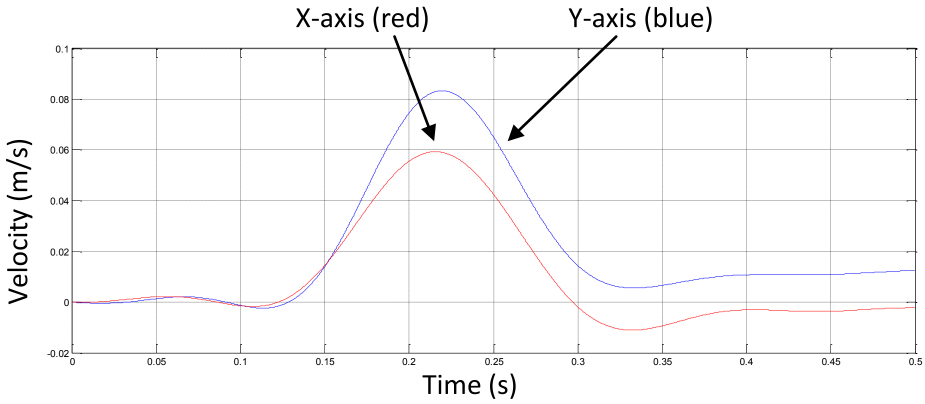

**Figure 5.38** HPAGS x and y-axis velocity data in rigid mode.

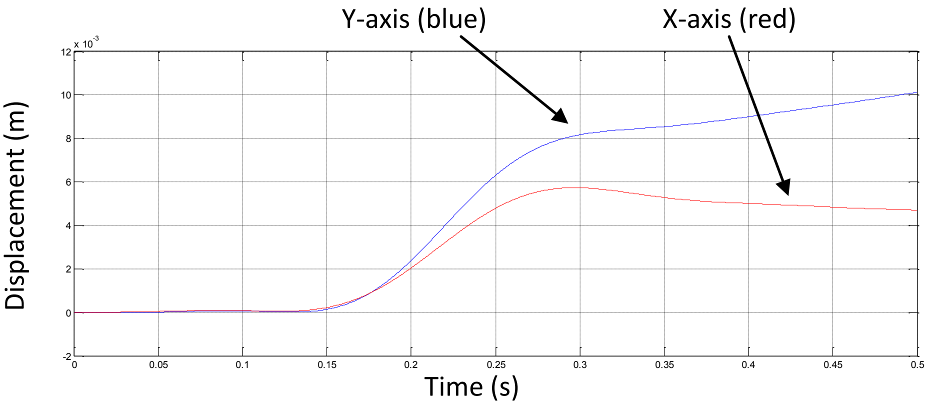

**Figure 5.39** HPAGS x and y-axis displacement data in rigid mode.

The motion in rigid mode is depicted diagrammatically in figure 5.40, with the sensor's initial position indicated by a black outline and a red sensor centre, and its final position all in blue.

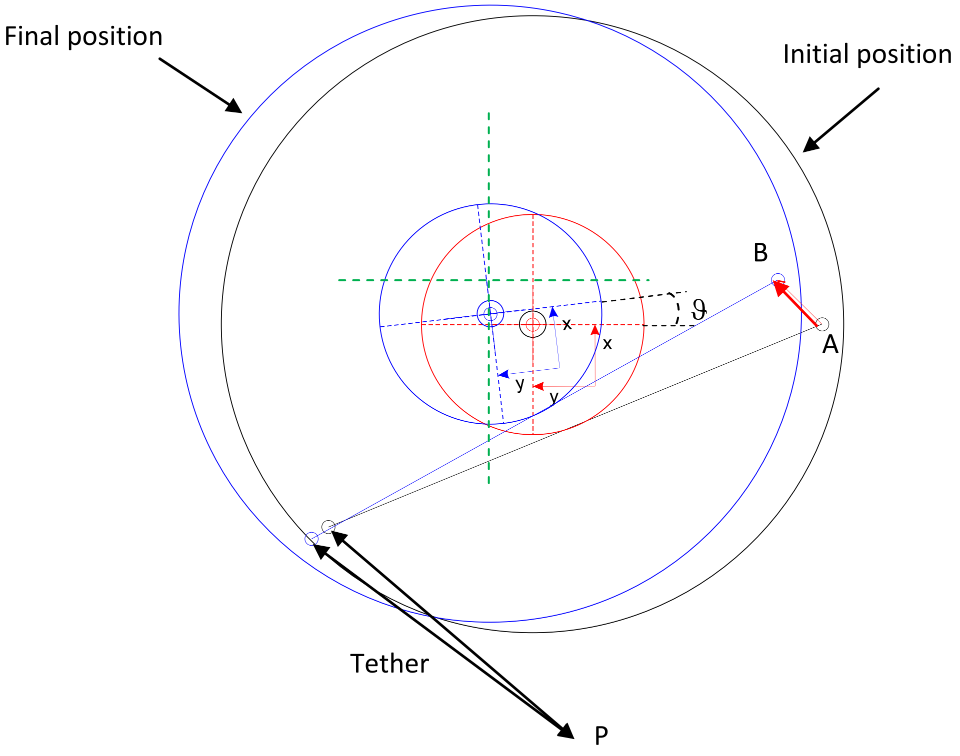

**Figure 5.40** HPAGS motion in rigid mode.

The green dashed cross indicates the position and orientation attained should the sensor was rigidly mounted on the machine bed. The difference in distance between the x-axis final position, marked in blue, and the green cross reference is markedly larger than that of the y-axis final position, indicating a shorter distance travelled, albeit in an arc of angle $\vartheta$, by the x-axis. This is in line with the experimental measurements depicted in figures 5.37 to 5.39, showing consistent lower acceleration, velocity and displacement values in the x-axis respectively. The angle $\vartheta$ measured on the graphical simulation model of figure 5.40, corresponded exactly to the angle of rotation measured on the location plate during the experiment, confirming the accuracy of the model. The results obtained are representative of a typical rigid instrument, albeit one of improved correction and sampling performance.

In order to compare these typical results to those of the HPAGS sensor in active gyro mode, the machine bed was returned to its original starting position and the experiment was repeated with the sensor's brakes off and the vertical gyros on. The resulting x and y-axis acceleration trends are shown in figure 5.41 below

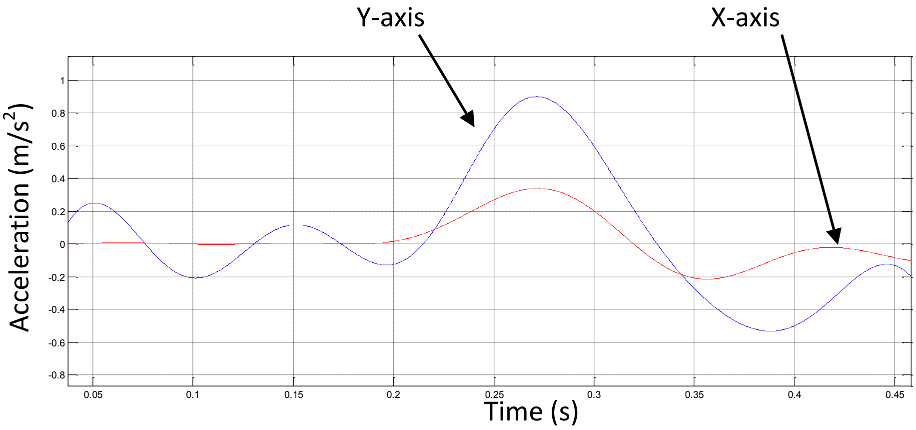

**Figure 5.41** HPAGS x and y-axis acceleration data in gyro mode.

A more substantial decline in the x-axis acceleration was noted, which was inevitably mirrored in the velocity, and the displacement trends, as shown in figures 5.42 and 5.43 respectively. Examination of the diagrammatic simulation of the sensor's motion while in gyro mode, shown in figure 5.44, confirmed that due to the gyro assisted alignment of the central sensing gimbal, the x-axis did indeed travel a much shorter distance in the x direction. Further, direct measurements on the model revealed near-identical end displacement values to those experimentally derived in gyro mode, shown in figure 5.43.

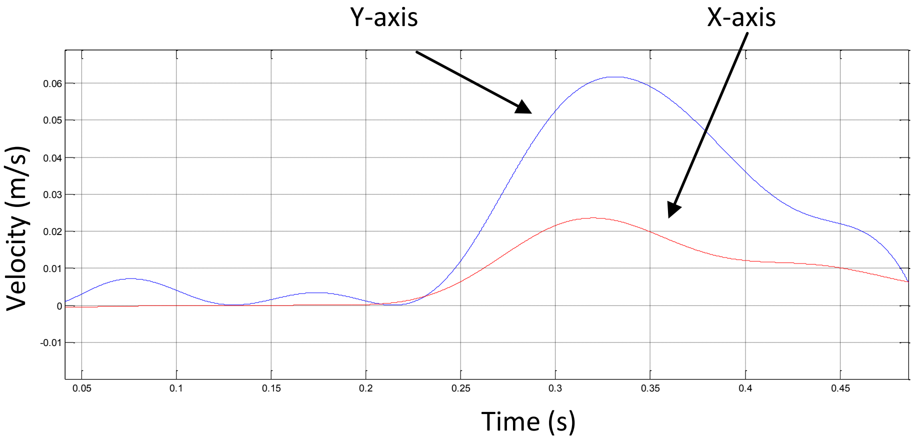

**Figure 5.42** HPAGS x and y-axis velocity data in gyro mode.

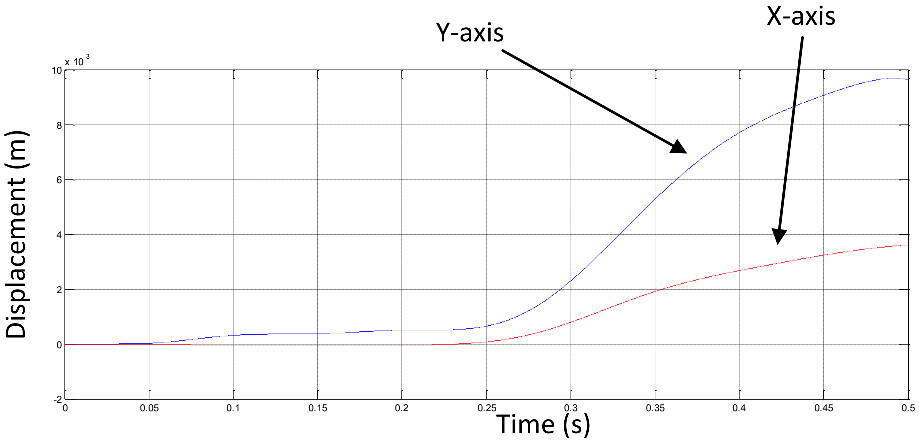

**Figure 5.43** HPAGS x and y-axis displacement data in gyro mode.

In the model of figure 5.44, which accurately describes the HPAGS sensor's motion, it can be observed that although the sensor body underwent the exact same change in attitude and location as that of the rigid mode experiment, the central gyroscopically aligned gimbal and sensor electronics, indicated by the blue x and y-axis, remained parallel to their initial orientation. This preservation of axial alignment allowed the complete de-coupling of the rotational motion imposed on the sensor body, thus allowing the acquisition of pure linear displacement with exceptional accuracy.

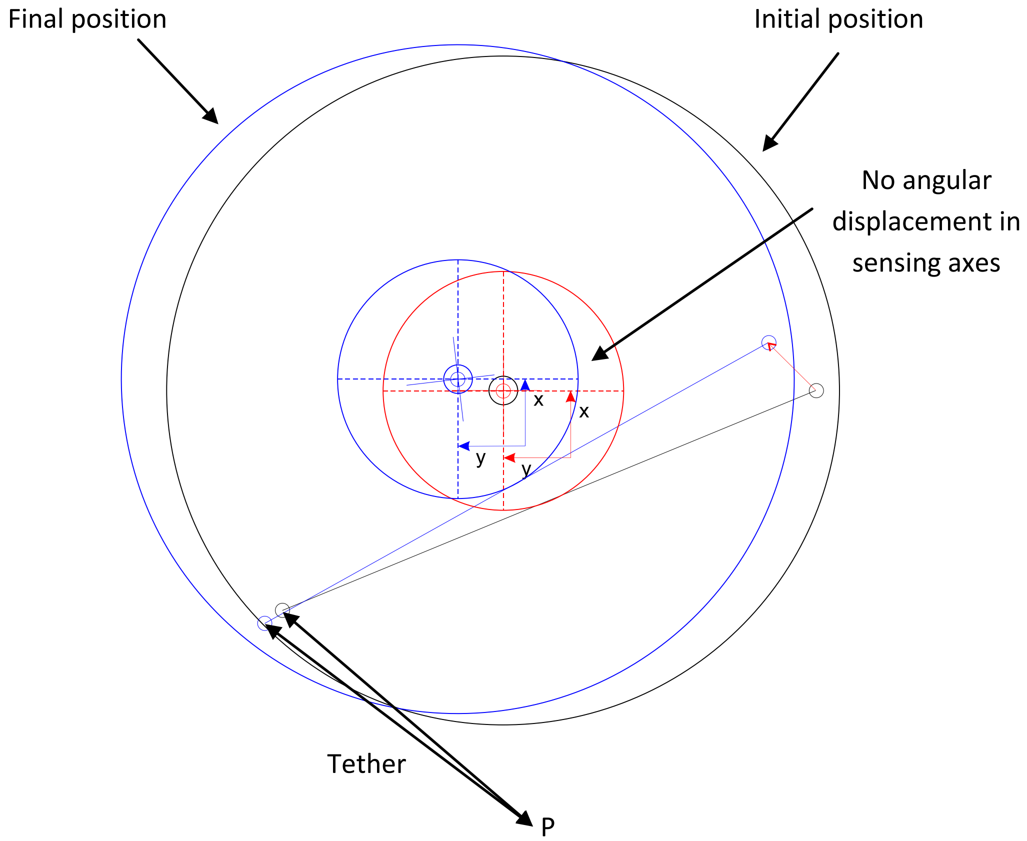

**Figure 5.44** HPAGS sensor's motion in gyro mode.

Exemplification of the performance attained by the gyro stabilisation can be graphically reviewed by direct comparison between gyro mode and rigid mode operation, with reference to actual displacement data, as shown in figure 5.45 below.

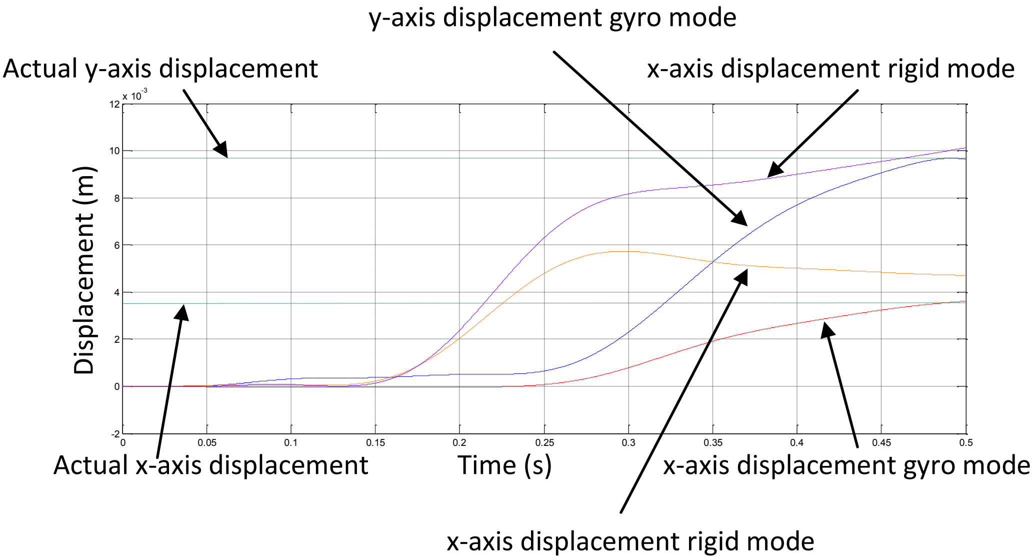

**Figure 5.45** HPAGS sensor's displacement comparison between gyro and rigid modes.

### *5.8.4 Conclusion*

The effectiveness of the HPAGS active gyro stabilised electromechanical module was experimentally tested and was shown to be able to effectively acquire true linear motion even when exposed to complex realistic motions containing linear and rotational accelerations. The inevitable gyro motor noise was efficiently removed by the higher order FIR low-pass filter, allowing for the acquisition of much improved linear acceleration trends and the subsequent derivation of more accurate velocity trends representative of the true motion along the original orthogonal axes of reference.

The resulting displacement trends in figure 5.45, also demonstrated the difference between the conventional rigid, and the HPAGS active gyro-enabled instrument's performance, clearly exemplifying the advantage of the gyro module's ability to maintain the sensor's original attitude, and therefore its capability to directly acquire true to the reference axes data, by successfully de-coupling the linear from the rotational accelerations.

# Chapter 6

## Conclusion

The difficulty of acquiring precise seismic data was discussed in chapter 1, identifying the underlying cause as one of reference, due to the problem that a clear separation of the observer from the phenomenon observed cannot be readily accomplished, since the observer is directly connected to the object of interest; the Earth.

The almost total dependency on inertial instruments for seismic recording and observation has given rise to one most prominent observable effect of data corruption in the time domain, regardless of instrument; the “runaway effect” or “Baseline Error”. This error results in erroneous linear, and exponential ground displacement offsets in numerically derived velocities and displacements respectively, invalidating the accuracy of these derived trends, as assumptions to their nature are made in order to secure an artificial baseline of zero offset error.

Various methods and advanced calibration techniques have been widely employed in an attempt to reconstruct a true seismic velocity and displacement trends, as the runaway, and other related phenomena, have been the focus of much research. Although modern seismographs have considerably improved over that last decade, displacement data derived from these still exhibits baseline errors, on occasion in the order of several meters.

The extensive work conducted over the years in the development of correction algorithms, filtering, and system models to address some of the problems associated with this type of data acquisition, was shown to be one of “smoothing” the effects rather one of curing the problems, and therefore unable to produce consistent long term results in the complexity of real environments.

The objective of this work therefore was to research the multiple sources of error, internal to the instrument and external, and derive realisable solutions with the aim to create the High Precision Active Gyro-Stabilised (HPAGS) seismic sensor, capable of the acquisition of highly accurate seismic data in realistic and complex environments. In order to achieve this, original theory, novel methods, and algorithms concerned with the correction or minimization of errors in current seismic sensing instruments were developed and experimentally tested.

Methods for the derivation of the dynamic response of MEMS sensors, direct generation of sensor signal dithering, quality preservation sampling criteria methodologies, and cross-axis sensitivity correction formulae, were developed and practically and methodically evaluated resulting in the development of the first six degree of freedom seismic sensor unit. The HPAGS sensor was found in concept capable of addressing the majority of the known issues, by additionally introducing novel correction circuits for auto-zero bias and auto-gain correction, along with their corresponding embedded algorithms.

The methodical investigation of errors and their novel potential solutions was detailed in chapter 3. The experimental evaluation of sensor noise in this chapter showed an exponential increase of noise with increase in ambient temperature, and a characteristic 1/f frequency response. Further, a peak was evident at the internal clock frequency, albeit outside the bandwidth of interest. Noise coupling from the power supply to the sensor was also shown to produce a significant detrimental effect on the sensor signal, and on the accuracy of the acceleration measurements.

It was also shown that specific actuation of the sensor’s self test pin, intended only for binary verification of operation by the manufacturer, successfully yielded frequency and dynamic sensor response characteristics, and was therefore successfully used in the resulting instrument..

Detailed experimental investigation into the sensor’s linearity demonstrated substantial evidence to support that cross-axis interference was the chief source of non-linearity in MEMS sensors and mathematical correction formulae were derived for the correction of this effect, enabling the reconstruction of true acceleration data trends from sensor measurements acquired in a real three dimensional environment.

Consideration of a complex motion containing both linear and rotational components, even in two dimensions, very quickly indicated that since a rotational motion can generate parasitic linear motion artefacts, as discussed in the introduction of this work, distinction between true linear and linear artefacts caused by rotations was impossible. It was also shown that attempts via the addition of multiple sensors and rotational sensors such as MEMS gyros, would be of limited use as a correction methodology, due to several physical limitations, leading to the design of gyro stabilised HPAGS sensor solution.

An analysis of the requirements and challenges presented by modern seismological instruments revealed that simply relying on best components and practices in order to achieve high resolution and long term stable measurements was indeed of limited use, even though instrument calibration could help to temporarily minimise some of these errors. Other environmental factors were also considered in this work, such as asymmetrical ground motion. Since soil is a non-uniform mixture, seismic waves propagating from sandy to rocky soil, would experience a change in shape amongst other artefacts such as reflections, inevitably introducing in some cases a non-linearity in the form of mechanical hysteresis to the seismic data, further supporting the need for a sensor able to de-couple translational from rotational motion.

With the utilisation of the primary MEMS circuit and the precision sinusoidal vibration platform, it was confirmed early on in this work that the direct use of a MEMS acceleration sensor for the measurement of seismic data, with or without primary filtering, inevitably resulted in erroneous velocity and displacement data after the necessary double numerical integration. The detailed aforementioned examination of the sensor itself identified numerous sources of error able to corrupt the seismic signal within the MEMS IC. Further, sensor limitations were investigated, such as the effects of temperature fluctuations on sensitivity and zero-g bias voltage. It was shown that the zero-g bias was quite susceptible to variations in temperature in a non-linear fashion and in different polarities between channels, making its removal by calibration rather inefficient.

The specific and methodical evaluation of the correction methods developed was discussed in section 5. The results concluded that the new auto-zero bias correction algorithm and circuit employed by the HPAGS sensor was able to provide a dramatic improvement to the accuracy of displacement trends derived by the numerical integration of acceleration data, while the use of the self test pin provided effective corrections in the form of impulse response de-convolution of the instrument transfer function. Further, it was shown that the gain correction circuit employed by the HPAGS sensor, successfully aided the reduction of errors resulting from component drifts in the front-end electronics by typically a factor of 60 or more.

The general cross-axis sensitivity correction formulae derived were practically shown to provide essential correction to realistic dynamic data derived from the HPAGS sensor, and thus were able to minimise baseline offset errors due to cross-axial coupling effects on seismic data trends.

The realisation of the gyro stabilisation module necessitated the use of DC motors resulting in motor-induced noise onto the signal. This noise, resided in the higher frequency bands allowing its exclusion from the signal via digital filtering. Although the obligatory use of DC motors for the actuation of the gyros did not entirely fulfil the long term requirements of the HPAGS sensor, it still enabled the provision of proof of concept and a strong case in support of gyro-stabilisation of seismic sensors via alternative low-vibration technologies, such as the mercury liquid drive also briefly discussed in this work.

Finally, the effectiveness of the HPAGS active gyro stabilised electromechanical module was experimentally tested and was shown to be able to effectively acquire true linear motion even when exposed to complex realistic motions containing linear and rotational accelerations. The resulting data demonstrated the difference in performance between conventional current rigid instruments and the HPAGS active gyro-enabled sensor, clearly exemplifying the advantage of the gyro module’s ability to maintain the sensor’s original attitude, and therefore its capability to directly acquire true to the reference axes data.

In conclusion, the research, evaluation, design, implementation, and experimental work described herein, present a multitude of novel pragmatic solutions to the problem of accurate seismic data acquisition, successfully verified by theoretical, simulation, and empirical means, and a proof of concept benchmark seismic instrument.

# Chapter 7

## Future work

Although experimentally proven to provide a large improvement on the accuracy of acceleration derived displacement trends, the HPAGS sensor is not without areas that could significantly benefit from improvement.

The auto zero circuit and algorithm allowed for a small error in trend deviation mainly due to the noise content in the feedback signal. This correction circuit could benefit from the inclusion of active filtering and a bipolar feedback ADC in order to allow for signal averaging and therefore significant noise reduction.

Alternative means of actuation of the gyros would also be a necessity for any future instruments designed to take advantage of rotational and linear motion de-coupling, as the noise imposed by the gyro motors was found to be difficult to filter out without the degradation of the signal, chiefly due to their close proximity in frequency and the resulting poor signal to noise ratio.

Miniaturisation and hermetic encapsulation of the electronics would also appear to be the natural progression for this sensor, as it would enable the improvement of signal to noise ratio by the addition of thermoelectric cooling, much like the one employed in commercially available microbolometer sensors.

The addition of a GPS would also aid accurate instrument positioning and time-stamping of the data, thus enabling the evaluation of seismic data from HPAGS instrument clusters.

# References

[1] P. Bernard, J. F. Karczewski, M. Morand, B. Dole and B. Romanowicz, “The G-Calibration: A New Method for an Absolute In-Situ Calibration of Long-Period Accelerometers, Tested on the Streckeisen Instruments of the Geoscope Network,” *Bulletin of the Seismological Society of America,* vol. 81, no. 4, pp. 1360-1372, 1991.

[2] P. W. Rodgers, “A Note on the Nonlinear Response of the Pendulous Accelerometer,” *Bulletin of the Seismological Society of America,* vol. 65, no. 2, pp. 523-530, 1975.

[3] P. Reasenberg, “Non-Linearity Test on an Accelerometer System Designed for the Seismic Nera-field Measurement,” *Bulletin of the Seismological Society of America,* vol. 59, no. 3, pp. 1213-1225, 1969.

[4] E. Wielandt and G. Streckeisen, “The Leaf-Spring Seismometer: Design and Performance,” *Bulletin of the Seismological Society of America,* vol. 72, no. 6, pp. 2349-2367, 1982.

[5] G. A. McLennan, “An Exact Correction for Accelerometer Error in Dynamic Seismic Analysis,” *Bulletin of the Seismological Society of America,* vol. 59, no. 2, pp. 705-715, 1969.

[6] V. Graizer, “The response to Complex ground Motions of Seismometers with Galperin Sensor Configuration,” *Bulletin of the Seismological Society of America,* vol. 99, no. 2B, pp. 1366-1377, 2009.

[7] W. H. K. Lee, “A Glossary of Rotational Seismology,” *Bulletin of the Seismological Society of America,* vol. 99, no. 2B, pp. 1082-1090, 2009.

[8] P. A. Watt, “The Application of a D.C. Amplifier to Seismic Recording,” *Bulletin of the Seismological Society of America,* vol. 50, no. 3, pp. 471-476, 1960.

[9] H. K. Gupta and K. Hamada, “Rayleigh and Love Wave Dispersion up to 140 Second Period Range in the Indonesia-Philippine Region,” *Bulletin of the Seismological Society of America,* vol. 65, no. 2, pp. 507-521, 1975.

[10] S. C. Shen, C. J. Chen and H. J. Huang, “A New Calibartion Method for MEMS Inertial Sensor Module,” in *The 11th IEEE International Workshop on Advanced Motion Control*, Nagaoka, 2010.

[11] A. J. Williams, “A Solid State Tilt Meter for Current Meter Attitude Determination,” *IEEE,* 2004.

[12] W. T. Ang, S. Y. Khoo, P. K. Khosia and C. N. Riviere, “Physical Model of a MEMS Accelerometer for Low-g Motion Tracking Applications,” in *IEEE International Conference on Robotics and Automation*, New Orleans, 2004.

[13] H. L. Wong and M. D. Trifunac, “Effects of Cross-Axis Sensitivity and Misalignment on the Response of Mechanical-Optical Accelerographs,” *Bulletin of the Seismological Society of America,* vol. 67, no. 3, pp. 929-956, 1977.

[14] D. T. H. Lai, R. Begg, E. Charry and M. Palaniswami, “Frequency Analysis of Inertial Sensor Data for Measuring Toe Clearence,” *IEEE,* 2008.

[15] D. M. Boore, “Effect of Baseline Corrections on Displacements and Response Spectra for Several Recordings of the 1999 Chi-Chi, Taiwan, Earthquake,” *Bulletin of Seismological Society of America,* vol. 91, no. 5, pp. 1199-1211, 2001.

[16] H.-C. Chiu, “Stable baseline Correction of Digital Strong-Motion Data,” *Bulletin of Seismological Society of America,* vol. 87, no. 4, pp. 932-944, 1997.

[17] E. H. Javelaud, T. Ohmachi and S. Inoue, “A Quantative Approach for Estimating Coseismic Displacements in the Near Field Strong-Motion Accelerographs,” *Bulletin of Seismological Society of America,* vol. 101, no. 3, pp. 1182-1198, 2011.

[18] G. Xin, Y. Dong and G. Zhen-hai, “Study on Errors Compensation of a Vehicular MEMS Accelerometer,” *IEEE,* 2005.

[19] M. D. Trifunac and V. W. Lee, “A Note on the Accuracy of Computed Ground Displacements from Strong Motion Accelerograms,” *Bulletin of the Seismological Society of America,* vol. 64, no. 4, pp. 1209-1219, 1974.

[20] Y.-M. Wu, T.-L. Lin, W.-A. Chao, H.-H. Huang, N.-C. Hsiao and C.-H. Chang, “Faster Short-Distance Earthquake Early Warning Using Continued Monitoring of Filtered Vertical Displacement: A Case Study of the 2010 Jiasian, Taiwan, Earthquake,” *Bulletin of the Seismological Society of America,* vol. 101, no. 2, pp. 701-709, 2011.

[21] A. A. Chanerley, N. A. Alexander, J. Berrill, H. Avery, B. Halldorsson and R. Sigbjornsson, “Concerning Baseline Errors in the Form of Acceleration Transients When Recovering Displacements from Strong Motion Records Using the Undecimated Wavelet Transform,” *Bulletin of the Seismological Society of America,* vol. 103, no. 1, pp. 283-295, 2013.

[22] U.-X. Tan, K. C. Veluvolu, W. T. Latt, C. Y. Shee, C. N. Riviere and W. T. Ang, “Estimating Displacement of Periodic Motion with Inertial Sensors,” *IEEE Sensors Journal,* vol. 8, no. 8, 2008.

[23] D. Hu, C. Zeng and H. Liang, “Autocalibration Method of MEMS Accelerometer,” in *International conference on Mechatronic Science*, Jilin, 2011.

[24] L. Frosio, F. Pedersini and A. Borghese, “Autocalibration of Triaxial MEMS Accelerometers with automatic ssensor model selection,” *IEEE Sensors ,* vol. 12, no. 6, 2012.

[25] W. E. Farrell and J. Berger, “Seismic System Calibration: 1. Parametric Models,” *Bulletin of the Seismological Society of America,* vol. 69, no. 1, pp. 251-270, 1979.

[26] I. Frosio, S. Stuani and N. A. Borghese, “Autocalibration of MEMS Accelerometer,” in *Instrumentation and Measurement Technology Conference*, Sorrento, 2006.

[27] H. Brander and B. Reichle, “Some methods for determining acceleration and tilt by use of pendulums and accelerometers,” *Bulletin of the Seismological Society of America,* vol. 63, 1973.

[28] C.-J. Lin, H.-P. Huang, C.-C. Liu and H.-C. Chiu, “Application of Rotational Sensors to Correcting Rotation-Induced Effects on Accelerometers,” *Bulletin of the Seismological Society of America,* vol. 100, no. 2, pp. 585-597, 2010.

[29] C.-J. Lin, C.-C. Liu and W. H. Lee, “Recording Rotational and Translational Ground Motions of TwoTAIGER Explosions in Northeastern Taiwan on 4 March 2008,” *Bulletin of the Seismological Society of America,* vol. 99, no. 28, pp. 1237-1250, 2009.

[30] S. Luczak, W. Oleksiuk and M. Bodnicki, “Sensing Tilt With MEMS Accelerometers,” *IEEE SENSORS JOURNAL,* vol. 6, no. 6, 2006.

[31] R. L. Nigbor, “Six-Degree-of-Freedom Ground-Motion Measurement,” *Bulletin of the Seismological Society of America,* vol. 84, no. 5, pp. 1665-1669, 1994.

[32] V. Graizer, “Tilts in Strong Ground Motion,” *Bulletin of the Seismological Society of America,* vol. 96, no. 6, pp. 2090-2102, 2006.

[33] E. H. Javelaud, T. Ohmachi and S. Inoue, “Short Note, Estimating Small Permanent Rotation from Strong-Motion Records: What Is Comparison with External Measurements Telling Us?,” *Bulletin of the Seismological Society of America,* vol. 102, no. 5, pp. 2257-2263, 2012.

[34] R. L. Boroschek and D. Legrand, “Tilt Motion Effects on the Double-Time Integration of Linear Accelerometers: An Experimental Approach,” *Bulletin of the Seismological Society of America,* vol. 96, no. 6, pp. 2072-2089, 2006.

[35] T. Tobita, S. Iai and T. Iwata, “Numerical Analysis of Near-Field Asymmetric Vertical Motion,” *Bulletin of the Seismological Society of America,* vol. 100, no. 4, pp. 1456-1469, 2010.

[36] R. Sleeman, A. Van Wettum and J. Trampet, “Three-Channel Correlation Analysis: A New Technique to Measure Instrumental Noise of Digitizers and Seismic Sensors,”

*Bulletin of the Seismological Society of America,* vol. 96, no. 1, pp. 258-271, 2006.

[37] S. Akkar and D. M. Boore, “On Baseline Corrections and Uncertainty in Response Spectra for Baseline Variations Commonly Encountered in Digital Accelerograph Records,” *Bulletin of the Seismological Society of America,* vol. 99, no. 3, pp. 1671-1690, 2009.

[38] D. M. Boore, “Analog-to-Digital Conversion as a Source of Drifts in Displacements Derived from Digital Recordings of Ground Acceleration,” *Bulletin of the Seismological Society of America,* vol. 93, no. 5, pp. 2017-2024, 2003.

[39] J. Zahradnik and A. Plesinger, “Toward Understanding Subtle Instrumentation Effects Associated with Weak Seismic Events in the Near Field,” *Bulletin of the Seismological Society of America,* vol. 100, no. 1, pp. 59-73, 2010.

[40] F. Mohd-Yasin, C. E. Korman and D. J. Nagel, “Measurement of Noise Characteristics of MEMS Accelerometers,” Department of Electrical & Computer Engineering The George Washington University, Washington, DC 20052, U.S.A., Washington, Unknown.

[41] M. D. Trifunac, F. E. Udwadia and A. G. Brady, “ANALYSIS OF ERRORS IN DIGITIZED STRONG-MOTION ACCELEROGRAMS,” *Bulletin of the Seismological Society of America,* vol. 63, no. 1, pp. 157-187, 1973.

[42] Y. Bock, D. Melgar and B. Crowell, “Real-Time Strong-Motion Broadband Displacements from Collocated GPS and Accelerometers,” *Bulletin of the Seismological Society of America,* vol. 101, no. 6, pp. 2904-2925, 2011.

[43] H. Wood, “ON A PIEZO-ELECTRICAL ACCELEROGRAPH,” *Bulletin of the Seismological Society of America,* vol. 11.

[44] P. C. Leary, D. V. Manov and A. Y. Li, “A FIBER OPTICAL BOREHOLE SEISMOMETER,” *Bulletin of the Seismological Society of America,* vol. 80, no. 1, pp. 218-225, 1990.

[45] R. Wildmer-Schnidrig, “What Can Superconducting Gravimeters Contribute to Normal-Mode Seismology?,” *Bulletin of the Seismological Society of America,* vol. 93, no. 3, pp. 1370-1380, 2003.

[46] K. U. Schreiber, A. Velikoseltsev, A. J. Carr and R. Franco-Anaya, “The Application of Fiber Optic Gyroscopes for the Measurement of Rotations in Structural Engineering,” *Bulletin of the Seismological Society of America,* vol. 99, no. 2B, pp. 1207-1214, 2009.

[47] J. Liang, F. Kohsaka, X. Li, K. Kunitomo and T. Ueda, “CHARACTERIZATION OF A QUARTZ MEMS TILT SENSOR WITH 0.001° PRECISION,” in *Transducers*, Denver, 2009.

[48] N. Z. Pooya and A. Abraham, “A Method for Calibrating Micro Electro Mechanical

Systems Accelerometer for Use as a Tilt and Seismograph Sensor," in *IEEE 12th International Conference on Computer Modelling and Simulation*, 2010.

[49] T. G. Constandinou and J. Georgiou, "A Micropower Tilt Processing Circuit," *IEEE,* 2008.

[50] J. Qian, B. Fang, W. Yang and X. Luan, "Accurate Tilt Sensing With Linear Model," *IEEE SENSORS JOURNAL,* vol. 11, no. 10, 2011.

[51] R. l. Nigbor, J. R. Evans and C. R. Hutt, "Laboratory and Field Testing of Commercial Rotational Seismometers," *Bulletin of the Seismological Society of America,* vol. 99, no. 2B, pp. 1215-1227, 2009.

[52] A. Eisenberg and T. V. McEvilly, "COMPARISON OF SOME WIDELY-USED STRONG-MOTION EARTHQUAKE ACCELEROMETERS," *Bulletin of the Seismological Society of America,* vol. 61, no. 2, pp. 383-397, 1971.

[53] N.-C. Tsai and C.-Y. Sue, "Design and Analysis of a Tri-Axis Gyroscope Micromachined by Surface Fabrication," *IEEE SENSORS JOURNAL,* vol. 8, no. 12, 2008.

[54] S. Gervais-Ducouret, "Next Smart Sensors Generation," *IEEE,* 2011.

[55] A. Katalin, "Microcontroller Based System for Vibration Analysis," *IEEE,* 2008.

[56] DAQ Systems, "Tri-Axial USB Digital Accelerometer with GPS," *Seismological Research Letters,* vol. 79, 2008.

[57] Z. L. Chang and J. L. Shaozhong, "Development of a tilt measurement system based on MEMS sensor and Cortex-M3," in *The Tenth International Conference on Electronic Measurement & Instruments*, 2011.

[58] G. Emore, J. Haase, K. Choi, K. M. Larson and A. Yamagiwa, "Recovering Seismic Displacements through Combined Use of 1-Hz GPS and Strong-Motion Accelerometers," *Bulletin of the Seismological Society of America,* vol. 97, no. 2, pp. 357-378, 2007.

[59] D. M. Tralli, W. Foxall, A. Rodgers, E. Stappaerts and C. Schultz, "Suborbital and Spaceborne Monitoring of Seismic Surface Waves," *IEEEAC,* 2005.

[60] P. Zwahlen, Y. Dong, A. M. Nguyen, F. Rudolf, P. Ullah and V. Ragot, "Breakthrough in High Performance Inertial Navigation Grade Sigma-Delta MEMS Accelerometer," *IEEE,* 2012.

[61] B. Alandry, N. Dumas, L. Latorre, F. Mailly and P. Nouet, "A CMOS Multi-sensor System for 3D Orientation Determination," in *IEEE Computer Society Annual Symposium on VLSI*, 2008.

[62] X. Zhang, X. Ke and Z. Zhang, “Research on Micro-Electro-Mechanical-Systems digital geophone,” *IEEE International Conference on Artificial Intelligence and Computational Intelligence,* 2010.

[63] J. F. Clinton and T. H. Heaton, “Potential Advantages of a Strong-motion Velocity Meter over a Strong-motion Accelerometer,” *Seismological Research Letters,* vol. 73, no. 3, 2002.

[64] P. Zwahlen, A.-M. Nguyen, Y. Domg, F. Rudolf, M. Pastre and H. Schmid, “NAVIGATION GRADE MEMS ACCELEROMETER,” in *IEEE*, 2010.

[65] A. Ya'akobovitz and S. Krylov, “MEMS ACCELEROMETER WITH MECHANICAL AMPLIFICATION MECHANISM FOR ENHANCED SENSITIVITY,” in *Transducers*, Denver, 2009.

[66] D. J. Milligan, B. D. Homeijer and R. G. Walmsley, “A Ultra-Low noise MEMS Accelerometer for Seismic Imaging,” in *IEEE*, 2011.

[67] J. Mizuno, K. Nottmeyer, T. Kobayashi, K. Minami and M. Esashi, “Silicon Bulk Micromachined Accelerometer with Simultaneous Linear and Angular Sensitivity,” in *IEEE international Conference on Solid-state Sensors and Actuators*, Chicago, 1997.

[68] J.-M. Stauffer, “Market Opportunities for Advanced MEMS Accelerometers and Overview of Actual Capabilities vs. Required Specifications,” in *IEEE*, 2004.

[69] J. Laine and D. Mougenot, “BENEFITS OFMEMS BASED SEISMIC ACCELEROMETERS FOR OIL EXPLORATION,” in *14th International Conference on Solid-State Sensors, Actuators and Microsystems*, Lyon, 2007.

[70] M. A. Lele and J. Gu, “Evaluation of Solid State Accelerometer Sensor for Effective Position Estimation,” in *8th World Congress on Intelligent Control and Automation*, Taipei, 2011.

[71] M. Gluek, A. Buhmann and Y. Manoli, “Autocalibration of MEMS accelerometers,” in *IEEE*, 2012.

[72] Y. V. Tarbeyev, Y. P. Kristov and A. Y. Sinelnikov, “A New Method for Absolute Calibration of High-Sensitivity Accelerometers and Other Graviinertial Devices,” *Bulletin of the Seismological Society of America,* vol. 84, no. 2, pp. 438-443, 1994.

[73] F. Reverter and O. Casas, “Interfacing Differential Capacitive Sensors to Microcontrollers: A Direct Approach,” *IEEE TRANSACTIONS ON INSTRUMENTATION AND MEASUREMENT,* vol. 59, no. 10, 2010.

[74] P. W. Rodgers, “FREQUENCY LIMITS FOR SEISMOMETERS AS DETERMINED FROM SIGNAL-TO-NOISE RATIOS. PART 2. THE FEEDBACK SEISMOMETER,” *Bulletin of the*

*Seismological Society of America,* vol. 82, no. 2, pp. 1099-1123, 1992.

[75] M. A. Riedesel, R. D. Moore and J. A. Orcutt, “LIMITS OF SENSITIVITY OF INERTIAL SEISMOMETERS WITH VELOCITY TRANSDUCERS AND ELECTRONIC AMPLIFIERS,” *Bulletin of the Seismological Society of America,* vol. 80, no. 6, pp. 1725-1752, 1990.

[76] F. Mohd-Ysin, C. E. Korman, D. J. Nage and H. T. Chuan, “Investigations of Spectral Peaks, Resonance Effect and 1/f Exponents on Noise Characteristics of MEMS Accelerometers,” in *IEEE*, 2004.

[77] A. Strollo, S. Parolai, K. H. Jackel, S. Marzorati and D. Bindi, “Suitability of Short-Period Sensors for Retrieving Reliable H/V Peaks for Frequencies Less Than 1 Hz,” *Bulletin of the Seismological Society of America,* vol. 98, no. 2, pp. 671-681, 2008.

[78] C. Collette, S. Janssens, P. Fernandez-Carmona, K. Artoos, M. Guinchard, C. Hauviller and A. Preumont, “Review: Inertial Sensors for Low-Frequency Seismic Vibration Measurement,” *Bulletin of the Seismological Society of America,* vol. 102, no. 4, pp. 1289-1300, 2012.

[79] W. Liang, C. Yang and Q. Donghai, “Design of feed-forward ΣΔ interface for MEMS,” in *IEEE 4th International Congress on Image and Signal Processing*, 2011.

[80] M. Wang, Y. Yang, R. R. Hatch and Y. Zhang, “Adaptive Filter for a Miniature MEMS Based Attitude and Heading Reference System,” in *IEEE*, 2004.

[81] C. Rithirun and P. Sooraksa, “The Implementation of Fuzzy Logic Control for Attitude Estimation of UAVs,” in *8th Electrical Engineering/ Electronics, Computer, Telecommunications and Information Technology (ECTI) Association of Thailand*, Thailand, 2011.

[82] P. Wu, Y. Ge, S. Chen and B. Xue, “De-noising Algorithm Based on Compression of Wavelet Coefficient for MEMS Accelerometer Signa,” in *Proceedings of the 2010 IEEE International Conference on Information and Automation*, Harbin, 2010.

[83] J.-g. Song, C.-x. Zhao, S.-h. Lin and H.-j. Liu, “Decomposition of Seismic Signal Based on Hilbert-Huang transform,” in *IEEE*, 2011.

[84] M. D. Trifunac, “A NOTE ON CORRECTION OF STRONG-MOTION ACCELEROGRAMS FOR INSTRUMENT RESPONSE,” *Bulletin of the Seismological Society of America,* vol. 62, no. 1, pp. 401-409, 1972.

[85] N. A. Alexander and A. A. Chanerley, “A Review of Procedures used for the Correction of Seismic data,” in *Proceedings of the Eighth International Conference on Civil and Structural Engineering Computing,*, Austria, 2011.

[86] L. Dong and K. Zhang, “Sensing and Control of MEMS Accelerometers Using Kalman Filter,” in *IEEE*, 2012.

[87] Mii-Iailo and D. Trifunac, “ZERO BASELINE CORRECTION OF STRONG-MOTION ACCELEROGRANIS,” *Bulletin of the Seismological Society of America,* vol. 61, no. 5, pp. 1201-1211, 1971.

[88] R. Wang, B. Schurr, C. Milkereit, Z. Shao and M. Jin, “An Improved Automatic Scheme for Empirical Baseline Correction of Digital Strong-Motion Records,” *Bulletin of the Seismological Society of America,* vol. 101, no. 5, pp. 2029-2044, 2011.

[89] J. Shoja-Taheri, “A NEW ASSESSMENT OF ERRORS FROM DIGITIZATION AND BASELINE CORRECTIONS OF STRONG-MOTION ACCELEROGRAMS,” *Bulletin of the Seismological Society of America,* vol. 70, no. 1, pp. 293-303, 1980.

[90] W. H. Boyce, “LETTERS TO THE EDITOR. INTEGRATION OF ACCELEROGRAMS,” *Bulletin of the Seismological Society of America,* vol. 60, no. 1, pp. 261-263, 1970.

[91] J. Hershberger, “RECENT DEVELOPMENTS IN STRONG-MOTION ANALYSIS,” *Bulletin of the Seismological Society of America,* 1954.

[92] D. Murray, “Integration of Accelerometer Data: Filter Analysis and Design Using Riccati Solutions,” *IEEE TRANSACTIONS ON AUTOMATIC CONTROL,* vol. 32, no. 2, 1987.

[93] F. Neumann, “AN APPRAISAL OF NUMERICAL INTEGRATION METHODS AS APPLIED TO STRONG-MOTION DATA,” *Bulletin of the Seismological Society of America.*

[94] N. Ciblak, “Determining the Angular Motion of a Rigid Body Using Linear Accelerometers Without Integration,” in *IEEE*, 2007.

[95] L. P. Yaroslavski, A. Moreno and J. Campos, “Frequency responses and resolving power of numerical integration of sampled data,” *Optical Society of America,* vol. 13, no. 8, 2005.

[96] E. J. Walter, “AN EXTENSION OF THE METHOD OF NUMERICAL INTEGRATION OF SEISMOGRAMS TO INCLUDE A THIRD INTEGRATION,” *BULLETIN OF THE SEISMOLOGICAL SOCIETY OF AMERICA,* 1994.

[97] A. T. Ringler, C. R. Hutt, J. R. Evans and L. D. Sandoval, “A Comparison of Seismic Instrument Noise Coherence Analysis Techniques,” *Bulletin of the Seismological Society of America,,* vol. 101, no. 2, pp. 558-567, 2011.

[98] W. T. Ang, P. K. Khosla and C. N. Riviere, “Nonlinear Regression Model of a Low-g MEMS Accelerometer,” *IEEE SENSORS JOURNAL,* vol. 7, no. 1, 2007.

[99] J. E. Vandemeer, G. L. Andrew and C. McNeil, “Analysis of Thermal Hysteresis on Micromachined Accelerometers,” *IEEE,* 2003.

[100] K. G. Hinzen, C. Fleisher and G. Schweppe, “Long Term Behavior of an Accelerometer Station,” *Seismological Research Letters,* vol. 83, no. 2, 2012.

[101] Z. Yang, H. W. Lu, Z. Wang, Z. Gui and L. Cai, “Six Degree-of-freedom Strong Ground Motions Measurement by Using Eight Accelerometers,” in *International Conference on Computer, Mechatronics, Control and Electronic Engineering*, 2010.

[102] V. M. Graizer, “Effect of tilt on strong motion data processing,” *Soil Dynamics and Earthquake Engineering,* vol. 25, 2005.

[103] Z. Lawrence, P. Bodin and C. A. Langston, “In Situ Measurements of Nonlinear and Nonequilibrium Dynamics in Shallow, Unconsolidated Sediments,” *Bulletin of the Seismological Society of America,* vol. 99, no. 3, pp. 1650-1670, 2009.

[104] P. Gueguen, M. Langlais, P. Foray, C. Rousseau and J. Maury, “A Natural Seismic Isolating System: The Buried Mangrove Effects,” *Bulletin of the Seismological Society of America,* vol. 101, no. 3, pp. 1073-1080, 2011.

[105] N. Maercklin, A. Zollo, A. Orefice, G. Festa, A. Emolo, R. De Matteis, B. Delouis and A. Bobbio, “The Effectiveness of a Distant Accelerometer Array to Compute Seismic Source Parameters: The April 2009 L’Aquila Earthquake Case History,” *Bulletin of the Seismological Society of America,* vol. 101, no. 1, pp. 354-365, 2009.

[106] F. T. Thwaites, F. B. Wooding, J. D. Ware, K. R. Peal and J. A. Collins, “A Leveling System for an Ocean-Bottom Seismometer,” Woods Hole Oceanographic Institution.

[107] J. Hershberger, “RECENT DEVELOPMENTS IN STRONG-MOTION ANALYSIS,” *Bulletin of the Seismological Society of America,* 1954.

[108] D. E. Hudson and G. W. Housner, “AN ANALYSIS OF STRONG-MOTION ACCELEROMETER DATA FROM THE SAN FRANCISCO EARTHQUAKE OF MARCH 22, 1957,” *Bulletin of the Seismological Society of America,* vol. 48, pp. 253-268, 1958.

[109] B. Fry, R. Benites and A. Kaiser, “The Character of Accelerations in the Mw 6.2 Christchurch Earthquake,” *Seismological Research Letters,* vol. 82, no. 6, 2011.

[110] P. Gueguen, M. Langlais, P. Foray, C. Rousseau and J. Maury, “A Natural Seismic Isolating System: The Buried Mangrove Effects,” *Bulletin of the Seismological Society of America,* vol. 101, no. 3, pp. 1073-1080, 2011.

[111] C. Collette, S. Janssens, P. Fernandez-Carmona, K. Artoos, M. Guinchard, C. Hauviller and A. Preumont, “Review: Inertial Sensors for Low-Frequency Seismic Vibration Measurement,” *Bulletin of the Seismological Society of America,* vol. 102, no. 4, pp. 1289-1300, 2012.

[112] A. Strollo, S. Parolai, K. H. Jakel, S. Marzorati and D. Bindi, “Suitability of Short-Period Sensors for Retrieving Reliable H/V Peaks for Frequencies Less Than 1 Hz,” *Bulletin of the Seismological Society of America,* vol. 38, no. 2, pp. 671-681, 2008.

# Appendix A

## Windows control software

```
Private Sub Command1_Click()
'Auto-Zero X Code A=65d
MSComm1.PortOpen = True
MSComm1.Output = "A"
MSComm1.PortOpen = False
Text1.Text = Text1.Text & vbNewLine & "X channel Autozero done"
With Text1
   .SelStart = Len(.Text)
   .SelLength = 0
End With
End Sub

Private Sub Command10_Click()
'Horizontal Gyro ON/OFF Code I=73d
MSComm1.PortOpen = True
MSComm1.Output = "I"
MSComm1.PortOpen = False
If Check2.Value = 0 Then
        Check2.Value = 1
        Label4.Caption = "ON"
        Else
        Check2.Value = 0
        Label4.Caption = "OFF"
End If
Text1.Text = Text1.Text & vbNewLine & "Horizontal Gyro Power Toggled"
With Text1
   .SelStart = Len(.Text)
   .SelLength = 0
End With
End Sub

Private Sub Command11_Click()
'Vertical Gyro ON/OFF J=74d
MSComm1.PortOpen = True
MSComm1.Output = "J"
MSComm1.PortOpen = False
If Check3.Value = 0 Then
        Check3.Value = 1
        Label5.Caption = "ON"
        Label6.Caption = "ON"
        Else
        Check3.Value = 0
        Label5.Caption = "OFF"
        Label6.Caption = "OFF"
End If
Text1.Text = Text1.Text & vbNewLine & "Vertical Gyro Power Toggled"
With Text1
   .SelStart = Len(.Text)
   .SelLength = 0
End With
End Sub
Private Sub Command12_Click()
'Brakes ON/OFF K=75d
MSComm1.PortOpen = True
MSComm1.Output = "K"
MSComm1.PortOpen = False
        If Check4.Value = 0 Then
        Check4.Value = 1
        Else
        Check4.Value = 0
```

```
End If
Text1.Text = Text1.Text & vbNewLine & "Brake Actuators Toggled"
With Text1
   .SelStart = Len(.Text)
   .SelLength = 0
End With
End Sub

Private Sub Command2_Click()
'Auto-Zero Y Code B=66d
MSComm1.PortOpen = True
MSComm1.Output = "B"
MSComm1.PortOpen = False
Text1.Text = Text1.Text & vbNewLine & "Y channel Autozero done"
With Text1
   .SelStart = Len(.Text)
   .SelLength = 0
End With
End Sub

Private Sub Command3_Click()
'Auto-Zero Z Code L=76d
MSComm1.PortOpen = True
MSComm1.Output = "L"
MSComm1.PortOpen = False
Text1.Text = Text1.Text & vbNewLine & "Z channel Autozero done"
With Text1
   .SelStart = Len(.Text)
   .SelLength = 0
End With

End Sub
Private Sub Command4_Click()
'Impulses Code C=67d
MSComm1.PortOpen = True
MSComm1.Output = "C"
MSComm1.PortOpen = False
Text1.Text = Text1.Text & vbNewLine & "All Channel Impulses Generated"
With Text1
   .SelStart = Len(.Text)
   .SelLength = 0
End With
End Sub
Private Sub Command5_Click()
'V Ref Directly to outputs  Code F=70d
MSComm1.PortOpen = True
MSComm1.Output = "F"
MSComm1.PortOpen = False
Text1.Text = Text1.Text & vbNewLine & "V Ref Now Connected to Outputs"
With Text1
   .SelStart = Len(.Text)
   .SelLength = 0
End With
Line7.Visible = False
Line9.Visible = False
Line11.Visible = False
Line8.Visible = True
Line10.Visible = True
Line12.Visible = True
End Sub

Private Sub Command6_Click()
'V Ref Through Channels G=71d
MSComm1.PortOpen = True
MSComm1.Output = "G"
MSComm1.PortOpen = False
Text1.Text = Text1.Text & vbNewLine & "V Ref Now Through Channels"
```

```
With Text1
   .SelStart = Len(.Text)
   .SelLength = 0
End With
Line7.Visible = True
Line9.Visible = True
Line11.Visible = True
Line8.Visible = False
Line10.Visible = False
Line12.Visible = False
Line1.Visible = False
Line2.Visible = False
Line3.Visible = False
Line4.Visible = True
Line5.Visible = True
Line6.Visible = True
Label1.Caption = "V=ZERO"
Label2.Caption = "V=ZERO"
Label3.Caption = "V=ZERO"
End Sub

Private Sub Command7_Click()
'Freq Sweep Code D=68d
MSComm1.PortOpen = True
MSComm1.Output = "D"
MSComm1.PortOpen = False
Text1.Text = Text1.Text & vbNewLine & "Frequency Sweep Activated"
With Text1
   .SelStart = Len(.Text)
   .SelLength = 0
End With
End Sub
Private Sub Command8_Click()
'Dithering ON/OFF E=69d
MSComm1.PortOpen = True
MSComm1.Output = "E"
MSComm1.PortOpen = False
If Check1.Value = 0 Then
            Check1.Value = 1
            Else
            Check1.Value = 0
End If
Text1.Text = Text1.Text & vbNewLine & "Dithering Mode Toggled"
With Text1
   .SelStart = Len(.Text)
   .SelLength = 0
End With
End Sub

Private Sub Command9_Click()
'V Ref Disabled Code H=72d
MSComm1.PortOpen = True
MSComm1.Output = "H"
MSComm1.PortOpen = False
Text1.Text = Text1.Text & vbNewLine & "V Ref Diasabled. Now In Normal Mode Operation"
With Text1
   .SelStart = Len(.Text)
   .SelLength = 0
End With
Line7.Visible = True
Line9.Visible = True
Line11.Visible = True
Line8.Visible = False
Line10.Visible = False
Line12.Visible = False
Line1.Visible = True
Line2.Visible = True
```

```
Line3.Visible = True
Line4.Visible = False
Line5.Visible = False
Line6.Visible = False
Label1.Caption = "V=0.5 V REF"
Label2.Caption = "V=0.5 V REF"
Label3.Caption = "V=0.5 V REF"
End Sub
```

# Appendix B

## Embedded software

```
                                        ;CODE VERSION 1 16/02/14 Seism
                org     0x00            ; RESET VECTOR
                goto    INIT            ;GOTO INIT, SKIP INTERUPT VECTORS


;>>>>>>>>>>>>>>>>>>>>>>> HIGH PRIORITY INT SERVICE ROUTINE INT0 >>>>>>>>>>>>>>


;INT Housekeeping routine.......................................................
                org     0x08;           HIGH PRIORITY INT VECTOR ADDRESS

        ;       bcf     0xFD5,7;        DISABLE TMR0 IN T0CON,7

        ;       bcf     0xFF2,2;        CLEAR TMR0 INTERUPT FLAG IN INTCON



;OUT            bsf     0xFD5,7;        ENABLE TMR0 IN T0CON,7

                retfie
;""""""""""""""""""""""""""""""""""""""""""""""""""""""""""""""""""""""""""""""""""""""""""""""""""""""""""""""""""""""""""""""
;


;>>>>>>>>>>>>>>>>>>>>>>>>>>>>>> INIT <<<<<<<<<<<<<<<<<<<<<<<<<<<<<<<<<<

INIT    org             0x90

;               movlw   0x0F;           ADCON1 BUG FIX
;               movwf   0xFC1;          ENABLE FOR SIMULATION ONLY!

;CLK CONFIG..........................................................
                movlw   0x72;           SET INTERNAL CLOCK TO 16MHZ
                movwf   0xFD3;          OSCCON = 0X72
;....................................................................

;       PORT A CONFIG...................................................
                movlw   0x01;
                movff   0xFE8,0xF38;    MAKE RA0 ANALOG...REST OF PORTA DIGITAL. ANSELA=1
                movlw   0x01
                movwf   0xF92;          TRISA=1, RAO AS INPUT, ALL OTHER AS OUTPUTS
                clrf    0xF80;          CLEAR PORTA DATA

;....................................................................


;       PORT B CONFIG...................................................
                movlw   0x00;
                movff   0xFE8,0xF39;    MAKE PORTB DIGITAL. ANSELB=0
                movlw   0x01
                movwf   0xF93;          SET TRISB, PORT B RB0 AS INPUT, REST OUTPUTS [RBO
AS INT0]
                clrf    0xF81;          CLEAR PORT B DATA
                clrf    0xF61;          DISABLE PORTB INTERNAL PULL UPS, WPUB=0
;......................................................................

;       PORT C CONFIG.....................................................
                movlw   0x00;
                movff   0xFE8,0xF3A;    MAKE PORT C DIGITAL. ANSELC=0
                movlw   0x80;
                movwf   0xF94;          TRISC, RC7 INPUT ALL OTHER PORTC OUTPUTS
                clrf    0xF82;          CLEAR PORT C DATA
```

```
;.......................................................................

;           POWER UP NORMAL CONFIG

                        bsf       0xF80,3;                SETTING SYNC Z,Y,X RESP TO HIGH...DACS TO NORM
MODE
                        bsf       0xF80,4;
                        bsf       0xF80,5;


                        bcf       0xF82,5;                I/P REF SW TO ZERO RC5=0
                        bcf       0xF81,1;                O/P REF SW TO ZERO RB1=0


;...............................................................................................

;           ADC CONFIG AN0

                        bsf       0xFC2,0;                ENABLE ADC MODULE IN ADCON0 BIT 0
                        bsf       0xFC0,0;                CONFIGURE ADC CLOCK TO 600KHZ INTERNAL IN
ADCON2
                        bsf       0xFC0,1;
                        bsf       0xFC0,3;                CONFIGURE ADC ACQ TIME TO 20TAD
                        bsf       0xFC0,4;
                        bsf       0xFC0,5;
;.......................................................................


;INTERUPTS CONFIG......................................................
            ;           movlw     0x10;                   SET VALUE FOR INT0 ENABLE
            ;           movwf     0xFF2;                  INT0 BIT ENABLED IN INTCON REG
;.......................................................................

;EUSART CONFIG..........................................................

                        movlw     0x19;                   25d into SPBRG1 - BAUD RATE 9600 FROM 16MHz FOSC.
                        movff     0xFE8, 0XFAF;
                        bcf       0xFAC,4;                CLEAR SYNC BIT IN TXSTA1- SET ASYNCHRONOUS MODE
                        bsf       0xFAB,7;                SET SPEN BIT IN RCSTA1 TO ENABLE SERIAL PORT
                        bsf       0xFAB,4;                SET CREN BIT IN RCSTA1 TO ENABLE RX HARDWARE
;..........................................................................


; SETUP...........................................................

                        bsf       0xF81,3;                SET FEEDBACK SWITCH TO X CHANNEL

                        movlw     0x80;                   SET DAC VAR TO 1.008V
                        movwf     0x5;

;..........................................................................
;""""""""""""""""""""""""""""""""""""""""""""""""""""""""""""""""""""""""""""""""""""""""""""""""""""""""""""""""""""""""""""""""""


;>>>>>>>>>>>>>>>>>>>>>>>>>>>>>>>> MAIN <<<<<<<<<<<<<<<<<<<<<<<<<<<<<<<<<
MAIN

                        btfsc     0xF9E,5;                TEST EUSART RECIEVE FLAG, SKIP IF NO RX
                        call      EUSART;                 CALL INSTRUCTION DECODER FUNCTION

                        goto      MAIN

;"""""""""""""""""""""""""""""""""""""""""""""""""""""""""""""""""""""""""""""""""""""""""""""""""""""""""""""""""""""""""""""""""""""""
```

```
;>>>>>>>>>>>>>>>>>>>>>>>>>>>>>>>>>> FUNCTIONS <<<<<<<<<<<<<<<<<<<<<<<<<<<<<<<<<<<<<<<<<


;Delay of 200us Approx.......................................................

DELAY
                movlw   0xFF            ;200us Approx
                movwf   0x01
LO              decfsz  0x01
                goto    LO

                return
;..............................................................................


;Delay of 25 ms Approx.....................................................
DELAY3          movlw   0x7F            ;25ms Approx
                movwf   0x01
dly3            movlw   0xFF
                movwf   0x00

L3              decfsz  0x00
                goto    L3
                decfsz  0x01
                goto    dly3

                return
;.................................................................................



EUSART;                  INSTRUCTION DECODER AND EXECUTION FUNCTION

IMP             movlw   0x43;            CHECK FOR IMPULSE INSTRUCTION ASCII 0X43
                movwf   0x02;           MOVE 0x43 TO LOCATION 02 FOR COMPARISON
                movff   0xFAE,0xFE8;    LOAD EUSART RECIEVE REGISTER RCREG1 DATA INTO W
                cpfseq  0x02;           COMPARE W WITH VALUE ASCII 0X43, SKIP IF EQUAL
                goto    VREF
                call    IMPULSE;        IMPULSE INSTRUCTION, CALL IMPULSE FUNCTION

VREF            movlw   0x46;           CHECK FOR V REF DIRECTLY TO OUTPUTS INSTRUCTION
                movwf   0x02;           MOVE 0x46 TO LOCATION 02 FOR COMPARISON
                movff   0xFAE,0xFE8;    LOAD EUSART RECIEVE REGISTER RCREG1 DATA INTO W
                cpfseq  0x02;           COMPARE W WITH VALUE ASCII 0X46, SKIP IF EQUAL
                goto    DISREF
                call    VREFOUT;        CALL V REF TO OUTPUTS INSTRUCTION


DISREF          movlw   0x48;           CHECK FOR V REF DISABLE INSTRUCTION ASCII 0X48
                movwf   0x02;           MOVE 0x48 TO LOCATION 02 FOR COMPARISON
                movff   0xFAE,0xFE8;    LOAD EUSART RECIEVE REGISTER RCREG1 DATA INTO W
                cpfseq  0x02;           COMPARE W WITH VALUE ASCII 0X48, SKIP IF EQUAL
                goto    VRIN
                call    NOVREF;         CALL NO V REF MODES INSTRUCTION

VRIN            movlw   0x47;           CHECK FOR V REF THROUGH CHANNELS INSTRUCTION
                movwf   0x02;           MOVE 0x47 TO LOCATION 02 FOR COMPARISON
                movff   0xFAE,0xFE8;    LOAD EUSART RECIEVE REGISTER RCREG1 DATA INTO W
                cpfseq  0x02;           COMPARE W WITH VALUE ASCII 0X47, SKIP IF EQUAL
                goto    AUTOZX
                call    VREFIN;         CALL V REF THROUGH CHANNELS INSTRUCTION

AUTOZX          movlw   0x41;           CHECK FOR AUTO ZERO X INSTRUCTION ASCII 0X41
                movwf   0x02; MOVE 0x41  TO LOCATION 02 FOR COMPARISON
                movff   0xFAE,0xFE8;    LOAD EUSART RECIEVE REGISTER RCREG1 DATA INTO W
                cpfseq  0x02;           COMPARE W WITH VALUE ASCII 0X41, SKIP IF EQUAL
                return
                call    AZX;            CALL THE AUTO ZERO X INSTRUCTION



                return
;..............................................................................................
```

```
IMPULSE;                                IMPULSE EXCITATION ALL CHANNELS 200us

                bsf     0xF82,3;        SET RC3 EST PIN TO HIGH FOR 200us DELAY
                call    DELAY
                bcf     0xF82,3;        RESET RC3 TO ZERO

        return
;.................................................................................................

VREFOUT;                                CONNECT V REF TO ALL OUTPUT CHANNELS.....
                bsf     0xF81,1;        O/P REF SW SET RB1=1 TO ALLOW V REF TO OUTPUTS
                return
;...................................................................................................

NOVREF;                                 NO V REF MODES ON ALL CHANNELS
                bcf     0xF81,1;        O/P REF SW CLEAR RB1=0 TO ALLOW DATA TO OUTPUTS
                bcf     0xF82,5;        I/P REF SW TO ZERO - ALLOW OUTPUTS INTO CHANNELS
                call    SRDAC;          SOFT RESET ALL DACS TO HALF WAY LEVEL
                return
;...................................................................................................

VREFIN;                                 VREF THROUGH ALL CHANNEL INPUTS
                bsf     0xF82,5;        I/P REF SW SET RC5=1 - ALLOW V REF INTO CHANNELS
                bcf     0xF81,1;        O/P REF SW CLEAR RB1=0 TO ALLOW DATA TO OUTPUTS
                call    ZDACS;          SET ALL  CHANNEL DACS TO ZERO
                return
;.....................................................................................................


ZDACS;  SET ALL DACS TO ZERO
                bcf     0xF80,5;        CLEAR SYNCX TO ENTER WRITE MODE
                bcf     0xF80,4;        CLEAR SYNCY TO ENTER WRITE MODE
                bcf     0xF80,3;        CLEAR SYNCZ TO ENTER WRITE MODE
                bcf     0xF80,7;        CLEAR DATA TO PROVIDE ALL ZEROS

                bsf     0xF80,6;        SET CLK TO HIGH
                                        ; PULSE CLK 24 TIMES-WRITE DATA ON FALLING EDGES
                bcf     0xF80,6;1
                bsf     0xF80,6
                bcf     0xF80,6;2
                bsf     0xF80,6
                bcf     0xF80,6;3
                bsf     0xF80,6
                bcf     0xF80,6;4
                bsf     0xF80,6
                bcf     0xF80,6;5
                bsf     0xF80,6
                bcf     0xF80,6;6
                bsf     0xF80,6
                bcf     0xF80,6;7
                bsf     0xF80,6
                bcf     0xF80,6;8
                bsf     0xF80,6
                bcf     0xF80,6;9
                bsf     0xF80,6
                bcf     0xF80,6;10
                bsf     0xF80,6
                bcf     0xF80,6;11
                bsf     0xF80,6
                bcf     0xF80,6;12
                bsf     0xF80,6;
                bcf     0xF80,6;13
                bsf     0xF80,6
                bcf     0xF80,6;14
                bsf     0xF80,6
                bcf     0xF80,6;15
                bsf     0xF80,6
                bcf     0xF80,6;16
                bsf     0xF80,6
                bcf     0xF80,6;17
                bsf     0xF80,6
                bcf     0xF80,6;18
                bsf     0xF80,6
                bcf     0xF80,6;19
```

```
                bsf      0xF80,6
                bcf      0xF80,6;20
                bsf      0xF80,6
                bcf      0xF80,6;21
                bsf      0xF80,6
                bcf      0xF80,6;22
                bsf      0xF80,6
                bcf      0xF80,6;23
                bsf      0xF80,6
                bcf      0xF80,6;24

                bsf      0xF80,5;            SET SYNCX TO ENTER IDLE MODE
                bsf      0xF80,4;            SET SYNCY TO ENTER IDLE MODE
                bsf      0xF80,3;            SET SYNCZ TO ENTER IDLE MODE


                return
;..........................................................................................

SRDAC;                                       SOFT RESET ALL DACS TO HALF V OUT
                bcf      0xF80,5;            CLEAR SYNCX TO ENTER WRITE MODE
                bcf      0xF80,4;            CLEAR SYNCY TO ENTER WRITE MODE
                bcf      0xF80,3;            CLEAR SYNCZ TO ENTER WRITE MODE

                bsf      0xF80,7;            SET DATA TO PROVIDE ALL ONES - SOFTWARE RESET

                bsf      0xF80,6;            SET CLK TO HIGH
                                             ;PULSE CLK 24 TIMES-WRITE DATA ON FALLING EDGE
                bcf      0xF80,6;1
                bsf      0xF80,6
                bcf      0xF80,6;2
                bsf      0xF80,6
                bcf      0xF80,6;3
                bsf      0xF80,6
                bcf      0xF80,6;4
                bsf      0xF80,6
                bcf      0xF80,6;5
                bsf      0xF80,6
                bcf      0xF80,6;6
                bsf      0xF80,6
                bcf      0xF80,6;7
                bsf      0xF80,6
                bcf      0xF80,6;8
                bsf      0xF80,6
                bcf      0xF80,6;9
                bsf      0xF80,6
                bcf      0xF80,6;10
                bsf      0xF80,6
                bcf      0xF80,6;11
                bsf      0xF80,6
                bcf      0xF80,6;12
                bsf      0xF80,6;
                bcf      0xF80,6;13
                bsf      0xF80,6
                bcf      0xF80,6;14
                bsf      0xF80,6
                bcf      0xF80,6;15
                bsf      0xF80,6
                bcf      0xF80,6;16
                bsf      0xF80,6
                bcf      0xF80,6;17
                bsf      0xF80,6
                bcf      0xF80,6;18
                bsf      0xF80,6
                bcf      0xF80,6;19
                bsf      0xF80,6
                bcf      0xF80,6;20
                bsf      0xF80,6
                bcf      0xF80,6;21
                bsf      0xF80,6
                bcf      0xF80,6;22
                bsf      0xF80,6
                bcf      0xF80,6;23
                bsf      0xF80,6
                bcf      0xF80,6;24
```

```
                bsf     0xF80,5;        SET SYNCX TO ENTER IDLE MODE
                bsf     0xF80,4;        SET SYNCY TO ENTER IDLE MODE
                bsf     0xF80,3;        SET SYNCZ TO ENTER IDLE MODE


                return
;.....................................................................................


AZX;...............AUTO ZERO X.....................................

                movlw   0x80;           SET DAC VAR TO 1.008V
                movwf   0x5;            DAC MSB VAR
                bsf     0xF81,3;        SET FEEDBACK SWITCH TO X CHANNEL
                clrf    0x6;            DAC LSB VAR
;               clrf    0x5;            CLEAR DAC MSB VAR

        ;       goto    INC;

AQ              bsf     0xFC2,1;        START ADC CONVERSION BY SETTING GO/DONE BIT IN
ADCON0
ADF             btfsc   0xFC2,1;        TEST GO/DONE BIT FOR END OF ADC CONVERSION. SKIP
IF READY
                goto    ADF;            ADC RESULT NOT READY. TEST AGAIN
                tstfsz  0xFC4;          TEST ADC RESULT H-BYTE. SKIP NEXT IF ZERO
                goto    INC
                return


INC             incf    0x6;            ADC NOT ZERO...INCREMENT LSB DAC VAR
                                        ;INCREASE NEG FEEDBACK VOLTAGE
                btfsc   0xFD8,0;        TEST CARRY FLAG FOR OVERFLOW, SKIP IF NO
                incf    0x5;            OVERFLOW. INC 0x5 DAC MSB VAR


;                                       FIRST 8 CONFIG DAC BITS
                bcf     0xF80,5;        CLEAR SYNCX TO ENTER WRITE MODE
                bcf     0xF80,7;        CLEAR DATA TO PROVIDE ALL ZEROS
                bsf     0xF80,6;        SET CLK TO HIGH
                                        ;PULSE; CLK 8 TIMES - WRITE CONFIG ON FALLING EDGES
                bcf     0xF80,6;1
                bsf     0xF80,6
                bcf     0xF80,6;2
                bsf     0xF80,6
                bcf     0xF80,6;3
                bsf     0xF80,6
                bcf     0xF80,6;4
                bsf     0xF80,6
                bcf     0xF80,6;5
                bsf     0xF80,6
                bcf     0xF80,6;6
                bsf     0xF80,6
                bcf     0xF80,6;7
                bsf     0xF80,6
                bcf     0xF80,6;8
                bsf     0xF80,6


;                                       NEXT 8 MSB VARIABLE BITS STROBED TO DAC
                movlw   0x9;            SET REPEAT VARIABLE TO STROBE 8 BITS
                movwf   0x4;

L1              decfsz  0x4;
                goto    STROBE
                goto    B2
STROBE          btfss   0x5,7;          TEST VAR MSB
                goto    ZSTR;           GOTO STROBE ZERO
                bsf     0xF80,7;        SET DATA TO 1 TO STROBE 1
                bcf     0xF80,6;        STROBE PULSE CLK
                bsf     0xF80,6
                rlncf   0x5;            ROTATE VAR LEFT FOR NEXT BIT TO STROBE
                goto    L1

ZSTR            bcf     0xF80,7;        CLEAR DATA TO STROBE ZERO
```

```
                bcf       0xF80,6;        STROBE PULSE CLK
                bsf       0xF80,6
                rlncf     0x5;            ROTATE VAR LEFT FOR NEXT BIT TO STROBE
                goto      L1


;                                         LAST 8 LSB VARIABLE BITS STROBED TO DAC
B2              movlw     0x9;            SET REPEAT VARIABLE TO STROBE 8 BITS
                movwf     0x4;

L2              decfsz    0x4;
                goto      STROBE2
                goto      OUT
STROBE2         btfss     0x6,7;          TEST VAR MSB
                goto      ZSTR2;          GOTO STROBE ZERO
                bsf       0xF80,7;        SET DATA TO 1 TO STROBE 1
                bcf       0xF80,6;        STROBE PULSE CLK
                bsf       0xF80,6
                rlncf     0x6;            ROTATE VAR LEFT FOR NEXT BIT TO STROBE
                goto      L2

ZSTR2   bcf               0xF80,7;        CLEAR DATA TO STROBE ZERO
                bcf       0xF80,6;        STROBE PULSE CLK
                bsf       0xF80,6
                rlncf     0x6;            ROTATE VAR LEFT FOR NEXT BIT TO STROBE
                goto      L2



OUT             bsf       0xF80,5;        SET SYNCX TO ENTER NORMAL MODE

                movlw     0xC8
                cpfsgt    0xFC4
                call      DELAY3;         ALLOW FOR FILTERS TO SETTLE AT NEW VOLTAGE.
        ;       call      DELAY3;         ALLOW FOR FILTERS TO SETTLE AT NEW VOLTAGE.
;               return;

                goto      AQ;             RE-ACQUIRE ADC RESULT TO TEST FOR ZERO.

;""""""""""""""""""""""""""""""""""""""""""""""""""""""""""""""""""""""""""""""""""""""""""


AZXF;...............AUTO ZERO X FINE TUNE.....................................



AQ1             bsf       0xFC2,1;        START ADC CONVERSION-SET GO/DONE BIT IN ADCON0
ADF1            btfsc     0xFC2,1;        TEST DONE BIT FOR END OF ADC CONV- SKIP IF DONE
                goto      ADF1;           ADC RESULT NOT READY. TEST AGAIN
                tstfsz    0xFC3;          TEST ADC RESULT LOW-BYTE. SKIP NEXT IF ZERO
                goto      INC1
                return;                   ADC LOW-BYTE=0


INC1            incf      0x6;            ADC NOT ZERO...INCREMENT LSB DAC VAR
                                          ;INCREASE NEG FEEDBACK VOLTAGE
                btfsc     0xFD8,0;        TEST CARRY FLAG FOR OVERFLOW, SKIP IF NO
                incf      0x5;            OVERFLOW. INC 0x5 DAC MSB VAR


;                                         FIRST 8 CONFIG DAC BITS
                bcf       0xF80,5;        CLEAR SYNCX TO ENTER WRITE MODE
                bcf       0xF80,7;        CLEAR DATA TO PROVIDE ALL ZEROS
                bsf       0xF80,6;        SET CLK TO HIGH
                                          ; PULSE; CLK 8 TIMES - CONFIG ON FALLING EDGES
                bcf       0xF80,6;1
                bsf       0xF80,6
                bcf       0xF80,6;2
                bsf       0xF80,6
                bcf       0xF80,6;3
                bsf       0xF80,6
                bcf       0xF80,6;4
                bsf       0xF80,6
                bcf       0xF80,6;5
                bsf       0xF80,6
```

```
                bcf     0xF80,6;6
                bsf     0xF80,6
                bcf     0xF80,6;7
                bsf     0xF80,6
                bcf     0xF80,6;8
                bsf     0xF80,6

;                                       NEXT 8 MSB VARIABLE BITS STROBED TO DAC

                movlw   0x9;            SET REPEAT VARIABLE TO STROBE 8 BITS
                movwf   0x4;

L11             decfsz  0x4;
                goto    STROBE1
                goto    B21
STROBE1         btfss   0x5,7;          TEST VAR MSB
                goto    ZSTR1;          GOTO STROBE ZERO
                bsf     0xF80,7;        SET DATA TO 1 TO STROBE 1
                bcf     0xF80,6;        STROBE PULSE CLK
                bsf     0xF80,6
                rlncf   0x5;            ROTATE VAR LEFT FOR NEXT BIT TO STROBE
                goto    L11

ZSTR1    bcf            0xF80,7;        CLEAR DATA TO STROBE ZERO
                bcf     0xF80,6;        STROBE PULSE CLK
                bsf     0xF80,6
                rlncf   0x5;            ROTATE VAR LEFT FOR NEXT BIT TO STROBE
                goto    L11


;                                       LAST 8 LSB VARIABLE BITS STROBED TO DAC
B21             movlw   0x9;            SET REPEAT VARIABLE TO STROBE 8 BITS
                movwf   0x4;

L21             decfsz  0x4;
                goto    STROBE21
                goto    OUT1
STROBE21        btfss   0x6,7;          TEST VAR MSB
                goto    ZSTR21;         GOTO STROBE ZERO
                bsf     0xF80,7;        SET DATA TO 1 TO STROBE 1
                bcf     0xF80,6;        STROBE PULSE CLK
                bsf     0xF80,6
                rlncf   0x6;            ROTATE VAR LEFT FOR NEXT BIT TO STROBE
                goto    L21

ZSTR21   bcf            0xF80,7;        CLEAR DATA TO STROBE ZERO
                bcf     0xF80,6;        STROBE PULSE CLK
                bsf     0xF80,6
                rlncf   0x6;            ROTATE VAR LEFT FOR NEXT BIT TO STROBE
                goto    L21



OUT1            bsf     0xF80,5;        SET SYNCX TO ENTER NORMAL MODE

                movlw   0xC8
                cpfsgt  0xFC4
                call    DELAY3;         ALLOW FOR FILTERS TO SETTLE AT NEW VOLTAGE.

                goto    AQ1;            RE-ACQUIRE ADC RESULT TO TEST FOR ZERO.

;:::::::::::::::::::::::::::::::::::::::::::::::::::::::::::::::::::::::::::::::::::


                end
```

# Appendix C

## Matlab function script

```
function [Axout, Ayout]=Chcorrect (Chx, Chy)

Cxy=0.02;
Cyx=0.02;
Sy=0.405;
Sx=0.405;

for n=1:length(Chx);

    %Gain correct each channel
    Chxc(n)=Chx(n)/3.33;
    Chyc(n)=Chy(n)/3.33;

    %Adjust for cross-axis sensitivity
    Ayo(n)=((Chyc(n)/Sy)-((Chxc(n)/Sx)*Cxy))/(1-(Cxy*Cyx));
    Axo(n)=(Chxc(n)/Sx)-(Ayo(n)*Cyx);

    %Adjust for outputs in m/s^2

    Ayout(n)=Ayo(n)*9.81;
    Axout(n)=Axo(n)*9.81;


end
```

# Appendix D

## Mechanical drawings

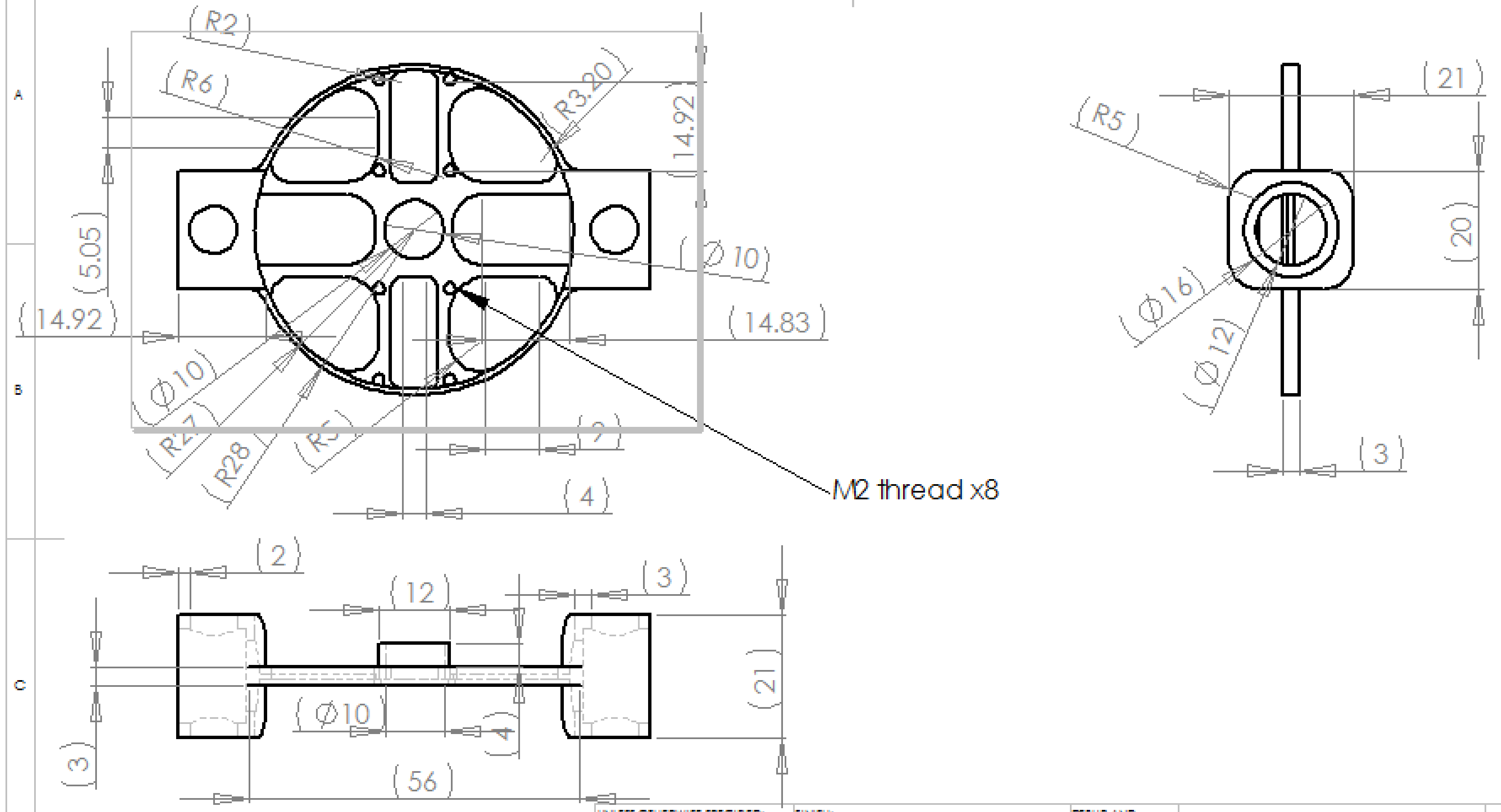

UNLESS OTHERWISE SPECIFIED:
DIMENSIONS ARE IN MILLIMETERS
SURFACE FINISH:
TOLERANCES:
LINEAR:
ANGULAR:

FINISH:

DEBUR AND
BREAK SHARP
EDGES

DO NOT SCALE DRAWING

REVISION: 3

PANOS

|  | NAME | SIGNATURE | DATE |
|---|---|---|---|
| DRAWN |  |  |  |
| CHK'D |  |  |  |
| APPV'D |  |  |  |
| MFG |  |  |  |
| Q.A |  |  |  |

TITLE:

MATERIAL: Aluminium

DWG NO.

A4

WEIGHT:

SCALE:1:1

SHEET 1 OF 1

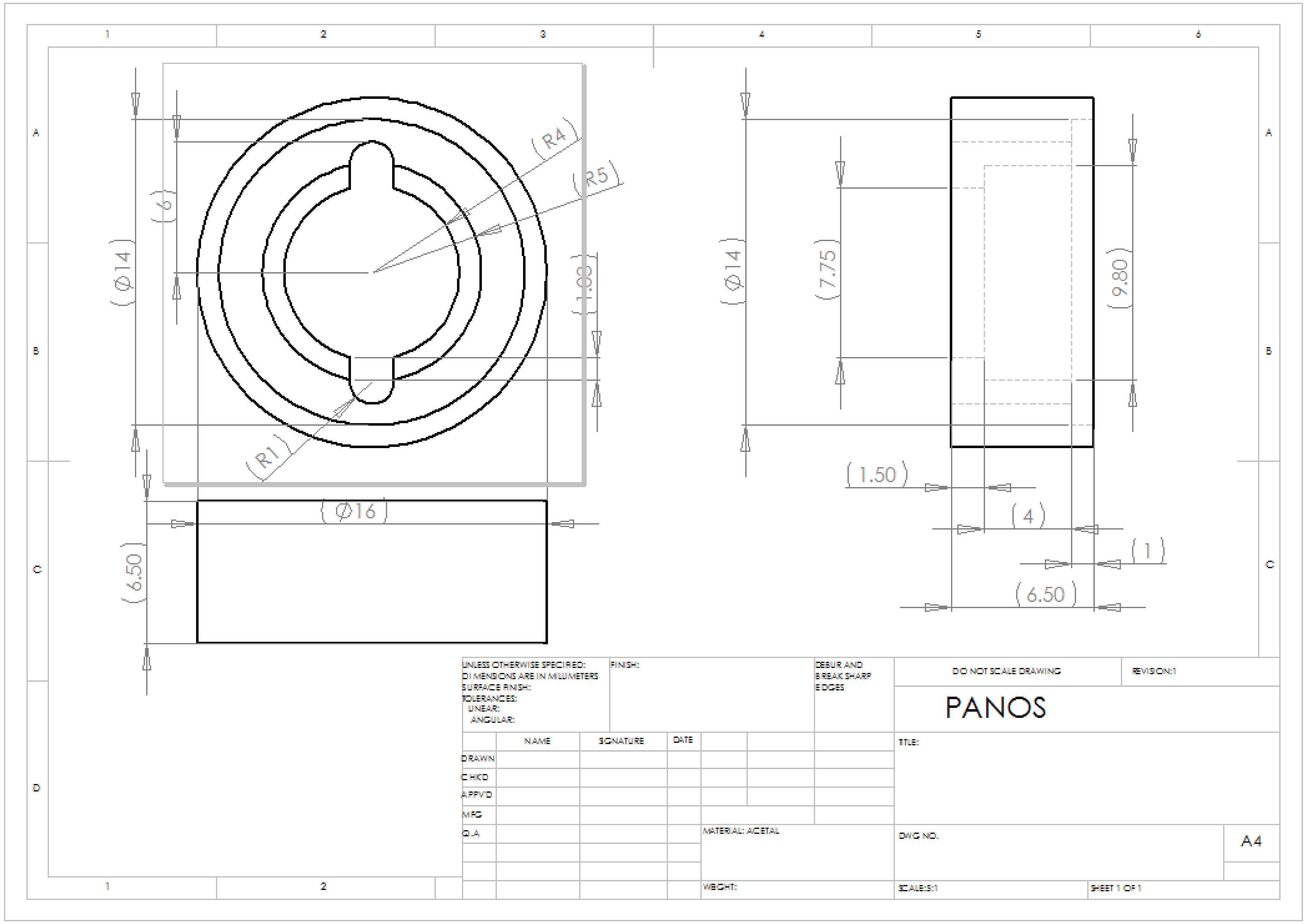
1
2
3
4
5
6
A
B
C
D
R4
R5
6
Ø14
1.00
R1
Ø16
6.50
Ø14
7.75
9.80
1.50
4
1
6.50
UNLESS OTHERWISE SPECIFIED:
DIMENSIONS ARE IN MILLIMETERS
SURFACE FINISH:
TOLERANCES:
LINEAR:
ANGULAR:
FINISH:
DEBUR AND BREAK SHARP EDGES
DO NOT SCALE DRAWING
REVISION:1
PANOS
NAME
SIGNATURE
DATE
DRAWN
CHKD
APPV'D
MFG
Q.A
TITLE:
MATERIAL: ACETAL
DWG NO.
A4
WEIGHT:
SCALE:5:1
SHEET 1 OF 1

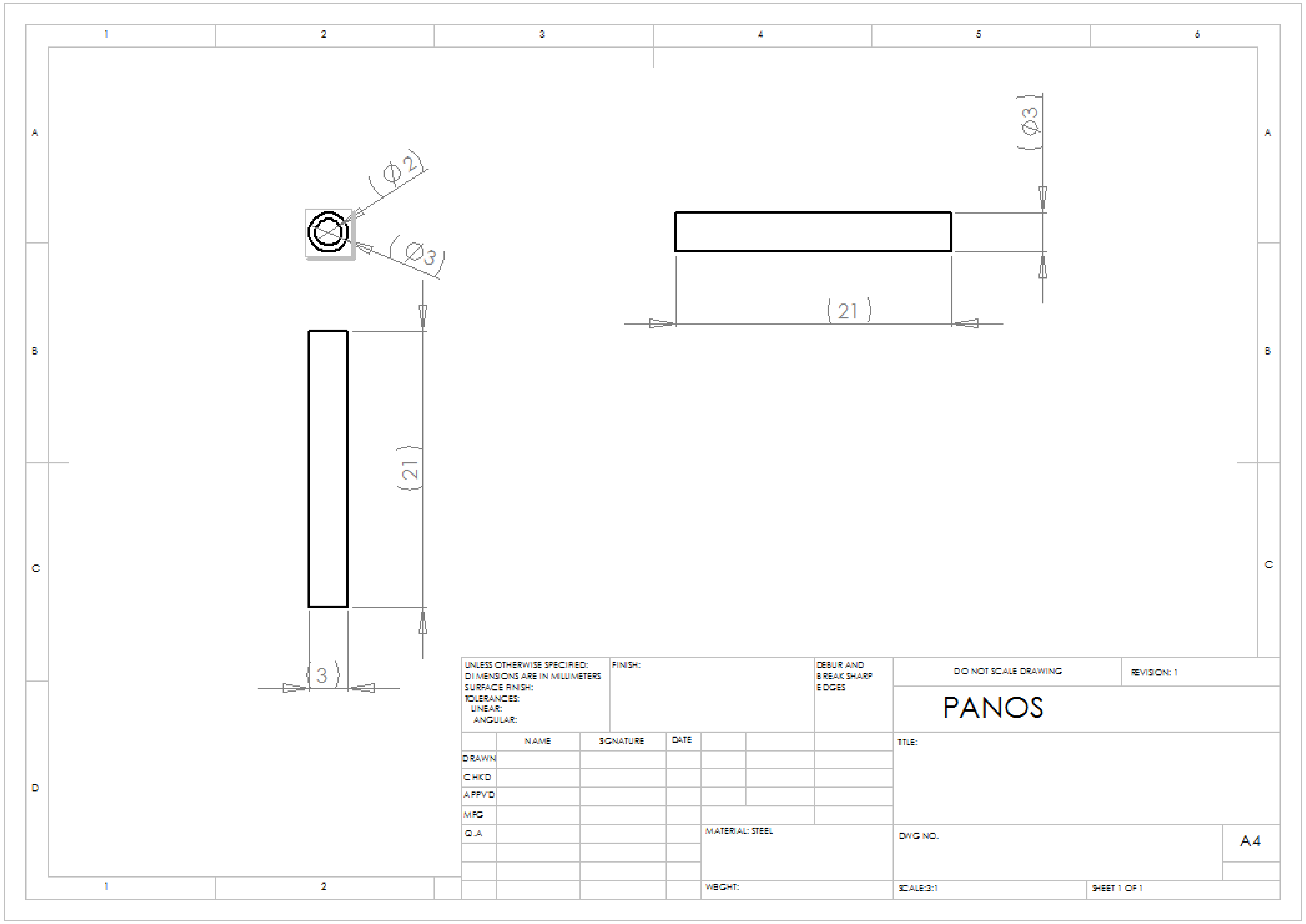

UNLESS OTHERWISE SPECIFIED:
DIMENSIONS ARE IN MILLIMETERS
SURFACE FINISH:
TOLERANCES:
LINEAR:
ANGULAR:

FINISH:

DEBUR AND
BREAK SHARP
EDGES

DO NOT SCALE DRAWING

REVISION: 1

PANOS

| | NAME | SIGNATURE | DATE |
|---|---|---|---|
| DRAWN | | | |
| CHK'D | | | |
| APPV'D | | | |
| MFG | | | |
| Q.A | | | |

TITLE:

MATERIAL: STEEL

DWG NO.

A4

WEIGHT:

SCALE:3:1

SHEET 1 OF 1

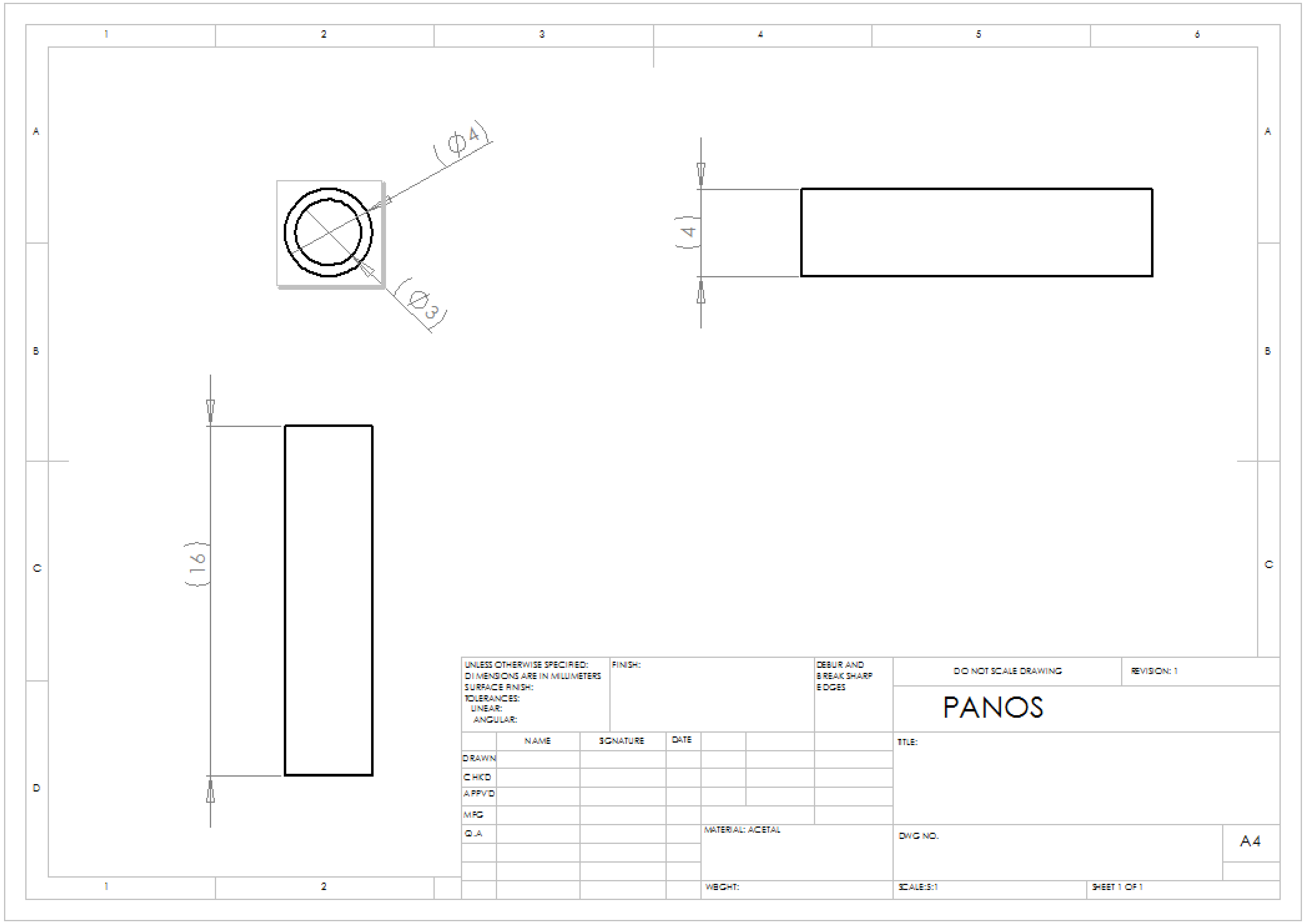
⌀4
⌀3
4
16
1
2
3
4
5
6
A
B
C
D
UNLESS OTHERWISE SPECIFIED:
DIMENSIONS ARE IN MILLIMETERS
SURFACE FINISH:
TOLERANCES:
LINEAR:
ANGULAR:
FINISH:
DEBUR AND BREAK SHARP EDGES
DO NOT SCALE DRAWING
REVISION: 1
PANOS
NAME
SIGNATURE
DATE
DRAWN
CHK'D
APPV'D
MFG
Q.A
TITLE:
MATERIAL: ACETAL
DWG NO.
A4
WEIGHT:
SCALE:5:1
SHEET 1 OF 1

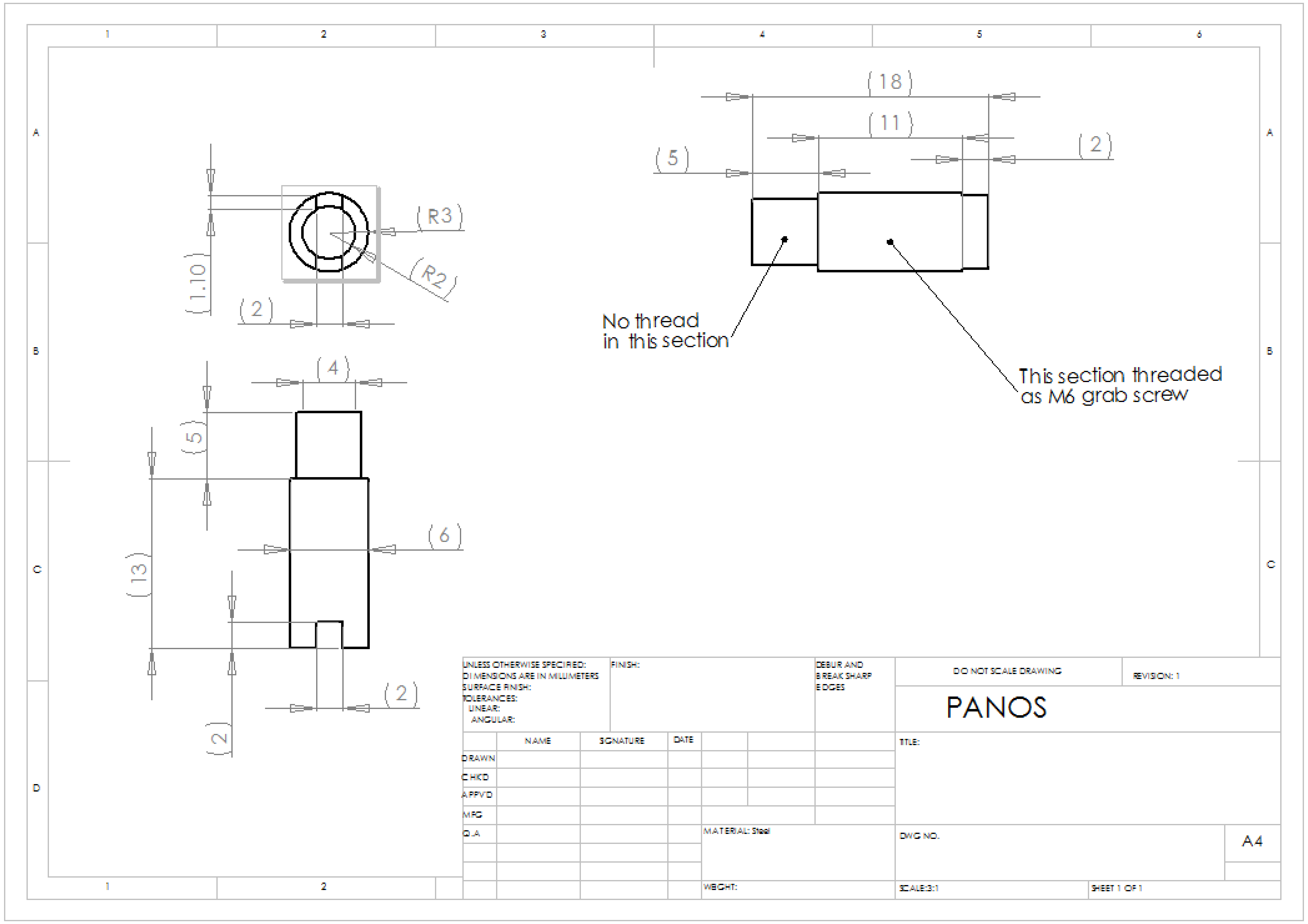 
(18)
(11)
(5)
(2)
No thread in this section
This section threaded as M6 grab screw
(R3)
(R2)
(1.10)
(2)
(4)
(5)
(6)
(13)
(2)
(2)
UNLESS OTHERWISE SPECIFIED:
DIMENSIONS ARE IN MILLIMETERS
SURFACE FINISH:
TOLERANCES:
LINEAR:
ANGULAR:
FINISH:
DEBUR AND BREAK SHARP EDGES
DO NOT SCALE DRAWING
REVISION: 1
PANOS
NAME
SIGNATURE
DATE
DRAWN
CHK'D
APPV'D
MFG
Q.A
TITLE:
MATERIAL: Steel
DWG NO.
A4
WEIGHT:
SCALE:3:1
SHEET 1 OF 1

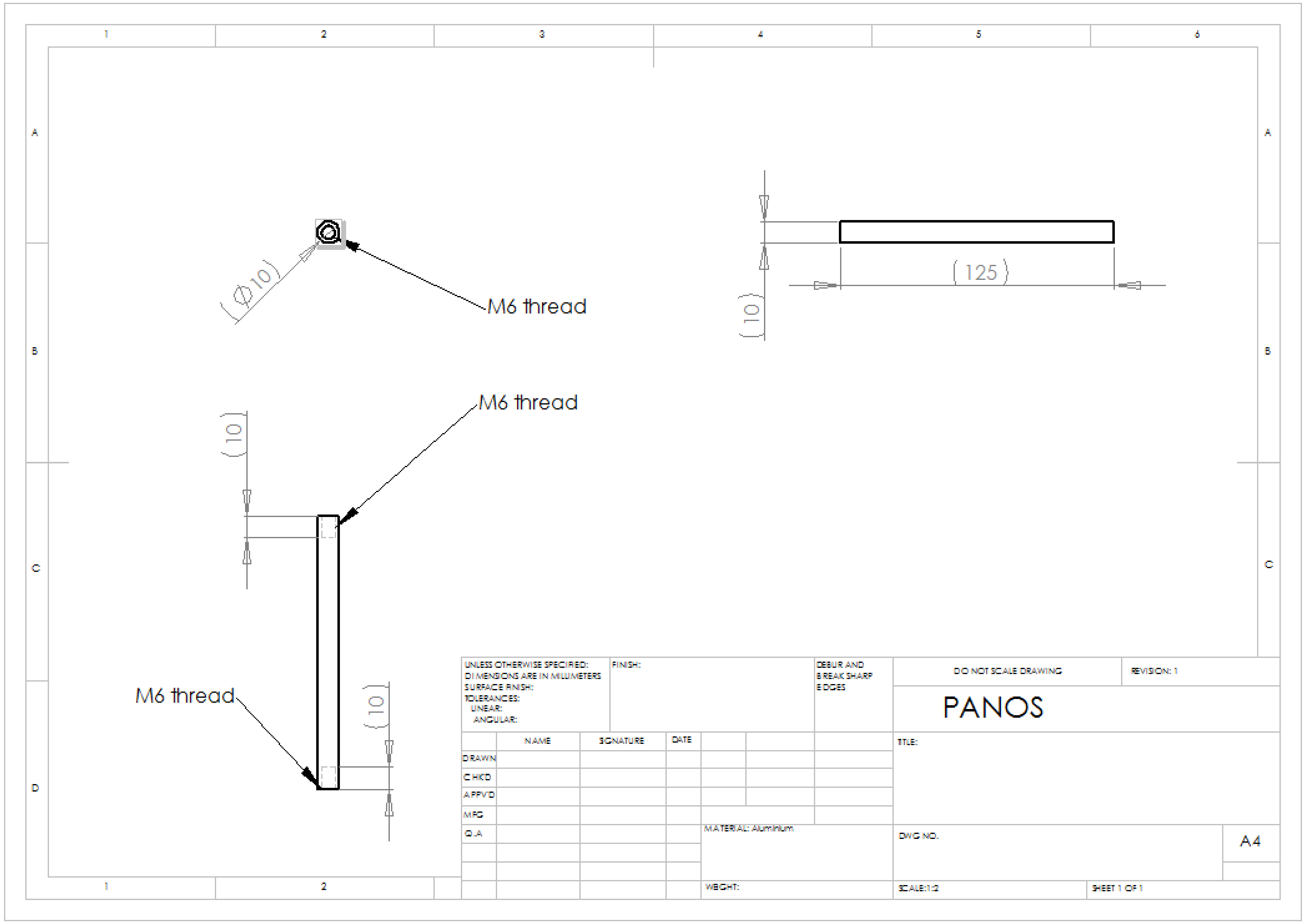
(Ø10)
M6 thread
(125)
(10)
M6 thread
(10)
M6 thread
(10)
UNLESS OTHERWISE SPECIFIED:
DIMENSIONS ARE IN MILLIMETERS
SURFACE FINISH:
TOLERANCES:
LINEAR:
ANGULAR:
FINISH:
DEBUR AND BREAK SHARP EDGES
DO NOT SCALE DRAWING
REVISION: 1
PANOS
NAME
SIGNATURE
DATE
DRAWN
CHK'D
APPV'D
MFG
Q.A
MATERIAL: Aluminium
WEIGHT:
TITLE:
DWG NO.
A4
SCALE:1:2
SHEET 1 OF 1

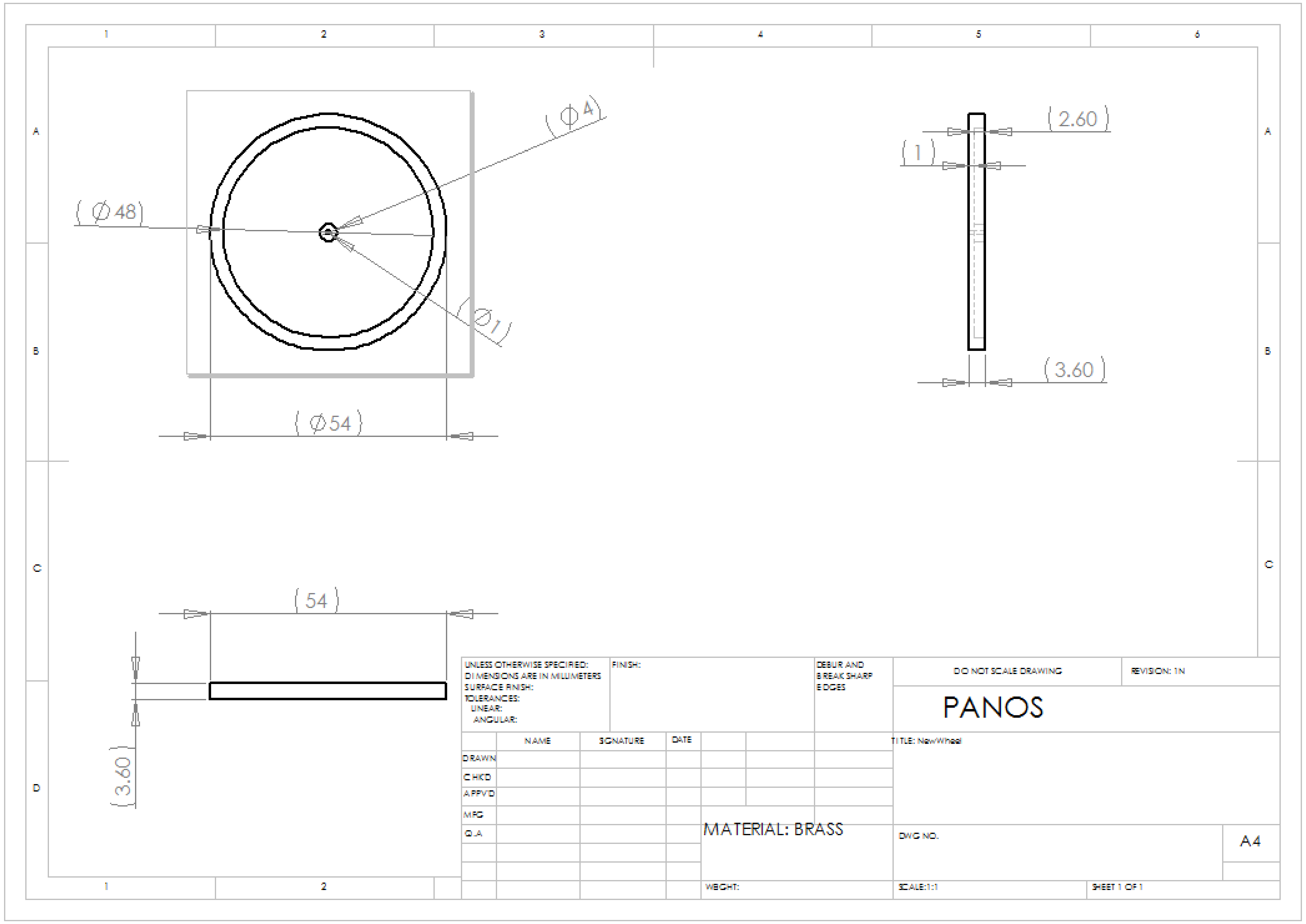
(Ø4)
(Ø48)
(Ø1)
(Ø54)
(2.60)
(1)
(3.60)
(54)
(3.60)
UNLESS OTHERWISE SPECIFIED:
DIMENSIONS ARE IN MILLIMETERS
SURFACE FINISH:
TOLERANCES:
LINEAR:
ANGULAR:
FINISH:
DEBUR AND BREAK SHARP EDGES
DO NOT SCALE DRAWING
REVISION: 1N
PANOS
NAME
SIGNATURE
DATE
DRAWN
CHK'D
APPV'D
MFG
Q.A
TITLE: NewWheel
MATERIAL: BRASS
DWG NO.
A4
WEIGHT:
SCALE:1:1
SHEET 1 OF 1

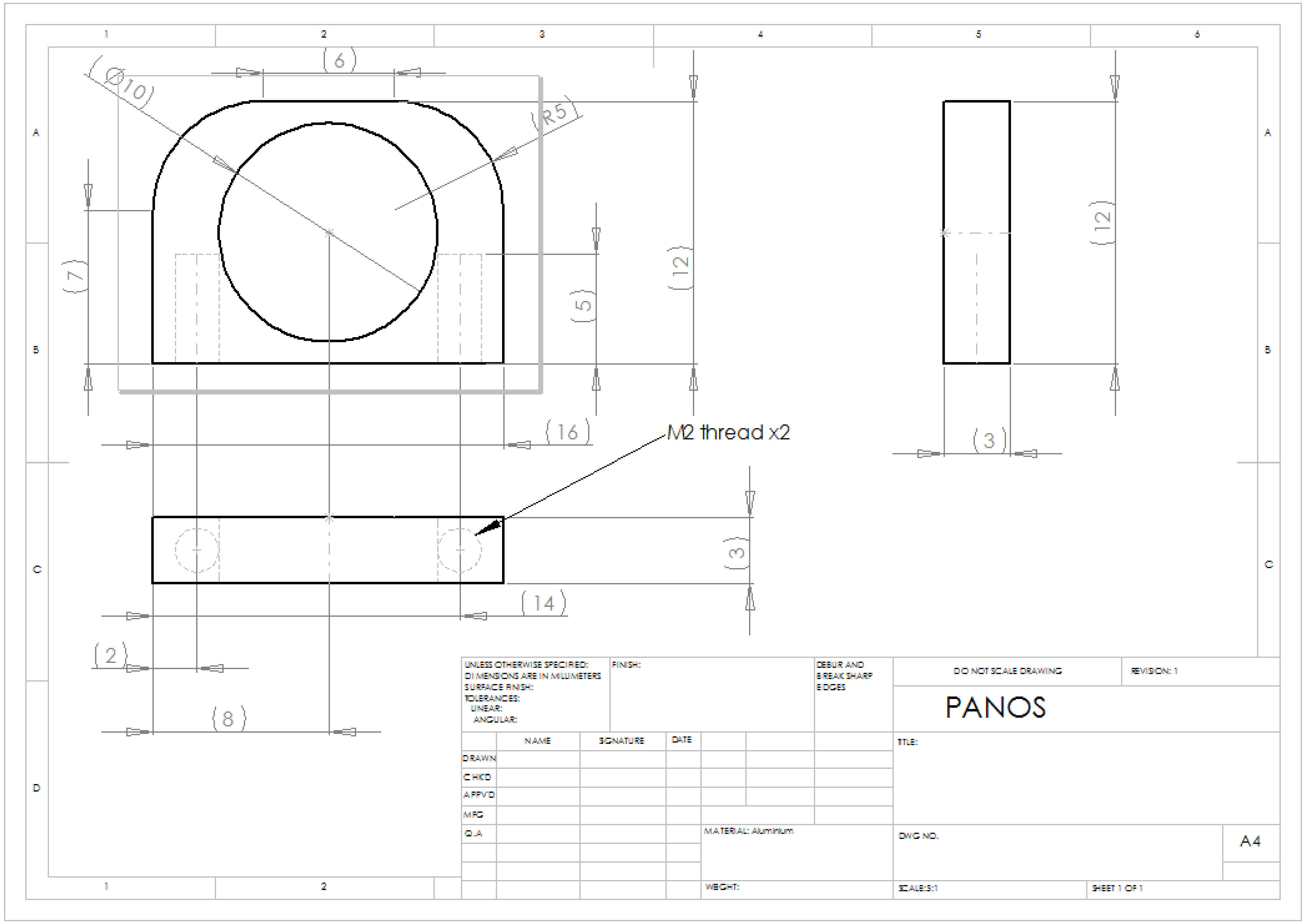

Ø10
6
R5
7
5
12
12
3
16
14
3
2
8
M2 thread x2
UNLESS OTHERWISE SPECIFIED:
DIMENSIONS ARE IN MILLIMETERS
SURFACE FINISH:
TOLERANCES:
LINEAR:
ANGULAR:
FINISH:
DEBUR AND BREAK SHARP EDGES
DO NOT SCALE DRAWING
REVISION: 1
PANOS
NAME
SIGNATURE
DATE
DRAWN
CHK'D
APPV'D
MFG
Q.A
TITLE:
MATERIAL: Aluminium
DWG NO.
A4
WEIGHT:
SCALE:5:1
SHEET 1 OF 1

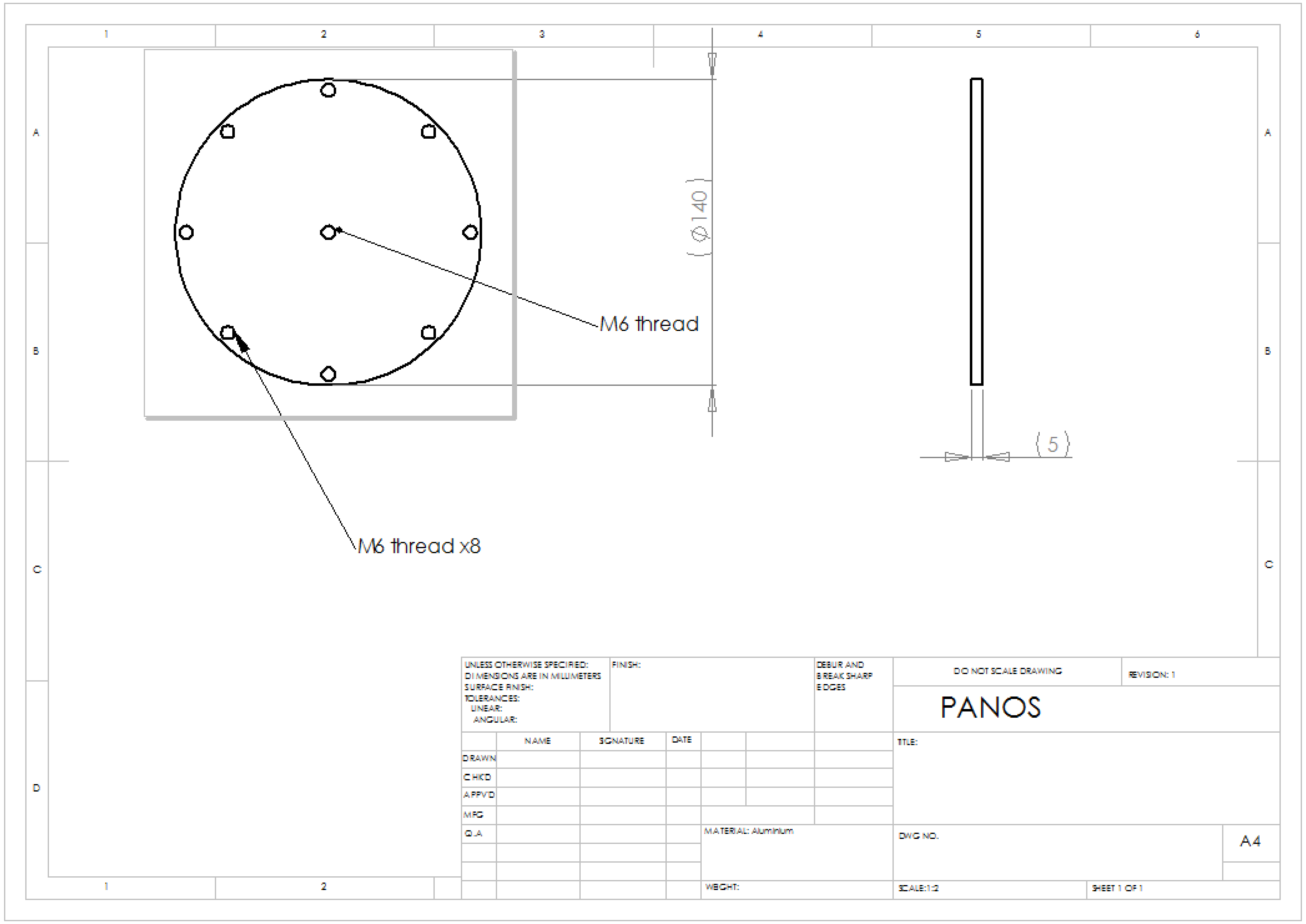
1
2
3
4
5
6
A
B
C
D
(Ø140)
M6 thread
M6 thread x8
(5)
UNLESS OTHERWISE SPECIFIED:
DIMENSIONS ARE IN MILLIMETERS
SURFACE FINISH:
TOLERANCES:
LINEAR:
ANGULAR:
FINISH:
DEBUR AND BREAK SHARP EDGES
DO NOT SCALE DRAWING
REVISION: 1
PANOS
NAME
SIGNATURE
DATE
DRAWN
CHK'D
APPV'D
MFG
Q.A
TITLE:
MATERIAL: Aluminium
DWG NO.
A4
WEIGHT:
SCALE:1:2
SHEET 1 OF 1

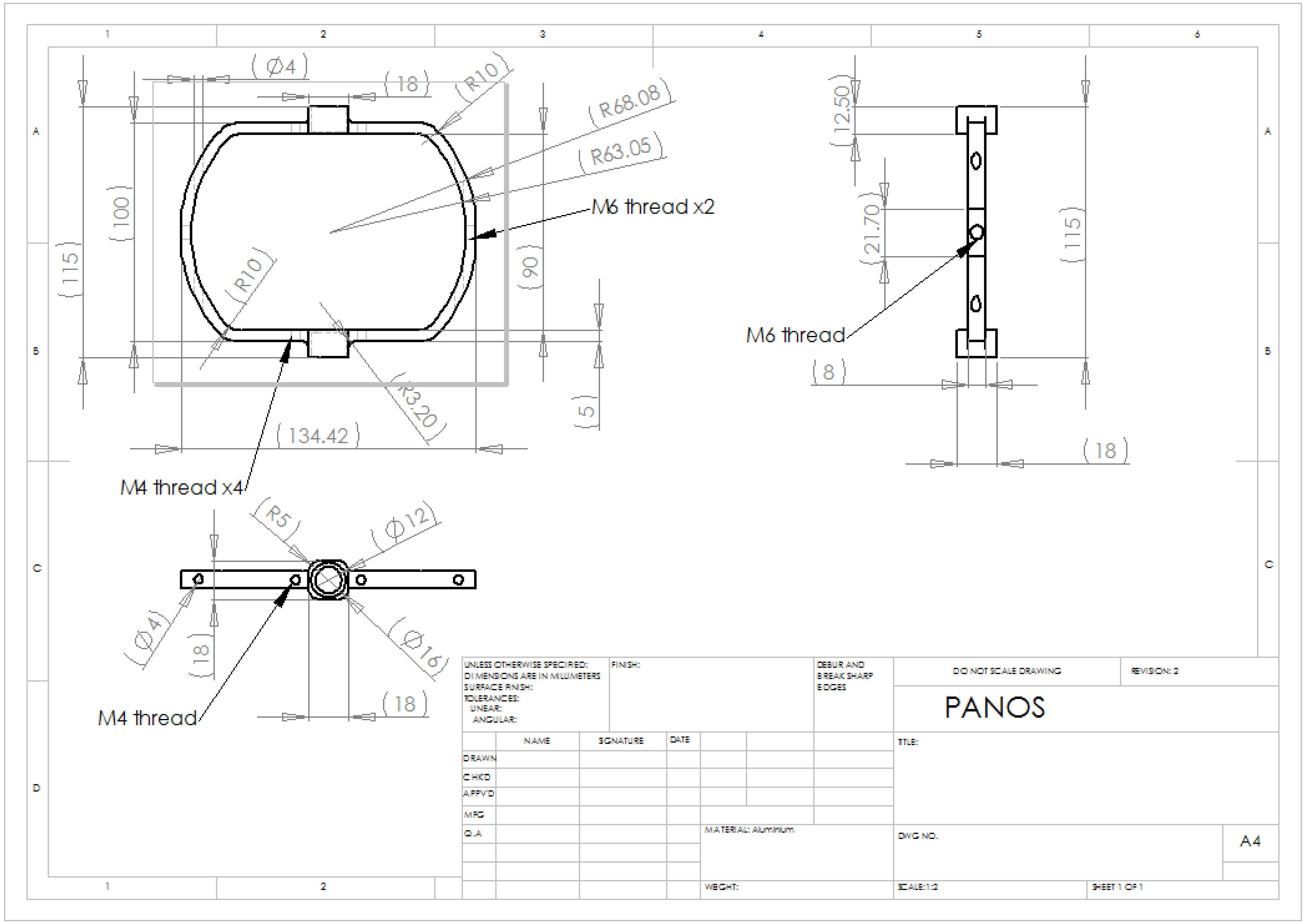

UNLESS OTHERWISE SPECIFIED:
DIMENSIONS ARE IN MILLIMETERS
SURFACE FINISH:
TOLERANCES:
LINEAR:
ANGULAR:

FINISH:

DEBUR AND BREAK SHARP EDGES

DO NOT SCALE DRAWING

REVISION: 2

PANOS

| | NAME | SIGNATURE | DATE |
|---|---|---|---|
| DRAWN | | | |
| CHK'D | | | |
| APPV'D | | | |
| MFG | | | |
| Q.A | | | |

TITLE:

MATERIAL: Aluminium

DWG NO.

A4

WEIGHT:

SCALE:1:2

SHEET 1 OF 1

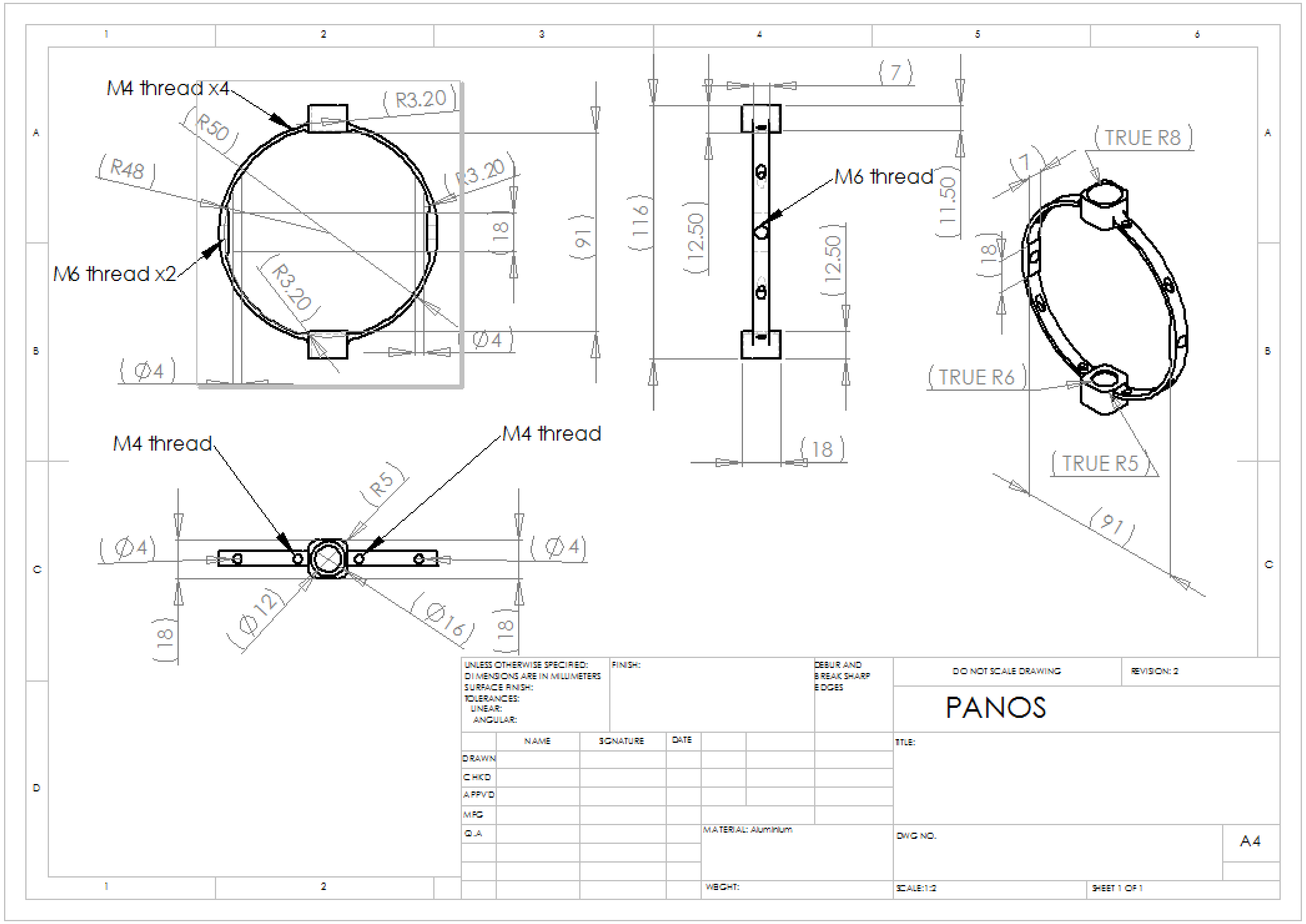

UNLESS OTHERWISE SPECIFIED:
DIMENSIONS ARE IN MILLIMETERS
SURFACE FINISH:
TOLERANCES:
LINEAR:
ANGULAR:

FINISH:

DEBUR AND
BREAK SHARP
EDGES

DO NOT SCALE DRAWING

REVISION: 2

PANOS

| | NAME | SIGNATURE | DATE |
|---|---|---|---|
| DRAWN | | | |
| CHKD | | | |
| APPV'D | | | |
| MFG | | | |
| Q.A | | | |

TITLE:

MATERIAL: Aluminium

DWG NO.

A4

WEIGHT:

SCALE:1:2

SHEET 1 OF 1